Direct Photon Tagged Jets in 200 GeV Au+Au Collisions at PHENIX

A Dissertation Presented

by

Megan Elizabeth Connors

to

The Graduate School

in Partial Fulfillment of the Requirements

for the Degree of

Doctor of Philosophy

in

Physics

Stony Brook University

December 2011

Stony Brook University

The Graduate School

Megan Elizabeth Connors

We, the dissertation committee for the above candidate for the Doctor of Philosophy degree, hereby recommend acceptance of this dissertation.

Professor Barbara V. Jacak – Dissertation Advisor
Department of Physics and Astronomy, Stony Brook University

Professor Alan Calder – Chairperson of Defense
Department of Physics and Astronomy, Stony Brook Univeristy

Professor Derek Teaney
Department of Physics and Astronomy, Stony Brook University

Dr. Michael J. Tannenbaum
Physics Division, Brookhaven National Laboratory

This dissertation is accepted by the Graduate School.

Lawrence Martin
Dean of the Graduate School

Abstract of the Dissertation

Direct Photon Tagged Jets in 200 GeV Au+Au Collisions at PHENIX

by

Megan Elizabeth Connors

Doctor of Philosophy

in

Physics

Stony Brook University

2011

A hot dense medium called the quark gluon plasma (QGP) has been created at the Relativistic Heavy Ion Collider (RHIC). Quarks and gluons are deconfined in the QGP state, but many of its properties are still under investigation. One interesting observation is that high momentum partons (quarks and gluons), which result from hard scatterings in the initial collision, lose energy as they travel through the medium. These partons fragment into the particles observed in the detector. Since fully reconstructing all the "jet" particles associated with the initial parton is complicated by the high multiplicity background produced in heavy-ion collisions, two particle correlations which trigger on a high momentum, p_T, particle and measure the yield of associated particles in the event as a function of the azimuthal angle, $\Delta\phi$, are used instead.

Di-hadron correlations are useful for observing suppression of the away-side ($\Delta\phi > \pi/2$) jet yield and some features potentially due to the medium's response to the lost energy. However, the hadron triggers, since they are fragments of a modified jet themselves, are biased to be near the surface of the medium and the jet energy is unknown. Since photons do not interact via the strong force, they are unmodified by the medium and provide an unbiased trigger. Direct photons result directly from the hard scattering. They balance the energy of the opposing parton and provide knowledge of the opposing jet momentum. Therefore, by measuring the hadron yield on the away-side, opposite the direct photon trigger, the jet fragmentation function, which describes how partons fragment into hadrons, can be measured as a function of $z_T = p_T^h/p_{T\gamma}$. By comparing the spectra in Au+Au collisions to that in p+p collisions, the effective modifications of the fragmentation function can be quantified.

Using the data collected by PHENIX during the 2007 RHIC Run, suppression of the away-side yield and the modified fragmentation function is measured via direct photon-hadron correlations. By including lower p_T hadrons in the measurement, the altered shape of the modified fragmentation function is studied. Possible enhancement of the lowest z_T particles suggests that the energy lost at high p_T is redistributed to low p_T particle production.

Dedication

For Mom, Dad, Dave and Riley...
May we too be equally great parents and role models so that our daughter
can achieve her dreams.

Contents

List of Figures

xi

xiv

List of Tables

Acknowledgements

This whole experience has been made more enjoyable by being part of great group. I owe many thanks to the Stony Brook RHIC group of past and present for all the coding advise and great (physics and non-physics) conversations. In particular, I am indebted to the SB γ-jet team. Justin Frantz has been a great teacher, collaborator and friend to me. Not only did he teach me about PHENIX coding and direct photons, but also about important unix commands such as awk. Matt Nguyen whose own thesis shows that he is the true γ-jet king. I thank him for all the code he has pointed me to, all the knowledge he has passed along and for making all my root canvases white. Justin and Matt are responsible for the crazy complex and ever evolving code which I think I have managed to make even uglier. My results rely heavily on their early work and I thank them for their quick responses and constant support and advice. Finally, the flow master, John Chen for his contributions to the γ-jet analysis as well as all our physics debates and food adventures. This team made all those crazy late nights a lot of fun and I feel privileged to have been part of such an amazing group. There are a few people beyond this group that have contributed to the results of this thesis who I also need to acknowledge, including my QM09 shepard, Anne Sickles, who continues to be a great friend and confidant. Anne and Andrew Adare's hard work regarding the hadron efficiencies is greatly appreciated and eased the QM craziness, a bit. Thank you to Ali, another γ-jetter, for reading my first thesis draft.

A special thank you to my advisor, Barbara, for all your guidance and advice and for helping me to develop into the scientist I am today.

Thank you to my committee members, for your flexibility and understanding nature as well as Mike Tannenbaum for his involvement and enthusiasm regarding this work.

To all my friends and family for all of their support throughout this process. Dave has been amazingly supportive through all my late night coding, traveling, and cranky moods. I am lucky to have such a wonderful husband and friend. To Riley for her harsh but cute comments on my thesis and making sure I made time for play.

Chapter 1

Introduction

Bang! The universe is born! As the universe rapidly expands, quarks and gluons move around freely in a soupy plasma. As the universe begins to cool, just one microsecond after birth, the quarks and gluons become bound together to form the building blocks of the matter we know today, in a universe approximately 12-15 billion years old. Can this primordial soup be created in a world which is now so different? If so, what are the properties of this medium? Such an unexplored state of matter leads to so many questions with unknown potential implications, it should not be surprising that a vibrant field of research has formed around it. A single thesis, of course, cannot even attempt to address all the questions associated with such an intriguing area of research. Presented here is simply one piece of the giant jigsaw puzzle which will some day reveal the state of our universe in its infancy. First, we start with a review of what is known about this matter, starting with some background on the interactions of these fundamental particles.

1.1 QCD and confinement

Quantum Chromodynamics (QCD) describes the interactions of the strong force between the color charged quarks and gluons and is analogous to the theory which describes the electro-magnetic force, Quantum Electrodynamics (QED). The QCD Lagrangian [20] is

$$L = \sum_q \bar{\psi}_{q,a}(i\gamma^\mu \partial_\mu \delta_{ab} - g_s\gamma^\mu t_{ab}^C A_\mu^C - m_q\delta_{ab})\psi_{q,b} - \frac{1}{4}F_{\mu\nu}^A F^{A\mu\nu} \qquad (1.1)$$

where $\psi_{q,a}$ are quark-field spinors for a quark of flavor q and mass m_q. The color-index, a, goes from 1 to 3 since the quark can be one of three colors. The

gluon fields are given by A_μ^C. Here C goes from 1 to 8 since there are actually 8 types of gluons. This term is necessary because the gluon fields can interact with themselves which is different from QED. The γ^μ are simply the Dirac γ-matrices and the t_{ab}^C are the eight 3x3 matrices which are the generators of the SU(3) color group. QCD is the SU(3) component of the SU(3)xSU(2)xU(1) Standard Model of particle physics.

The coupling constant, α, is scale dependent in both QED and QCD. This means the strength depends on the momentum transfer, Q, at which you measure it. In QED the coupling constant increases with increasing momentum. However, in QCD the coupling actually drops with increasing momentum and increases dramatically at low Q as shown in Fig. 1.1. This leads to the confinement of quarks and gluons into hadrons under the normal conditions of our current universe. If you tried to pull the quarks apart, which requires exceeding the large coupling, α_s, you put enough energy into the system to produce a new quark anti-quark pair from the vacuum. Therefore, all quarks and gluons are currently bound within color neutral mesons and baryons. Mesons are composed of a quark and anti-quark while baryons consist of 3 quarks. However, at higher Q, the coupling decreases and asymptotic freedom is achieved resulting in unbound quarks and gluons.

In perturbative QCD, (pQCD), the coupling constant, α_s, can be expressed using the renormalization scale, μ_R, as

$$\mu \frac{\delta \alpha_s}{\delta \mu} \quad = \quad 2\beta\left(\alpha_s\right) \tag{1.2}$$

$$= \quad -\frac{\beta_0}{2\pi}\alpha_s^2 - \frac{\beta_1}{4\pi^2}\alpha_s^3 - \frac{\beta_2}{64\pi^3}\alpha_s^4 - \cdots , \tag{1.3}$$

where

$$\beta_0 = 11 - \frac{2}{3}n_f, \tag{1.4}$$

$$\beta_1 = 51 - \frac{19}{3}n_f, \tag{1.5}$$

$$\beta_2 = 2857 - \frac{5033}{9}n_f + \frac{325}{27}n_f^2. \tag{1.6}$$

The b_n terms actually depend on the renormalization scheme used. The equations given here are for the commonly used modified minimal subtraction
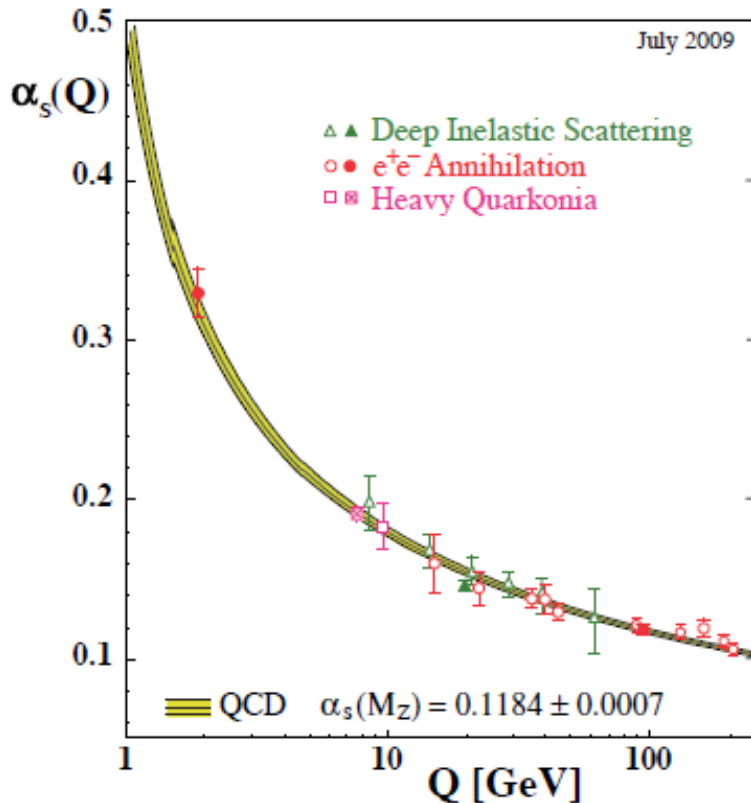
Figure 1.1: The coupling constant as a function of the momentum transfer from pQCD along with various experimental measurements. The world average for the coupling strength at the Z boson mass is also given in the plot.

scheme [21]. The negative sign in Eqn. 1.3 leads to the asymptotic freedom. To first order, b_0,

$$\alpha_s(\mu) = \frac{1}{b_0 ln(Q^2/\Lambda^2)}. \tag{1.7}$$

The analytic solution in terms of the modified minimal subtraction scheme including higher order terms can be written as

$$\alpha_s(\mu) = \frac{4\pi}{\beta_0 \ln\left(\mu^2/\Lambda_{QCD}^2\right)} \left[1 - \frac{2\beta_1}{\beta_0^2} \frac{\ln\left[\ln\left(\mu^2/\Lambda_{QCD}^2\right)\right]}{\ln\left(\mu^2/\Lambda_{QCD}^2\right)} + \frac{4\beta_1^2}{\beta_0^4 \ln\left(\mu^2/\Lambda_{QCD}^2\right)} \right.$$
$$\left. \times \left(\left(\ln\left[\ln\left(\mu^2/\Lambda_{QCD}^2\right)\right] - \frac{1}{2} \right)^2 + \frac{\beta_2\beta_0}{8\beta_1^2} - \frac{5}{4} \right) \right]. \tag{1.8}$$

1.2 Formation of the Quark Gluon Plasma
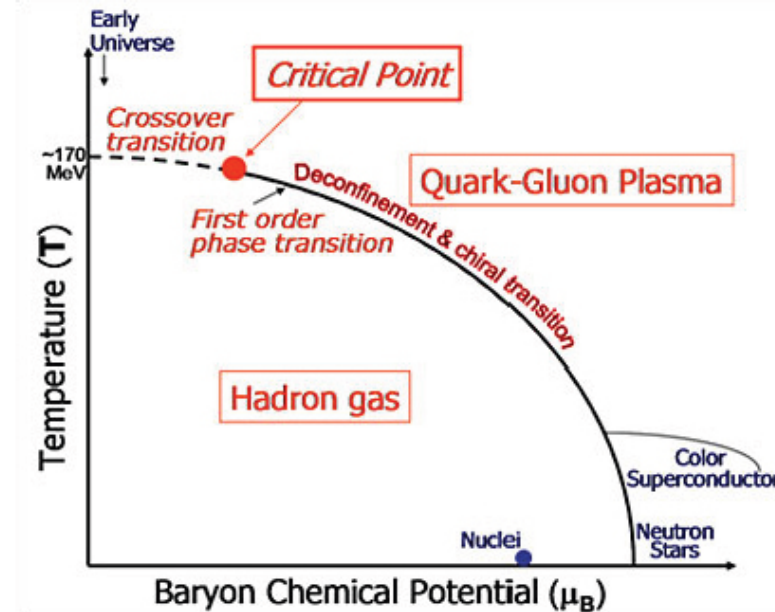
Figure 1.2: QCD phase diagram

Although under the current conditions of the universe quarks and gluon are confined in hadrons, under extremely high density and temperature, like that which existed shortly after the Big Bang, deconfinement can occur. A

4

cartoon of the QCD phase diagram is shown in Fig. 1.2. These conditions can be achieved in high energy collisions between heavy ions. At the Relativistic Heavy Ion Collider (RHIC), which will be described in more detail in the experimental section, Au ions are collided at 200 GeV per nucleon pair. When accelerated to relativistic speeds, the ions become Lorentz contracted and are then collided. The stages of the collision are depicted in Fig. 1.3. Initial collisions between nucleons produce high momentum particles that are later used as probes of the produced hot dense matter. The other particles in the overlapping collision area thermalize and create a hot dense medium in which quarks and gluons are deconfined. This state is referred to as the quark gluon plasma (QGP). As the system expands and cools, the partons hadronize into confined states via fragmentation and recombination. The hadron gas continues to expand and cool until freeze out occurs, when there is no longer an interacting system of particles. The particles then continue on an outward trajectory, and some of them may decay before finally hitting the detectors.
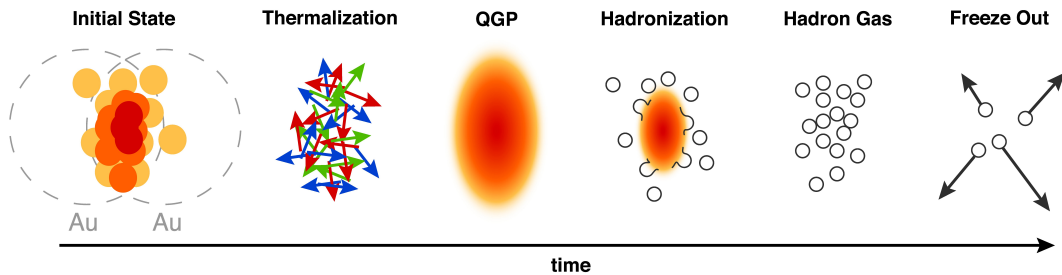
Figure 1.3: Stages of a heavy ion collision from the initial collision geometry to freeze out of particles, which eventually hit the detectors [1].

Evidence that RHIC has created the QGP in collisions at 200GeV are discussed in the following sections. It is interesting to also note that RHIC has now undertaken a search for the critical point shown in Fig. 1.2 by varying the energy of the Au+Au collisions. This low energy scan should help to map out more clearly where these transitions occur and result in a more complete QCD phase diagram.

1.2.1 Elliptic Flow

Since the colliding ions do not always hit directly head on, there is an overlap region of interacting partons as shown in Fig. 1.4. We refer to events where the ions collide nearly head on, with a large overlap, as central events and collisions with smaller overlap as peripheral. Particularly for semi-central collisions, the shape of the overlapping region is elliptical, as illustrated in Fig. 1.4. This
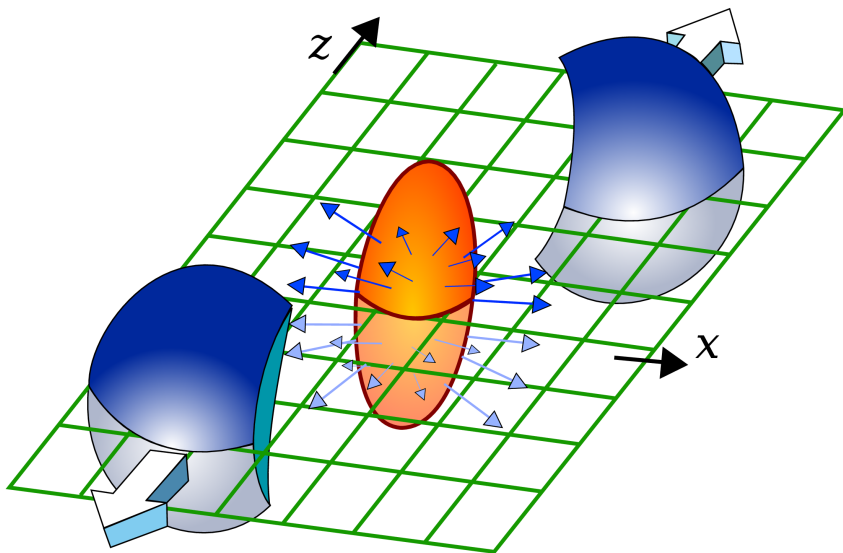
Figure 1.4: The reaction plane of the collision is shown here for a collision in which the overlap region has an almond like shape. This anisotropy results in flow of particles in the direction of the reaction plane. The reaction plane is defined by the direction of the beams, z, and the impact parameter which connects the centers of the colliding nuclei and happens to be along the x direction in this plot.

"almond-shape" results in a spatial anisotropy which causes an anisotropy in momentum space. The pressure gradient causes more particles to flow along the direction of the reaction plane. This effect is called elliptic flow and can be quantified by v_2 which is defined as

$$v_2 \Psi_2 = \langle \cos(2(\phi - \Psi_2)) \rangle. \qquad (1.9)$$

ϕ is the azimuthal angle with respect to the reaction plane angle, Ψ_2 which is defined by the beam direction, z, and the impact parameter which is the line connecting the center of the colliding nuclei. The reaction plane is drawn as a grid in Fig. 1.4.

Evidence of Quark Deconfinement

The experiments at RHIC have measured v_2 for a variety of identified hadrons, as shown in Fig. 1.5, including mesons and baryons of various masses [2]. The distributions seem to cluster into two distinct groups. It is most notable when plotted versus the kinetic energy, KE_T, measured transverse to the beam direction. These groups seem to be defined by the number of valence quarks in the particle. The mesons, (pions and kaons), form one cluster while the baryons, (Λ, Ξ and protons) form the other.
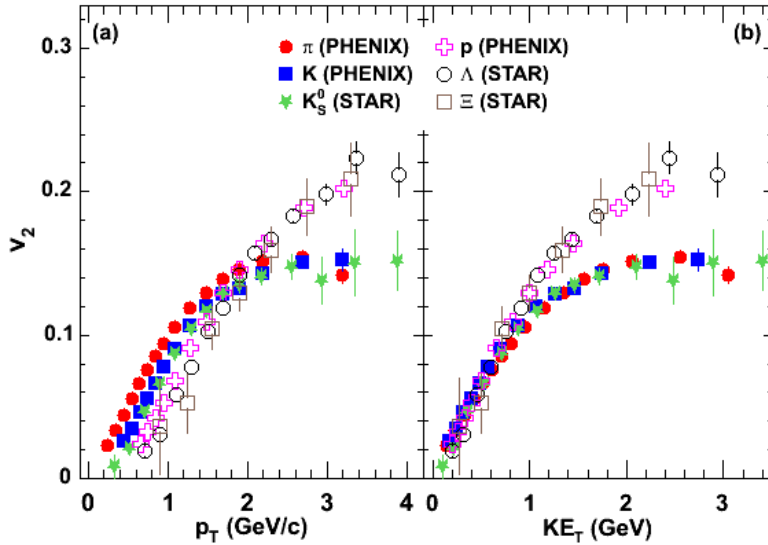
Figure 1.5: v_2 as a function of transverse momentum and energy [2].

If the v_2 is scaled by the number of valence quarks, n_q, for the measured particle and plotted as a function of the scaled transverse kinetic energy, KE_T/n_q, the hadrons all appear to lie on one universal curve, as shown in Fig. 1.6. This feature shows that v_2 depends on the number of valence quarks which indicates that the quarks themselves, not the hadrons, are flowing. Therefore, the quarks must be deconfined when the flow is built up, which is indicative of a quark-gluon plasma phase. The elliptic flow is described well by hydrodynamics which indicates the medium has liquid properties [2]. Another property of the plasma, temperature, has also been measured to be consistent with expectations from lattice QCD for the QGP phase i.e. the temperature of the produced medium is greater than the critical temperature required to achieve deonfinement. This measurement is discussed later in Section 1.4.
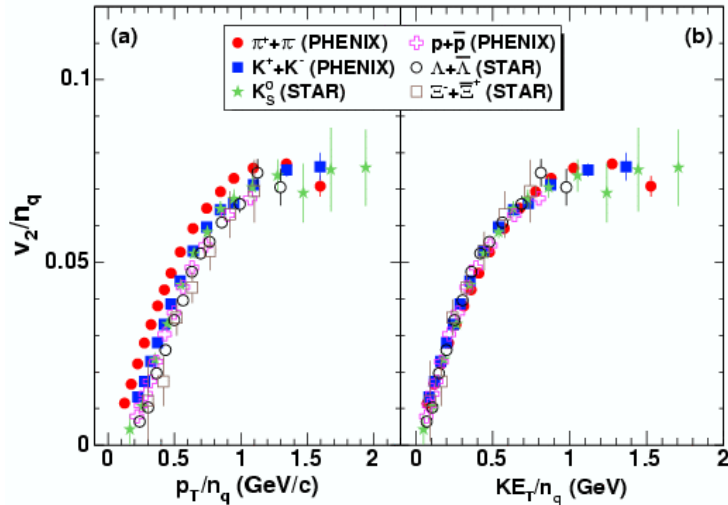
Figure 1.6: v_2 as a function of transverse momentum and energy, all scaled by the number of constituent quarks, n_q [2].

1.2.2 Jet Suppression

Another piece of evidence that dense matter has been created at RHIC is the observed jet suppression. A jet of particles is formed when a high momentum parton, which likely came from a hard scattering in the initial stage of the collision, fragments into an observable cluster of particles. Experimentally this cluster of particles is defined as a jet according to jet reconstruction algorithms. However, in high multiplicity events like those produced in heavy ion collisions, the jet sits among a large background and is difficult to separate out with

traditional jet reconstruction algorithms. Therefore, high momentum particles were measured first as a proxy for studying jets in heavy ion collisions.

Single Particle Observables

First the spectrum of various particles was measured in both Au+Au and p+p collisions. Then, to compare the yield measured in Au+Au collisions to the expectation from the yield measured in p+p, the nuclear modification factor, R_{AA}, is calculated.

$$R_{AA} = (\frac{d\sigma_{AA}}{dp_T})/(T_{AB}\frac{d\sigma_{pp}}{dp_T}), \tag{1.10}$$

where σ is the inelastic cross-section and T_{AB} is the nuclear thickness function. The cross-section gives the probability for the initial partons to result in a final state particle. The thickness function is proportional to the number of binary collisions, N_{coll}, as in the following definition of R_{AA}.

$$R_{AA} = (\frac{dn_{AA}}{dp_T})/(N_{coll}\frac{dn_{pp}}{dp_T}). \tag{1.11}$$

The results for R_{AA} for a variety of particles is shown in Fig. 1.7. In particular, if we focus on the hadrons at high p_T, above 2 GeV/c, we observe $R_{AA} < 1$, which means that the yield is suppressed. The direct photons, however, have an R_{AA} consistent with 1 which means they are not suppressed. This is expected since photons do not interact via the strong force, and therefore, should be able to exit a quark-gluon plasma unmodified, while particles which result from a strongly interacting quark or gluon will be modified. In particular, we expect the parton will lose energy as it traverses the medium. Various models which include collisional and radiative energy loss exist to explain the R_{AA} measurements. However, they fail to converge on a single value for physical variables to describe the medium such as the transport coefficient, $\widehat{q}$, [22–27]. The parameter, $\widehat{q}$, can be defined as

$$\widehat{q} = \rho \int dq_T^2 \frac{d\sigma}{dq_T^2} q_T^2, \tag{1.12}$$

which is the average squared transverse momentum broadening per unit length, where ρ is the local particle density of the medium and σ is the cross section of interactions between the jet parton and medium particles [28,29]. To better constrain these models and learn more about the plasma, other measurements such as v_2 and two particle correlations have also been studied [4,30–32].
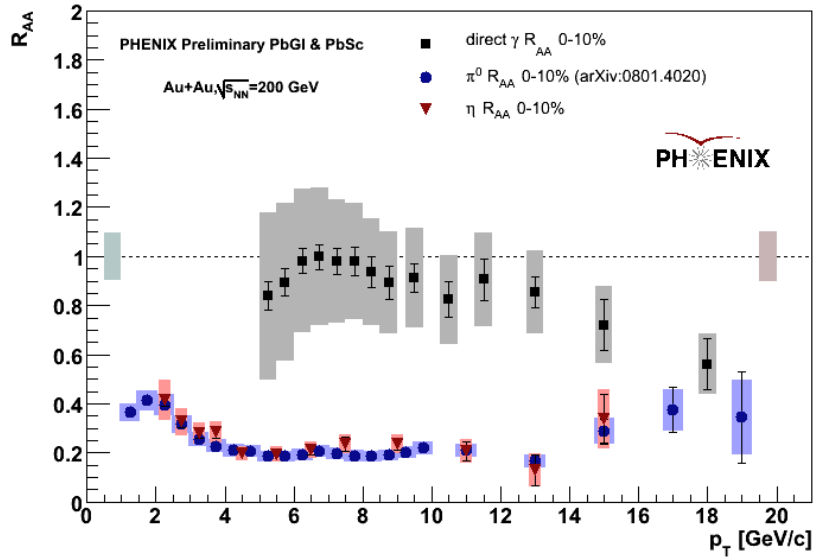
Figure 1.7: The nuclear modification factor for π^0 and η mesons compared to direct photons which do not interact with the medium, all measured by PHENIX for central 200 GeV Au+Au collisions.

Two Particle Correlations

Another way to study energy loss effects on jets at RHIC, again using high p_T particles as a proxy, is by measuring two particle correlations. If one triggers on a high p_T charged hadron and measures the azimuthal angle, $\Delta\phi$, between the trigger and the other associated charged hadrons in the event, a correlation function like that shown in the cartoon of Fig. 1.8 can be generated. The jet from which the trigger particle comes appears as a peak around $\Delta\phi = 0$ and the recoil jet appears as the peak around $\Delta\phi = \pi$. The away side peak is broadened since kinematically the away side jet can swing along the η direction and k_T, the initial pair momentum of the colliding partons, can create an imbalance in the jets' energy and cause them to be acoplanar. η, also referred to as psuedorapidity, is defined as $\eta = -\ln(\tan(\theta/2))$, where θ is the polar angle with respect to beam direction.

In p+p collisions, the underlying event will appear in the correlation function as a flat pedestal as depicted in the cartoon. This underlying event can be subtracted by assuming a flat background and using the Zero Yield At Minimum (ZYAM) method [33]. As the name suggests, we assume that the yield between the near side and away side jets is zero near $\Delta\phi \approx 1.5$. Alternatively, one can use the Absolute Normalization Method (ABS) to determine the background level without relying on any assumptions on the shape of the

correlation function [33]. These methods are described in more detail in the Analysis section, Sec. 4.
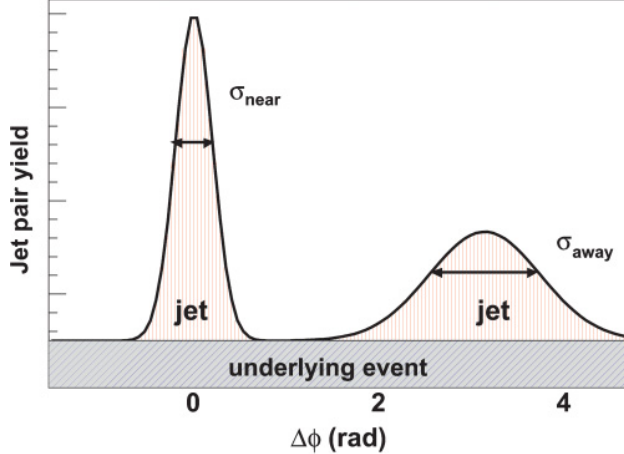
Figure 1.8: Two particle correlations with a high momentum hadron yield a near side peak around $\Delta\phi = 0$ for the trigger jet and an away-side peak around $\Delta\phi = \pi$ from the opposing jet. The underlying event creates a flat pedestal.

The cartoon is only representative for p+p collisions. The background in heavy ion collisions is much larger and is not flat since particles in the same event will be correlated with one another due to elliptic flow. Since we are interested only in the correlations due to jets, this flow shape must be removed. We define the jet function as JF($\Delta\phi$)=CF($\Delta\phi$)-FL($\Delta\phi$), where CF($\Delta\phi$) is the angular correlation function and FL($\Delta\phi$) is the flow contribution to the two particle correlations. The flow can be described by a Fourier decomposition,

$$FL(\Delta\phi) = \sum_n c_n cos(n\Delta\phi) \tag{1.13}$$

where the coefficients are $c_n = v_n^t v_n^a$. The traditional view was that all odd terms canceled due to the symmetries of the collision, while v_2, arising from elliptic flow, was the dominant even order term. Therefore, only v_2 is used for subtracting the flow term from the correlation functions according to Eqn. 1.14 in the RHIC results presented in this thesis. However, recent work has found that fluctuations in the initial geometry can lead to non-zero odd order terms and enhance even order terms which maybe responsible for the observed ridge and shoulder structures discussed briefly later [4, 34].

11

$$\frac{1}{N^t}\frac{dN^{pair}}{d\Delta\phi} = \frac{1}{N^t}\frac{N_{real}^{pair}}{2\pi\epsilon^a}\left[\frac{dN_{real}^{pair}/d\Delta\phi}{dN_{mix}^{pair}/d\Delta\phi} - b_0\left(1 + 2\langle v_2^t v_2^a\rangle\cos\left(2\Delta\phi\right)\right)\right], \quad (1.14)$$

Hadron-hadron correlations measured at the STAR experiment at RHIC in p+p, d+Au and Au+Au collisions are shown in Fig. 1.9 [3]. Similar to the cartoon shown in Fig. 1.8, the p+p data exhibit a peak around $\Delta\phi = 0$ and $\Delta\phi = \pi$, evidence of the triggered and opposing jet respectively. In the Au+Au data, the near side peak is present around the trigger but the away-side peak is clearly suppressed. The d+Au correlation is important for interpreting this suppression. The d+Au data is consistent with the p+p, which means the suppression in the Au+Au data is due to the dense medium created and not cold nuclear matter effects.
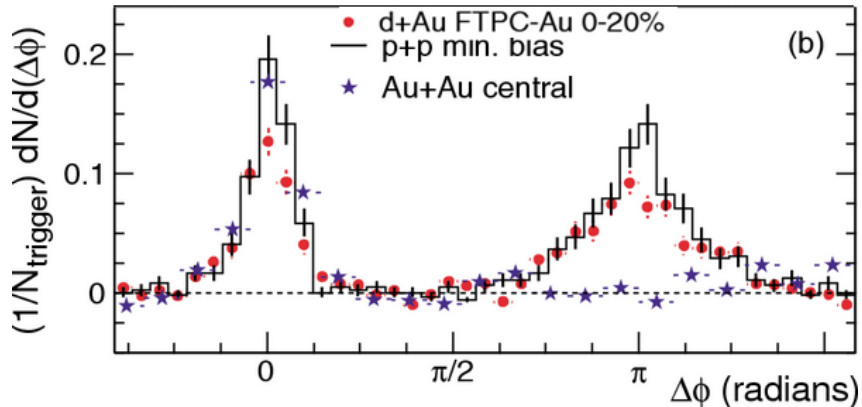
Figure 1.9: Hadron-hadron correlations measured in p+p, d+Au and Au+Au collisions. The near side jet peaks around $\Delta\phi = 0$ in all three systems but the away-side which peaks around $\Delta\phi = \pi$ in p+p and d+Au, is suppressed in Au+Au [3].

As the p_T of the trigger and associated hadrons are lowered, the away-side jet reappears but with a modified shape as shown in Fig. 1.10 [4]. Instead of a peak around $\Delta\phi = \pi$, a double peak structure emerges with a dip at $\Delta\phi = \pi$. This double peaked structure is known as the "shoulder" and what remains of the peak in the region $|\Delta\phi - \pi| < \pi/5$ is referred to as the "head" region. Modification was observed not only on the away-side but on the near-side as well. A plot of the jet function in $\Delta\eta - \Delta\phi$ space shows the near-side peak sits on a "ridge" that spans the entire measured length along the η direction. This ridge is clearly observed in the right panel of Fig. 1.10 [5]. A great

deal of work has gone into understanding the origin of these structures with much discussion of Mach-cones. However, most recently it has been proposed that considering fluctuations in the initial state and including flow terms such as v_3 in the subtraction procedure may be the correct explanation of such features [34]. This continues to be an active area of investigation.
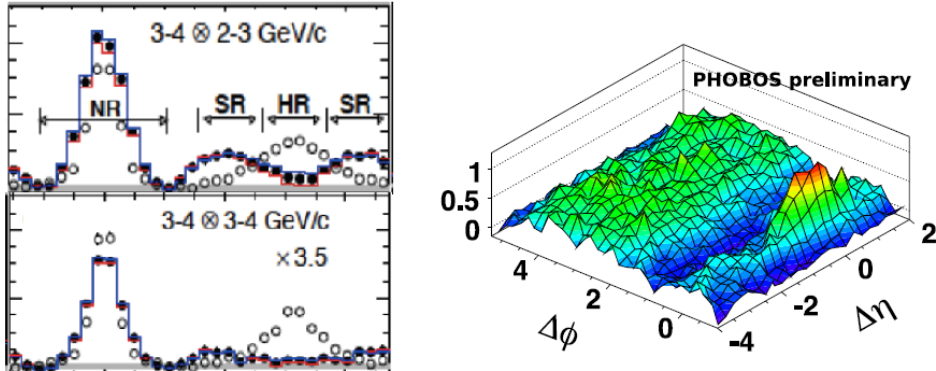
Figure 1.10: Potential medium response is observed in di-hadron correlations. (Left) The PHENIX measurement as a function of $\Delta\phi$ shows a double peak structure on the away-side [4]. This structure is decomposed into "shoulder" (SR) and "head" (HR) regions. For higher p_T associated hadrons, the jet is almost completely suppression. (Right) $\Delta\eta - \Delta\phi$ di-hadron correlations as measured by PHOBOS show a "ridge" on the near-side [5].

Although hadron-hadron correlations have revealed a great deal about energy loss in the medium, they are limited by the fact that the initial parton momentum is unknown and cannot be used to directly measure the fragmentation function.

1.3 Fragmentation Functions

It is generally assumed that the different stages of the hard scattering in a nuclear collision are factorizable and therefore the cross section can be written as

$$d\sigma = \sum_{a,b,c} \int dx_a dx_b dz\, f_a\left(x_a\right) f_b\left(x_b\right) d\hat{\sigma}\left(p_a, p_b, p_c\right) D_c^h\left(z\right). \qquad (1.15)$$
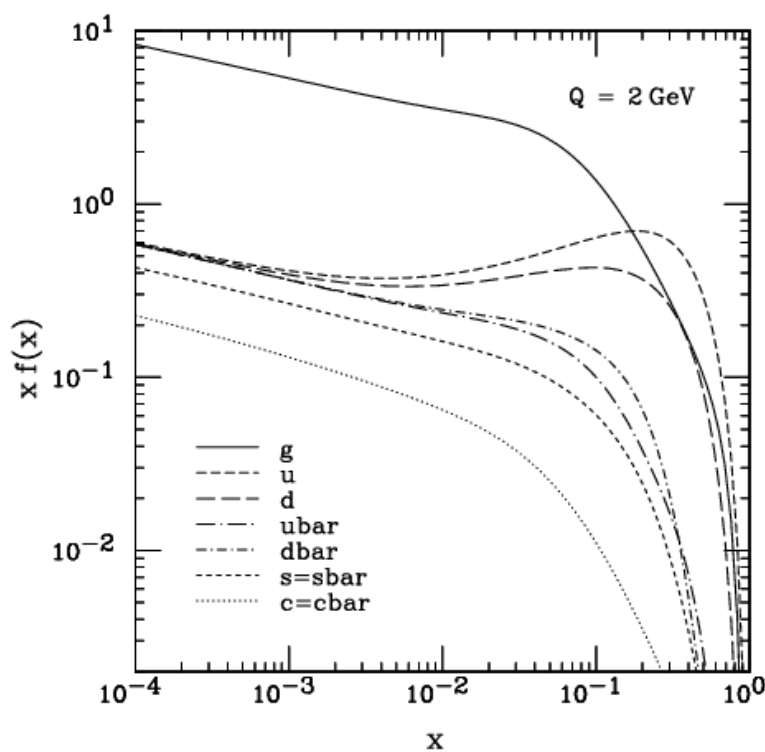
Figure 1.11: A sampling of PDFs from CTEQ [6].
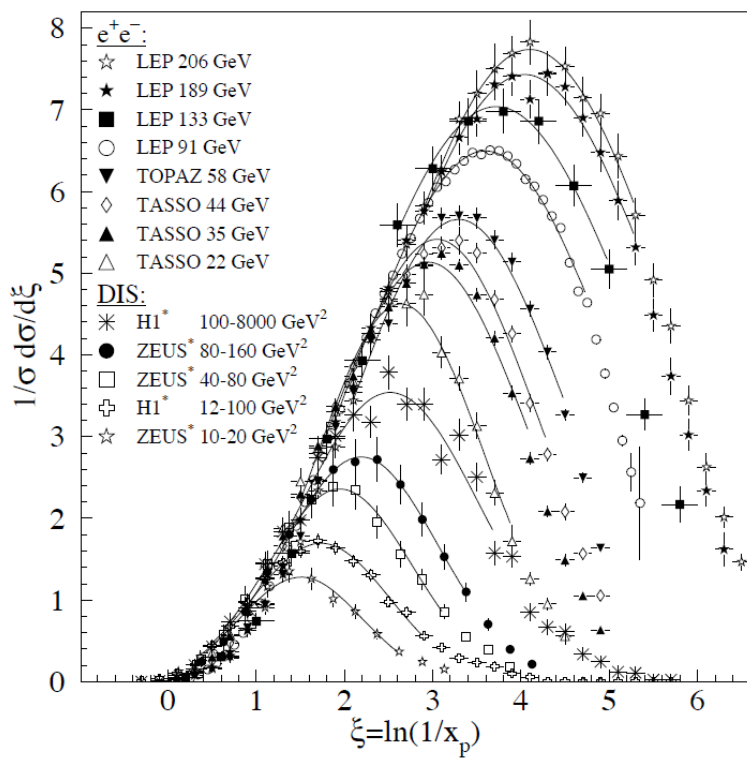
Figure 1.12: A sampling of fragmentation functions measured in e^+e^- collisions by the TASSO collaboration [7].

The first term is the parton distribution function (PDF), *f(x)*. The PDF describes the partons, a and b, in the initial state and can be measured via deep inelastic scattering experiments of a lepton off of a nuclear target. The Bjorken x is the momentum fraction of the colliding particles carried by each parton. For example, some PDFs are shown in Fig. 1.11. The hard scattering cross section, $\hat{\sigma}$, is calculated from the relevant Feynman diagrams. Finally, the fragmentation function, $D_c^h(z)$, describes the probability for an outgoing parton, c, to yield a hadron, h, with momentum fraction, $z = p_h/p_c$. The fragmentation function for a variety of parton and hadron types have been measured. Fig. 1.12 shows a sampling of these measurements made in e^+e^- collisions at various energies [7]. e^+e^- collisions are cleaner than p+p collisions since no partons exist in the initial state. Since the fragmentation function describes the final state, it is independent of the collision system. However, effects that exist in other stages of the collision could alter the experimentally observed fragmentation function. For example, in Au+Au collisions, partons lose energy while traversing the medium and therefore fragment at a lower energy. The simplest expectation would be a shift of the observed fragmentation function, $D^{medium}(z)$, for constant fractional energy loss, $\Delta E/E$, which can be written as

$$D^{medium}(z) = D^{vacuum}\left(\frac{z}{1 - \frac{\Delta E}{E}}\right). \tag{1.16}$$

Modifications to the observed fragmentation function give insight to how the parton loses energy in the medium. Therefore, it is interesting to compare the observed fragmentation function in Au+Au collisions to that in p+p collisions. Experimentally, the hadronic yield within a jet of known momentum as function of z, or similar a variable (see next paragraph), is a measure of the fragmentation function. Therefore the ratio of the yields measured in the two collision systems is equivalent to the ratio of the fragmentation functions. When discussing per trigger yields in two particle correlations, this ratio is referred to as I_{AA}.

Since generally p_T, not p, is measured experimentally, an alternative variable, $z_T = \frac{|p_T^h|}{|p_T^{jet}|}$, is defined to approximate z. Sometimes, for two particle correlations, where the azimuthal angle $\Delta\phi$ between a trigger and associated particle is measured, another variable, $x_E = \frac{p_T^{assoc}\cos(\Delta\phi)}{p_T^{trigger}}$, is used. Here the numerator is the projection of the associated particle momentum along the trigger, or assumed jet axis. To understand the relationship between these variables in hadronic collisions, the math to relate them is worked out in a later section.

1.4   Direct Photons
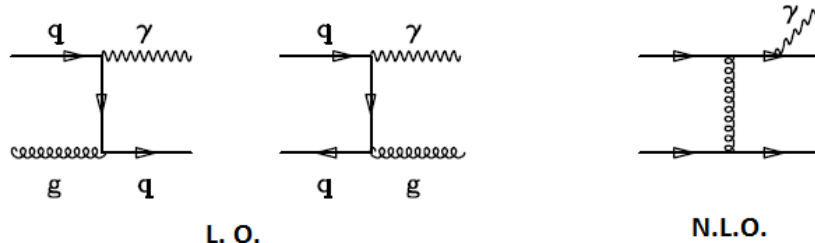
Figure 1.13: On the left are the leading order Feynman diagrams for direct photon production. The diagram on the right is next-to-leading order. Photons from resulting from this diagram are typically referred to as fragmentation photons.

Direct photons are produced in hard scatterings between partons in the initial collision. At leading order, the dominant processes for direct production are the QDC Compton-like scattering process, $g + q - > \gamma + q$, and quark-anti-quark annilation which are both shown in Fig. 1.13. Data from the Tevatron, however, teaches us that NLO effects are important for describing the direct photon spectrum [35]. This suggests that photons which result from the fragmentation of a parton, as illustrated by the right most diagram in Fig. 1.13, are also relevant, especially in the low p_T regime. Experimentally, the inclusive photons measured by the detector are predominately from mesons decays such as $\pi^0 \rightarrow \gamma\gamma$. In experimental measurements, the term direct photons means that the decay photon contribution and only the decay photon contribution has been explicitly removed from the inclusive sample of measured photons. Therefore, all diagrams in Fig. 1.13 contribute to the direct photon spectrum. The direct photon spectrum measured in $p + p$ collisions at RHIC by PHENIX [8] are plotted in Fig. 1.14 and compared to NLO calculations [9]. The excellent agreement between the data and NLO curves is demonstrated by the ratio in the bottom panel of Fig. 1.14 and implies that NLO can accurately describe the $p + p$ data, which will be used as a baseline for interpreting the heavy ion results.

1.4.1   Photons in Heavy Ion Collisions

Since photons do not interact via the strong force and therefore should be unmodified by the QGP, direct photons are an excellent probe of the medium for a variety of measurements. First, in the low momentum regime, photons
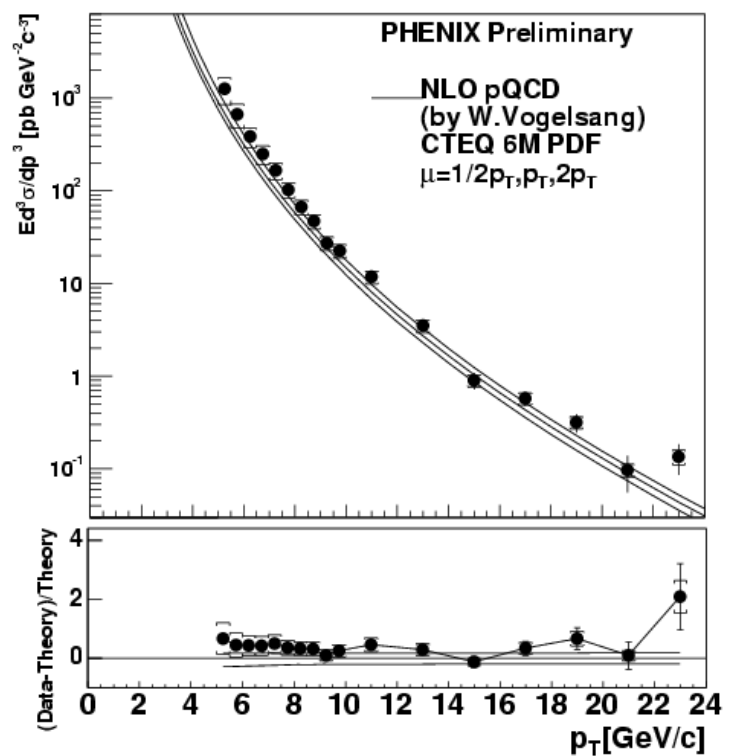
Figure 1.14: The direct photon spectrum measured in p+p collisions at PHENIX compared to NLO calculations [8, 9].

can be used to estimate the temperature of the medium. An excess of photons can be interpreted as resulting from black body radiation [36]. However, in this momentum range traditional photon measurements with the EMCal are difficult due to the large backgrounds. Therefore, the photon spectrum is measured for virtual photons, which are observed experimentally as e^+e^- pairs. By comparing the measured Au+Au spectra to the scaled p+p measurement, as shown in Fig. 1.15 [37], the excess of thermal photons is observed. An exponential fit to the excess gives an inverse slope of $T = 221 \pm 19^{stat} \pm 19^{sys}$ MeV, which is believed to be related to the initial temperature of the medium. This data shows qualitative agreement with hydrodynamical models with initial temperatures, $T_{init} = 300 - 600$ MeV at formation time, $\tau_0 = 0.6 - 0.15$ fm$/c$. All these temperatures are above the Lattice QCD predicted phase transition from hadronic matter to QGP at around 170 MeV. The dotted red curve in the plot, for example, uses $T_{init} = 370$ MeV in the calculation for the most central collisions.

The spectrum for higher p_T direct photons which result from initial hard scatterings in Au+Au collisions has also been measured by PHENIX. The data points for the most central 0-10% collisions are included in Fig. 1.17. The curves from [10] show how the higher order contributions and medium induced effects dipicted by the Feynman diagrams in Fig. 1.16 contribute to the measured spectrum. These additional sources arise from the annihilation of a high energy parton with a thermal parton from the medium, the in-medium bremsstrahlung of a jet, and thermal radiation of the QGP.

The spectrum for higher p_T direct photons which result from initial hard scatterings in Au+Au collisions can be compared to p+p collisions. The resulting R_{AA}, shown in Fig. 1.7, is approximately 1 for direct photons. Unlike hadrons which are suppressed due to energy loss, photons escape the medium unmodified. The dip in the highest p_T bin may be a fluctuation or may be due to the possible isospin effect resulting from the lack of neutrons in the initial state of the baseline measurement. To investigate this, direct photons are being studied in d+Au collisions.

1.4.2 γ_{dir} hadron Correlations

As evident from the LO Feynman diagrams (Fig. 1.13), the momentum of the direct photon balances that of the opposing parton. Therefore, even in heavy ion collisions, the photon momentum can be used to approximate the opposing jet momentum, since the photon momentum should be unmodified. Knowing the initial parton momentum allows us to directly measure the fragmentation function, $D(z)$, although, recall that experimentally we actually measure $z_T = p_T^h/p_T^{\gamma_{\mathrm{dir}}}$.
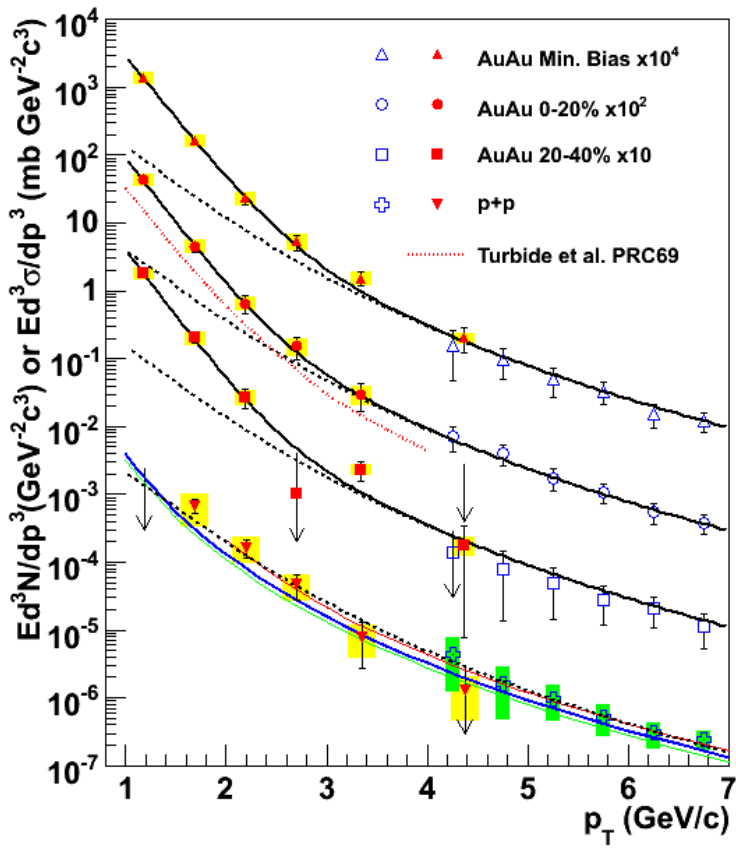
Figure 1.15: The direct photon invariant cross section in p+p (inverted triangles) and yields from various centrality bins of the Au+Au data are shown. The open and closed data points indicate two different analysis. The curves near the p+p points are from NLO pQCD calculations. A fit to the p+p data scaled by T_{AA} (dashed lines) is plotted as a comparison to the Au+Au data. The red curve is a theoretical model for 0-20% Au+Au.
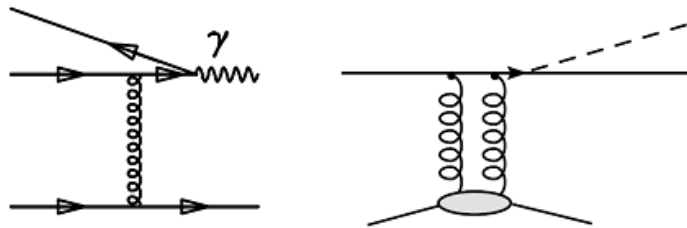
Figure 1.16: Feynman diagrams for additional photon sources in heavy ion collisions.
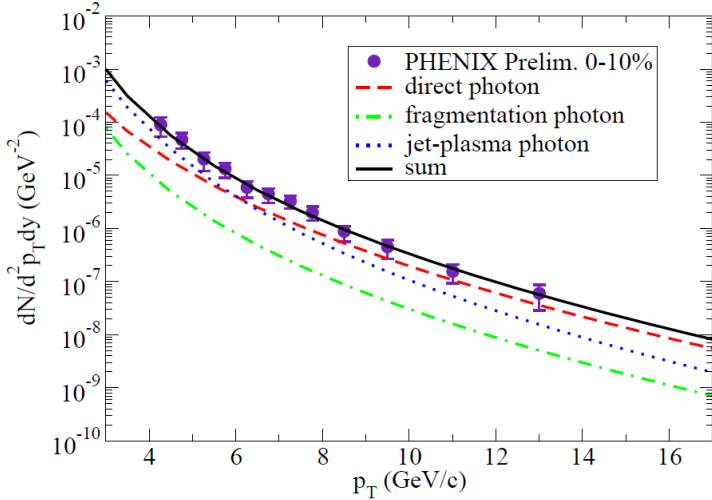
Figure 1.17: How each photon source contributes to the measured direct photon spectrum according to [10].

Using a high p_T hadron to trigger on a jet biases your measurement to hard scatterings near the surface and toward partons with lower expected energy loss. This is illustrated by the distribution of scatterings within the medium shown in Fig. 1.18 according to [38]. Since direct photons are not modified by the medium, selecting on high p_T should not introduce such a surface bias. Because the γ_{dir} provides an experimental handle on the jet energy, $\gamma_{\mathrm{dir}} - h$ correlations are considered a "golden-channel" for studying jet energy loss without surface bias. Several energy loss models have been proposed [10,13,39], with predictions for $\gamma_{\mathrm{dir}} - h$ observables. Their ingredients differ and require experimental tests of their predictions to disentangle their accuracy.
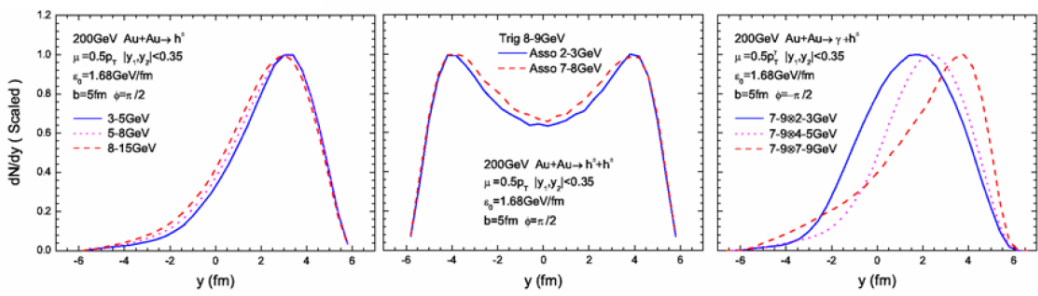
Figure 1.18: The position distribution for various probes according to the ZOWW energy loss model.

21

k_T **Effect**

Since partons can move around within a nucleon, they carry an intrinsic momentum transverse to the nucleon's momentum, called intrinsic k_T, which is expected to be on the order of 300 MeV/c. However, the k_T measured experimentally is much larger and approximately 3 GeV/c [18]. In nuclear collisions, k_T leads to a non zero momentum of the colliding parton pair, $p_T^{pair} = \sqrt{2}k_T$. In the LO Feynman diagrams described earlier, the direct photon is produced exactly back-to-back with the outgoing parton and with the same energy. However, the x-component of k_T causes an imbalance in the energies of the photon and parton while the y-component causes their trajectories to be acoplanar. Note that a simple imbalance in the in the momentum fraction, x, of the two incoming partons, such that $x_1 \neq x_2$ results in a non-zero $\Delta\eta$ of the outgoing partons in the lab frame. We referred to this effect earlier when describing the η difference between the trigger particle and away-side jet as the η swing. It is important to understand the effect of the k_T smearing on the energy since we assume $p_T^\gamma \approx p_T^{jet}$ such that $z_T \approx z$. k_T can be measured with two particle correlations including $\gamma_{\mathrm{dir}} - h$, by first measuring the width of the p_{out} distribution where $p_{out} = p_T^h \sin\Delta\phi$. p_{out} is the momentum vector which is transverse to the trigger axis and points to the partner hadron as shown in Fig. 1.19. The trigger axis is the assumed jet axis of the away-side jet. This figure is simpler for $\gamma_{\mathrm{dir}} - h$ than di-hadron correlations because the photon is not a jet fragment and does not acquire an additional momentum kick, j_T. During the fragmentation process the resulting hadrons are not aligned with the jet axis and momentum kick they receive away from the jet axis is called j_T and is depicted in Fig. 1.19.
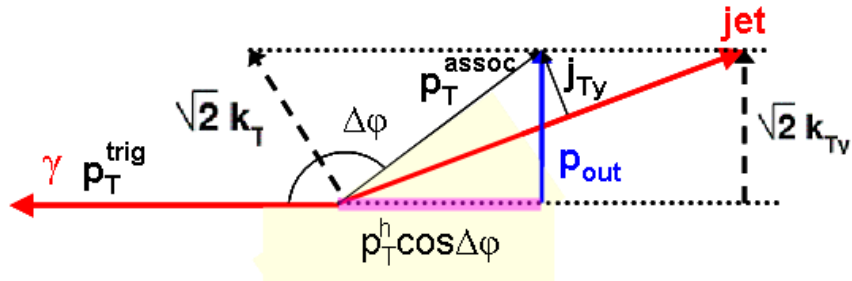
Figure 1.19: A cartoon describing the various momentum components with an outgoing photon and opposing parton which fragments into a jet.

k_T also alters the meaning of the fragmentation variables used. The math below is done to illustrate the relationship between the different fragmentation variables, z, z_T and x_E taking k_T into account.

First let us recall $z_T = p_T^h/p_T^\gamma$, and $x_E = \frac{p_T^{h-\cos\Delta\phi}}{p_T^\gamma}$. Based on simple trigonometric relations and Fig. 1.19, we can write the relationship between, z_T, x_E and p_{out} as

$$z_T^2 = x_E^2 + \frac{|p_{OUT}|^2}{p_T^{\gamma 2}}. \tag{1.17}$$

We then use the known relationship [18],

$$|p_{OUT}|^2 = x_E^2 \left[2\langle|k_{Ty}|\rangle^2 + \langle|j_{Ty}|\rangle^2\right] + \langle|j_{Ty}|\rangle^2 \tag{1.18}$$

for di-hadron correlations to replace p_{out} in Eqn. 1.17. However, the first j_{Ty} term in Eqn. 1.18 results from the fragmentation of the near-side trigger hadron. Since we use $\gamma_{\rm dir}$ triggers which are not fragments of a jet, $j_{Ty} = 0$ and this term is dropped in the following equations. The substitution of p_{out} gives z_T in terms of x_E and k_T as

$$z_T^2 = x_E^2 + \frac{x_E^2 \left[2\langle|k_{Ty}|\rangle^2\right] + \langle|j_{Ty}|\rangle^2}{p_T^{\gamma 2}}, \tag{1.19}$$

which for clarity is rewritten as

$$z_T^2 = x_E^2 \left(1 + \frac{\left[2\langle|k_{Ty}|\rangle^2\right]}{p_T^{\gamma 2}}\right) + \frac{\langle|j_{Ty}|\rangle^2}{p_T^{\gamma 2}}. \tag{1.20}$$

The relationship between these variables depends on the average j_{Ty} of the opposing hadron, which from previous measurements is about 600 MeV$/c$ [18]. The fact that the relationship between z_T and x_E depends on k_T gives another reason why knowing k_T is important. However, if the trigger momentum is much greater than k_T and j_T, z_T actually equals x_E. Unfortunately, for us this is not the case. We discuss the difference between z_T and x_E more in a moment but first we will derive the relationship between these variables and z. If we define z in terms of the projection of the associated hadron's momentum onto the true jet axis, we have

$$z = \frac{\vec{p_T^h} \cdot \vec{p_T^{jet}}}{|p_T^{jet}|^2}. \tag{1.21}$$

Based on the geometry from Fig. 1.19, we write

$$z = \frac{\sqrt{|p_T^h|^2 - |j_{Ty}|^2}}{p_T^\gamma}. \tag{1.22}$$

Here we are assuming $p_T^\gamma = p_T^{jet}$ even though the x component of k_T smears this equality. Squaring the equation and substituting in z_T gives

$$z^2 = z_T^2 - \frac{|j_{Ty}|^2}{p_T^{\gamma 2}}. \tag{1.23}$$

Substituting the above derived relation between z_T and x_E from Eqn. 1.20, z can be written in terms of x_E as

$$z^2 = x_E^2(1 + \frac{\left[2\langle|k_{Ty}|\rangle^2\right]}{p_T^{\gamma 2}}). \tag{1.24}$$

Therefore, x_E differs from our definition of z by a scale factor which depends on the k_T and the p_T of the photon trigger. Although we expect that both the x_E and z_T distributions approximate the fragmentation function defined by z, there is clearly a difference, and one particular variable does not always make a better approximation of z than the other. However, it is clear that as the trigger momentum increases significantly above k_T and j_T, all these variables become more and more equivalent.

We can also learn about the relationship between these variables directly from the data. A comparison of the x_E and z_T distributions is presented in [11] and shown in Fig. 1.20. The yields clearly differ and the ratio increases slightly as these variables approach 1. However, since the difference in the variables should be the same regardless of the collision system, the I_{AA}, which is a ratio of the yield in Au+Au divided by the yield in $p + p$ as a function of z_T or x_E, should yield the same conclusions.

Introduction to Theoretical Work

γ_{dir}-h correlations were proposed as a "golden channel" for studying energy loss [12] in the QCD medium since they provide a means to determine the jet energy experimentally and can therefore be carefully compared to theoretical models. In particular, it was proposed to compare the theoretical calculations of $D(z)$ to the experimentally measured γ_{dir}-h away-side yield via the ratio of the in medium case to the vacuum $p + p$ case. Experimentally, this ratio is referred to as $I_{AA} = Y_{AA}/Y_{pp}$ where Y refers to the hadron yield opposite the γ_{dir} trigger. As an example, an early theoretical prediction is shown in Fig. 1.21.
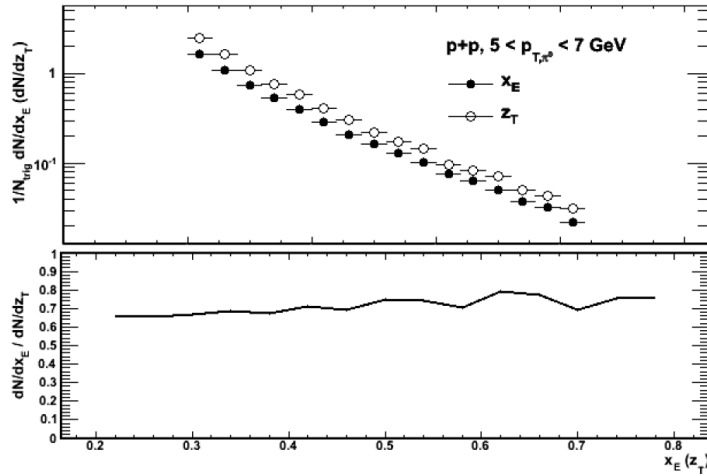
Figure 1.20: Comparison between the x_E and z_T distributions (top) for π^0 triggers with $5 < p_T < 7\text{GeV/c}$ and their ratio (bottom) [11].
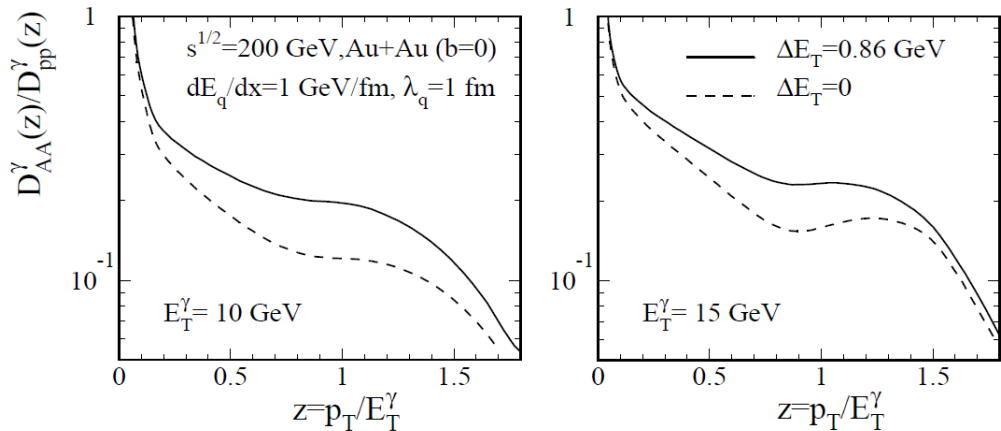
Figure 1.21: Ratio of the fragmentation functions for two different jet energies as a function of z. The calculations with and without E_T broadening included are shown as solid and dashed lines respectively [12].

The ZOWW Model and Geometric Dependence

The first model discussed, labeled ZOWW, is calculated using NLO pQCD by Zhang, Owens, Wang and Wang [13]. Using a Monte Carlo the photon and photon-hadron cross sections are determined. Since this is NLO, photon production includes fragmentation photons. An isolation cut reduces this contribution to less than 10% for photons with $p_T > 7GeV/c$. The average energy loss of the opposing quark, produced at position, r, and traveling along direction, n, is given by

$$\Delta E \approx \left\langle \frac{dE}{dL} \right\rangle \int_{\tau_0}^{\infty} d\tau \frac{\tau - \tau_0}{\tau_0 \rho_0} \rho_g(\tau, b, r + n\tau). \tag{1.25}$$

The energy loss depends on the initial time, τ_0, and gluon density, ρ_0. The hard-sphere model is used to describe the nuclear overlap geometry which is estimated to be at most 10% different from the more accurate Wood-Saxon geometry. The average quark energy loss per unit length in a 1-d expanding medium, $\left\langle \frac{dE}{dL} \right\rangle$, is parameterized by

$$\left\langle \frac{dE}{dL} \right\rangle = \epsilon_0 (E/\mu_0 - 1.6)^{1.2}(7.5 + E/\mu_0). \tag{1.26}$$

The gluon energy loss is 9/4 of the above quark energy loss. The KKP fragmentation functions in vacuum and CTEQ6M pdfs are used. By simultaneously fitting the observed suppression in the single and di-hadron spectra, the energy loss parameters are determined to be ϵ_0=1.68GeV/fm, μ_0=1.5GeV and τ_0=1.2fm/c.

The resulting I_{AA} is plotted in Fig. 1.23. The ZOWW curve [13] shows suppression at high z_T and less suppression at low z_T. This shape results from the geometric dependence of the hard scatterings. High z_T is more surface biased since it requires the associated hadron to have higher momentum while low momentum hadrons (low z_T pairs) probe deeper into the medium, reducing the observed suppression. This geometric dependence on z_T is illustrated in Fig. 1.22.

Renk's Models

Thorsten Renk developed a LO model to describe $\gamma_{\mathrm{dir}} - h$ correlations using the Armesto-Salgado-Wiedemann (ASW) energy loss weights and a 3D hydrodynamical expansion. The ASW weights provide the probability for a parton to lose a total energy of ΔE due to an arbitrary number of medium induced gluon emissions. The I_{AA} from this model is included in Fig. 1.23. The energy loss is attributed to gluon radiation but is not propagated into observable
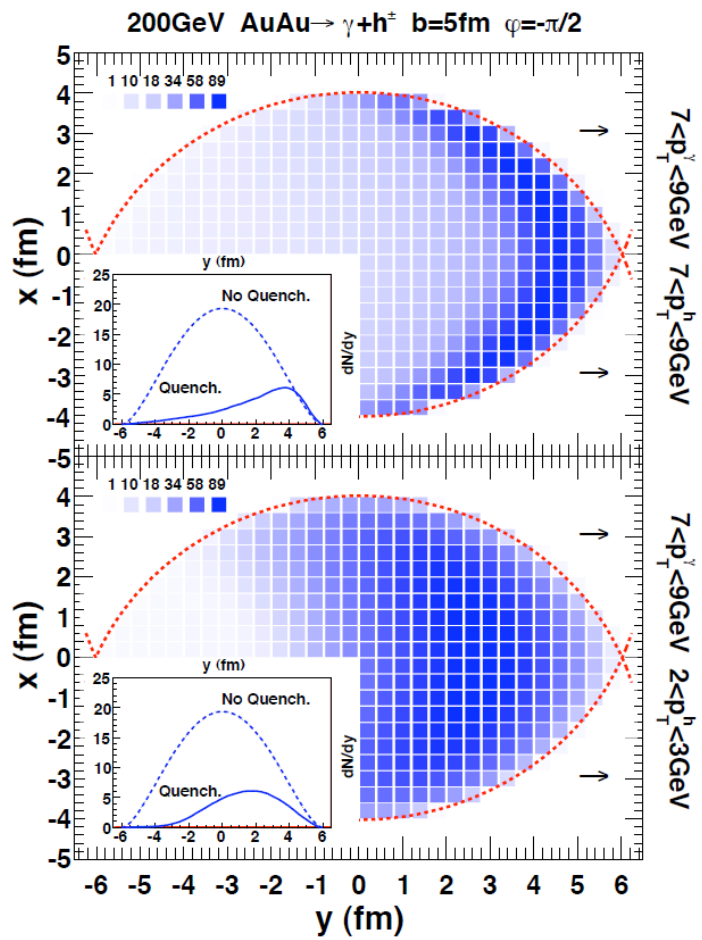
Figure 1.22: The position distribution of hard scattering probed in the medium by pairs at high z_T(top) and low z_T(bottom) according to the ZOWW energy loss model [13].
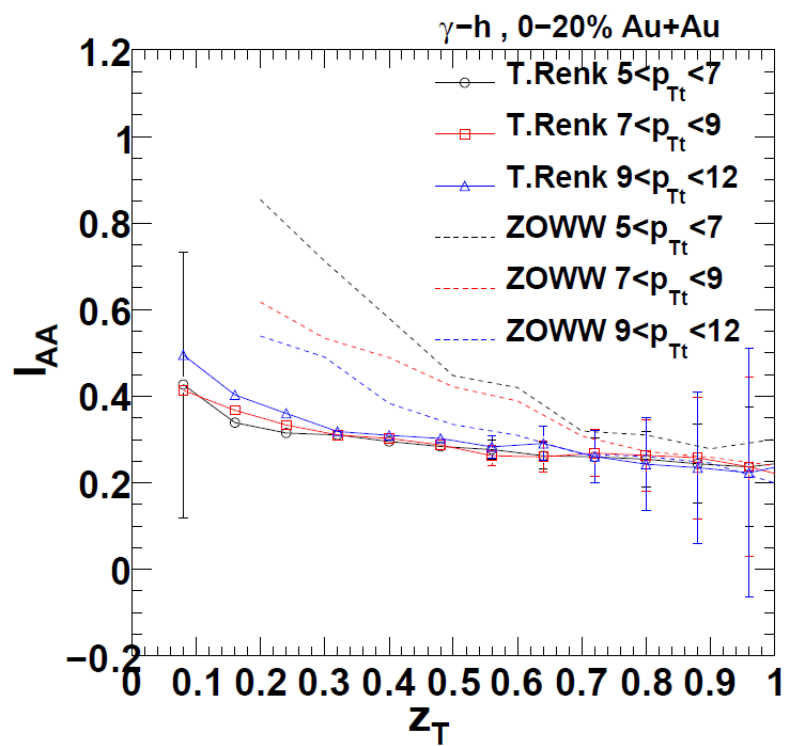
Figure 1.23: Renk's ASW model compared to the ZOWW calculation for I_{AA}.

yield, as with the ZOWW model. Renk's curve [39], does not have a strong z_T dependence because he allows for fluctuations in his energy loss model, which wash out the geometric dependence effects observed in the ZOWW model.

More recently Renk has also developed a model which does trace the lost energy. According to his YAJEM calculation, the energy loss via gluon radiation is redistributed to soft particle production. Therefore, the model predicts a suppression at high z_T because high momentum partons lose energy, and an enhancement at low z_T due to an increase in low momentum particles. The YAJEM prediction is plotted in Fig. 1.24 along with Renk's ASW curves. The soft particle production in YAJEM enhances the low z_T region such that at very low z_T, the I_{AA} is above unity, while previously discussed energy loss models predict suppression at all z_T.
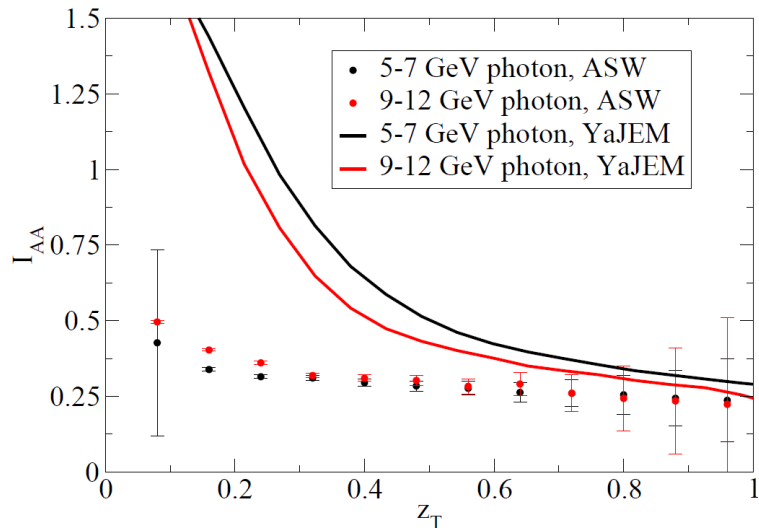
Figure 1.24: Renk's ASW model compared to the YAJEM I_{AA}.

BW-MLLA Model

Similar, but prior to YAJEM, Borghini and Weidemann proposed a framework in which the lost energy results in an increase in soft particle production. Again partons primarily lose energy in the medium due to gluon radiation. Their calculation, which uses the modified leading log approximation (BW-MLLA) and the local parton hadron duality (LPHD) assumption, is able to reproduce the measured fragmentation function in e^+e^- data [40]. Their vacuum calculation is compared to the quark fragmentation function from e^+e^- data from TASSO and OPAL in Fig. 1.25. The fragmentation functions are

plotted as a function of $\xi = -ln(z)$. Modeling the energy loss as an increased parton splitting probability, they are able to calculate both the suppression of high p_T jet fragments as well as the redistribution of energy to lower p_T fragments and resulting enhancement at low z. Their in-medium predictions at both RHIC and LHC energies are also plotted in Fig. 1.25. By comparing the vacuum curve to the in-medium curve at the same jet energy, one sees that the medium causes suppression at low ξ and enhancement at high ξ. We should note that unlike the previously discussed models, this calculation is not specifically for $\gamma_{\text{dir}} - h$ correlations. It is actually for hadrons from jets with known energy and therefore $\xi < 0$ is impossible since the hadron momentum cannot be greater than the total jet energy. However, because of k_T and possible fragmentation photons in the trigger sample, $\xi < 0$ (i.e. $z_T > 1$) is kinematically possible for $\gamma_{\text{dir}} - h$ measurements.
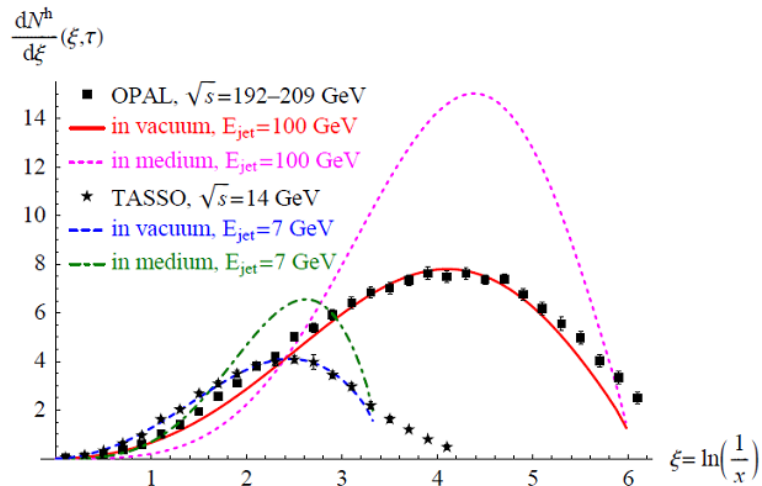
Figure 1.25: BW-MLLA fragmentation function calculation for in vacuum and in medium compared to e^+e^- data.

Experimental Measurements

The first published measurement of γ_{dir}-hadron correlations in heavy ion collisions came from PHENIX data collected during the 2004 Au+Au RHIC run [17]. The Au+Au results were compared to results from p+p collisions collected during the 2005 and 2006 RHIC runs. These results are presented in the results section of this thesis. A statistical subtraction procedure is used in both and will be explained in detail in the Analysis section of this thesis. During the 2007 Au+Au RHIC run, PHENIX collected a factor of four

more statistics, allowing for a more detailed study of the γ_{dir}-hadron correlations over a wider kinematic range. The STAR collaboration has also made measurements of $\gamma_{\mathrm{dir}} - h$ [41].

1.5   Purpose of This Dissertation

Studying direct photon-hadron correlations is an excellent way to do jet tomography of the medium. The goal is to learn how partons lose energy and where that energy goes in the medium. Initial measurements of direct photon-hadron correlations from the 2004 RHIC run have been published and compared to p+p using the same methods. These results, however, are limited statistically and in z_T. A factor of 4 more Au+Au data was collected during the 2007 RHIC run. The direct photon-hadron correlation analysis of this newer dataset with an expanded kinematic range is the focus of this thesis. The latest $p + p$ analysis presented in [11], which uses improved techniques to reduce the uncertainties in the measurement, is also discussed and used as the baseline measurement to which the Run 7 Au+Au data is compared. The purpose is to maximize the impact of this important analysis by fine tuning the techniques used and minimizing the uncertainties of the measurement.

This thesis will first review the experimental details related to collecting the necessary data from the PHENIX experiment at RHIC. Analysis details related to two particle correlations in general and the γ_{dir}-h extraction, along with a discussion of the resulting systematic uncertainties, are presented. A review of the first PHENIX γ_{dir}-h from the Run 4 Au+Au data will be presented, followed by the Run 7 results using the same early $p + p$ baseline. An extension of these results is then presented using the latest $p + p$ baseline to reduce the uncertainties. Ground work for future developments to the method is also established. Finally the implications of this measurement on our understanding of energy loss in the medium and proposed future studies are discussed.

Chapter 2

Experimental Details

2.1 RHIC
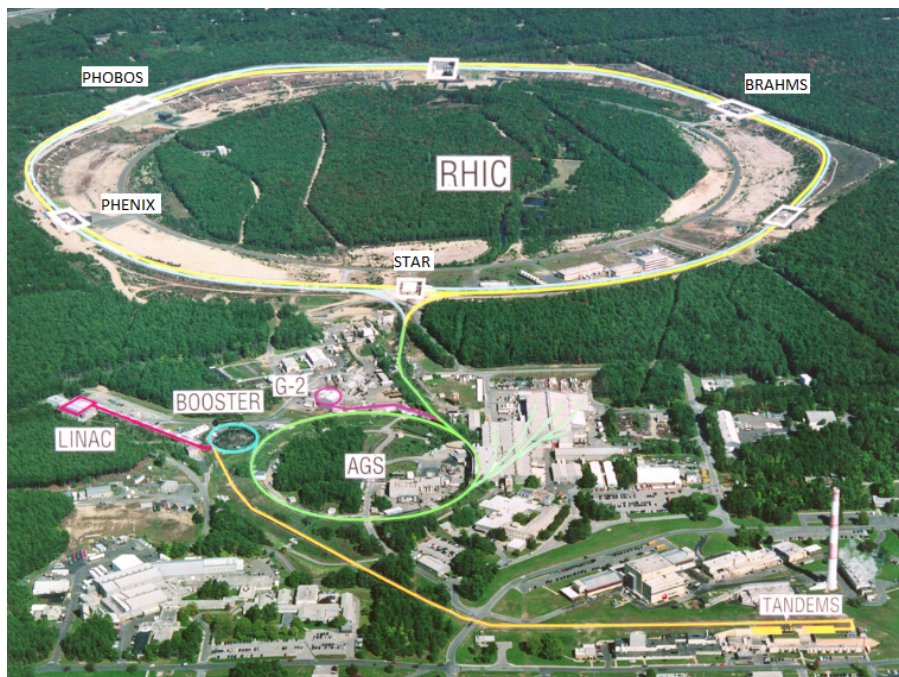
Figure 2.1: Aerial view of RHIC. The location of the four experiments are labeled along the ring. The tandems, AGS and other components which aid in the production and acceleration of the beams are also included and marked in the image.

The Relativistic Heavy Ion Collider (RHIC) is a synchrotron collider located at Brookhaven National Lab. It is a 2.4 mile in circumference ring. RHIC

is a very versatile machine which can collide polarized protons up to 500 GeV and a variety of heavy ion species including copper, gold and soon uranium at various energies up to 200 GeV, as well as, produce asymmetric collisions such as deuteron on gold. Particles start at the tandems, pass through the boosters, are accelerated to 99.7% the speed of light in the Alternating Gradient Synchrotron (AGS) and are finally injected into the RHIC ring. The primary goals of the collider and the detectors along the ring are to measure the gluon contribution to the spin of the proton and to study the quark-gluon plasma. In addition to the spin program goals, the $p + p$ collisions provide valuable baseline measurements for studying the medium produced in heavy-ion collisions. To study these high energy collisions, there are four experiments, PHENIX, STAR, BRAHMS and PHOBOS, located along the ring [42–45]. Currently only the two larger experiments, PHENIX and STAR, are still collecting data. The data used in this dissertation was collected at PHENIX, the Pioneering High Energy Nuclear Interaction eXperiment, which is described in the next section.

2.2 PHENIX

The PHENIX experiment was optimized to measure photons, electrons and muons which are all direct probes of the collisions. PHENIX is comprised of two central arms which sit around the beam pipe, as shown on the left in Fig. 2.2. They cover $\pi/2$ in azimuth and ± 0.35 units of psuedorapidity. In the 2007 RHIC run, the Hadron Blind Detector, HBD, sat closest to the beam pipe. The HBD is designed to distinguish between single and double electron tracks and is discussed more later in this section for sentimental reasons, although it plays no role in the analysis of this thesis. The PHENIX tracking system for charged particles consists of the drift chamber (DC) and pad chambers (PC). The central magnets create a field in the area between the beam pipe and DC. The bend of the particle tracks within the magnetic field allow us to determine their charge and momentum. The primary particle identification detectors in the central are the time-of-flight (TOF) detector, which distinguishes between pions, kaons and protons, and the ring imaging Cerenkov detector (RICH) for electron identification [46]. The electromagnetic calorimeter (EmCal) is used to detect photons and electrons and consists of eight sectors along ϕ, six of which are made of lead scintillators (PbSc) and two of lead glass (PbGl). Further out in psuedorapidity are the muon detectors which track (MuTr) and identify (MuId) muons. The Muon Piston Calorimeter (MPC) sits at the nose of the muon magnets. The MPC is named for its location in PHENIX but actually measures photons and pions in the forward and backward direction.

Correlations between particles in the MPC and central arm in d+Au collisions are used to probe low x and study initial state effects. There are also event characterization detectors such as the beam beam counter (BBC), zero degree calorimeter (ZDC) and Reaction Plane detector (RXPN) which measure the collision vertex, reaction plane and centrality in heavy ion collisions.
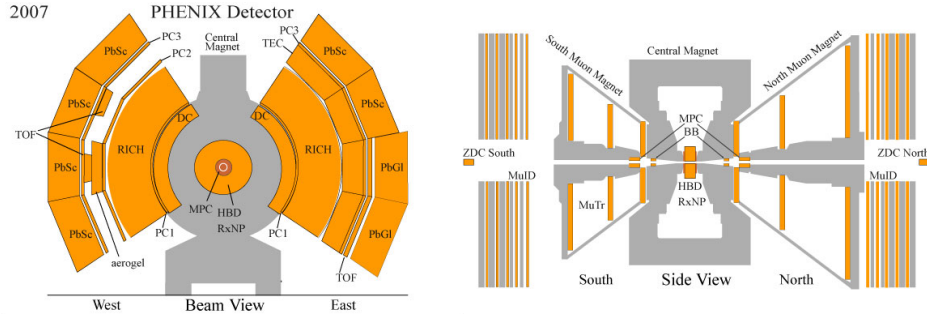
Figure 2.2: The PHENIX central arm looking down the beam pipe (left). An overhead view of PHENIX where the beam travels horizontally through the center of the cartoon (right).

2.2.1 Event Characterization Detectors

Beam Beam Counter

The beam beam counters are each composed of 64 photomultiplier tubes. They have full azimuthal coverage and are located at approximately $3.0 - 3.9$ units in psuedorapidity. They are used as a trigger for the data acquisition system as well as for event characterization. The trigger efficiency in Au+Au collisions is $92 \pm 2\%$ based on a full PHENIX detector simulation using the HIJING event generator. The $\tilde{8}\%$ of collisions where the colliding ions graze one another are not triggered because of they do not leave significant charge in the BBCs. How we categorize the different collision geometeries is discussed later in this section. Coincidences between the two detectors is used to determine z-vertex, the position of the collision along the the beam axis according to Eqn. 2.1.

$$z - vertex = \frac{(T_S - T_N)c}{2} \qquad (2.1)$$

T_S and T_N are the times the BBC registered a hit in the south and north detectors, respectively. The timing resolution of each element is 52 ± 4 ps (rms) [47].

The total charge deposited in the BBC is monotonically correlated with the centrality of the collision. Therefore this is used in conjunction with the

ZDC to determine the centrality as described later in this section. The BBC can also be used to determine the reaction plane of the collision, which is important for measuring the elliptic flow of the overlap region. However, the v_2 used for the results presented in this thesis use the reaction plane detector described later in this section to determined reaction plane.

Zero Degree Calorimeter

The ZDCs are hadronic calorimeters located outside the dipole magnets, approximately 18m from the interaction point. Because the magnetic field sweeps away all charged particles, the ZDCs only measure neutral particles. The purpose of these detectors is two fold. First, coincidences between the north and south ZDC are used to determine the z-vertex position of the collision, similar to the BBC. The z-vertex resolution is 2.5cm and is cross-checked with the BBC vertex measurement. Second, for heavy-ion collisions, they are also used to determine centrality in conjunction with the BBC. By measuring the spectator neutrons, the number of participants can be calculated.
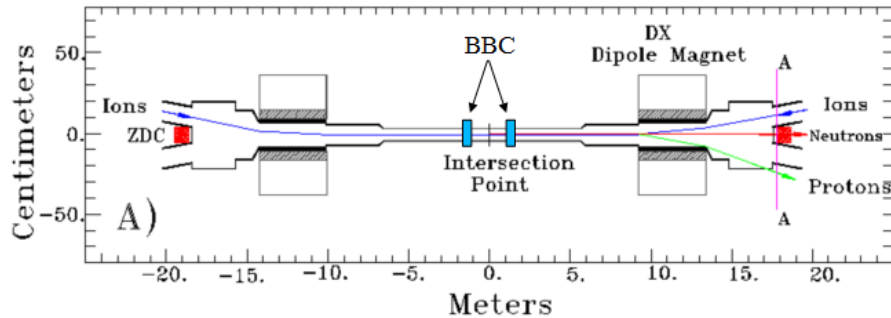
Figure 2.3: Position of the ZDC and BBC detectors and the dipole magnets.

Centrality Determination

Centrality is used to classify the initial collision geometry. By measuring the centrality, we can approximate the impact parameter of the colliding nuclei, as well as the number of participants and binary collisions. Centrality is defined in terms of a percentile where 0-5% refers to the most central or head-on collisions, and 92% is the most peripheral or grazing collisions measured. The centrality classes are divided according to the event multiplicity by measuring the energy deposited in the ZDC and BBC for each event. Fig. 2.4 shows energy measured in the ZDC versus the charge measured in the BBC. The color bands indicate different centrality classes.
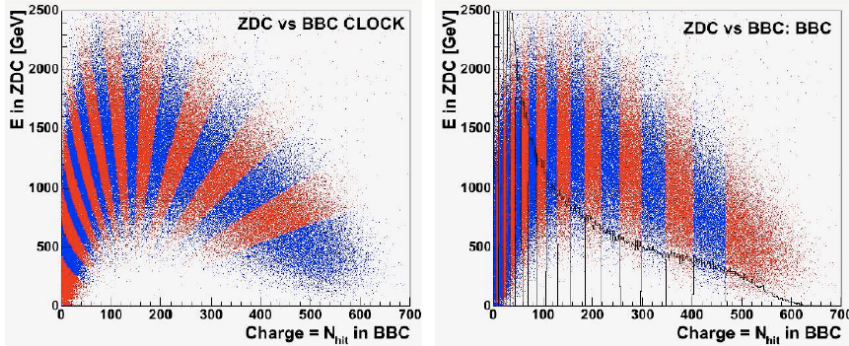
Figure 2.4: ZDC vs BBC charge used to determine the centrality. The different colors show the different centrality selections. The most central collisions correspond to the right most band and the left most band is the most peripheral collisions. Both the clock method (left) and the BBC method (right) for defining the centrality are shown [14].

The BBC charge scales with the centrality of the collision, i.e. the most central collisions deposit the most charge in the BBCs. Spectator protons are swept away by the dipole magnets but unbound spectator neutrons are observed in the ZDC. For the most peripheral collisions, little energy is observed in the ZDC since most of the neutrons remain bound. Moving toward more central collisions, the amount of energy deposited in the ZDC increases because more neutrons are freed in these collisions. However, the ZDC energy drops for the most central collisions as more neutrons also participate in the collision.

A Monte-Carlo event generator, HIJING, designed to generate a multiplicity spectrum like measured experimentally [48]. HIJING can then translate the centrality classes determined experimentally to the initial collision geometry parameters. The Glauber model, which uses a Wood-Saxon potential to describe the nucleus, is used to relate the number of participating nucleons, N_{part}, or the number of binary collisions, N_{coll} to the impact parameter, b, of the colliding nuclei. The most central collisions, 0-5%, have small impact parameters and correspond to large N_{part} and N_{coll} values. The percentage refers the percentile of the total Au+Au cross-section. The MC is matched to the data according to the total integral and then applying the same percentile cuts.

Reaction Plane Detector

The reaction plane of an event is defined by the beam direction and the impact parameter which is the line connecting the center of the colliding ions. By measuring the anisotropy of the particles in the forward direction, the reaction plane angle, Φ_R, is determined with respect to a constant arbitrary angle in the laboratory coordinate system. The event plane,

$$\Phi_n = \frac{1}{n}\tan^{-1}\left(\frac{Y_n}{X_n}\right).$$ (2.2)

is measured from the nth harmonic particle distribution. X_n and Y_n are the event flow vectors, defined as

$$Y_n = \sum_i \sin(n\phi_i), X_n = \sum_i \cos(n\phi_i).$$ (2.3)

The resolution of this measurement improves with increasing multiplicity and anisotropy. Therefore the best resolution is achieved in mid-central collisions where the multiplicity is still high but the overlap region is more 'almond-like.' To minimize the effect of correlated jet particles in the measurement, it best to use detectors as far away from central rapidity as possible which makes the BBC a good candidate. However, to further improve the resolution, a new detector was added which is dedicated to measuring the reaction plane.

Prior to the 2007 RHIC run, the Reaction Plane detector, RXPN, was installed on the nosecone of the PHENIX central magnets. It has full 2π coverage in azimuth, ϕ, and spans $1 < \eta < 2.8$ in pseudorapidity. There is a North and South detector with the same design located at approximately ± 3.9 cm respectively from the nominal vertex position. Each detector has 24 trapezoidal scintillators which are oriented in two rings. Each ring includes 12 scintillator paddles evenly segmented in ϕ. Wavelength shifting fibers connect the scintillators to the photomultiplier tubes which read out the signal. A 2cm thick lead converter directly in front of the scintillators allows neutral particles to also be measured. Using the second harmonic to determine the reaction plane, the resolution of the RXPN is a factor of approximately 2 better than the BBC resolution [49].

2.2.2 Electromagnetic Calorimeter

$\gamma_{\text{dir}} - h$ correlations are extracted from the data by measuring inclusive $\gamma - h$ and $\pi^0 - h$ correlations. π^0 are measured via their decay into two photons by reconstructing the invariant mass of the photon pairs in the event. Therefore,
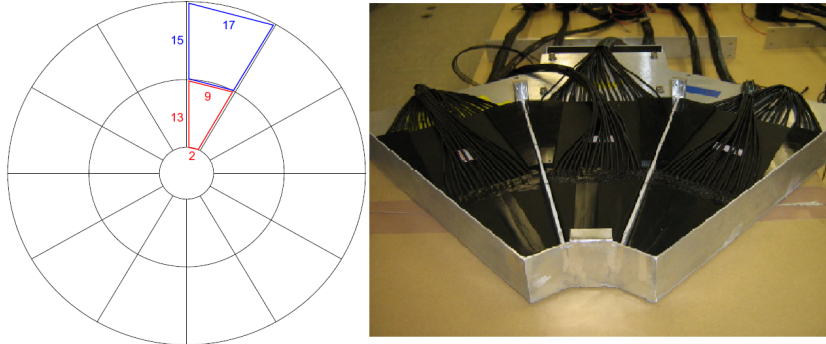
Figure 2.5: Left: A schematic of the paddle orientation of the RXPN detector. Right: An assembled tray containing 3 paddles of the RXPN detector prior to installation.

as the first step in this analysis, we need to measure photons. PHENIX has a high resolution electromagnetic calorimeter which is used to measure high momentum photons and π^0s. Additionally, in p+p collisions, the EmCal is used as a Level-1 trigger to select events with high energy, E_T, particles.

Six of the EMCal sectors are made of lead scintillator and two are lead glass, with an energy resolution of $\sigma_E/E = 8.1\%/\sqrt{E} \oplus 2.1\%$ and $5.9\%/\sqrt{E} \oplus 0.8\%$ respectively.

The PbSc is a shashlik type sampling calorimeter comprised of alternating tiles of Pb and scintillator. A module is comprised of four towers, as shown in Fig. 2.6. A single tower contains 66 of these sampling tiles, which are optically connected by wavelength shifting fibers. The fibers collect the light from the tiles and are read out by phototubes. 36 modules form a supermodule and eighteen supermodules form one sector. The timing resolution for the PbSc is ∼100 ps for electromagnetic showers and ∼270 ps for hadronic showers. The time of flight capabilities allow PHENIX to also identify low momentum pions and protons using the PbSc.

The PbGl is a Cerenkov detector, and is not used for hadron identification. It has a timing resolution of ∼300 ps, which is not as good as the PbSc, but the granularity and energy resolution are better. Using two different types of detectors, each with their own advantages, allows us to gain a better understanding of our systematic uncertainties and provides useful crosschecks for our measurements. Each PbGl sector is comprised of 192 supermodules. One supermodule contains 24 modules, as illustrated in Fig. 2.7. Carbon fiber and epoxy resin hold the modules together. The modules are read out by photomultipliers at the base of the module, housed behind 0.5 mm steel sheets. At the opposite end of the module is the calibration and gain monitoring system.
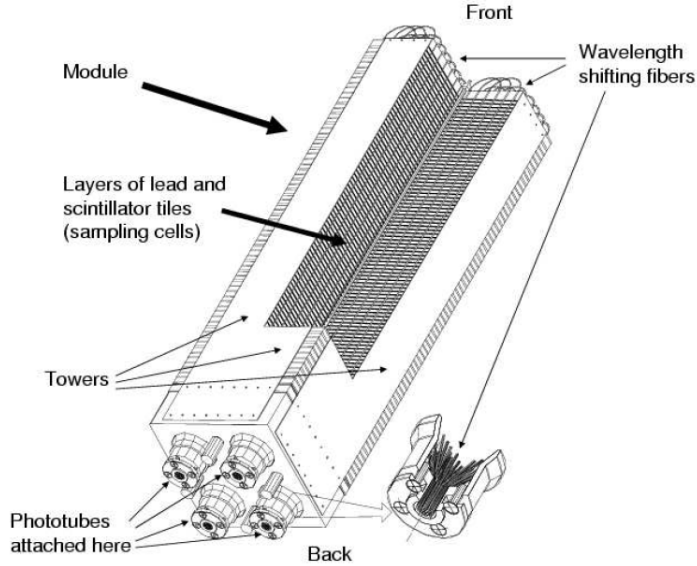
Figure 2.6: A schematic of a PbSc module, which is comprised of four towers of alternating layers of lead and scintillator tiles.

There is a hole in the plastic foil for each module, which allows in light from the LED system. The LED board is enclosed by the reflective cover.

2.2.3 Central Tracking

To study the fragmentation of the jet opposing the trigger photon, we measure inclusive charged hadrons. Charged hadrons are measured with the PHENIX tracking system which consists of a drift chamber and pad chambers. These detectors track the position of the particles and can be used to determine their momentum. The tracking has a momentum resolution of $0.7 \oplus 1.1p$.

Drift Chamber

Charged particles pass through the Drift Chamber (DC) and ionize the gas. The gas in the PHENIX DC is 50% Argon and 50% Ethane. The charge then drifts in the electric field toward the wires, which signals a hit. A cartoon in Fig. 2.8 shows how the wires are arranged in the chamber. There are gate wires to direct the drifting charge toward the anode wires, which measure the signal. There are back wires which also collect charge, such that the anode wires only receive signal from one direction. The drift space in this configuration is 2-2.5
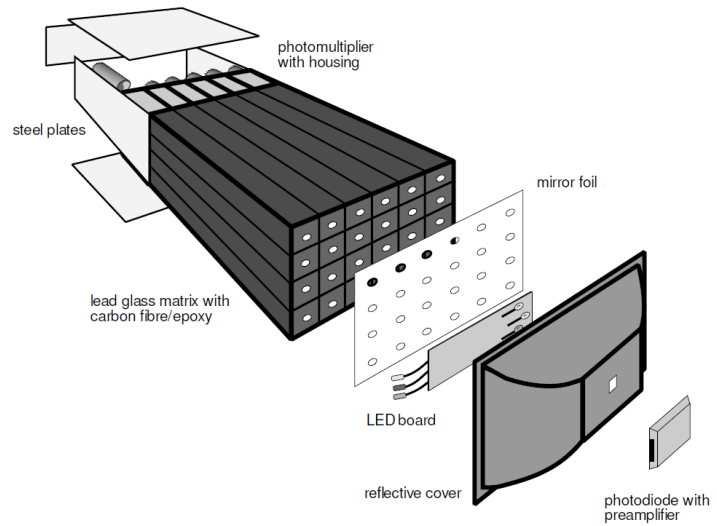
Figure 2.7: This cartoon shows a supermodule containing 24 PbGl modules.
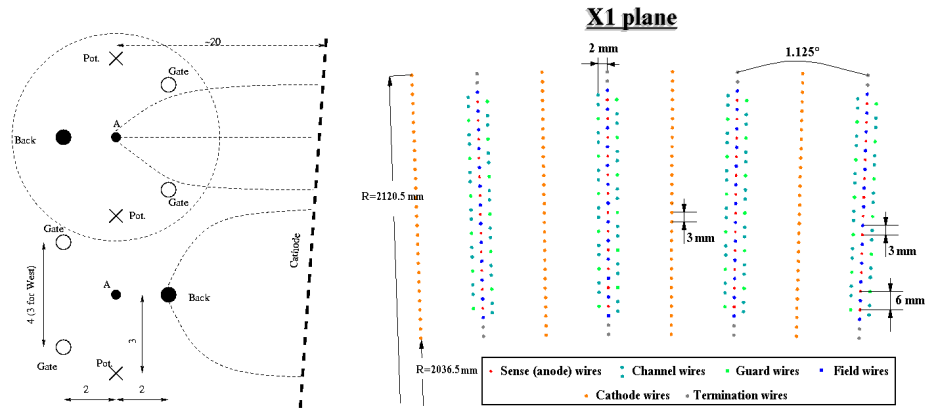
Figure 2.8: Wire configuration of the PHENIX drift chamber directs the ionization charge toward the anode wires. The cross-section of the X1 layer is shown as an example of the orientation of the wires.

cm. These wires are housed in a titanium frame. The single wire resolution and efficiency are 165 μm and above 95% respectively.

Fig. 2.9 shows the different layers of the DC. There are X layers and UV layers. The X layers are comprised of 12 planes of wires radially as shown in Fig. 2.8, while each U and V layer has only 4 planes. The right hand image of Fig. 2.9 illustrates just one of 80 sectors arranged along the ϕ direction of each arm. In total, the drift chamber contains 12800 wires. The track reconstruction is based primarily on the hit information from the X layers. However, because of the crossing pattern of the wires in the U and V layers, these layers provide tracking information along the z direction.
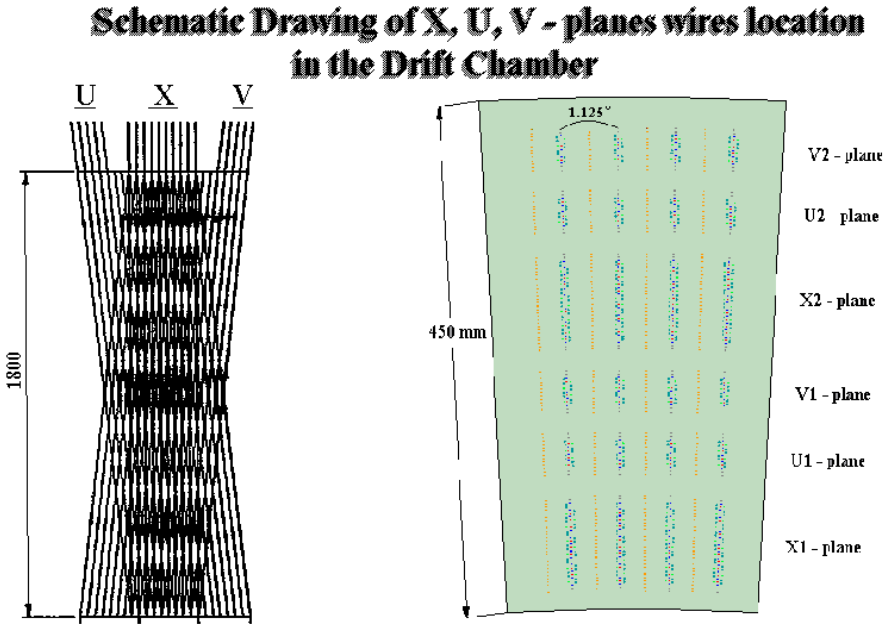
Figure 2.9: The different wire layers within the PHENIX drift chamber are labeled. The wires in the U and V layers cross the X layer wires to provide position information along the z direction.

To properly reconstruct the location of the tracks within the drift chamber, it is important to know the drift velocity of the charge within the gas. The drift velocity is determined using the online calibration code for each run. Several regions which were declared dead in the 2006 RHIC Run were revived for the 2007 Run by altering the voltage applied to the wires in that region. Because the voltage was different in these areas, the drift velocity changed. Therefore the calibration code was adjusted to determine the drift velocity for

41

each region instead of obtaining an average for each arm. In some cases, the back wire (see Fig. 2.8) could not hold charge. In that case, the back wire is simply turned off. No functioning back wire means that not only does the electric field in this region change, but also the anode wire registers hits from both sides.

First, the maximum time a track takes to reach the anode wire is determined using the raw timing distribution, as illustrated in Fig. 2.10. The histogram shows the distribution of times at which a signal was observed. The initial time at which the wire started collecting charge is determined by fitting the left hand side with a Hagedorn function. The left hand side of the distribution has nearly twice as many hits as the right hand side. The smaller times have more hits because the back wire is a finite distance away from the anode wire and cannot prevent the anode wire from collecting charge from these small distances. Therefore, this feature is not observed for the regions where the back wire had to be turned off. Instead, those histograms register hits at the level of the peak at small times shown here for all times. The maximum time required to reach the wire is the difference in time between the right edge of the histogram as determined from a similar Hagedorn fit and the initial time. This maximum amount of time corresponds to charges at the neighboring wires which was determined by a calculations of the electric field and physical distance between wires. The drift velocity is defined as

$$v_{drift} = \frac{d_{max}}{t_f - t_0},$$ (2.4)

where d_{max} is the maximum distance from the wire a charge can travel, t_f is the time at which a track from distance d_{max} signals a hit in the wire and t_0 is the initial time. Again, t_0 and t_f are determined by fits to the timing distribution shown in Fig. 2.10.

Pad Chambers

The pad chamber (PC) is comprised of multiwire proportional chambers. There are three separate pad chamber detectors in PHENIX. PC1 is the inner most and is used in the track reconstruction. PC2 and PC3 are further away from the beam pipe, and are typically used in the analysis stage to purify the sample of tracks. PC2 exists only in the west arm and is not used in this particular analysis. The distance between a track projection and a hit in the PC3 is measured along the beam direction, z, and in azimuth, ϕ. The distributions of these distances are peaked around zero. By fitting them to a Gaussian, we can determine how many sigma way a hit is from the track projection. Cutting on the sigmalized variables reduces background in the charged track sample
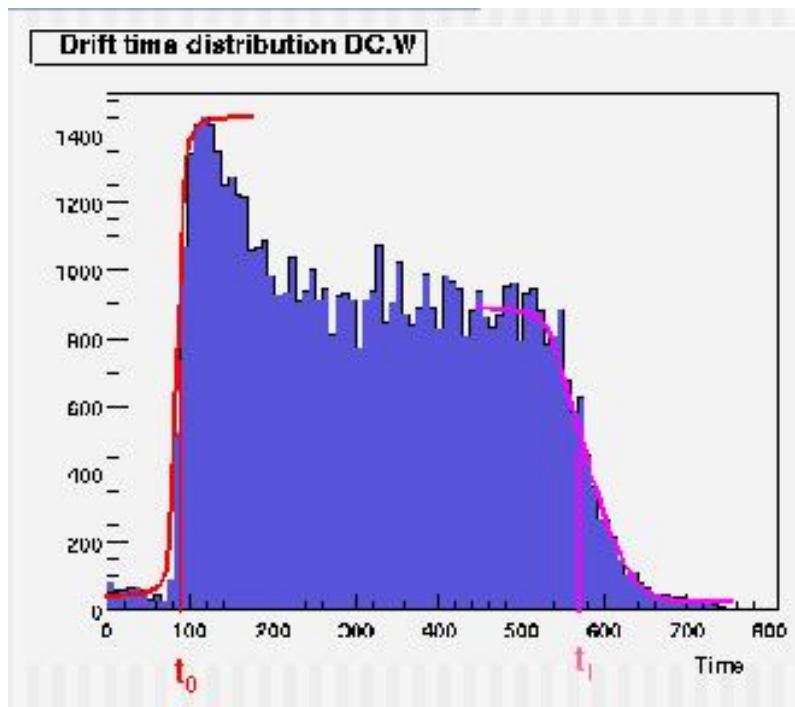
Figure 2.10: The timing distribution of hits in the drift chamber used to determine t_0 and t_f from the fits to the edges of the distribution.

and will be discussed further in analysis discussions in Chapter 3.
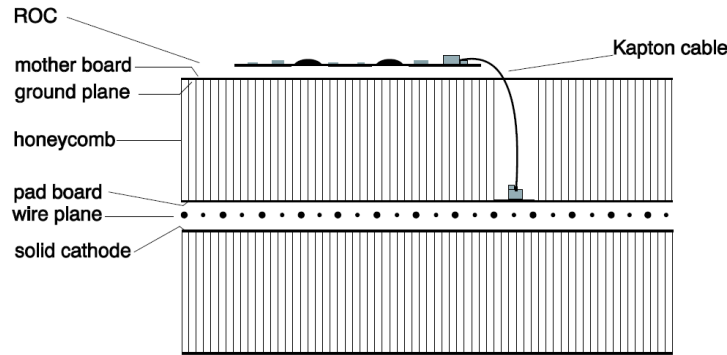
Figure 2.11: A cartoon that shows the different planes of the PC.

Each PC consists of a single plane of anode and field wires in gas sandwiched between cathode planes. One of the cathode planes is actually segmented into pixels. Three pixels form one cell. To signal a hit, a cell must detect an avalanche in all three pixels to reduce background noise. The signal is amplified and discriminated by the Readout Card (ROC) as labeled in Fig. 2.11. The other cathode plane is a solid copper layer. The PHENIX design achieved an ± 1.7 mm resolution in z and maintains the same angular resolution in all three PCs by scaling the size according to the radial distance.

PC1 consists of 8 chambers along ϕ in each arm. Because it is an inner detector, the radiation thickness of PC1 is minimized by requiring no structural frame. The stiff honeycomb structure of the planes makes this possible, but the lack of frame means the gas chamber must be glued shut. The resulting thickness is less than 1.2% of a radiation length. Radiation thickness is less of a concern for the outer PC2 and PC3, so fiberglass frames with O-rings instead of glue were used.

Tracking Quality

Every reconstructed track is given a quality number based on the number of hits used in the reconstruction. Typically good tracks are defined as having a quality value of 31 or 63. To earn a quality of 31 or 63, the track reconstruction requires a hit in both the X1, X2, and one of the UV layers of the DC as well as a hit in the PC1. For 63 the hit in the PC1 and UV layers are unique matches while for 31 there are multiple PC1 hits but the UV wires can be used to determine the best choice.

RICH: Electron Identification and Vetoing

Since the goal of measuring charged tracks in this correlation analysis is to measure hadrons, we need to reject electrons from the sample of charged tracks. PHENIX was specifically designed to identify electrons very well. One of the primary detectors used for this is the Ring Imaging CHrenkov (RICH) detector located directly behind the PC1 in the central arms. Spherical mirrors reflect the Chrenkov light produced by electrons passing through the radiator gas onto PMTs, as illustrated by the first cartoon in Fig. 2.12. 48 mirror panels form the two spherical surfaces. The detector and gas were designed to be only 2% of a radiation length in total thickness to minimize conversions. The minimum and maximum ring expected for electrons is illustrated in the same figure. The radiator gas used is CO_2; this produces an average of 12 photons in a ring of 11.8 cm for an electron with $\beta = 1$ traveling a path length of 1.2 m through the gas. High momentum pions, starting with $p_T > 4.65$ GeV/c, also produce radiation and therefore, a signal in the RICH. For this reason, the electron veto using the RICH is not applied for hadrons above 5 GeV/c in this analysis.
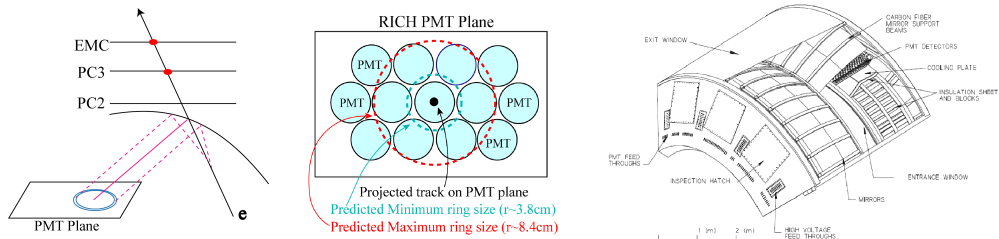
Figure 2.12: Cartoon of the RICH detector and how it works.

2.2.4 Hadron Blind Detector

The heavy ion group at Stony Brook played an important role in building the Hadron Blind Detector (HBD), which was installed for the first time in heavy ion collisions during Run 7. For this reason, a description of the HBD is provided here, even though it has no bearing at all on the analysis presented.

One of the major physics goals of the HBD is to improve the measurement of the di-electron mass spectrum. This measurement is extremely challenging due to large backgrounds. However, these backgrounds would be greatly reduced if one could distinguish between single electrons and those which actually come from pairs. Using Gas Electron Multiplier (GEM) technology, the

HBD is able to make this distinction based on the number of photoelectrons measured for each track.

The HBD is a proximity-focusing Cherenkov detector [50]. Unlike the RICH, it is windowless and does not require mirrors since CF_4 can act as both the radiator and detector gas. The Cherenkov light is collected on a photosensitive cathode. The detector uses a triple GEM stack configuration with CsI evaporated on the top GEM as the photocathode layer, as illustrated in the left image of Fig. 2.13.
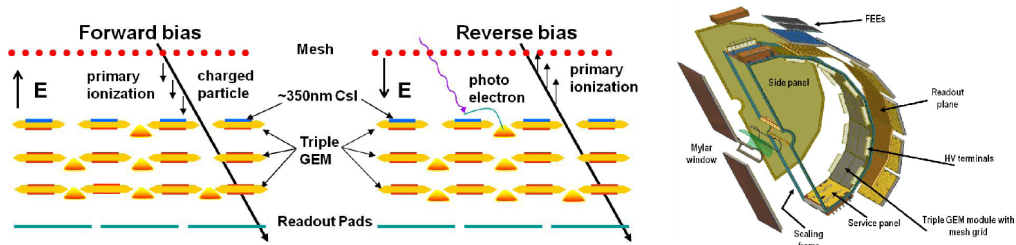
Figure 2.13: (Left) The triple GEM stack design of the HBD. (Right) Schematic of one HBD half.

Data from the Run 9 $p + p$ Run was used to study the ability of the HBD to discriminate between single electrons and pairs. Tracks from the central arm were projected onto clusters in the HBD. If two tracks pointed to a single HBD cluster, it was deemed a double electron hit and if only one track pointed to a single HBD cluster, it was deemed a single electron hit. The HBD response to a single and double electron hit are plotted in Fig. 2.14. The distribution for single hits on the left shows a peak around 20 photoelectrons (p.e.) while the double electron hit distribution peaks around 40 p.e., double the charge left by single electrons. This demonstrates the HBD single versus double hit recognition capabilities. Additionally, the detector performed well in terms of noise, stability, position resolution, hadron rejection and single electron detection efficiency [50].

A rebuild of the detector installed in the west arm was done prior to the 2010 Au+Au run, based on a procedure used in the successful rebuild of the east HBD. Analysis of the first physics results from this data using the HBD is currently underway.

2.2.5 PHENIX Data Sets

A summary of the PHENIX data collected to date is given in Table 2.1. The particle species and beam energies is listed for each RHIC Run along with the
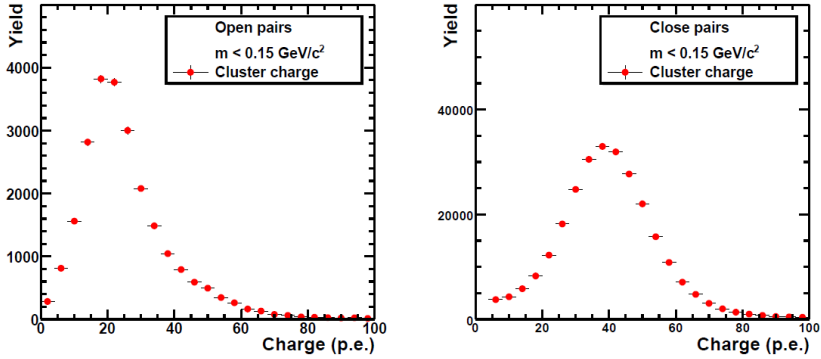
Figure 2.14: (Left) HBD response to single electrons according the charge per cluster measured in number of photoelectrons (p.e.). (Right) HBD response to electron pairs.

amount of data collected. The improvements in luminosity by the accelerator over time are evident in the table. The increasing size of the data sets collected allows for more precision measurements. The statistics are particularly important for studying rare probes such as direct photons.

The analysis presented in this thesis uses $p+p$ data at 200 GeV from Run 5 and 6 combined as a baseline for the Run 4 and Run 7 Au+Au measurements. The heavy ion analysis was established for the Run 4 analysis, but a factor of 4 more statistics was collected in Run 7 which greatly improves the measurements. The focus of this thesis is analysis done with the Run 7 Au+Au data. Since Run 7 is so much larger than the Run 4 data set, no attempt was made to combine these data sets since the statistics gained would be small compared to the systematic uncertainties in combining them.

Table 2.1: A summary of PHENIX data sets through 2011.

RHIC Run (Year)	particle species	beam energy (GeV)	sampled events	$\int Ldt$
1 (2000)	Au+Au	130	10 M	1 μb^{-1}
2 (2001-2)	Au+Au	200	170 M	24 μb^{-1}
	p+p	200	3.7 B	0.15 pb^{-1}
3 (2002-3)	d+Au	200	5.5 B	2.74 nb^{-1}
	p+p	200	6.6 B	0.35 pb^{-1}
4 (2003-4)	Au+Au	200	1.5 B	241 μb^{-1}
	Au+Au	62.4	58 M	9 μb^{-1}
5 (2005)	Cu+Cu	200	8.6 B	3 nb^{-1}
	Cu+Cu	62.4	400 M	0.19 nb^{-1}
	Cu+Cu	22.4	9 M	2.7 μb^{-1}
	p+p	200	85 B	3.8 pb^{-1}
6 (2006)	p+p	200	233 B	10.7 pb^{-1}
	p+p	62.4	28 B	0.1 pb^{-1}
7 (2007)	Au+Au	200	5.1 B	813 μb^{-1}
8 (2008)	d+Au	200	160 B	80 nb^{-1}
	p+p	200	115 B	5.2 pb^{-1}
9 (2009)	p+p	500	308 B	14 pb^{-1}
	p+p	200	936 B	16 pb^{-1}
10 (2010)	Au+Au	200	8.2 G	1.3 nb^{-1}
	Au+Au	62.4	700 M	0.11 nb^{-1}
	Au+Au	39	250 M	40 μb^{-1}
	Au+Au	7.7	1.6 M	0.26 μb^{-1}

Chapter 3

Analysis Details for Two Particle Correlations

In this chapter, we will discuss the analysis details relating to two particle correlation measurements. Since the main focus of this thesis is on the Run 7 analysis, details related to that particular run will be emphasized. However, some figures use the Run 4 Au+Au. Differences in the analysis between the different runs will also be discussed. Details relating to the $p + p$ analysis have been presented in a previous thesis [11]. The direct photon extraction will be discussed in the next chapter.

3.1   Event and Particle Selection

Standard PHENIX event cuts are used, cutting on z-vertex < 30 cm. The centrality bins used in this analysis are 0-20%, 20-40%, 40-60% and 60-92%.

To construct $\gamma - h^\pm$ correlations, we use high energy photons and π^0 as triggers. The triggers are binned in p_T as 5-7, 7-9, 9-12 and 12-15 GeV/c. The associated charged hadrons used range from 0.5-7 GeV/c. The following cuts are used to select these particles.

The triggers are measured using the EMCal. A hot and dead EMCal tower map is applied to all of the data which excludes any dead or hot towers, as well as those directly surrounding them, and the edges of the detector. These edges are excluded, since some of the energy for clusters centered in towers at the edges of the detector are likely to not fully deposit their energy within the acceptance resulting in the wrong energy. EMCal clusters are also limited along the z direction to $|z_{EMC}| < 155$ cm. Photons are identified in the PbSc based on a shower shape cut of $\chi^2 < 3$. Hadrons are vetoed from our trigger sample by projecting tracks from the DC onto the EMCal. If a projected track

points near the candidate photon cluster, that cluster is assumed to be energy from a hadron and is excluded from the photon sample.

The invariant mass, $m_{\gamma\gamma}$ is calculated according to

$$m_{\gamma\gamma} = 2E_1 E_2 \cos(1 - \psi) \tag{3.1}$$

for all photon pairs in each event where ψ is the angle between the photons. Each photon is required to have $E_\gamma > 1.0$ GeV to reduce the combinatorial background in the mass distribution. The leading photon is also required to pass all of the previously described photon cuts, while a looser $|z_{EMC}| < 165$ cm cut is applied to the second EMCal cluster. Invariant mass distributions are shown in Fig. 3.1 for the different trigger p_T bins. We consider pairs which fall into the mass window, $[0.12 GeV/c^2, 0.16 GeV/c^2]$ as π^0 triggers. Because the π^0 triggers will ultimately be used for determining $\gamma_{\text{dec}} - h$ correlations for the same trigger p_T range, $5 GeV/c < p_{T_\gamma} < 15 GeV/c$, as the inclusive photon correlations, we actually use π^0 triggers with $4.0 GeV/c < p_T < 17.0 GeV/c$. The energy of the photon pair must also fulfill $(E_{\gamma1} + E_{\gamma2}) > 4.0 GeV$. For the 40% most central collisions, a strict energy dependent asymmetry cut was applied for $4.0 < E_{\pi^0} < 5.25$ such that $\alpha < 0.15 + 0.85(E_{\pi^0} - 4.0)^2/1.25^2$, where $\alpha = |E_{\gamma1} - E_{\gamma2}|$. The asymmetry cut reduces the combinatorial background since the multiplicity of low energy photons is high in these collisions.
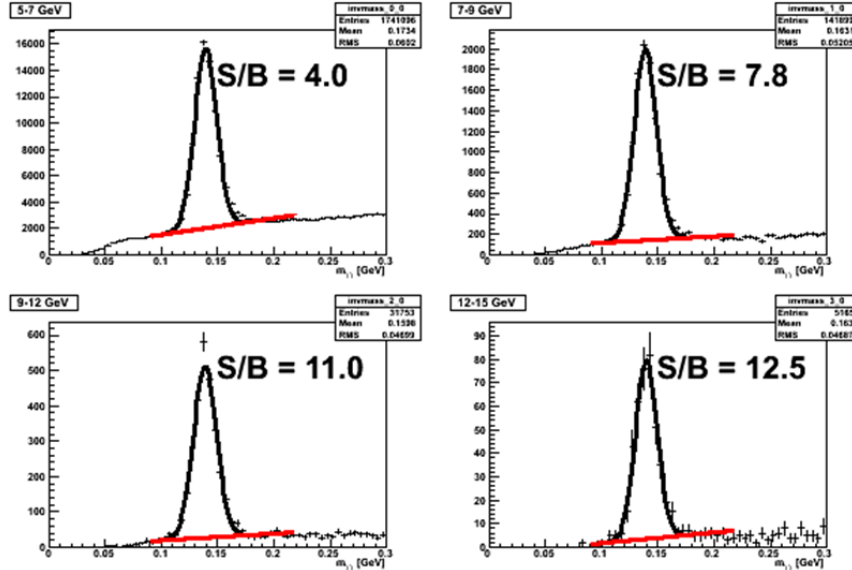
Figure 3.1: The invariant mass distribution for photon pairs from the Run 7 0-20% central data. The S/B ratio for the π^0 peak is listed for each trigger bin as determined from the fits.

For the charged hadrons, good tracks were selected according to the standard PHENIX quality cut. (In PHENIX code this refers to the requirement, *quality* == 31||63 as described in Chapter 2.) To remove electrons from our sample, tracks which leave a signal in the RICH are excluded. Since π^0s start radiating in the RICH around p_T =4.7 GeV/c, this cut is only applied to tracks with $p_T < 5.0$ GeV/c. Because the tracking code assumes a vertex in the center of the beam pipe, electrons from conversions near the edge of the detectors can be misreconstructed as high p_T tracks. To reduce this background contamination in our sample of charged tracks, a radial PC3 matching cut is applied. Tracks reconstructed by the DC and PC1 are projected onto the PC3. To pass the cut the sigmalized distance between the projection and the nearest PC3 hit must satisfy $\sqrt{(\sigma\phi_{pc3}^2 + \sigma z_{pc3}^2)} < 2.0$. By comparing this cut to looser matching cuts, we can observe the effect of this background at high p_T as shown in Fig. 3.2 from the Run 4 data.
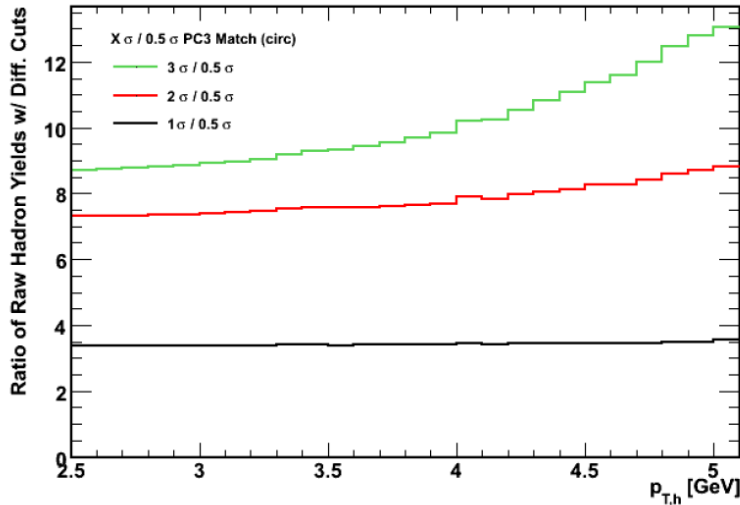
Figure 3.2: Ratio of different PC3 matching cuts on the charged hadron spectrum as measured from the Run 4 data. The increase at high p_T is due to contamination from misreconstructed conversion electrons.

Assuming the 0.5σ cut is pure signal, Fig. 3.2 shows that the 1σ cut is almost as pure since the ratio is flat for all p_T, but gains a factor of about 3.5 more statistics. Since this is a statistically limited measurement, it is important to find a cut which maintains purity while preserving statistics. The ratio of the 2σ cut is flat until about 4 GeV/c where the ratio starts to increase slightly. This increase indicates the presence of background in the sample. However, we should note that this ratio at about 7.5 includes more

than twice as many hadrons. The 3σ ratio shows a small increase in statistics over the 2σ ratio but a clear influence of high p_T background. Based on this study, we decided to use a 2σ cut.

In Run 4, the hadrons measured extended up to $p_T = 5\text{GeV/c}$. However, with the additional statistics in Run 7 we would like to try to extend that measurement to include a 5-7 GeV/c bin. The ratio between the 2σ and 3σ cuts were measured in Run 7 in a similar analysis of π^0-h correlations [15]. Those results are shown in Fig. 3.3. This plot demonstrates the effect of including a high p_T trigger. This condition leads to a more pure sample of hadrons. Since contamination is clearly a concern above 5 GeV/c, studies were done to approximate the effect of this background on the yield. By measuring correlations for tracks excluded by the PC3 cut and comparing them to the real correlations, it was determined that the yields on the away-side differed on average by about 8%. Therefore, for the Run 7 analysis an additional systematic uncertainty of 8% is included on the final yields. We were initially concerned that the presence of the HBD in Run 7 and reduced magnetic field could enhance the electron contamination of our hadron tracks. However, no strong effects are actually observed in the data.

3.1.1 Run selection

To insure that the quality of the data used for this analysis is good, several quality analysis (QA) checks are done to exclude bad runs. First, runs which indicate any change in the magnetic field are considered bad. Bad runs are also excluded if the reconstructed π^0 peak position is misplaced. Converter runs, where extra conversion material is introduced into the detector, are also excluded. Additional QA was performed by comparing the shape of the mixed event correlations for each run to the summed mixed event background. The shape of the background depends on detector conditions. It is important that the mixed event distribution accurately represents the background to properly extract the physics correlations in the measurement. The ratio between the background correlations for each run and the summed correlation is fit to a flat line. The fits with $\chi^2 > 3$ are checked by eye. A hard cut off based on the χ^2 is not used because occasionally the χ^2 is high due to high statistics in that run and not because the run is actually bad. An example of a good run with a large χ^2 is plotted in Fig. 3.4 and the mixed event $\Delta\phi$ correlation for a bad run is plotted in Figure 3.5. The black points for the selected run should be similar to the summed correlations shown in red. The run shown in Fig. 3.5 is considered bad because of the large differences near the peaks of the correlation functions. Also note the difference in the scales of the ratio plots shown on the right-hand side of Fig. 3.4 and Fig. 3.5. The variations
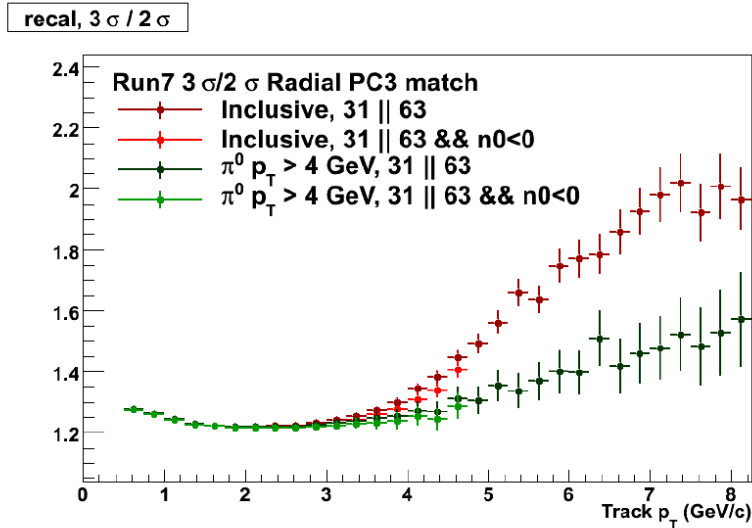
Figure 3.3: The ratio of 3σ to 2σ PC3 matching cuts for π^0 triggered tracks from [15] shows the background contamination at high p_T in Run 7. The 31||63 refers to the track quality cut used. This standard cut is applied to all data points included on the plot. n0 refers to the RICH cut used to veto electrons below the pion threshold. The darker data points do not include a RICH cut and are slightly but noticeably above the lighter colored data points which do use the RICH cut to exclude electrons. The red points correspond to all tracks including those which not triggered by a high p_T π^0. Requiring a trigger, clearly reduces the background contamination. An 8% systematic uncertainty was included for hadrons with $p_T > 5\text{GeV}/c$ due to the increasing background in this range. Despite changes in the detector configuration, no additional contamination was observed in the Run 7 study.

in the ratio for the good run are much smaller than in the plot of the bad run. These are examples from the Run 7 data but the same QA procedure was done on the Run 4 and $p + p$ data sets. Of the 871 total runs collected by and produced by PHENIX during the 2007 RHIC run, 15 runs are determined to be bad based on this procedure and are excluded from the analysis.
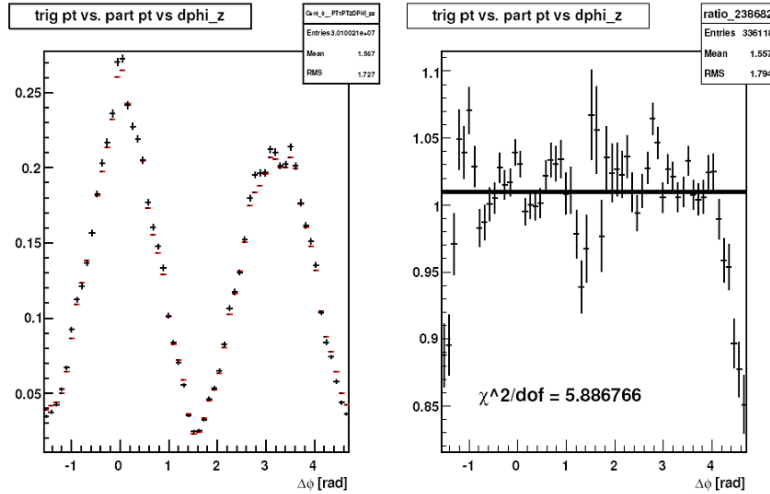
Figure 3.4: Mixed event background for one good run compared to the sum of several runs. The ratio of the backgrounds is plotted on the right. This is considered an acceptable run although the χ^2 is a bit high.

3.2 Two-particle Correlations

A basic primer on two-particle correlations was presented in the Introduction of this thesis. For convenience Eqn. 1.14 is repeated here.

$$\frac{1}{N^t}\frac{dN^{pair}}{d\Delta\phi} = \frac{1}{N^t}\frac{N^{pair}_{real}}{2\pi\epsilon^a}\left[\frac{dN^{pair}_{real}/d\Delta\phi}{dN^{pair}_{mix}/d\Delta\phi} - b_0\left(1 + 2\langle v^t_2 v^a_2\rangle\cos\left(2\Delta\phi\right)\right)\right] \quad (3.2)$$

N^{pair}_{real} refers to the number of pairs in real events and N^{pair}_{mix} refers to pairs created by mixing trigger particles from one event with associated particles in other events. Real and mixed events are also sometimes referred to as foreground and background. Each trigger particle is mixed with associated particles from other events which have similar centralities and z vertex values. Since the triggers and associated particles come from different events, the only
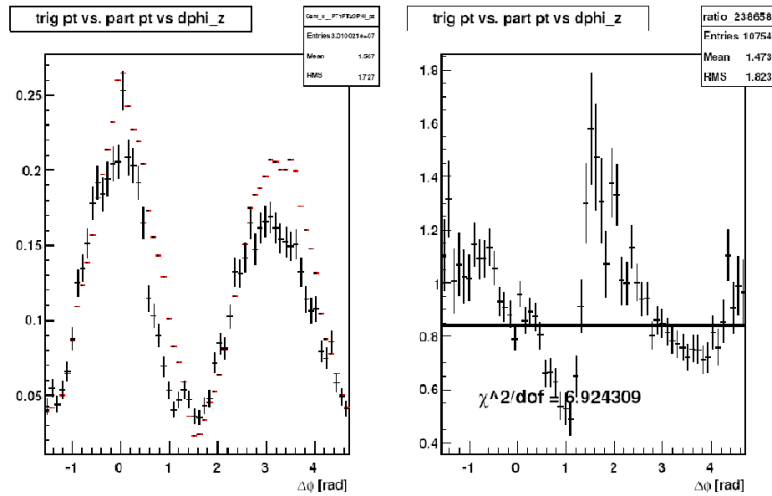
Figure 3.5: Mixed event background for one run compared to the sum of several runs. The ratio of the backgrounds is plotted on the right. This run is excluded from the analysis because of the mismatch in shapes shown here.

correlations present in the mixed pairs should result from detector acceptance effects. The shape of the PHENIX detector leads to the double peak structure observed in the mixed events shown in Fig. 3.4. If the central arms at PHENIX were exactly back to back, no measurement at $\Delta\phi = \pi/2$ could be made. For this reason, the PHENIX arms are orientated such that there is an approximate 70° gap between the tops of the arms, but this configuration still limits the acceptance for pairs at $\Delta\phi = \pi/2$ and causes the double peak structure in the mixed events. Other efficiency effects and dead areas in various detectors result in distortions to these peaks. We can correct the real pair distribution for these effects by diving the real pairs by the mixed pair distribution as a function of $\Delta\phi$. This is why the quality analysis explained in the previous section is important.

Since we are interested in only the correlations due to the jets, the correlation due to flow must also be removed. As discussed previously, Eqn. 1.14 only takes into account elliptic flow and assumes that higher order terms are negligible. The elliptic flow for the trigger and associated particles are denoted by v_2^t and v_2^a respectively. The determination of their values is discussed in the next section.

The normalization of the flow modulation, b_0, is determined in two ways. The zero yield at minimum (ZYAM) method is used to remove the flat underlying event in the p+p analysis. As the name suggests, we assume that the yield between the near side and away side jets is zero near $\Delta\phi \approx 1.5$.

To minimize effects due to fluctuations in the data a fit is typically used to determine the ZYAM level. The level is set at the minimum of the fit function. To approximate the error in the method the data points are randomly shifted according to their statistical uncertainties and are then refit. By doing this procedure several times (on the order of 50 times is sufficient), an upper and lower value for the uncertainty on the level can be determined. Alternatively, one can use the Absolute Normalization Method (ABS) to determine the background level without relying on any assumptions on the shape of the correlation function. This feature is particularly useful for correlations with low statistics and modified shape which is why the ABS method is used the Au+Au analysis.

3.2.1 Fill Time Method for making z_T distributions

In the Run 4, the first Run 7 and early $p + p$ analyses, the z_T distributions were measured by doing the full analysis in p_T bins and then transforming that into $z_T = \langle p_{T,h} \rangle / \langle p_{T,\gamma} \rangle$. This resulted in some overlapping points along z_T. Ideally we would like to combine these points, since, as we will show later, they all appear to lie along the same curve within our current uncertainties. The best way to do this is to bin the histogram in z_T at the beginning when we first pass over the data files. To do this one needs to know all the corrections ahead of time. Therefore, while passing over the full data, we fill the histograms with weights which include all the corrections which have a p_T dependence. The weights were determined from Equation 3.3 which describes how to remove the flow component from the correlations.

$$\frac{1}{N^A} \frac{dN^{AB}}{d\Delta\phi} = \frac{\frac{dN^{AB}(\Delta\phi)}{N^A \epsilon d\Delta\phi}}{Acc(\Delta\phi)} - b_0'(1 + v_2^A v_2^B cos(2\Delta\phi)) \frac{\frac{dN^{AB}_{mix}(\Delta\phi)}{N^A_{mix} \epsilon d\Delta\phi}}{Acc(\Delta\phi)} \qquad (3.3)$$

where

$$Acc(\Delta\phi) = \frac{\pi dN^{AB}_{mix}(\Delta\phi)}{\int d\Delta\phi \frac{dN^{AB}_{mix}(\Delta\phi)}{d\Delta\phi}}. \qquad (3.4)$$

The first term is the correlation function which is filled with real events and weighted by the efficiency correction and acceptance correction as measured on a previous pass of the data. The second term is measured using mixed events. The weights on the second term include the flow modulation, efficiency and acceptance. Normalizing by the number of triggers is done at the end. The b_0' correction to the normalization is also applied at the end and not included in the weight factor, although it could be.

The inclusive photon-hadron jet functions using this fill time method are compared to the traditional p_T binned results in Figure 3.6. In most cases it is difficult to see both sets of data points since they overlap. This cross check validates the implementation of the fill time method. Comparisons of the final γ_{dir}-h z_T distributions for the two methods also showed consistency. Throughout the remainder of this Thesis, these two methods will be referred to as the p_T binning method and the filltime method.
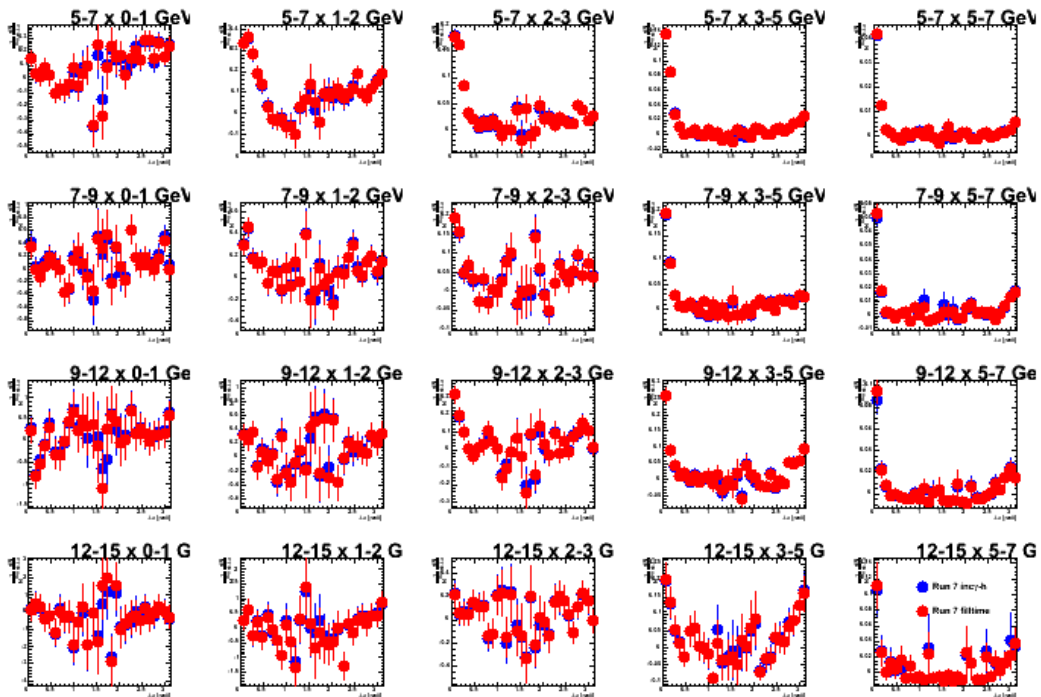
Figure 3.6: inclusive $\gamma - h$ correlations for the traditional method (blue) compared to the filltime method (red).

3.2.2 Elliptic Flow

As explained previously, in heavy ion collisions the correlation due to flow must be removed. This requires a measurement of the v_2 for both the trigger and associated particles. First we will discuss the associated hadron v_2 and then discuss the v_2 values for the γ_{inc}, π^0 and γ_{dec} triggers.

The charged hadron v_2 is taken from a separate analysis and plotted in Fig. 3.7 for Run 4. The Run 7 charged hadron v_2 values used in this Run 7 correlation analysis are listed in Table 3.1.
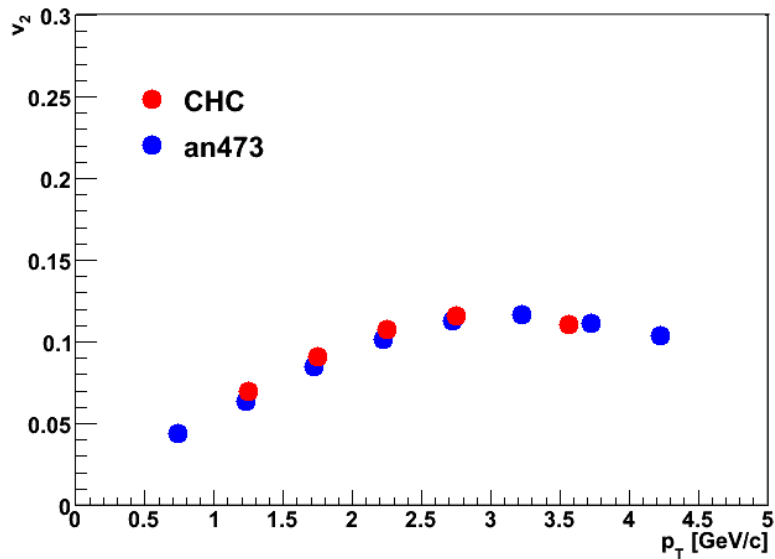
Figure 3.7: Run 4 unidentified charged hadron v_2 used in this analysis in red compared to another PHENIX analysis in blue.

Table 3.1: Charged hadron v_2 values for 0-20% in Run 7

$p_{T,h}$ [GeV/c]	v_2	Stat err	Sys. err
0.5-1	0.0440219	0.000145508	0.00137609
1-2	0.0745276	7.62922e-05	0.002022
2-3	0.109507	0.000216781	0.0030719
3-5	0.110372	0.000591522	0.003229
5-7	0.08275	0.00844	0.005

The v_2 for the triggers used in this analysis was actually measured in a separate analysis which used the same cuts and p_T binning. The Run 4 and Run 7 analysis use different but consistent v_2 values as improved measurements became available for the Run 7 analysis. The BBC was used to determine the reaction plane for the Run 4 v_2, while in Run 7 the new higher resolution RXPN detector was used. An extrapolation to higher p_T had to be done for the triggers in Run 4 due to a lack of statistics, which was not necessary in Run 7. Fig. 3.8 and Fig. 3.9 show plots of the γ_{inc} and π^0 v_2, respectively, for the most central 0-20% Run 4 data. The plots show the extrapolation of the π^0 v_2 used to determine the γ_{dec} v_2 in blue. The v_2 for $p_T > 6\mathrm{GeV}/c$ is assummed to be constant. More recent results suggest that this is not true [51]. However, this assumption is reasonable within the uncertainties of the measurements presented here.
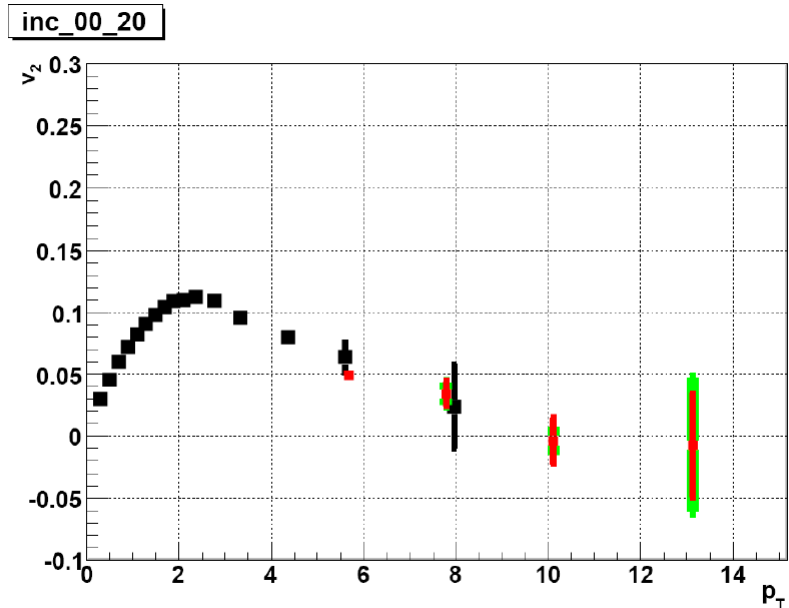
Figure 3.8: Run 4 inclusive photon v_2 for 0-20%. The red points are those used in this analysis while the black points are preliminary measurements for comparison.

The trigger v_2 values used for the 0-20% Run 7 analysis are listed in Table 3.2. These values were likewise determined in a separate analysis with the same binning. For these Run 7 v_2 measurements, the RXPN detector was used to determine the angle of the event plane. The improved resolution from this new detector reduces the systematic uncertainty in the v_2 measurements.
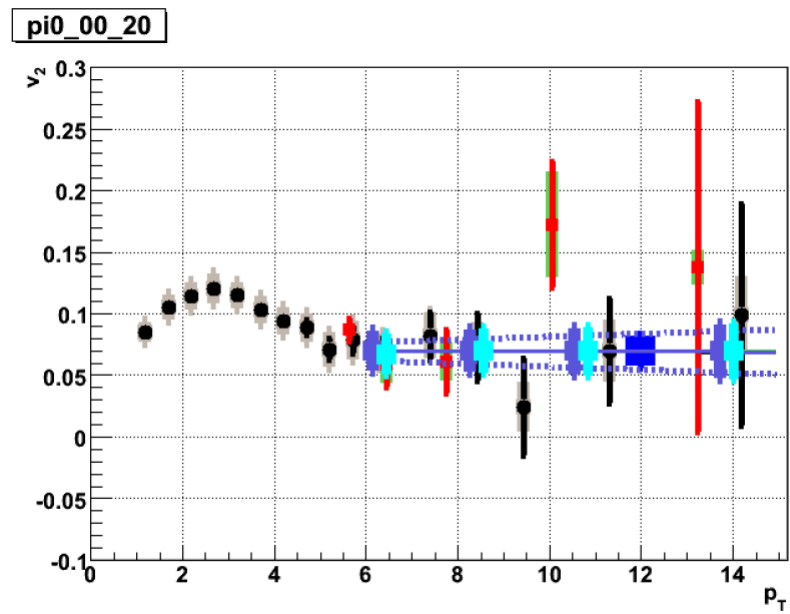
Figure 3.9: Run 4 π^0 and decay photon v_2 for 0-20%. The red points are those used in this analysis while the black points are preliminary measurements for comparison. The solid line is an extrapolation to obtain values beyond the v_2 measurement in p_T. The dashed line indicates the error on the extrapolation.

Table 3.2: Trigger particle v_2 values for 0-20% in Run 7

Trigger	$p_{T,\gamma}$ [GeV]	v_2	Stat err	Sys. err
π^0	5-7	0.0835297	0.00287215	0.0118235
	7-9	0.0755782	0.00531345	0.00960588
	9-12	0.0839048	0.0101393	0.0180581
	12-15	0.105555	0.0258798	0.0475144
decay γ	5-7	0.0802729	0.00259655	0.0106477
	7-9	0.0769908	0.00440387	0.0111283
	9-12	0.0831338	0.00951379	0.0208089
	12-15	0.102667	0.0238731	0.0361649
inclusive γ	5-7	0.0423226	0.00175307	0.0076029
	7-9	0.0461296	0.00454517	0.00432369
	9-12	0.0398415	0.00836215	0.00344175
	12-15	0.0169588	0.0189458	0.00465717

Using the decay mapping function, which will be discussed in the next chapter, the π^0 v_2 values are transformed to decay photon v_2. The values of the decay photon v_2 are included in the table as well as in Fig. 3.10, where they can be compared to a seperate measurement for the decay photon v_2. The two different results agree well.

3.2.3 Elliptic Flow for Filltime Method

Ideally, for the filltime method distributions one would use a continuous function of $v_2(p_T)$ in the weights. However, since the decay weighting is performed for discrete bins, it is more reasonable to use the measured trigger v_2 in those same bins and only use a smooth continuous function for the partner v_2. The discrete trigger bins used are tabulated in Table 3.2. They were measured using the reaction plane detector. The hadron bins used are in Table 3.1. Figure 3.11 shows the measured hadron v_2 in red and the interpolated v_2 used for the weights in black. The values in the table are still used at high $p_{T,h}$ (5-7GeV/c) and for propagating the errors.

Excluding Higher Order Flow Terms

The existence of higher order terms was alluded to in the Introduction but only the v_2 contribution is actually subtracted. Initially, it was assumed that all other terms were negligible because odd order terms are zero based on symmetries of the initial geometry and v_2 is the dominant even order term. However, recent work has been done which shows that fluctuations in the
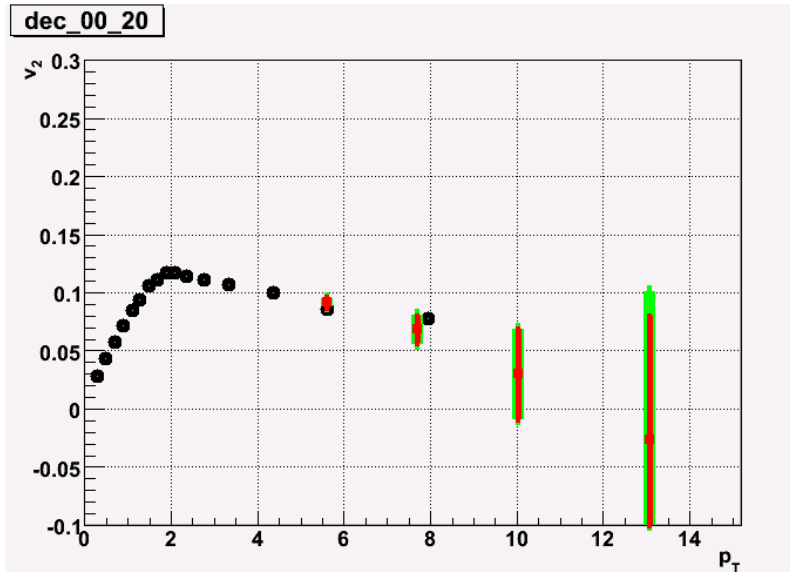
Figure 3.10: The decay photon v_2 value used in this Run 7 analysis in red compared to another analysis in black.
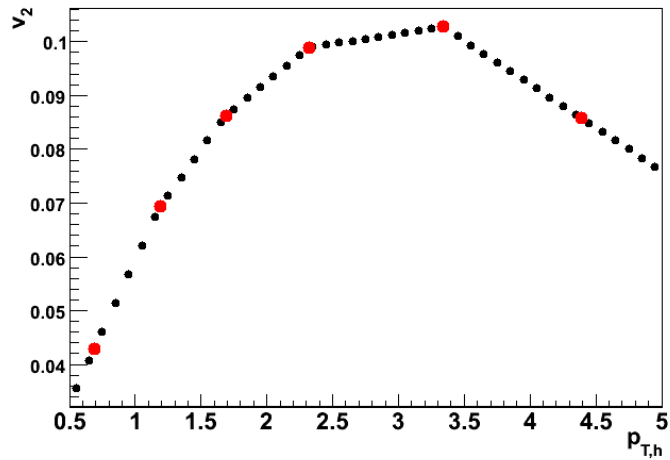
Figure 3.11: The measured hadron v_2 is shown in red, with the interpolation between data points used for the weighting in black.

initial geometry can lead to non-negligible odd and higher order even terms. Although the community seems to now agree that these fluctuations are relevant, it remains unclear how to properly account for them when extracting the jet yield and first attempts to do so have just begun in h-h correlations. Furthermore, PHENIX has not yet measured these additional terms for the triggers used in this analysis or all the hadron p_T bins used. However, in lieu of these recent studies, it seems appropriate to at least try to estimate a systematic uncertainty due to excluding these terms.

As a first look at how the v_3 term would affect the measured yields, the v_3 values for unidentified hadrons measured by PHENIX [52] are used. This study is done for the 20-40% centrality bin. The value at the highest measured p_T bin, 3-5 GeV/c, was used for all the trigger particles as well as for our highest p_T hadron bin (5-7 GeV/c). Similarly on the low end, the v_3 measured for the 1-2 GeV/c bin was also used for our 0.5-1 GeV/c hadrons. The γ_{inc}-h jet functions determined by subtracting out v_2 only are shown as the black points in Fig. 3.12 while the jet functions with v_3 as well as v_2 subtracted are the red points. Since the underlying background decreases as you move to higher p_T, it is not surprising that the points lie nearly on top of one another for the higher p_T bins. A difference is visible, however, for the lowest p_T bins. The shape change is clearly visible in the 5-7 GeV/c x 0.5-1 GeV/c p_{T_γ} x p_T^h bin. The most notable feature is that by including the v_3, the apparently broadened away-side peak is narrowed. Narrowing the peak does not mean that the yield has decreased, though, because the height of the peak itself has increased. This results from the dip at π from the $\cos(3\Delta\phi)$ modulation.

We should note that by using the same background normalization, b_0, as determined for the ABS method, for both subtractions, the total yield over all $\Delta\phi$ of the jet function remains constant. Only the shape of the jet function is actually modified. Since the integral of $\cos(3\Delta\phi)$ is positive for $\pi/2$ to π, subtracting this shape will reduce the yield on the away-side, while increasing the yield on the near-side. Therefore, one could argue that an observed enhancement of the away-side in I_{AA} is due to ignoring v_3, which makes understanding how this modulation could affect our final results important. To check the potential impact v_3 could have, we plot the resulting $\gamma_{\mathrm{dir}} - h$ for the two different subtractions in Fig. 3.13. The error bars plotted are of course highly correlated but one point with errors clearly encompasses the other data point, indicating that this effect is small compared to the other systematic uncertainties. To see how this affects the integrated away-side yield, these plots are rebinned in Fig. 3.14. Again the difference nearly disappears as we move toward the higher p_T bins. The difference at low p_T clearly shows the shift of yield from the away-side to the near-side. The largest change on the away-side

is less than a 15% effect. An uncertainty from this study was propagated into the fill time method for the Run 7 data by changing the weighting histogram used to subtract flow. The difference between the final results was then added as a systematic uncertainty. Since this effect decreases the yield at all p_T, but in different amounts, the error is correlated but not a global scale uncertainty since the size of the uncertainty depends on the size of the background being subtracted.
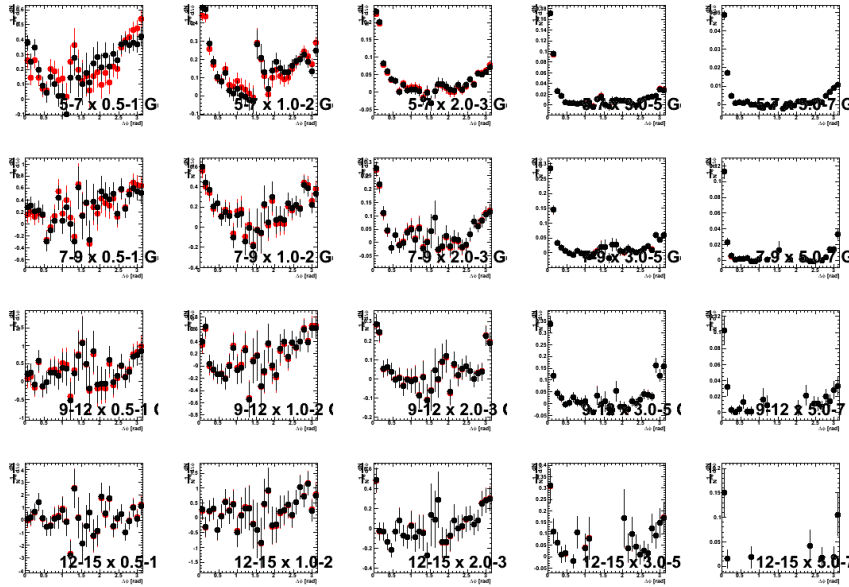
Figure 3.12: The γ_{inc}-h jet functions with v_2 only (black) and v_2 plus v_3 (red) subtracted.

3.2.4 Absolute Normalization

To extract the jet yields, the ABS method was used to determine the normalization level for the background. The idea behind this method is that the background level, b_0, can be determined based on the mean number of triggers and partners per event. This method, therefore, is sometimes referred to as Mean Seeds Mean Partners (MSMP).

A scale factor, ξ, is required to account for the centrality resolution which results from our finite binning in the mixing procedure. The jet function given in Eqn. 3.2 can be rewritten as follows for trigger particles, A, and partner particles, B.

64
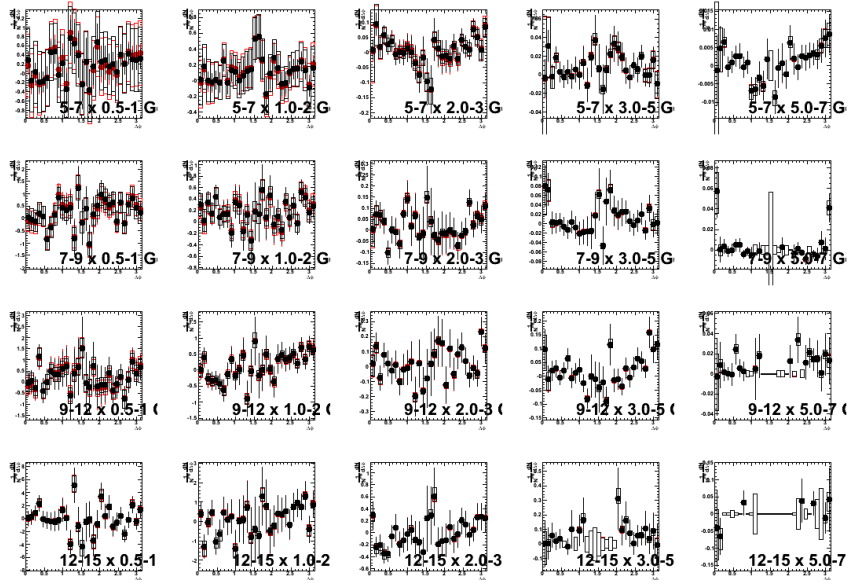
Figure 3.13: The γ_{dir}-h jet functions with v_2 only (black) and v_2 plus v_3 (red) subtracted.
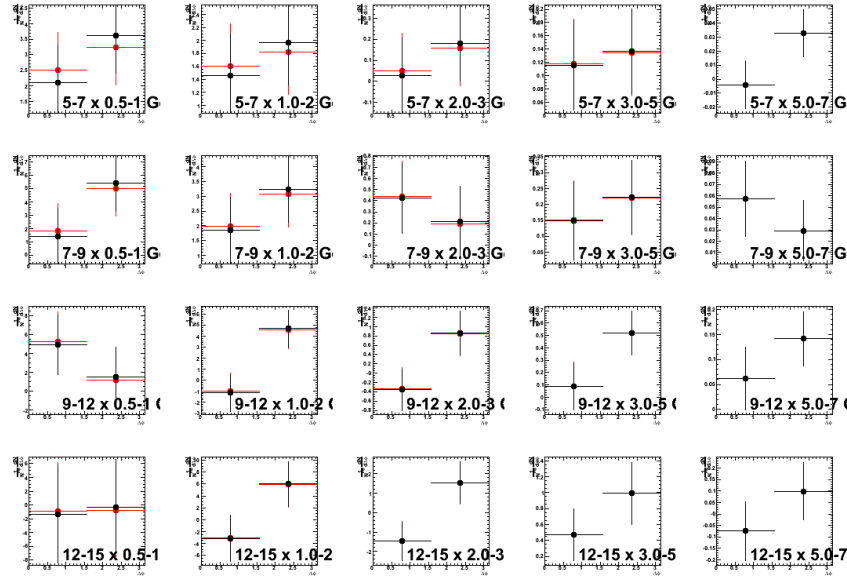
Figure 3.14: The γ_{dir}-h jet functions with v_2 only (black) and v_2 plus v_3 (red) subtracted. This plots have been rebinned to more clearly show the near and away-side yields.

$$\frac{1 dN^{AB}}{N^A d\Delta\phi} = \frac{\frac{dN^{AB}(\Delta\phi)}{N^A \epsilon d\Delta\phi}}{Acc(\Delta\phi)} - \xi(1 + v_2^A v_2^B cos(2\Delta\phi))\frac{\frac{dN_{mix}^{AB}(\Delta\phi)}{N_{mix}^A \epsilon d\Delta\phi}}{Acc(\Delta\phi)} \qquad (3.5)$$

where

$$Acc(\Delta\phi) = \frac{\pi dN_{mix}^{AB}(\Delta\phi)}{\int d\Delta\phi \frac{dN_{mix}^{AB}(\Delta\phi)}{d\Delta\phi}}. \qquad (3.6)$$

The ξ correction factor is determined by fitting the number of trigger, n^A, and partner particles, n^B, as a function of centrality for each p_T. The distributions are plotted as a function of both N_{coll} and N_{part} and fit with two different functional forms. The two functional forms, the inverse tangent (3.7) and saturated exponential (3.8), are chosen to describe the data based on their smoothness and well-controlled behavior for large N, where N refers to either N_{coll} or N_{part}.

$$n^{\{A,B\}} = \gamma \arctan(\beta N^\alpha) \qquad (3.7)$$

$$n^{\{A,B\}} = \gamma(1 - e^{-\beta N^\alpha}) \qquad (3.8)$$

The average of these different fits and variables gives the value of ξ and their maximum spread provides an estimate of the systematic error on the method. As an example, Fig. 3.16 shows the centrality distributions for 5-7 GeV/c inclusive photons (top) and 1-2 GeV/c hadrons (bottom) as a function of N_{part}(left) and N_{coll}(right). The results of these fits are used in the determination of ξ according to

$$\xi = \frac{\langle n^A n^B \rangle}{\langle n^A \rangle \langle n^B \rangle} \equiv \frac{\sum_i P_i n^A n^B}{\sum_i P_i n^A \sum_i P_i n^B}, \qquad (3.9)$$

where P_i is the probability for a given N value to contribute to the given centrality bin. The probabilities are based on the Glauber calculation. The N_{part} and N_{coll} distributions from the Glauber Monte Carlo are plotted in Fig. 3.15.

An example of the resulting ξ as a function of centrality from Run 7 for the same p_T bins is shown in Fig. 3.17. Since ξ corrects for the change in the particle production rate over the centrality, this correction becomes more significant for the more peripheral events where the particle production rate changes more rapidly. The ξ correction is also larger for wider centrality bins. The ξ is determined completely separately for each data set, since the different detector configurations could affect the value, however, they are consistent.
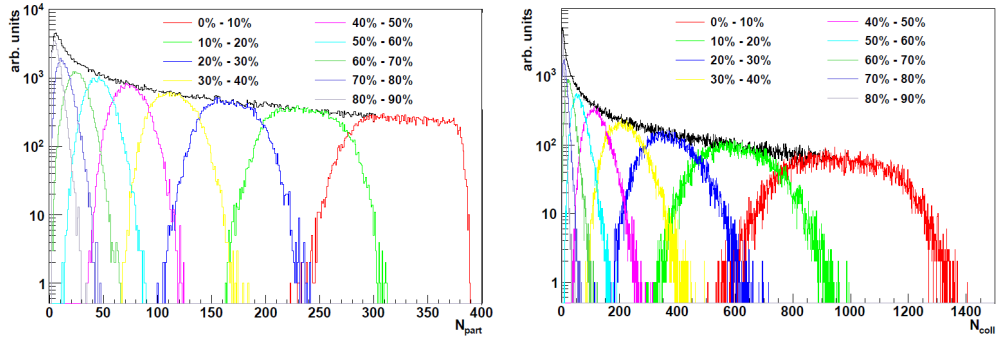
Figure 3.15: The N_{part} (left) and N_{coll} (right) distributions from the Glauber Monte Carlo for various centrality bins.
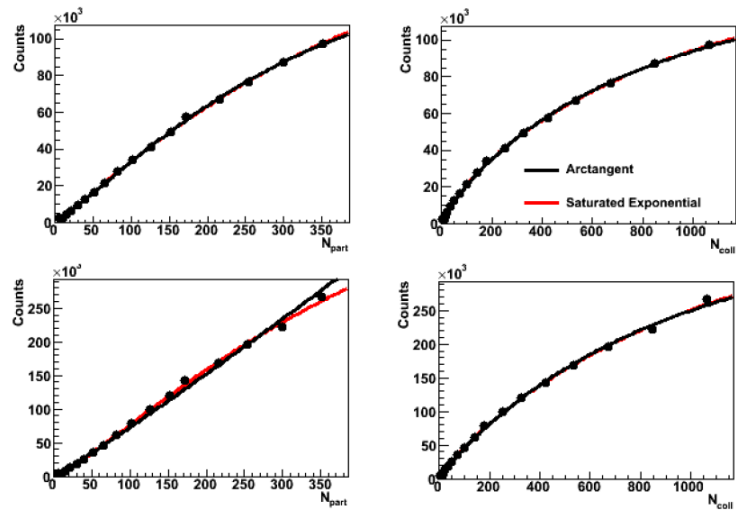
Figure 3.16: Fits used to determine the normalization constant, ξ , for trigger p_T 5-7 GeV/c and partners 1-2 GeV/c from the Run 4 data.
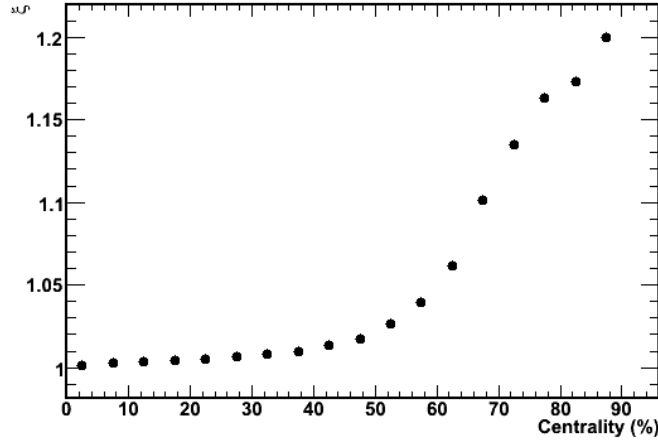
Figure 3.17: The ξ for $5 < p_T < 7$ GeV/c photons with associate hadrons between $1 < p_T < 2$ GeV/c as determined by the Run 7 data.

3.2.5 Absolute Normalization for Filltime Method

The ξ for different p_T is plotted in Figure 3.18. Since no strong $p_{T,h}$ dependence is observed the fill time method uses one value for all bins which was applied during the subtraction procedure, not at fill time. This is plotted as pink points in Figure 3.18.

3.2.6 Hadron Efficiency and Occupancy corrections

Since this analysis focuses on per trigger yields, the trigger efficiency cancels in the jet function definition. However, the hadron efficiency, ϵ_h, must be included. ϵ_h actually encompasses a few different sources of lost hadrons. The most obvious loss results from the limited acceptance, due to the shape of the PHENIX aperture in $\Delta\phi$ as well as dead portions of the detector. Although PHENIX has excellent single wire efficiency and track reconstruction, we must also include these effects in the correction. The detector efficiency and acceptance are combined into what is referred to as the single particle efficiency correction to address how the detector responds to the presence of a single particle track. In heavy ion collisions, tracks may also be lost or misreconstructed due to the large number of hits in the detector. This effect is accounted for with the occupancy correction.

There are currently two methods used in PHENIX to determine the hadron efficiency and occupancy corrections. The first is to scale to a previously corrected PHENIX measurement. This method is referred to as bootstrapping,
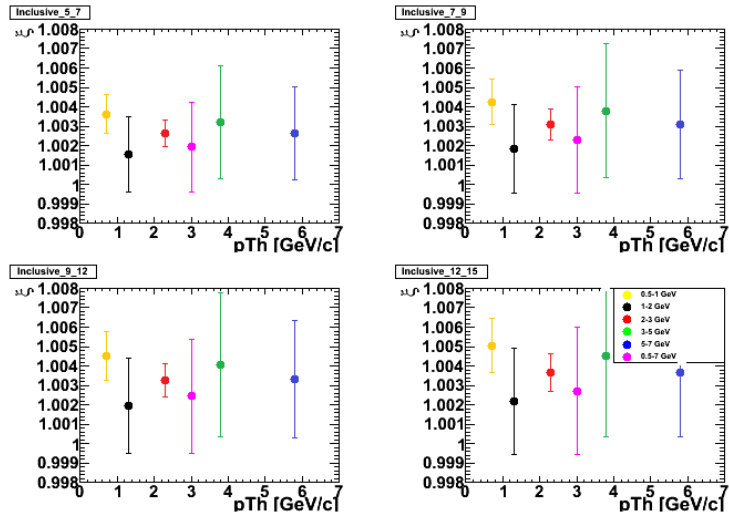
Figure 3.18: The ξ for inclusive photons for each trigger p_T bin as a function of p_T^h. All points overlap within errors. Therefore, the pink point, plotted at 3 GeV/c is used for all hadrons in the filltime method.

and encompasses both the efficiency and occupancy correction. The second method requires a full GEANT simulation of the detector. This is how the data was initially corrected in the Run 2 measurements used as the baseline in the bootstrap method. The bootstrap method is used for the Run 4 Au+Au and the initial Run 5 and 6 p+p γ_{dir}-h measurements. The Run 7 hadron efficiency is determined from a detector simulation as well as an updated version of p+p results with reduced systematic uncertainties.

The Bootstrap Method

The first step in the bootstrap method is to fit the fully corrected published data [53]. The ratio of the raw spectra measured in this analysis to the published spectra gives the hadron efficiency, ϵ_h, as a function of p_T, plotted in Fig. 3.19 for the Run 4 analysis. The inverse of this function, $1/\epsilon_h$, gives the correction which is applied to the yield measured in the current analysis. The uncertainty in the bootstrap method itself is estimated to be 10% for all p_T. Since background is known to be an issue above 3 GeV/c, a fit to the points in the range 1-3GeV/c is used to extrapolate the efficiency values for $p_T > 3$ GeV/c. The extrapolated fit used to determine the values for 3-5 GeV/c leads to an additional 2% uncerainty which brings the total uncertainty to 10.1% for this bin. There is a 7% uncertainty associated with the extrapolation for the the 5-10 GeV/c bin, which leads to a total uncertainty of 12.2%. However,

69

this 5-10 GeV/c bin is not included in the final Run 4 results.
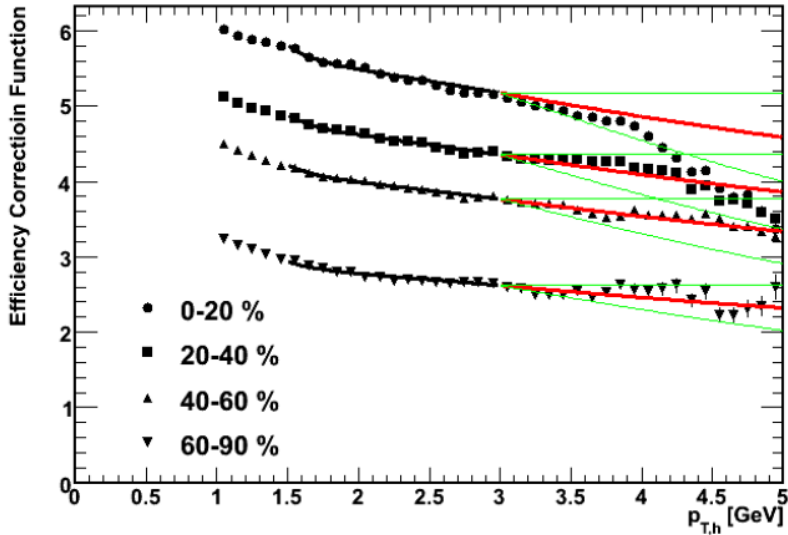
Figure 3.19: The hadron efficiencies determined via the bootstrap method for Run 4. The black points are the ratio between the two data sets while the black line is a fit. The red line is an extrapolation of the fit and the green lines indicate the error associated with the extrapolation.

GEANT Simulation Method

The efficiency and occupancy corrections are determined from Monte Carlo studies in Run 7 with a full GEANT simulation of the detector response which we call "PISA" in PHENIX. The p_T binned results use a preliminary value of the efficiency and occupancy corrections. These values were updated for the fill time results. However, they are consistent and determined in the same basic way. The efficiencies for the $p + p$ baseline used in the fill time results are determined using the same simulation framework but in a separate study [11].

Occupancy Correction for Run7 Au+Au

The occupancy correction accounts for the loss in tracking efficiency due to the high multiplicity of tracks in the event. To calculate this correction, a simulated track is embedded in real event data. The efficiency of the reconstruction framework to properly reconstruct the true track can then be measured. This study was derived from the work in [15]. However, unlike that analysis, this

analysis uses a RICH veto for the hadron identification, which introduces additional occupancy effects. Results from the study are shown in Figures 3.20 and 3.21. While the results extent to higher p_T, no RICH veto is applied in the analysis for $p_T > 5$GeV/c since the pions increasingly fire the RICH.
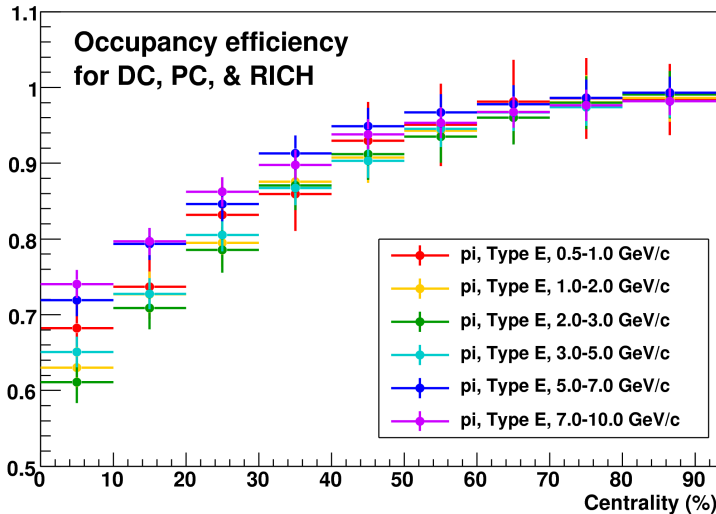
Figure 3.20: Occupancy efficiency for DC, PC and RICH veto as a function of centrality for different p_T selections.

For the p_T binning results, the RICH embedding code was not working properly. For that analysis a purely data driven method of determining the centrality dependence of the RICH veto was used. This gave a RICH occupancy efficiency of $\approx 90 \pm 1\%$ in the most central 10% of the collisions. For the DC and PC efficiency Ref. [15] finds $70 \pm 2\%$ (for $1 < p_T < 5$GeV/c). Multiplying these gives a DC/PC/RICH occupancy efficiency of $63 \pm 2\%$ which is very consistent with the corresponding values in Fig. 3.21.

Single Particle Correction for Run7 Au+Au

Similarly, the correction determined here is based on previous simulation work [15]. However, again, the current analysis uses a RICH veto for hadron tracks with $p_T < 5$ GeV/c. The results for Run 7 Au+Au are shown in Fig. 3.22. A comparison to the bootstrap method from [15] is also shown.

Since the pions actually start firing the RICH before 5 GeV/c, there is a dip in the efficiency plots starting near 4.7 GeV/c. To account for this, a second fit (in blue) is used. The plot includes parameters in black for the (red) fit without the dip as well as parameters in blue for the (blue) fit which includes
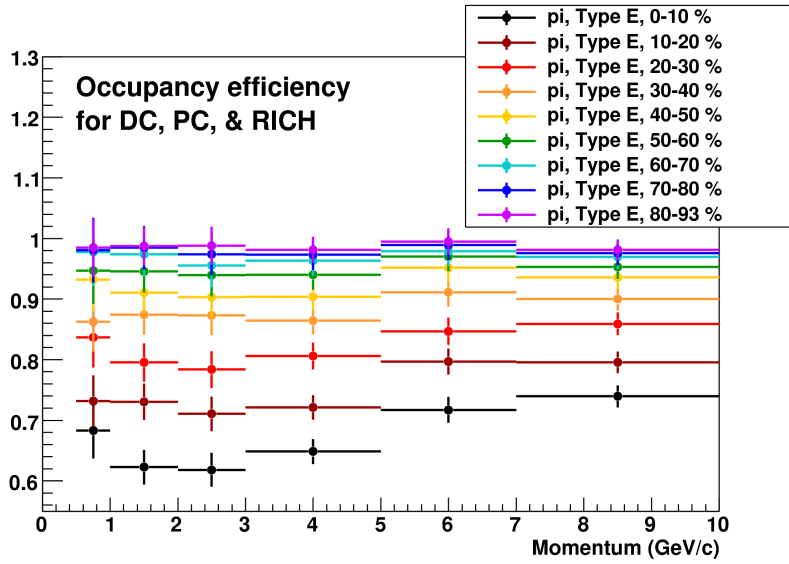
Figure 3.21: Occupancy efficiency for DC, PC and a RICH veto as a function of p_T for different centrality selections.
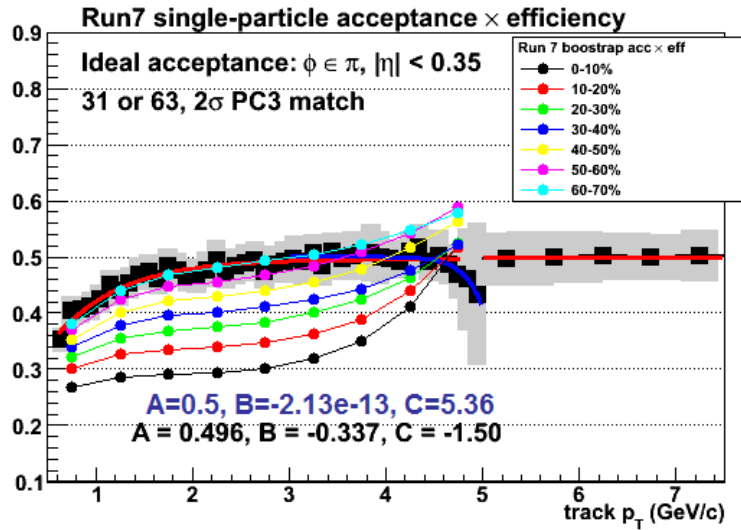
Figure 3.22: Single particle efficiency including RICH veto as a function of p_T for the Run 7 setup (black squares) are fit with the functional form, $A + Be^{Cx}$. The blue fit is used for $p_T < 5$ GeV/c and red is for $p_T > 5$ GeV/c. The parameters for the different fits are shown in blue and black respectively. The systematic uncertainty in these efficiencies is 7.9%.

the dip. The fits agree well where they overlap. The resulting correction, $2/\epsilon_h$, based on the efficiencies, ϵ_h, shown here contains a factor of two since the efficiency was determined for an ideal acceptance in ϕ of π for PHENIX but our data needs to be corrected to the full ϕ acceptance of 2π.

GEANT Summary

Since the RICH embedding code was fixed, this analysis applies the updated corrections described in [15]. For the most central (0-20%) events, the embedding efficiency was determined to be 0.680 $p_{Th} < 5 GeV/c$ where the RICH cut was applied. The embedding efficiency for $p_{Th} > 5 GeV/c$ used the fit in Andrew Adare's Thesis repeated here in Eqn. 3.10.

$$\epsilon = 0.761 + 1.640 \exp{-4.734 p_{Th}} \tag{3.10}$$

The single particle efficiencies use the following fits.

$$\epsilon = 0.496 - 0.337 \exp{-1.50 p_{Th}} (p_{Th} < 3.0) \tag{3.11}$$

$$\epsilon = 0.500 - 2.13 x 10^{-13} \exp{5.36 p_{Th}} (3.0 < p_{Th} < 5.0) \tag{3.12}$$

$$\epsilon = 0.496 - 0.337 \exp{-1.50 p_{Th}} (p_{Th} > 5.0) \tag{3.13}$$

Although, only the combined plots are shown here, pions, protons, and kaons are all studied separately. Their efficiencies are combined based on the measured particle ratios. Since the PHENIX measurement of these particle ratios does not cover all the p_T bins used here, an extrapolation is used. The uncertainty of this extrapolation is taken into account in the final error estimate of the method. There is an estimated 7.2% uncertainty on the single particle efficiency and a 5% uncertainty from the embedding. The largest source of uncertainty arises from matching the detector simulation to the data. Comparisons of the tracking as a function of $\Delta\phi$ and z are shown in Fig. 3.23. Combining the uncertainty from the single particle efficiency and the embedding results in an 8.8% overall scale uncertainty in the yields.
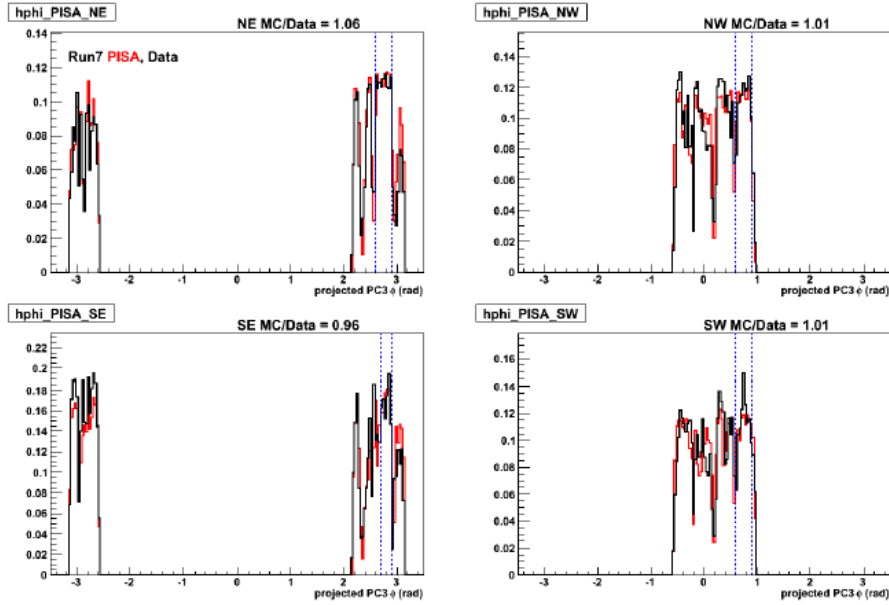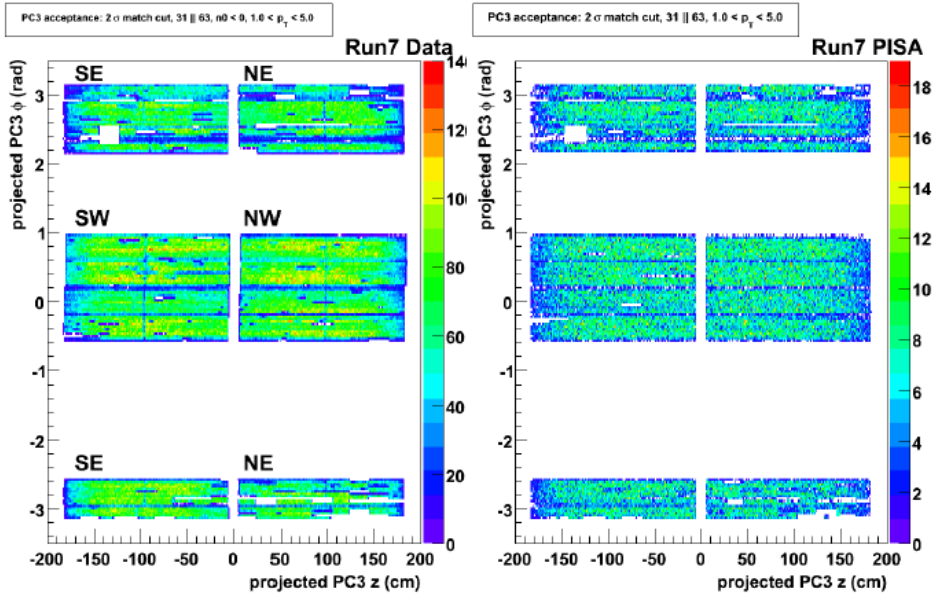
Figure 3.23: Comparison between data and simulation. (Top) A 2D plot of $\Delta\phi$ versus z shows holes due to the DC and PC as lines and boxes respectively. (Bottom) A projection along $\Delta\phi$ shows how well the simulation matches the data for each arm (East or West) and half chamber in z (North or South).

Chapter 4

Analysis Details for Direct Photons

The various sources of photons are discussed in the Introduction of this thesis. However, for the analysis we define three groups of photons: inclusive, decay and direct. Inclusive photons refers to all the photons measured in an event. Decay photons result from meson decays such as $\pi^0 \rightarrow \gamma + \gamma$. Direct photons, in this analysis, refers to all photons which are not decay photons. Therefore,

$$N_{direct} = N_{inclusive} - N_{decay}, \tag{4.1}$$

where N_γ is the number of photons of that type. This means that in addition to the LO diagrams in Fig. 1.13, the NLO sources including fragmentation photons and any additional medium induced sources can contribute to our signal. However, these sources are much smaller than the large contribution of decay photons in the inclusive sample. Ideally, decay photons can be removed from the inclusive trigger sample on an event by event basis. Techniques to do this are used in the $p + p$ analysis but these techniques do not remove all the decay photons and are challenging to apply in the high multiplicity events in the Au+Au analysis. Therefore, in Au+Au, and in addition to the event by event techniques in p+p collisions, a statistical subtraction method is applied in which the $\gamma_{\mathrm{inc}} - h$ and $\gamma_{\mathrm{dec}} - h$ are measured over all events and then used to extract $\gamma_{\mathrm{dir}} - h$.

4.1 Introduction to the Statistical Subtraction Method

To extract the $\gamma_{\text{dir}} - h$ correlations, $\gamma_{\text{inc}} - h$ and $\gamma_{\text{dec}} - h$ correlations need to be measured. The $\gamma_{\text{inc}} - h$ correlations require a high p_T photon trigger (5-15 GeV/c), which is used to make $\Delta\phi$ distributions with associated hadrons (0.5-7 GeV/c) in the event. The decay photon correlations are extracted by measuring $\pi^0 - h$ correlations for (4-17GeV/c) π^0s and mapping them to their decay photon p_T. The details of this mapping procedure are explained in a later section.

Recall that for correlation functions, the yield is measured in terms of number of pairs per trigger. The relationship between the per trigger yield, Y, for γ_{dir}-h, γ_{inc}-h and γ_{dec}-h can be written as

$$N_{inclusive}Y_{inclusive} = N_{direct}Y_{direct} + N_{decay}Y_{decay}. \qquad (4.2)$$

By rearranging Eqn. 4.2, the statistical subtraction equation used to determine the direct photon-hadron correlation is found to be

$$Y_{direct} = \frac{R_\gamma Y_{inclusive} - Y_{decay}}{R_\gamma - 1}. \qquad (4.3)$$

where R_γ is the ratio between inclusive and decay photons, written as

$$R_\gamma = N^\gamma_{inclusive}/N^\gamma_{decay}, \qquad (4.4)$$

and has been previously measured by PHENIX for Au+Au in Run 4 [17]. Note that R_γ is proportional to our S/B ratio in this subtraction since it can also be rewritten as

$$R_\gamma = 1 - N^\gamma_{direct}/N^\gamma_{decay}. \qquad (4.5)$$

4.2 R_γ

The R_γ values used in this analysis were measured in a separate analysis (actually two) [54]. The data are from Run 4 and the analysis was done separately for the PbGl and PbSc parts of the EMCal. The results for the PbSc analysis are shown in Fig. 4.1 as open circles labeled "AN567." Both the PbSc and PbGl results were rebinned into the p_T bins used in the present analysis according to the appropriate p_T spectrum of photon triggers. These rebinned values are plotted in the same figure as blue and red points respectively. Finally

these two measurements were combined using a weighted average which depends on both the systematic and statistical uncertainties, according to the PDG method [20] to yield the final values used in this analysis. The combined values are the black points in Fig. 4.1 and are tabulated in Table 4.1. The systematic error bars on the combined result are plotted as open black boxes. For clarity, only the statistical errors were plotted for all the other sets of points in the figure.
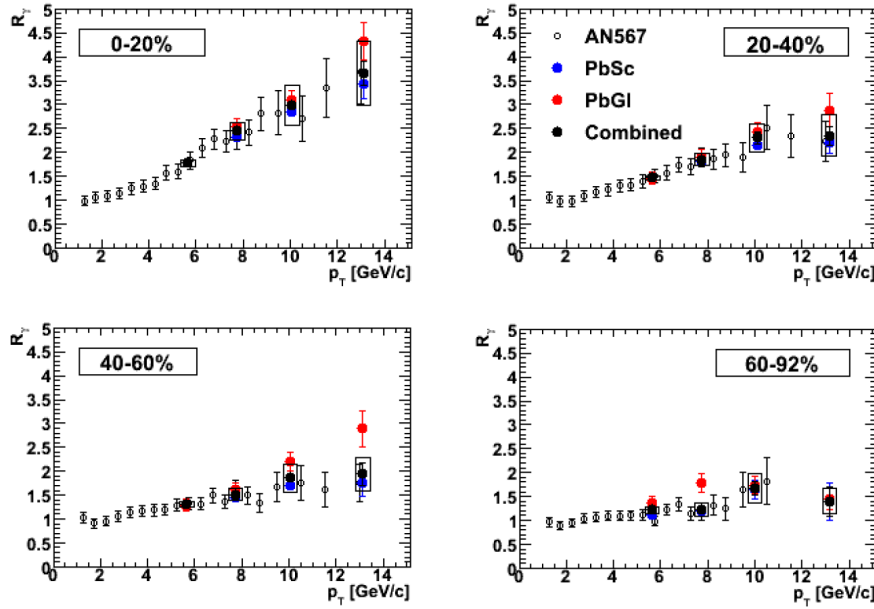
Figure 4.1: R_γ as measured in the PbSc analysis (open circles) and rebinned according to the bins for the current analysis (red points). The rebinned PbGl measurement are shown in blue. Finally the values used in this analysis which combine the PbGl and PbSc measurements are plotted as black points with systematic errors plotted as open boxes.

The trends in these plots show that our S/B improves for the more central events and at higher p_T. This arises from the π^0 suppression observed in the medium. Since direct photons are not suppressed by the the medium while the number of decay photons decreases, the resulting ratio increases.

These plots show the fully corrected R_γ values. However, for the actual statistical subtraction the separation efficiency needs to be included. The separation efficiency refers to the efficiency for measuring merged photon clusters from high p_T π^0s. We apply a correction which is determined from a Monte Carlo simulation with a Gaussian smearing applied to the photon spectra for each Au+Au centrality and in $p + p$.

77

Table 4.1: Extracted R_γ values used as input to direct γ-h per-trigger yield subtraction (Equation 4.3). These values are interpolated from previous PHENIX measurements as described in the text.

Centrality	p_T^γ	R_γ	Stat.	Sys.
0-20%	5-7	1.77	±0.09	±0.06
	7-9	2.45	±0.09	±0.18
	9-12	2.99	±0.11	±0.41
	12-15	3.66	±0.24	±0.68
20-40%	5-7	1.46	±0.10	±0.04
	7-9	1.85	±0.10	±0.12
	9-12	2.30	±0.12	±0.28
	12-15	2.35	±0.20	±0.44
40-60%	5-7	1.30	±0.09	±0.05
	7-9	1.52	±0.07	±0.13
	9-12	1.85	±0.10	±0.30
	12-15	1.94	±0.24	±0.36
$p+p$	5-7	1.18	±0.01	±0.06
	7-9	1.33	±0.01	±0.05
	9-12	1.53	±0.03	±0.05
	12-15	1.79	±0.09	±0.07

4.3 Decay Photon Mapping

The decay photon per trigger yield was determined by applying a weighting factor at fill-time as follows:

$$Y_{decay} = \frac{\int \wp(p_{T\pi^0} \to p_{T\gamma})\varepsilon^{-1}(p_{T\pi^0})N_{\pi^0-h}\,dp_{T\pi^0}}{\int \wp(p_{T\pi^0} \to p_{T\gamma})\varepsilon^{-1}(p_{T\pi^0})N_{\pi^0}\,dp_{T\pi^0}}. \tag{4.6}$$

Here $\wp$ represents the probability from the decay mapping from π^0 p_T to decay photon p_T and ε is the π^0 reconstruction efficiency. Although not explicitly written in the equation above, the z dependence of $\wp$ and ε are also

Table 4.2: Separation efficiency correction applied to the fully corrected R_γ.

p_T [GeV/c]	0-20%	20-40%	40-60%	p + p
5-7	1.5	1.0	0.8	0.6
7-9	1.8	1.3	1.0	0.8
9-12	2.2	1.6	1.4	1.0
12-15	2.2	1.8	1.6	1.2

accounted for in the analysis.

Most of the decay photons are from π^0 decays. Therefore, $\pi^0 - h$ correlations are measured and then mapped to the $\gamma_{\text{dec}} - h$. The second largest source of decay photons is from η. For p+p, $\eta - h$ correlations are measured and likewise mapped to their decay contribution. For higher mass meson decays, a small correction is applied which in Au+Au also includes a correction for the η.

This mapping requires a weighting function which translates a π^0 of given p_T to a given decay photon p_T bin. In this analysis, the p_T binning used for the decay photons are 5-7 GeV/c, 7-9 GeV/c, 9-12GeV/c and 12-15GeV/c. The weighting function can be determined analytically. The probability for a π^0 of p_T^π to decay into a photon at any given E_γ is uniform between 0 and p_T^π. Therefore we can express the likelihood of of yielding a photon at any E^γ in terms of the decay phase space as $dN^\gamma/dE^\gamma = 2/p_T^\pi$. Kinematically the decay photon can not have more energy than her parent π^0. Therefore the probability is zero for $p_{T\pi^0} < p_{T\gamma_{\text{dec}}}$. The probability increases until the upper edge of the $p_{T\gamma_{\text{dec}}}$ bin is reached. The probability above the bin limit decreases according to the shape of the integrated dN^γ/dp_T^γ spectrum. An example of this weighting function determined analytically for the 5-7 GeV/c decay photon bin is shown as a dashed line in the middle panel of Fig. 4.2. The general expression for the probability function, $P(p_T^{\pi^0})$, for a decay photon bin, $a < p_T^\gamma < b$, is

$$
P_{a-b}(p_T^\pi) = \begin{cases} 0 & , p_T^\pi < a \\ \int_a^{p_T^\pi} dp_T^\gamma \frac{2}{p_T^\pi} = 2\left(1 - \frac{a}{p_T^\pi}\right) & , a < p_T^\pi < b \\ \int_a^b dp_T^\gamma \frac{2}{p_T^\pi} = 2\left(\frac{b-a}{p_T^\pi}\right) & , p_T^\pi > b \end{cases} \tag{4.7}
$$

However, detector effects can alter this distribution. Therefore, the probability weighting function that is actually used in this analysis uses a Monte Carlo generator to throw particles into a simulated PHENIX EMCal. π^0s are decayed into photon pairs according to the appropriate branching ratio. To generate enough statistics at all p_T the initial π^0 spectrum is flat in p_T and later weighted by the measured π^0 spectrum for the appropriate collision system. The simulated EMCal response is designed to match the PHENIX EMCal's energy resolution, position resolution and acceptance including the appropriate dead and hot tower maps which will be discussed later.

The resulting probability function is also shown in the middle panel of Fig. 4.2. The detector effects mostly smooth out or smear the sharp edges of the distribution, including the peak and tails. One important effect, not taken

into account in our fast MC is the effect of merged decay photon clusters at high p_T. Since the opening angle is small for pairs which decay from high p_T mesons, they are removed from the inclusive sample by the shower shape cut. The efficiency to detect these photons is determined from a full GEANT simulation. The efficiency is plotted in the bottom panel of Fig. 4.2 and is applied to the probability function in the middle panel. The probability function is also determined separately for bins along z. The largest effect on the shape is observed near the edges of the detector.
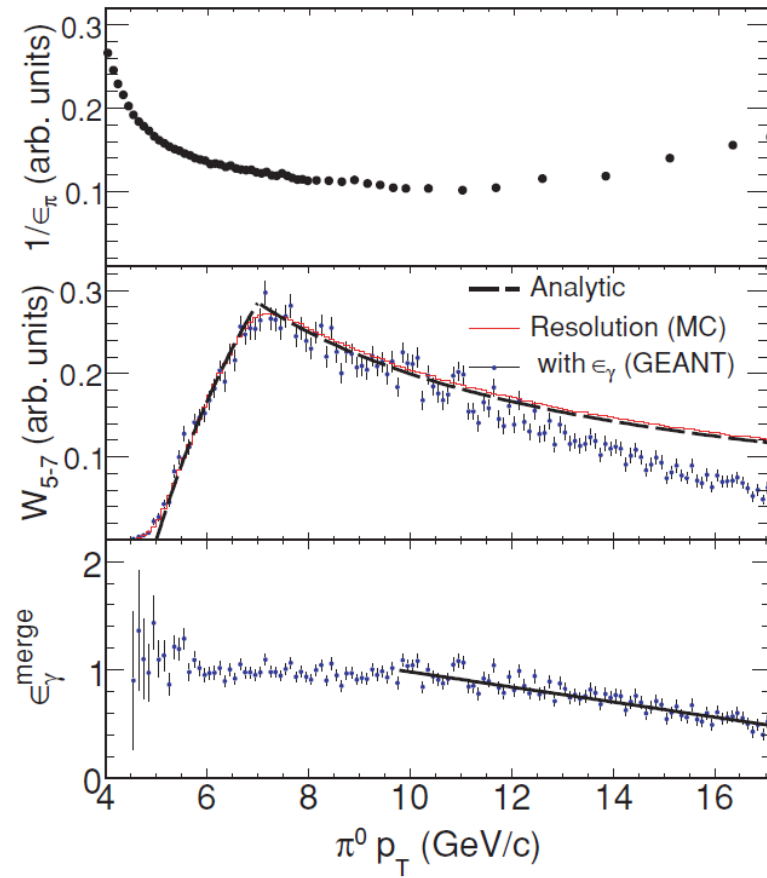
Figure 4.2: Top: The π^0 reconstruction efficiency in arbitrary units. Middle: Probability as a function of $\pi^0 p_T$ for a π^0 to decay into a 5-7GeV/c decay photon. Bottom: The efficiency to measure a photon in the PHENIX EMCal.

4.3.1 Input and Verification of the Simulation

Exodus is a PHENIX developed Monte Carlo generator which decays particles based on the branching ratios and p_T spectra, both of which can be altered to the system you are interested in. A private version, which includes the PHENIX EMCal acceptance, was used to determine the decay mapping function. An updated dead and hot tower map for the EMCal was used based on the data analyzed in Run 7 as shown in Fig. 4.3. Each input p_T spectrum for Exodus was determined using the functional form,

$$Y = (Ap_T^{-B} * (1 - \frac{1}{1 + e^{(p_T - 3.75)/0.1}}) + \frac{C}{((1 + p_T/D)^E)} \frac{1}{(1 + e^{p_T - 3.75}/0.1)})p_T, \tag{4.8}$$

which combines a Hagedorn function with a power law and smoothly fits the data over all p_T. It was fit to the run 4 π^0 data from [55] and the Run 2 γ_{dir} data from [56]. For η the same shape as the π^0 was used but it was weighted by $N_\eta(\gamma)/N_{\pi^0}(\gamma) = 0.19$ since we are only interested in η particles which decay into two photons. (The branching ratio for $\eta \to 2\gamma$ is 0.39, so we divide by 2 to represent the branching ratio to each individual photon.) The $N_{\gamma_{\mathrm{dir}}}/N_{\pi^0}$ used was 0.0138.

An EMCal dead tower map was generated from the data and used as an input for the simulation for each data set. These maps from Run 4 and Run 7 are shown in Fig. 4.3. The white boxes clearly indicate masked towers. Some are actually dead, while others are masked because they are considered hot. A hot tower is one that fires frequently and may not correspond to actual signal. Towers around the edges are also masked to avoid clusters which do not deposit all their energy within the acceptance.
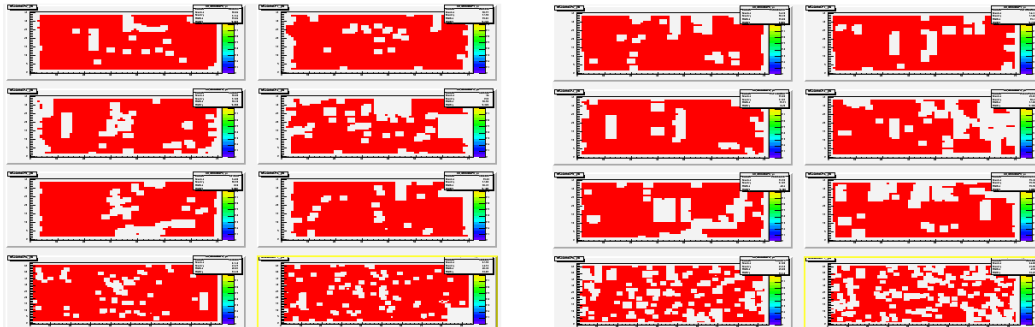
Figure 4.3: The EMCal tower map for Run 4 (Left) and Run 7 (Right). The top 6 sectors correspond to the PbSc sectors and the bottom two correspond to the PbGl with finer segmentation.

To verify that these inputs accurately reflect the data, the p_T spectrum for inclusive photons and π^0 triggers that we use in our analysis was compared to the output of the MC and are plotted in Fig. 4.4 and Fig. 4.5. The integrals for 5–15 GeV/c for both the inclusive and π^0 in the MC agree with the data within 6%.
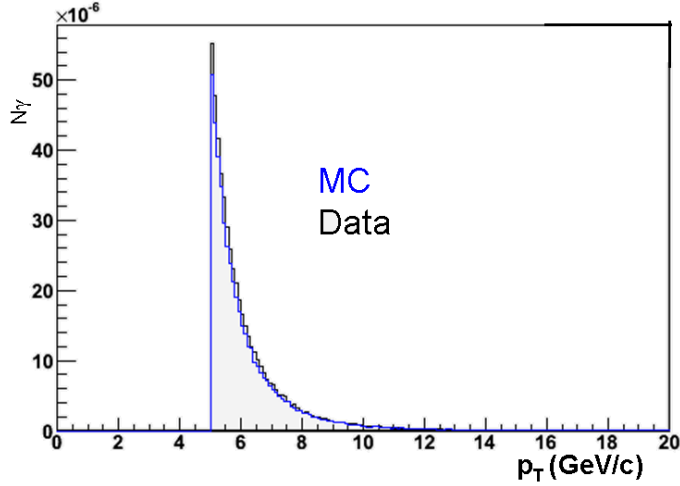
Figure 4.4: The number of inclusive photons per event vs p_T in the run 7 data (black) and in the Monte Carlo (blue)

The simulation was also tuned to match the width and position of the π^0 peaks measured in Run 4 by adjusting the energy and position resolution of the EMCal as shown in Fig. 4.6 and Fig. 4.7. The resolutions used are:

$$\sigma_{E,pbsc} = E\sqrt{0.08^2 + (\frac{0.081}{\sqrt{E}})^2} \qquad (4.9)$$

$$\sigma_{E,pbsc} = E\sqrt{0.06^2 + (\frac{0.09}{\sqrt{E}})^2} \qquad (4.10)$$

$$\sigma_x = \sqrt{0.16^2 + (\frac{0.67}{\sqrt{E}})^2} \qquad (4.11)$$

4.3.2 π^0 Trigger Efficiency

The π^0 trigger efficiency is determined by scaling the raw π^0 spectra measured in this analysis to a power law fit to the published data [55]. The published
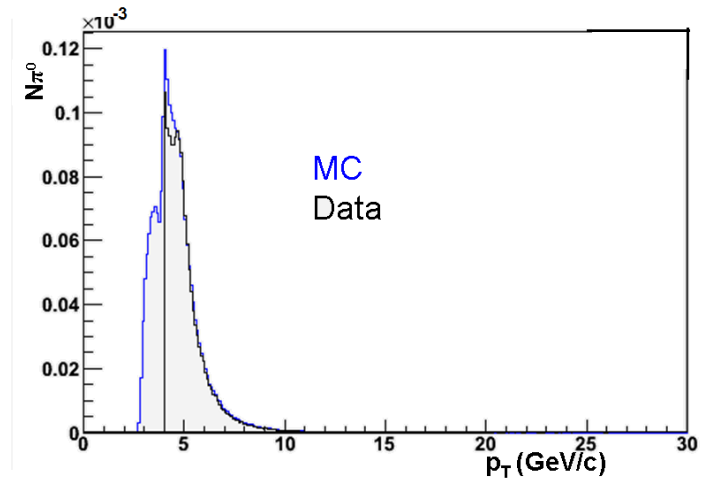
Figure 4.5: The number of π^0 triggers per event vs p_T in the run 7 data (black) and in the Monte Carlo (blue)
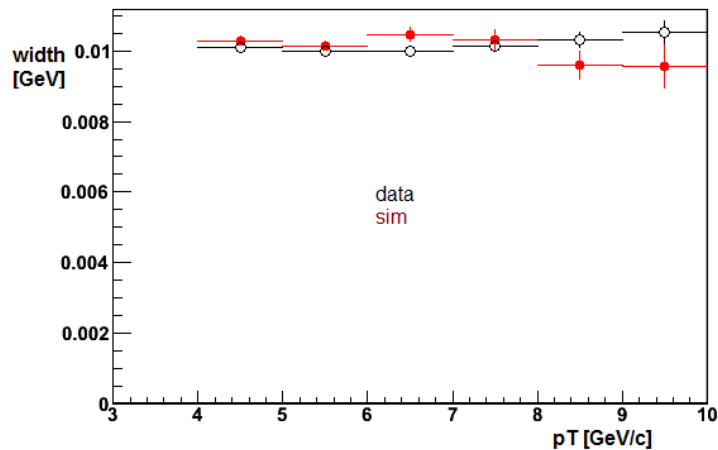
Figure 4.6: Comparison between the π^0 peak width measured in simulation and Run 7 data.
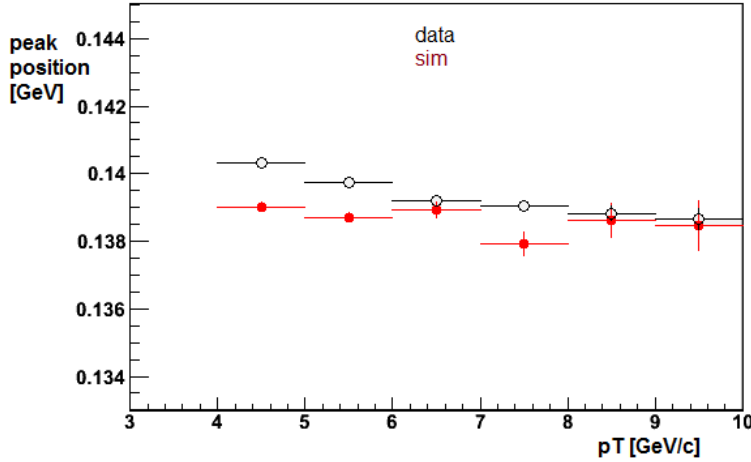
Figure 4.7: Comparison between the π^0 peak position measured in simulation and data.

data in the same centrality bins as the present analysis and corresponding fits are plotted in Fig. 4.8. In Figure 4.9 the efficiencies are plotted for all the centrality bins for Run 7. (This was also preformed separately for the Run 4 data [11].) The normalization is arbitrary. The difference seen at low p_T is due to the strict asymmetry cut applied in the two most central bins.

4.3.3 π^0 Cutoff Correction

A π^0 of any momentum greater than that of the γ_{dec} can contribute to that γ_{dec} bin but we only measure correlations for π^0s up to 17 GeV/c. Therefore, we must include a correction to our decay yield to account for the contribution from mesons at higher p_T. This correction is determined from a power law fit to the $\pi^0 - h$ yield as a function of p_T for each hadron p_T bin as shown in Fig. 4.10. The fit can then be used to determine the correction by calculating the yield deficiency, D_{cutoff}, according to

$$
D_{\mathrm{cutoff}} = 1/C_{\mathrm{cutoff}} = \frac{\int_{<17} dp_T^{\pi-h} P(p_T^{\pi-h}) \frac{dN^{\pi-h}}{dp_T^{\pi-h}} / \int_{<\infty} dp_T^{\pi-h} P(p_T^{\pi-h}) \frac{dN^{\pi-h}}{dp_T^{\pi-h}}}{\int_{<17} dp_T^{\pi} P(p_T^{\pi}) \frac{dN^{\pi}}{dp_T^{\pi}} / \int_{<\infty} dp_T^{\pi} P(p_T^{\pi}) \frac{dN^{\pi}}{dp_T^{\pi}}}.
$$

(4.12)

The lower bound of the integrals in the equation is the lower bound of the π^0 p_T bin being corrected. The π^0 and $\pi^0 - h$ yields are determined from the data with the π^0 trigger efficiency applied. The cutoff calculations are listed in Table

84
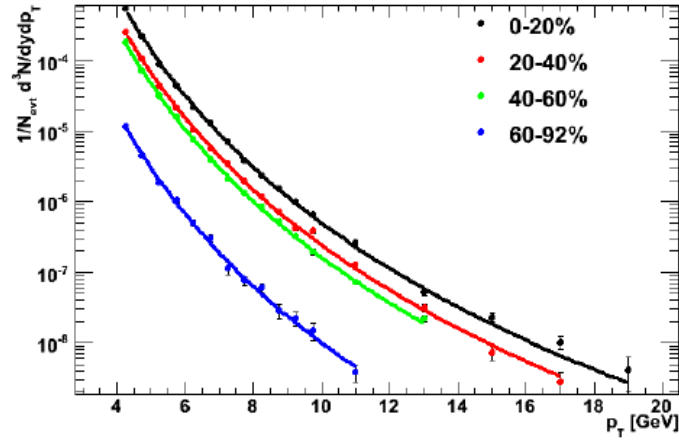
Figure 4.8: The published π^0spectra for 0-20% (black), 20-40% (red), 40-60% (green) and 60-92% (blue) Au+Au.
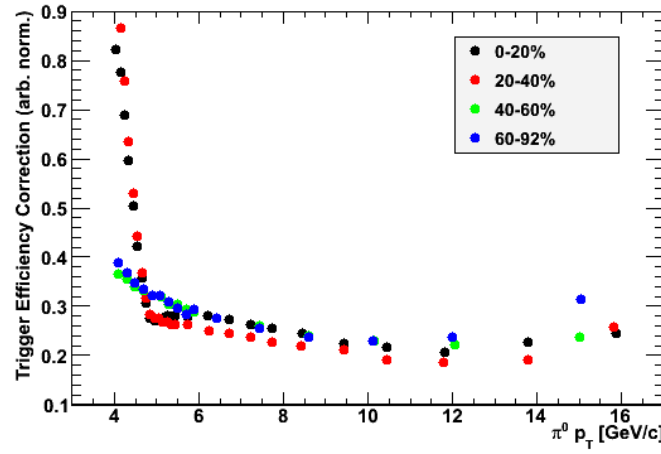
Figure 4.9: The Run 7 π^0trigger efficiency for 0-20% (black), 20-40% (red), 40-60% (green) and 60-92% (blue).

4.3 for each trigger p_T bin. Since I_{AA} and R_{AA} for these yields are generally flat (except for the lowest p_T^h), the spectral shapes in Au+Au and $p + p$ are similar. Therefore, C_{cutoff} should be the same for all Au+Au centralities and the $p + p$ data. The corrections listed in Table 4.3 are based on the Au+Au data and are indeed consistent with the $p + p$ corrections [11]. A conservative 50% error was assigned to this correction. Although this uncertainty may be generous, it is still small compared to the other uncertainties and statistical errors when propagated to the final yields in this measurement.
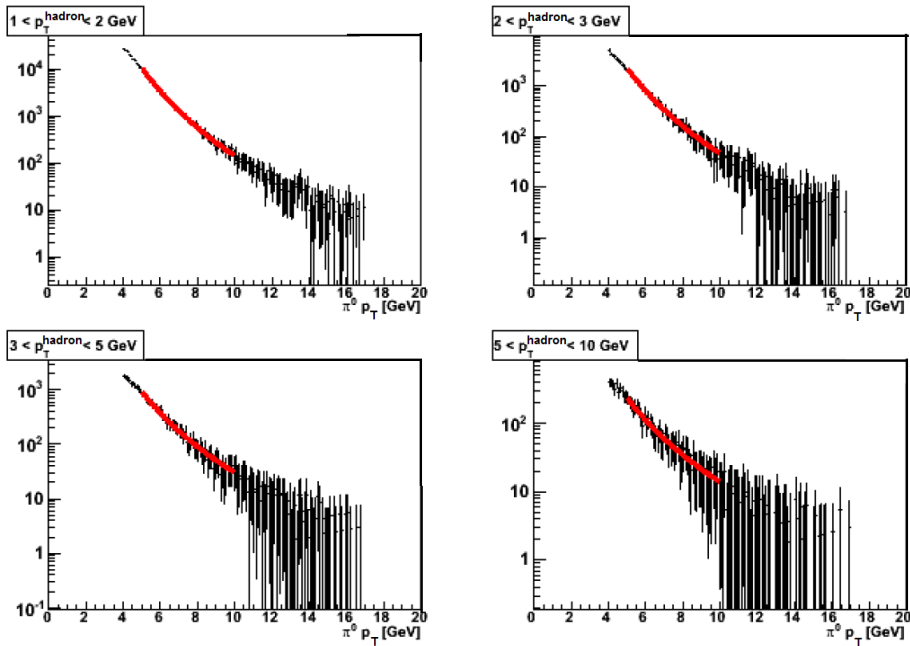
Figure 4.10: π^0 trigger spectra for associated hadrons at 1-2, 2-3, 3-5 and 5-10GeV/c

4.4   p+p Baseline

There are two $p + p$ measurements which can be used as a baseline. The first uses the same method as in the Au+Au analysis and the second uses event by event techniques and a modified statistical subtraction to reduce the uncertainties in the measurement. For historical reasons both are used in the results and comparisons discussed later. As demonstrated later in the results section, both methods agree with each other and are legitimate baselines for comparison to the Au+Au.

Table 4.3: Cutoff corrections for the π^0 spectra.

p_T^γ [GeV]	p_T^{hadron} [GeV]	Correction
5-7	0.5-1	1.0
	1-2	1.0
	2-3	1.0
	3-5	0.998
	5-10	0.994
7-9	0.5-1	0.998
	1-2	0.998
	2-3	0.996
	3-5	0.992
	5-10	0.977
9-12	0.5-1	0.993
	1-2	0.993
	2-3	0.983
	3-5	0.969
	5-10	0.930
12-15	0.5-1	0.977
	1-2	0.977
	2-3	0.944
	3-5	0.908
	5-10	0.825

4.4.1 Statistical Method Only

The first analysis of the p+p data followed the same procedures as the Run 4 Au+Au analysis. The inputs of course were adjusted to the p+p data sets. These details have been presented in an earlier thesis [11], but the major ingredients will be reviewed here.

Run 5 R_γ

The R_γ was measured in an analysis using the Run 5 data separate from the γ_{dir}-h analysis [11] and is plotted in Fig. 4.11. Since the R_γ is fully corrected for detector effects, a correction has to be applied to account for the separation efficiency as discussed in Section 4.2. The correction is listed along with the values for Au+Au in Table 4.2 of Section 4.2.
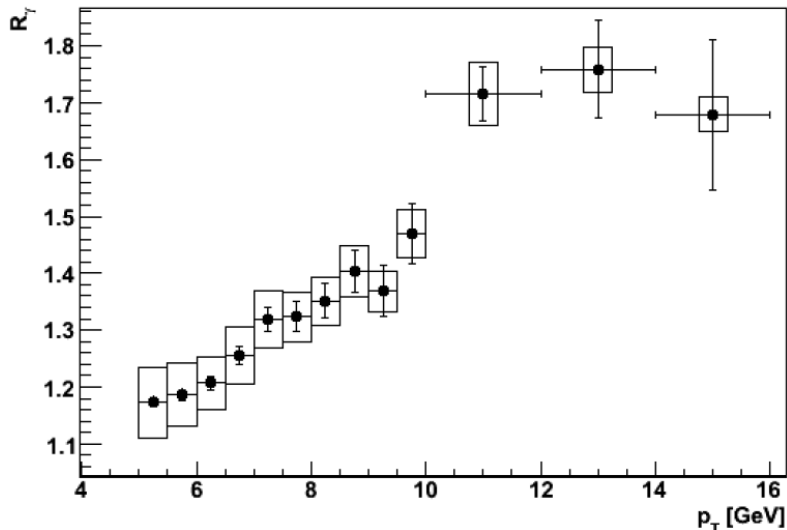
Figure 4.11: R_γ from Run 5 p+p used in the extraction of γ_{dir}-h from Run5 and Run 6 p+p.

Hadron Efficiency

As in the Run 4 analysis, the hadron efficiency was determined using the bootstrap method. The hadron spectra in this analysis are scaled to match the published. The efficiency correction is determined separately for Run 5 and Run 6 and are both shown in Fig. 4.12.
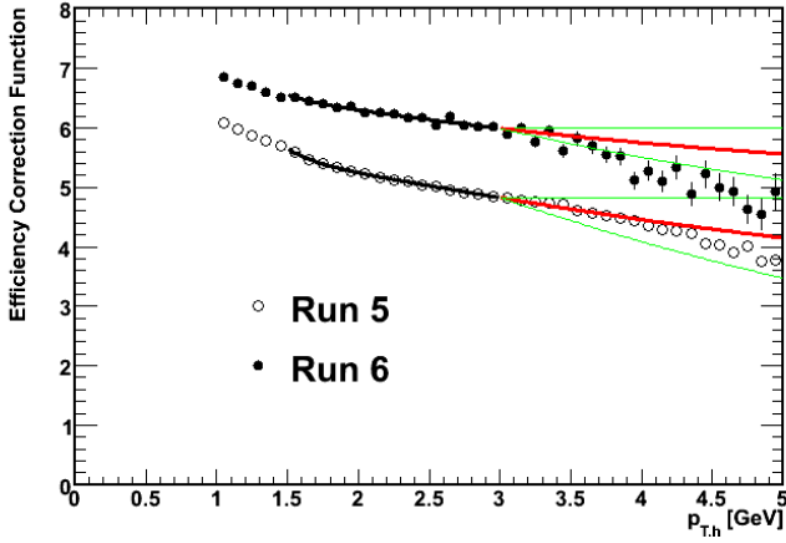
Figure 4.12: The hadron efficiency for the p+p data sets as determined from the bootstrap method.

4.4.2   Implementation of the Isolation and Tagging Cuts

The baseline p+p measurement used in the final results section of this thesis is derived from the published PHENIX paper, [16]. The results are derived from [16] rather than taken directly such that the binning and hadron p_T range matches those chosen for the final Run 7 Au+Au measurements. To derive these results, the same framework and data were used as for [16] and cross checks were performed to demonstrate the ability to replicate the published results.

For some comparisons the definition of ξ is changed from $\xi = -\ln(x_E)$ in [16] to $\xi = -\ln(z_T)$, and the momentum range of the hadrons is adjusted from $p_T = 1 - 10$ GeV/c to $p_T = 0.5 - 7$ GeV/c. The inclusion of the lower p_{Th} data requires an underlying event subtraction. For each bin in ξ a flat line was subtracted via ZYAM. Because of the altered $\Delta\phi$ shape due to the isolation cut a fit was not used to determine the minimum. (Several fits were attempted and typically resulted in an over subtraction.) Instead an average of the three lowest points outside of the isolation cut were used to approximate the underlying event level. This procedure may lead to under-subtraction but one can see by eye that this is not a significant problem for this analysis. The correlation functions, ZYAM level, and resulting away-side jet functions are plotted for a sampling of ξ bins in Fig. 4.13. Additional plots are included in the appendix. The error in the average is propagated into the statistical

errors of the p+p yields as the uncorrelated systematic error on the ZYAM subtraction.
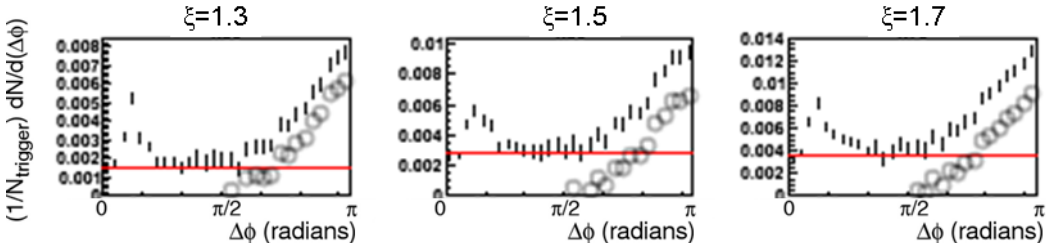
Figure 4.13: Correlation functions are projected along $\Delta\phi$ for several ξ bins in black. The ξ of each plot is labeled above it. The ZYAM level is shown as a red line and the resulting jet function for the away-side is shown as open circles. These correlation functions are for 5-7 GeV/c inclusive isolated photon triggers.

Isolation Cuts

First an isolation cut is applied to the inclusive photon triggers. The total momentum and energy, E_{cone}, in the event within a 0.3 rad cone around the trigger photon is summed and compared to the energy of the photon, E_γ. If $E_{cone} > 10\% E_\gamma$, the photon is assumed to be from a jet and is excluded from our inclusive trigger sample. In addition to removing the decay photons, this also reduces the fragmentation photon contribution. Similar isolation cuts have applied to direct photon spectra in previously analyzed PHENIX $p + p$ data. Comparing that data to NLO calculations suggests that the fragmentation photon contribution is reduced from about 30% to roughly 10% [57].

Tagging

Tagging refers to the procedure of removing decay photons, which you are able to tag as contributing to the measured π^0 or η peaks, from the inclusive sample of photons on an event by event basis. The invariant mass distribution for the $p + p$ data is shown in Fig. 4.14. To reduce the contribution of combinatorial pairs, only photons with > 1 GeV of energy are considered. The yellow bands indicate the mass range used in the tagging procedure for the π^0 and η peaks. The red bands near the η peak are used in the side band analysis to determine the uncertainty due to the combinatorial background. Trigger photons which contribute to the yellow signal regions are excluded from the inclusive samples.

Since not all decay photons can be tagged in this method a subtraction to remove the 'missed' decay photons is still required.
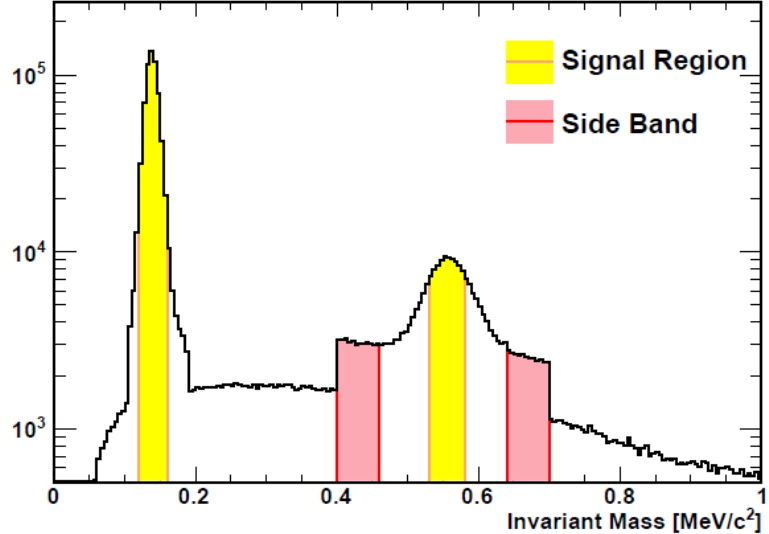
Figure 4.14: The invariant mass distribution for p+p data shows the mass windows used for the tagging cuts. The sharp features in the distribution are the result of event filtering cuts [16].

Modified Subtraction and R'_γ

The pure statistical subtraction method is done according to Eqn. 4.13. A similar subtraction is done here to remove any decay photons from the inclusive sample which survived the event-by-event cuts. The modified subtraction equation is written as

$$Y_{\text{dir}} = \frac{R'_\gamma Y_{\text{inc}} - Y_{miss}}{R'_\gamma - 1}. \tag{4.13}$$

where Y_{miss} refers to the decay photons in the inclusive sample that were not tagged and R'_γ can be thought of as an effective R_γ and is described in detail below.

The decay mapping function for the subtraction of the missed decay photons must also be determined for the tagging method. The same MC as discussed earlier is used, but here only the photons which pass the acceptance and cannot be tagged as a π^0 are included in the mapping histograms. Generally a photon cannot be reconstructed because its partner was outside of the detector acceptance. An example of the mapping function for all decay photons

91

along with the mapping function for missed decay photons are plotted in Fig. 4.15. The tagging procedure preferentially removes decay photons from high p_T π^0 since the smaller opening angle increases the probability for detecting both decay partners within the acceptance of the detector. Therefore there is a distinct shape difference for the two mapping functions.
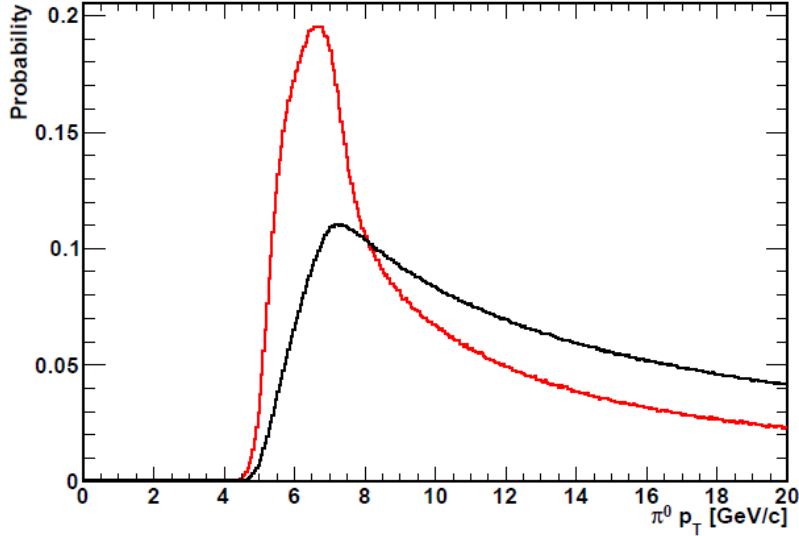
Figure 4.15: The decay photon mapping function as a function of π^0 p_T for all decay photons (black) and for decay photons missed by the tagging cut (red).

The final ingredient in this modified subtraction procedure is R'_γ, which is defined according to

$$R'_\gamma = \frac{N_{incl} - N_{tag} - N^{niso}}{N^{iso}_{miss}} \equiv \frac{N'_{incl}}{N^{iso}_{miss}}. \tag{4.14}$$

N'_{incl} is the number of inclusive photons which survive the tagging and isolation cuts while N^{iso}_{miss} refers to the decay photons which appeared isolated and were missed by the tagging cut. N^{iso}_{miss} is the number of actual decay photons remaining in the N'_{incl} sample. To determine the fraction of decay photons remaining in the inclusive sample we define

$$N^{iso}_{miss} = N_{dec} - N_{tag} - N^{niso}_{miss} \tag{4.15}$$

where N_{dec} is the total number of decay photons, N_{tag} is the number of decay photons that were tagged as decays and N^{niso}_{miss} is the number of decay photons which survived the tagging cut but were removed by the isolation cut. This

assumes that all tagged photons are truly decay photons. Falsely tagged photons are a small effect in the low multiplicity $p + p$ collisions but are included as a systematic uncertainty in the method. The fraction of π^0s which are isolated depends on the π^0 momentum and not the decay kinematics. Therefore the previously determined probability P^{miss} can be used to map the number of isolated π^0s from π^0 p_T to γ_{dec} p_T according to

$$N_{miss}(p_T^\gamma) = P^{miss}(N_{\pi^0}(p_T^{\pi^0})). \tag{4.16}$$

Since we know which π^0s are isolated and which are not we can also write

$$\frac{N_{miss}^{iso}}{N_{miss}^{niso}} = P^{miss}(\frac{N_{\pi^0}^{iso}}{N_{\pi^0}^{niso}}). \tag{4.17}$$

Combining Eqn. 4.15 and Eqn. 4.17 gives

$$N_{miss}^{iso} = \frac{N_{dec} - N_{tag}}{1 + P^{miss}\frac{N_{\pi^0}^{iso}}{N_{\pi^0}^{niso}}} \tag{4.18}$$

which can be inserted into Eqn. 4.14 to obtain

$$R'_\gamma = \frac{\frac{N'_{incl}}{N_{incl}}}{1/R_\gamma - \epsilon_{tag}}(1 + P^{miss}\frac{N_{\pi^0}^{iso}}{N_{\pi^0}^{niso}}). \tag{4.19}$$

Here $\epsilon_{tag} \equiv N_{tag}/N_{incl}$ and we recall $R_\gamma \equiv N_{incl}/N_{dec}$. All of the terms in this equation are measured from the data except the mapping function, which was determined from the Monte Carlo as described previously.

The effects of these cuts on the raw inclusive photon spectrum can be seen in Fig. 4.16. The black curve is the inclusive photon spectra without any cuts applied. The red curve is the number of photons which are not tagged as photons and finally the green curve is the number of photons which survive both the isolation and tagging cuts. Comparing R'_γ to R_γ shows that the signal to background ratio for the subtraction is improved by a factor of 2-5 depending on the photon p_T.

4.5 A Study for Tagging in Au+Au

As mentioned previously, applying event by event techniques in a high multiplicity environment such as Au+Au collisions is complicated. Although, traditional isolation cuts would obviously not work since the average energy in
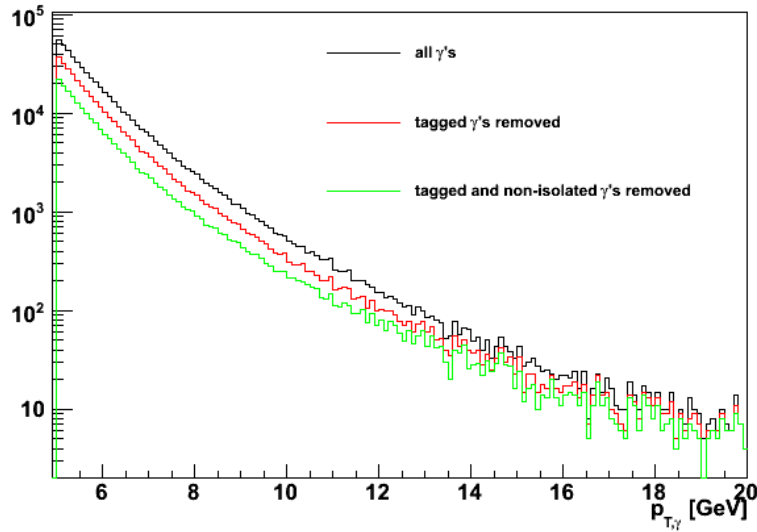
Figure 4.16: The raw p_T spectrum of inclusive photons before any cuts (black), after the tagging cuts (red) and after tagging and isolation cuts are applied (green).

a 0.3 radian cone is always greater than the photon energies we are studying, the technique of tagging decay photons based on the reconstructed invariant mass may be feasible. The tagging method has been established in the $p + p$ measurement and explained in the previous section. However, in Au+Au events the probability of falsely tagging a γ_{dir} as a γ_{dec} is greater due to the increased multiplicity and must be taken into account in the subtraction equation through an appropriately calculated R'_γ.

4.5.1 R'_γ

To determine the appropriate R'_γ for the tagging method in Au+Au let us first define the following:

$$N_{tag} = N_{tagtrue} + N_{tagfalse} \tag{4.20}$$

$$\varepsilon_{false} = N_{tagfalse}/N_{tag} \tag{4.21}$$

Here there are no terms related to the isolation cut, like in the $p + p$ case, but the falsely tagged photons, $N_{tagfalse}$, are included. Since R_γ can be written as

$$R_\gamma = \frac{N_{incl}}{N_{\text{dec}}}, \tag{4.22}$$

94

R'_γ for the case were tagged decay photons are removed from the N_{inc} and N_{dec} is

$$R'_\gamma = \frac{N_{incl} - N_{tag}}{N_{miss}}. \tag{4.23}$$

N_{miss} is defined as

$$N_{miss} = N_{\text{dec}} - N_{tagtrue} = N_{\text{dec}} - (1 - \varepsilon_{false})N_{tag} \tag{4.24}$$

After combining the above equations, one can express R'_γ as

$$R'_\gamma = \frac{1 - \frac{N_{tag}}{N_{incl}}}{R_\gamma^{-1} + (\varepsilon_{false} - 1)\frac{N_{tag}}{N_{incl}}} \tag{4.25}$$

and propagate the error from R_γ as

$$\sigma R'_\gamma = \sigma R_\gamma \frac{1 - \frac{N_{tag}}{N_{incl}}}{(1 + R_\gamma(\varepsilon_{false} - 1)\frac{N_{tag}}{N_{incl}})^2} \tag{4.26}$$

Equation 4.25 was used to calculate the R'_γ for the tagging method. ε_{false} is determined from the simulation while all other terms are obtained from data. Figure 4.17 shows the calculated R'_γ in red. The black points show R_γ as measured in Run 4 and used in the statistical method. The blue points are R'_γ derived purely from the simulation for comparison but are not used. This plot does not include the systematic uncertainties. Due to the large uncertainty in R'_γ determined for the first implementation of this method, this analysis was discontinued. However, additional studies to optimize the tagging cuts used may improve the situation. An improved measurement of R_γ, from a newer larger data set would also reduce the uncertainty in R'_γ. Since improving the signal to background in the subtraction results in smaller statistical uncertainties, this method may prove to only be useful in the highest $p_{T\gamma}$ bins were the results are mostly statistically limited.

4.5.2 Mapping Functions

The method of mapping measured π^0s to decay photons to extract the γ_{dec}-h correlations are described previously. This procedure was repeated for this analysis using the above described Monte Carlo in single particle mode where only π^0s are thrown to determine the mapping for the Run 7 data. For the tagging method, single particle mode is used but only the photons which pass the acceptance and cannot be tagged as a π^0s are included in the mapping
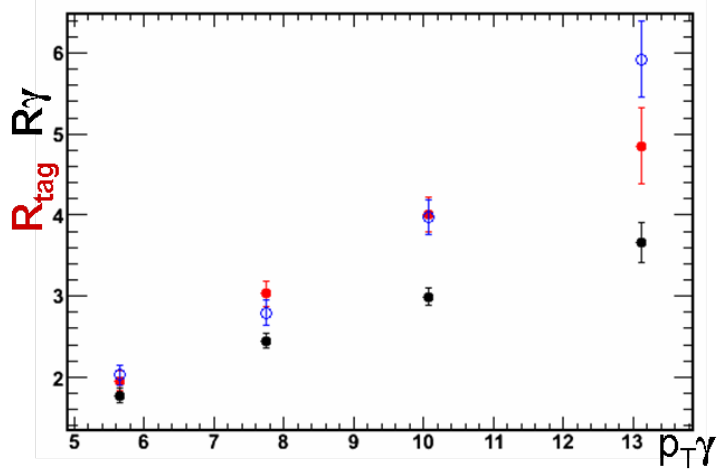
Figure 4.17: The black points show R_γ as measured in Run 4 and used in the statistical method. The red points are R'_γ using the data and simulation in the above equation. The blue points are not used. They are R'_γ derived purely from the simulation. (Only statistical error bars are plotted here)

histograms. An example of each of these are plotted in Figure 4.18. The tagging procedure preferentially removes decay photons from high p_T π^0. This effect is also observed in the $p + p$ analysis.
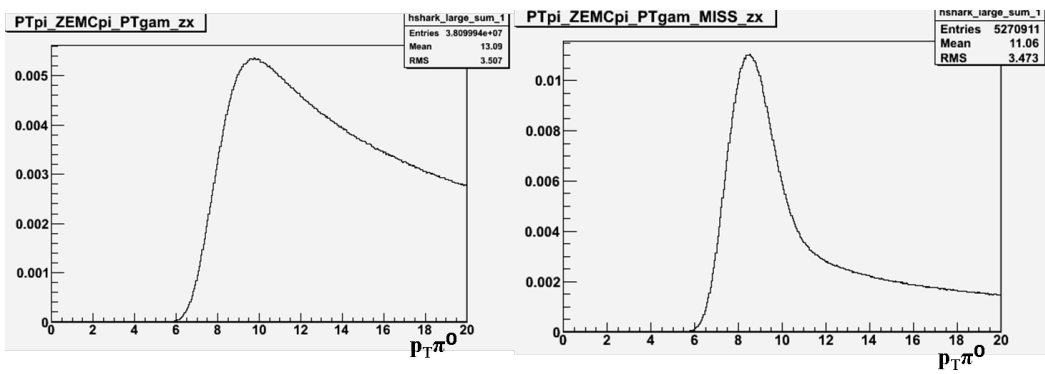
Figure 4.18: These two plots show the decay probability for 7–9 GeV/c decay photons as a function of the parent π^0 p_T. The left is for all decay photons that pass our acceptance and cuts while the right plot is for decay photons that were not removed in our tagging method.

Chapter 5

Systematic Uncertainties

5.1 Summary of Systematic Errors

There are five main sources of systematic error in this analysis. The first is a systematic error on the subtraction method (described in Eqn. 4.3) due to the statistical and systematic uncertainties in R_γ, which are listed in Table 4.1. Then there is the systematic error from the determination of the decay contribution. The uncertainties in the extraction of the jet functions from the v_2 measurements listed in Table 3.2 and the normalization in the ABS method are also taken into account. Last is the global scale uncertainty due to the hadron efficiency calculation. A discussion on each of these sources is provided in the following subsections, but let's discuss how each of these contribute to the final yield. Because statistics run out at high p_T while the signal to background ratio is worse at low p_T, different sources of uncertainty dominate in different p_T bins. Fig. 5.1 shows how each source contributes for the different trigger and partner p_T bins based on the Run 7 data. The dominant uncertainty for the low p_T^h bins is generally due to v_2 (green) or the background normalization (blue), labeled MSMP. Since the background in the correlation functions is large for these p_T^h bins, the normalization and modulation become very important. For high p_T triggers, the uncertainty due to R_γ (black) starts to dominate. The value of R_γ is generally larger at higher p_T but its statistical error and systematic uncertainties are both greater. The uncertainty due to the decay mapping procedure (red) dominates for some of the low trigger p_T bins, since the combinatorial background under the π^0 mass peak is largest there. The scale uncertainty is excluded from these plots and discussion because it is a constant percentage at all p_T.
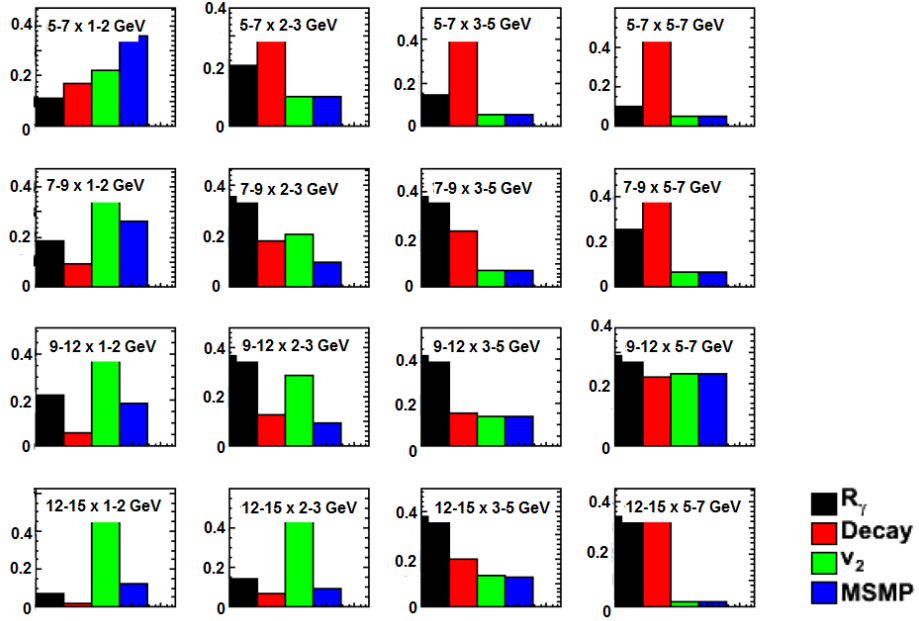
Figure 5.1: This breakdown of the systematic uncertainties for the various p_T bins for the Run 7 analysis shows the percentage that each source of uncertainty contributes to the total systematic uncertainty. The dominant source of uncertainty varies based on the p_T of the trigger and associated particles. The four sources shown include the uncertainty due to the R_γ measurement used in the direct photon extraction (black), the determinization of the decay photon correlations (red), the v_2 values used in the jet subtraction (green), and the (MSMP) determination of the background level in the jet subtraction (blue).

5.1.1 R_γ and Inclusive Photons

The statistical and systematic uncertainties in R_γ are listed in Table 4.1. The major sources leading to the systematic uncertainty in the R_γ measurements include the non-linear energy scale, the π^0 extraction, contributions to the decay photon yield besides π^0s and cluster merging for photons with E > 10 GeV [54]. Since one value of R_γ is used within a given trigger p_T bin, the uncertainty in our measurement resulting from R_γ is completely correlated. However, the statistical uncertainty from R_γ leads to an uncorrelated error across trigger p_T bins. A previously determined 1% uncertainty on the inclusive photon yield [57] was propagated to a conservative 1% on the yield in our correlation measurement.

5.1.2 Decay Mapping

The systematic error from the determination of the decay contribution consists of the 3% error on the method plus the cut off correction, which is at most 2%, and the π^0 combinatorial error. The dominant error is from the π^0 combinatorial error. This uncertainty results from the fact that the π^0s, as measured from the invariant mass of photon pairs, contain a mixture of true π^0s and combinatorial background. For low momentum triggers the peak clearly sits on a significant background, which decreases as the π^0 p_T is increased, as shown in 3.1. We can write the relationship between the measured per trigger yield, Y_{meas}, the true, Y_{true}, and background yields, Y_{bg} as

$$Y_{meas} = \frac{1}{N_{trig}}(N_{bg}Y_{bg} + N_{sig}Y_{true}). \tag{5.1}$$

To determine the combinatorial error, $\sigma_{\pi^0{}_{comb}} = (Y_{true} - Y_{meas})/Y_{meas}$, we substitute $S/B = N_{sig}/N_{bg}$ and rearrange Eqn. 5.1 to get

$$\sigma_{\pi^0{}_{comb}} = \frac{1 - Y_{bg}/Y_{meas}}{S/B(Y_{bg}/Y_{meas})}, \tag{5.2}$$

The S/B, which ranges from 4 to 15, is extracted from the plots in Fig. 3.1 and is applied in Eqn. 5.2 for each trigger p_T bin. Y_{meas} is what is measured and used in the analysis but Y_{bg} can be determined in several different ways. First, one can do a "side-band" analysis, which is most common method for determining the π^0 combinatorial error. Instead of using π^0 triggers from the mass peak window, as used in Y_{meas}, the yield is determined using triggers which are about 2σ above and below the mass peak. Since the triggers in this mass region are not true π^0 they should describe how the background under the mass peak contributes to the measured correlation. If these pairs are

completely uncorrelated with the associated hadrons, the yield should be zero. Plugging in zero for Y_{bg} in Eqn. 5.2 gives the same $\sigma_{\pi^0_{comb}}$ as $Y_{bg}/Y_{meas} = 2$. This is an extreme case because some correlated yield should expected since the photons in these pairs are most likely still decays from π^0s, even though they are incorrectly paired.

For some Run 7 results, an alternative method was used to try to more accurately determine the ratio Y_{bg}/Y_{meas}. This method uses the previously described Monte Carlo to map and correct the measured decay photon p_T to the true p_T. The ratio is determined by iteratively applying this correction to the data and measuring the yield as a function of p_T. Ten iterations are done for each hadron p_T bin but the values stabilize after only a few iterations. To simplify the filltime method, a conservative value of 2 was used for the Y_{bg}/Y_{meas} for all p_T combinations.
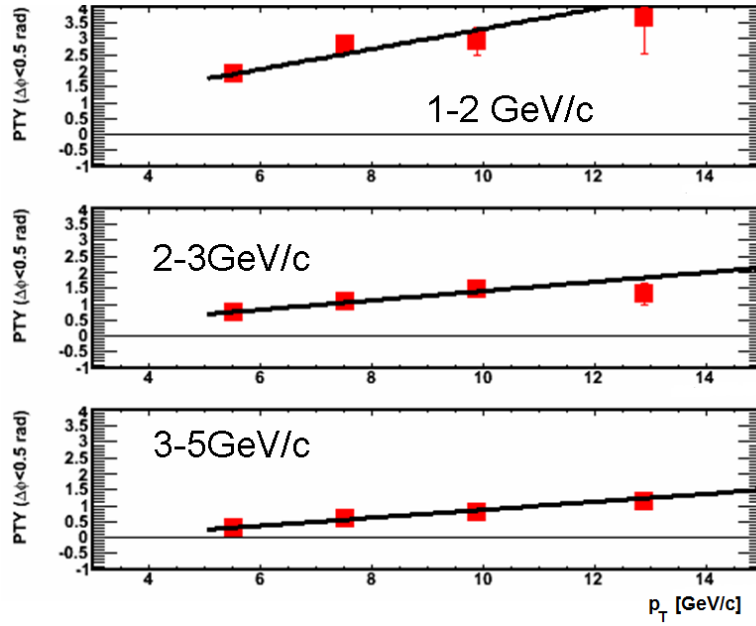
Figure 5.2: Near-side per trigger yield as a function of π^0 p_T for $\pi^0 - h$ correlations. A linear fit is used in the method to determine the π^0 combinatorial yield.

The resulting systematic error in the decay mapping is mostly correlated across p_T^h bins. However, the cutoff correction is actually determined separately for each bin. The uncertainty due to the π^0 combinatorial background is correlated for a given p_{T_γ} but is mostly uncorrelated across p_{T_γ} bins.
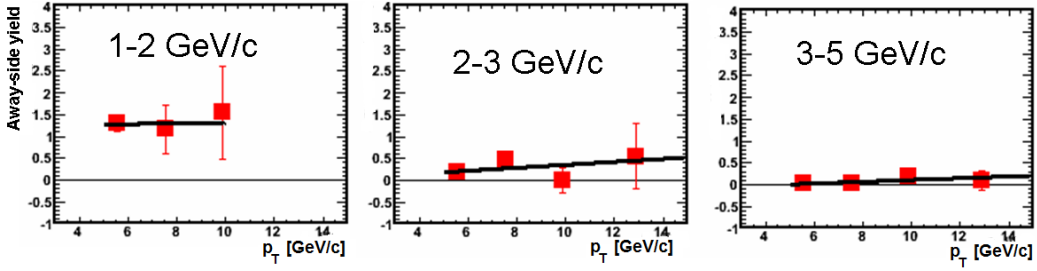
Figure 5.3: Away-side per trigger yield as a function of π^0 p_T for $\pi^0 - h$ correlations. A linear fit is used in the method to determine the π^0 combinatorial yield.

5.1.3 Jet Function Extraction Uncertainties

The uncertainties in the extraction of the jet functions are due to the uncertainty in the v_2 measurements and the background normalization from the ABS method.

The uncertainties for v_2 are listed in Table 3.2. The systematic error in v_2 is mostly correlated since the dominant source of uncertainty arises from the resolution of the reaction plane determination. It is propagated as a correlated error in the $\gamma_{\mathrm{dir}} - h$ extraction since the same hadron v_2 is used in both the $\gamma_{\mathrm{inc}} - h$ and $\gamma_{\mathrm{dec}} - h$ correlations. Furthermore, for low trigger p_T the inclusive sample is dominated by decay photons, while at high p_T the reaction plane resolution dominates. All of these indicate that the v_2 error should be treated as correlated.

The error from the ABS method for determining the normalization of the background is also propagated as correlated since the method is the same and the hadrons sampled are the same for the different triggers. Since a similar background level is expected for both correlations, the levels should at least change in the same direction. Since part of the error in the ABS method is due to statistics, it is uncorrelated between p_T bins.

5.1.4 Hadron Corrections

For Run 4, the bootstrap method was used to determine the hadron efficiencies. A 10% global scale uncertainty on the method at all p_T plus an additional uncertainty on the extrapolation at high p_T results in a total uncertainty of 12.2% for the highest p_T bin.

The 8.8% global scale uncertainty from the hadron efficiency calculation for Run 7 is described in an earlier section and arises from matching the detector

response between data and simulation. In addition, an 8% systematic error was included in bins that include hadrons above 5.0 GeV/c to account for the contamination observed in the high p_T sample of tracks.

5.1.5 Propagation of Systematic Errors

Due to the non-linearity arising from the $(R_\gamma - 1)$ term in the subtraction equation, the systematic errors are generally propagated by determining an upper and lower value by adjusting the central value to the top and bottom of its error bars. This is done independently for each source. Then the correlated errors are summed together in quadrature while any uncorrelated components are added in quadrature with the statistical uncertainty.

The systematic errors on the ratio, I_{AA}, are determined by raising and lowering the Au+Au and p+p yields by their corresponding errors together since the uncertainties in the decay procedure are correlated and the uncertainty in R_γ is mostly correlated.

5.1.6 Propagation of Systematic Errors in the Filltime Method

The R_γ and decay errors are handled during the subtraction procedure in the same way as described previously. To determine the v_2 error, additional histograms are used where the c_2 term in the weight is replaced by $c_2 + error$ and $c_2 - error$. (Recall $c_2 = v_2^{trig} v_2^{assoc}$.) The error on the final spectra was determined by calculating the difference between the results of using these histograms to the actual result. The MSMP method has two sources of uncertainty. The first comes from the ξ correction. Since ξ is applied during the subtraction, its uncertainty is propagated through the code as completely correlated. The second component to the error comes from the statistical error in the normalization. In the filltime method, where the normalization is based on histograms filled while passing over the data which contain the associated statical uncertainty, this error is propagated directly into the final statistical error bars during the subtraction.

5.1.7 Propagation of Systematic Errors for the Combined Trigger Bins

The analysis was preformed in 4 separate trigger bins and combined at the end by weighting each trigger bin according to a fit to the direct photon spectrum [56]. A power law was fit to the fully corrected direct photon spectrum

measured in a separate analysis which gives a power of -6.55 and constant of 1.38 for the 0-20% most central collisions.

Although the v_2 and R_γ uncertainties have an uncorrelated component across the trigger bins, these errors are treated as though they are completely correlated. Because of the large statistical uncertainties in this measurement, we are not concerned with the slightly larger systematic uncertainty which results from propagating these uncorrelated errors as correlated. All other systematic uncertainties are correlated errors and were each propagated through the averaging. These different sources of systematic error are then summed in quadrature and plotted as gray bans in the final plots. The following data table for the ξ distribution, Table 5.1, shows how each source of uncertainty contributes to the total systematic uncertainty in the results. Generally the uncertainty due to the decay weighting dominates. However, at high ξ, or low p_{Th}, the normalization error can dominate due to the large background in the correlation functions.

Table 5.1: ξ distributions from 0-20% Au+Au collisions for 5-12GeV/c triggers combined with the systematic errors broken down by source.

ξ	Yield	Stat	Total Sys	$R\gamma$	Decay	v_2	ABS
0.2	4.1e-3	6.6e-3	+4.4e-3	+8.4e-4	+4.2e-3	+6.1e-5	+3.1e-4
			-4.4e-3	-1.1e-3	-4.2e-3	-4.4e-5	-3.1e-4
0.6	2.5e-2	2.0e-2	+9.7e-3	+8.5e-4	+9.0e-3	+4.7e-4	+2.7e-3
			-9.7e-3	-1.1e-3	-9.0e-3	-4.6e-4	-2.7e-3
1.0	1.4e-1	5.4e-2	+3.9e-2	+1.4e-3	+3.2e-2	+3.3e-3	+1.8e-2
			-3.9e-2	-1.3e-3	-3.2e-2	-3.3e-3	-1.8e-2
1.4	1.5e-1	1.1e-1	+9.8e-2	+1.1e-2	+7.4e-2	+1.1e-2	+6.3e-2
			-9.8e-2	-1.4e-2	-7.4e-2	-1.1e-2	-6.3e-2
1.8	5.1e-1	1.7e-1	+1.7e-1	+1.5e-2	+9.5e-2	+2.5e-2	+1.4e-1
			-1.7e-1	-1.3e-2	-9.5e-2	-2.4e-2	-1.4e-1
2.2	5.5e-1	3.4e-1	+2.0e-1	+1.1e-2	+4.1e-2	+2.9e-2	+1.9e-1
			-2.0e-1	-1.3e-2	-4.1e-2	-2.3e-2	-1.9e-1
2.6	1.1	5.8e-1	+2.6e-1	+6.1e-2	+1.5e-2	+4.6e-2	+2.4e-1
			-2.6e-1	-4.0e-2	-1.5e-2	-7.2e-2	-2.4e-1

Chapter 6

First $\gamma_{\mathrm{dir}} - h$ Results

The first measurement of γ_{dir}-hadron correlations in heavy ion collisions from PHENIX uses data collected during the 2004 Au+Au RHIC run [17]. The Au+Au results are compared to results from p+p collisions collected during the 2005 and 2006 RHIC runs combined. All of the results presented in this Chapter use the statistical subtraction procedure. The isolation and tagging cuts described in the Analysis section of this thesis have not been applied in this p+p analysis. Both the p+p and Au+Au results presented here use the bootstrapped hadron efficiency values described in Chapter 3.

A sample set of jet functions is shown here in Fig. 6.1 for p+p in the top panel and Au+Au in the bottom panel. As a reminder, the jet function refers to the fully corrected correlation function with the elliptic flow contribution removed. The yield measured is per trigger. For inclusive photon-hadron correlations, there is a clear peak on both the near and away sides, which is also true for hadron-hadron correlations. However, since the direct photon is not part of a jet, it is not surrounded by particles, which results in little to no yield on the near side around $\Delta\phi = 0$. A peak still exists on the away-side though for $\gamma^{direct} - h$ correlations from the opposing jet. This is evident in both the p+p and Au+Au data, although the away-side jet is clearly suppressed in Au+Au.

The fragmentation function can be measured by integrating the away-side and plotting the yield as a function of z_T. Since this analysis was done in p_T bins, $\langle z_T \rangle = \langle p_T^h \rangle / \langle p_T^{\gamma_{\mathrm{dir}}} \rangle$ is actually used. The $\langle z_T \rangle$ distributions for p+p and the 0-20% most central Au+Au collisions are shown in Fig. 6.2. The 90% confidence level for the upper limit is given for points whose error bars span zero. Both the p+p and Au+Au data show that a universal scaling seems to hold across jet energies as a function of z_T. It is not expected that the scaling will hold for Au+Au collisions except for two special cases: surface emission and fractional energy loss. Surface emission means that all the observed associated
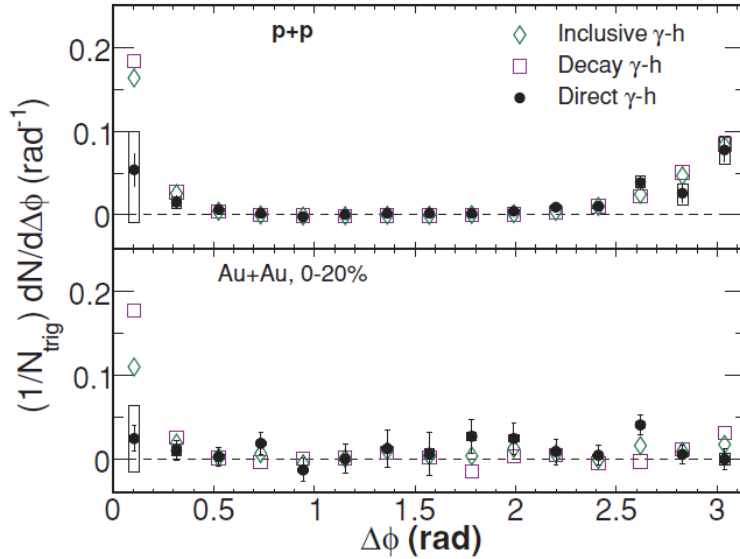
Figure 6.1: The $\Delta\phi$ distribution for $\gamma^{dir} - h$ (black points), $\gamma^{dec} - h$ (open squares) and $\gamma^{inc} - h$ (diamonds) in p+p (top) and 0-20% most central Au+Au collisions (bottom) [17]. The momentum range of the triggers and associated hadrons are $5 < p_T^{trig} < 7$ and $3 < p_T^h < 5$.

hadrons are from the surface of the produced medium. This could, perhaps, be due to a dense opaque core such that nothing exits except the jets near the surface, which "punch through". This would result in a suppressed number of measured particles while maintaining the same fragmentation function slope. Constant fractional energy loss in the medium would preserve the z_T scaling for the different p_T triggers in Au+Au but would result in a steeper slope.

Since z_T scaling is observed, all the points are fit to a single curve. A simple exponential function, $N = N_0 e^{-bz_T}$, is used to extract a slope, b, for the two distributions. For p+p, the fit gives a $\chi^2/\text{DOF}=12.8/10$ and $b = 6.9 \pm 0.8$. Although an exponential fit may not be the best fit to the data, it gives an acceptable χ^2/DOF and the slope can be compared to expectations from previous fragmentation functions. The expected slope for the quark fragmentation function is b=8.2, while for gluons b=11.4 [18]. The measured slope for the p+p data is more consistent with quark fragmentation, which agrees with the expectation that the Compton scattering process dominates for p+p collisions since there are more gluons than anti-quarks available for quarks to scatter. The fit to the the Au+Au distribution has a $\chi^2/\text{DOF}=12.8/10$ and gives a slope, $b = 5.6 \pm 2.2$. This slope is consistent with the measured p+p slope. A suppressed yield but same slope and preserved z_T scaling could indicate that

the associated particles measured are only those which originate near the surface. However, we should note that the $\Delta\phi$ range was limited on the away-side, which may cause the measured sample to be dominated by "punch through" jets.
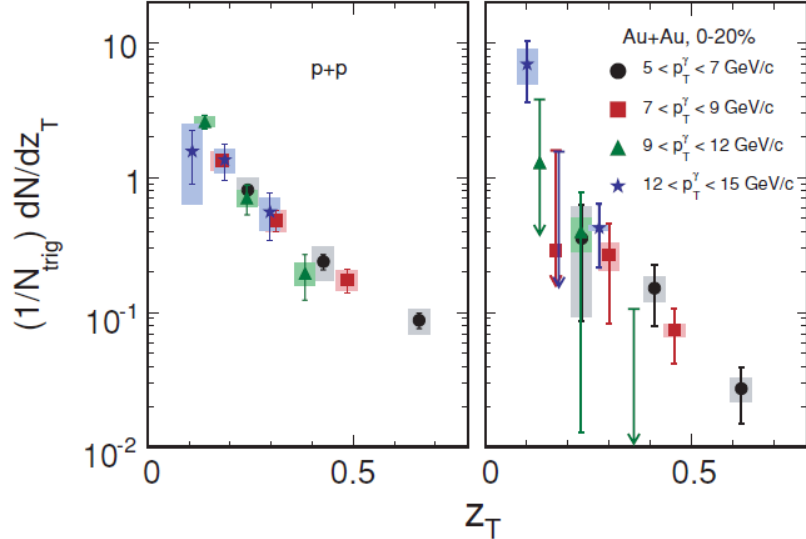
Figure 6.2: The z_T distribution for $\gamma^{dir} - h$ in p+p (left) and 0-20% most central Au+Au collisions from Run 4 (right) [17].

To better quantify the modification of the fragmentation function in Au+Au compared to $p + p$, the ratio of the spectra, I_{AA}, is measured. I_{AA} vs z_T is shown in Fig. 6.3. Also included in the figure is the ZOWW calculation which was described in Chapter 1. Their NLO pQCD energy loss model seems to represent the data reasonably well for the ϵ_0 values indicated, which fall within the range set by the PHENIX $\pi^0 R_{AA}$ measurement. ϵ_0 is proportional to the initial gluon density of the medium. We note that the ZOWW model implements an isolation cut on the trigger photon which is not applied to this data. The isolation cut removes the contribution from fragmentation photons which are not explicitly removed in our procedure. However, the lack of nearside yield in Fig. 6.1 indicates that the fragmentation photons do not significantly alter in our correlation measurement.

The I_{AA} for associated hadrons on the away-side with $3 \text{ GeV}/c < p_T^h < 5\text{GeV}/c$ is averaged over all trigger p_T bins, $5 < p_T^h < 15\text{GeV}/c$, for three different centrality bins, 0-20%, 20-40%, and 40-60%. The average I_{AA} is plotted in Fig. 6.4 as a function of N_{part}. An average $I_{AA} = 0.32 \pm 0.12 \pm 0.09$ is measured in the most central bin, exhibiting a clear suppression. Also included in this plot
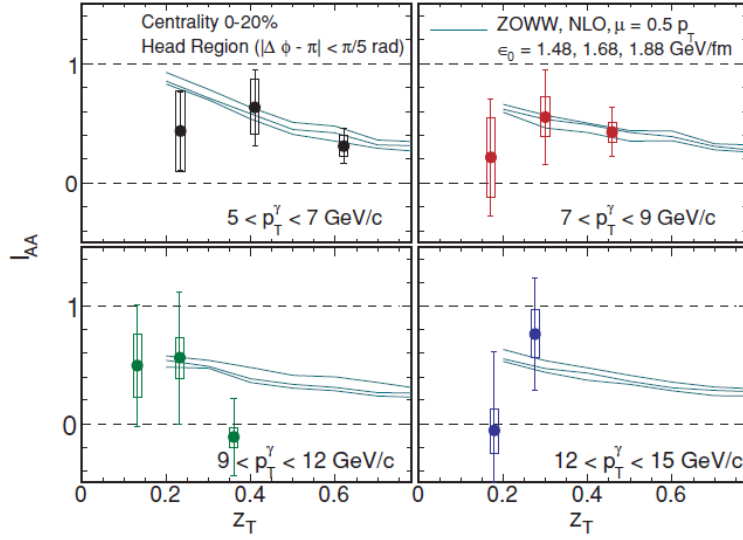
Figure 6.3: I_{AA} as a function of z_T for four different trigger bins compared to the ZOWW energy loss prediction [17].

are the centrality dependence for the high p_T $\pi^0 R_{AA}$ and the h-h I_{AA} in a similar trigger and partner p_T range. The γ_{dir}-h I_{AA} is remarkably similar to both of these other suppression measurements, particularly in the most central bin. This could indicate that surface emission dominates in these measurements but is also consistent with the geometric dependence described in Chapter 1. Since this average $\gamma_{dir} - h$ I_{AA} corresponds to high z, the assoicated hadrons are more likely to come from the surface and result in an observed suppression similar to surface biased jet suppression measurements.

In summary, these results show a suppression in the away-side γ_{dir}-h yield in the range, $|\Delta\phi - \pi| < \pi/5$. This suppression is consistent with both the h-h I_{AA} and the π^0 R_{AA}. An apparent z_T scaling seems to be present in both the $p + p$ and Au+Au distributions. This scaling, combined with the consistent slope measured between the two data sets, seems to indicate that the only hadrons which escape the medium in this z_T range are those from the surface. However, more statistics are required to make a good and precise comparison between the two data sets.
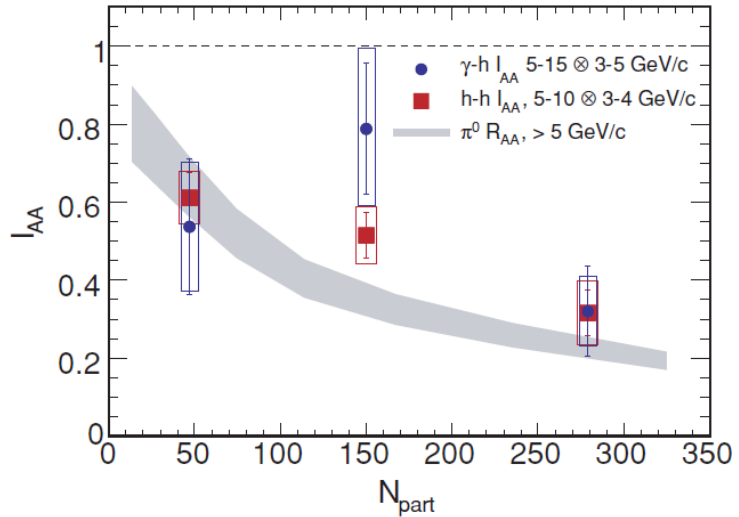
Figure 6.4: I_{AA} as a function of N_{part} for $\gamma_{\mathrm{dir}} - h$ with $3 < p_T^h < 5$ GeV/c and $5 < p_{T\gamma} < 15$ GeV/c. This data is compared to the h-h I_{AA} for $5 < p_T^{trig} < 10$ GeV/c and $3 < p_T^{assoc} < 4$ GeV/c as well as the $\pi 0$ R_{AA} for $p_T^{\pi^0} > 5$. All these ratios are consistent within the current uncertainties [17].

Chapter 7

Results and Discussion: p_T Binning Method

The 2007 data set is a factor of four larger than the previously shown 2004 data. The set of results from Run 7 presented in this chapter uses the previously published method where everything is binned in p_T. The $p + p$ baseline used is the same as in Chapter 6, which is extracted using the statistical method where no event-by-event techniques have been implemented. Similar to the previous chapter, the focus will be on the most central bin, 0-20%, which has better statics due to the higher multiplicity. The centrality dependence of the I_{AA} is also explored.

7.1 $\Delta\phi$ Distributions

The jet functions for the γ_{inc}-h, γ_{dec}-h and resulting γ_{dir}-h measured from the 0-20% most central Run 7 data are plotted in Fig. 7.1. These are per trigger yields as a function of $\Delta\phi$. The γ_{dir}-h are again consistent with the expectation of little to no correlated yield on the near-side around $\Delta\phi = 0$, since direct photons are not part of a jet, while a peak is observed in γ_{inc}-h and γ_{dec}-h since those triggers do come from jets.

For plot clarity the systematic uncertainties are only plotted for the γ_{dir}-h points. The systematic uncertainties are largest for the lowest p_T bins due to the larger background. At high p_T the measurement is limited by the statistics available. We note that the statistical uncertainties are typically largest around $\Delta\phi = \pi/2$. This is due not only to the shape of the correlated yield but to the acceptance shape of the PHENIX detector as discussed previously (Chapter 3). More statistical precision is necessary before carefully studying the shape of the jet function and comparing these $\Delta\phi$ distributions to theoretical models [58]
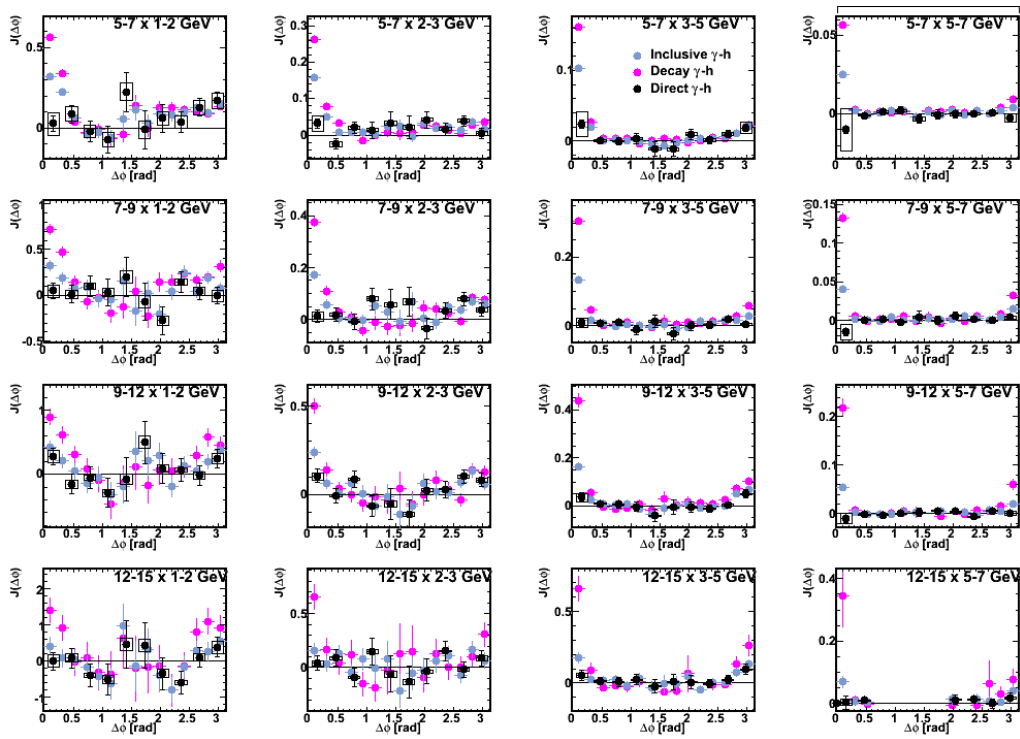
Figure 7.1: The γ_{dir}-h jet functions measured from the Run 7 data for the 0-20% most central collisions.

can be done. For now, we focus our detailed studies on the yield integrated over different ranges of $\Delta\phi$.

7.2 The Near Side

Since direct photons are not part of a jet, we expect little to no correlated yield on the near-side around $\Delta\phi = 0$. We observed this qualitatively in the previous section and Chapter but will present a more quantitative study here. Since fragmentation photons are not explicitly removed from our trigger sample, some nearside yield may be observed in both $p+p$ and Au+Au collisions. Additionally, in Au+Au collisions, photons from medium interactions could also contribute to a nearside yield which may be enhanced compared to the $p+p$ measurement. On the other hand, parton energy loss could lead to a suppression of fragmentation photons at high p_T. The yield on the nearside, $|\Delta\phi| < \pi/3$, is plotted in Fig. 7.2 for the γ_{dir}-h correlations measured in $p+p$ and Au+Au collisions. For comparison, the nearside yield for π^0-h correlations is also plotted. Since the π^0 triggers do come from jets, the yield on the nearside is significant compared to the near-side for the γ_{dir}-h for the same collision species. It is also interesting to compare the near-side yield in the γ_{dir}-h measurement to zero. To do so, a zoomed version of this plot is shown in Fig. 7.3. As you can see, there is some near-side yield present in the $p+p$ measurement, indicating a small contribution from fragmentation photons. The Au+Au measurement is consistent with the $p+p$ measurement. This suggests one of two possible scenarios. One possibility is that the same number of fragmentation photons are produced in both collisions and there are no additional medium induced photon sources observed in this p_T range. Alternatively, the competing effects of suppression due to energy loss and enhancement due to induced Bremsstrahlung emission may cancel, leaving the observed yield relatively unmodified. In any case, we are confident that we are measuring direct photons as we described and that the small fraction of possible fragmentation photons is not significantly altering our results. Finally, we note that the lack of enhancement in the Au+Au nearside to that in $p+p$ also has implications for interpretations of the ridge observed in di-hadron correlations. Any model to explain the observed ridge must also be able to explain this observable.

7.3 Yield on the Away-side

The goal of this analysis is actually to study the modifications to the away-side jet, opposite the direct photon trigger. Therefore the yield of the away-side is
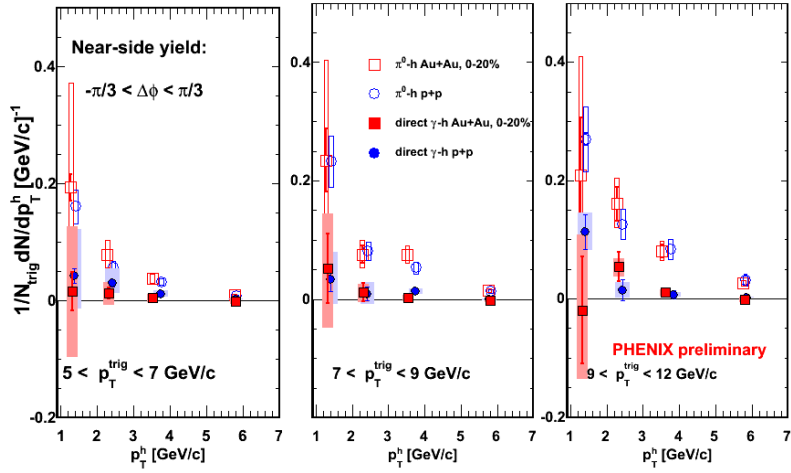
Figure 7.2: The nearside yield for γ_{dir}-h and π^0-h correlations in $p + p$ and $Au + Au$ collisions.
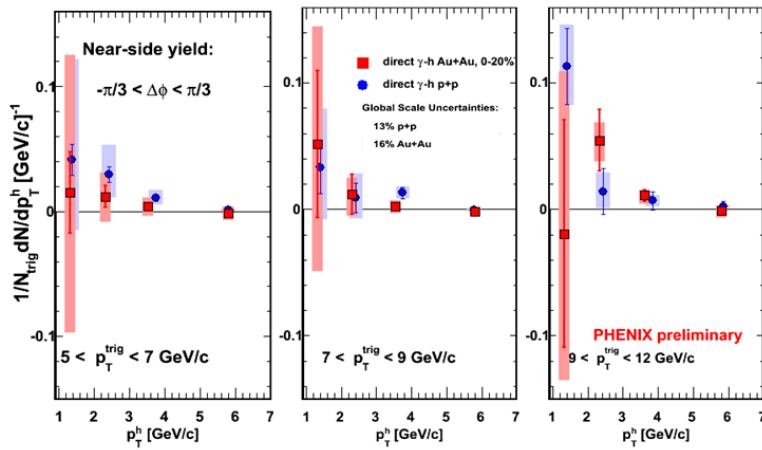
Figure 7.3: The nearside yield for γ_{dir}-h in $p + p$ and $Au + Au$ collisions. This is the same data plotted in Fig. 7.2 but this plot is more zoomed in.

measured. This study, like that in the previous Chapter, focuses on what is referred to as the head region in $\Delta\phi$ which is defined as $|\Delta\phi - \pi| < \pi/5$.

To measure the modification of the fragmentation function of the opposing parton, the away-side yield of the resulting $\gamma_{direct} - h$ jet function is measured in the head region, $|\Delta\phi - \pi| < \pi/5$, and plotted as a function of z_T. For correlations between trigger and associated particles, $z_T = \langle p_{T,assoc}\rangle/\langle p_{T,trig}\rangle$. For $\gamma_{direct} - h$, $z_T = \langle p_{T,h}\rangle/\langle p_{T,\gamma}\rangle \cong \langle p_{T,h}\rangle/\langle p_{T,jet}\rangle$ and is used to approximate z. The z_T distributions are shown in Figure 7.4. The blue points are for $p+p$ collisions from the 2005 and 2006 data combined and the red points are from $Au + Au$ collisions from the 2007 data.
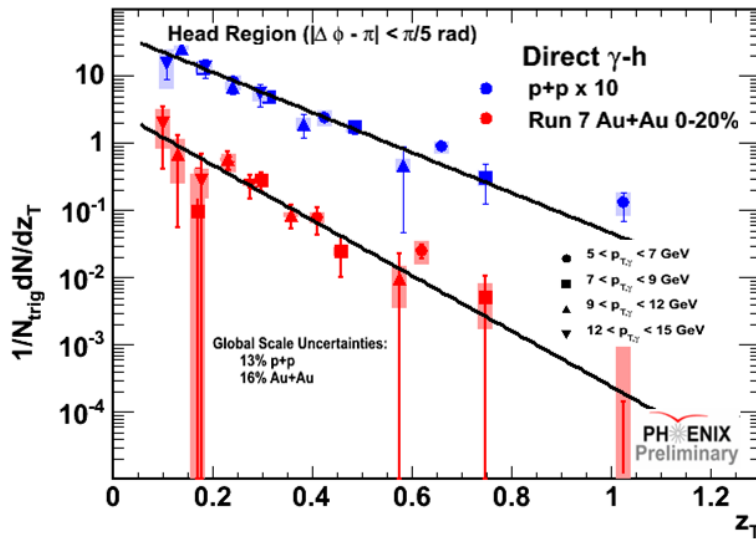
Figure 7.4: The away-side yield for γ_{dir}-h in $p+p$ scaled by a factor of 10 and $Au + Au$ collisions as a function of z_T. The lines are a simple exponential fit to the datasets.

All p_T bins appear to obey approximate z_T scaling. Therefore, all points for each collisional system are fit with the function, $\frac{dN}{dz_T} = Ne^{-bz_T}$. For $p+p$ the slope was measured to be $b = 6.9 \pm 0.6$ which is the same value measured in the previous chapter but with a slightly smaller error. The error is reduced because of the additional data points for the 5-7GeV/c p_T^h bins. The fit gives a similar χ^2/DOF=14.04/13. The slope in $Au + Au$ is $b = 9.5 \pm 1.4$ with a χ^2/DOF=10.0/13 for the fit. The slope in this Au+Au data exceeds that in $p+p$. The increased statistics of the Run 7 data improve the uncertainty on the Au+Au slope. A steeper fragmentation function is expected in the QCD medium, due to constant fractional energy loss of the away-side parton. However, the statistical uncertainties in these data limit the significance of the

difference to only 1.3 σ. Again we should note that the uncertainties here are determined from the statistical and uncorrelated systematic errors since the correlated systematics are not expected to change the slope. The slope of the Au+Au data is consistent within 1 σ of the the slope for quark fragmentation, b=8.2. If we claim that the slope for the $p + p$ data is consistent with this, the conclusion would then be that there is no modification to the shape. It is important to understand and reduce our uncertainties to clarify this.

7.4   Away-side I_{AA}

To quantify the suppression observed in the $\gamma_{\mathrm{dir}} - h$ channel, the I_{AA} is measured by taking the ratio of the red Au+Au points to the blue p+p points. The I_{AA} for each trigger p_T bin is shown in Fig. 7.5. All four trigger bins show a suppression in the Au+Au yield since the results are all consistent with $I_{AA} < 1$. By eye, the data suggests a negative slope, however, the large uncertainties and fluctuations in the data make each panel consistent with a flat line.
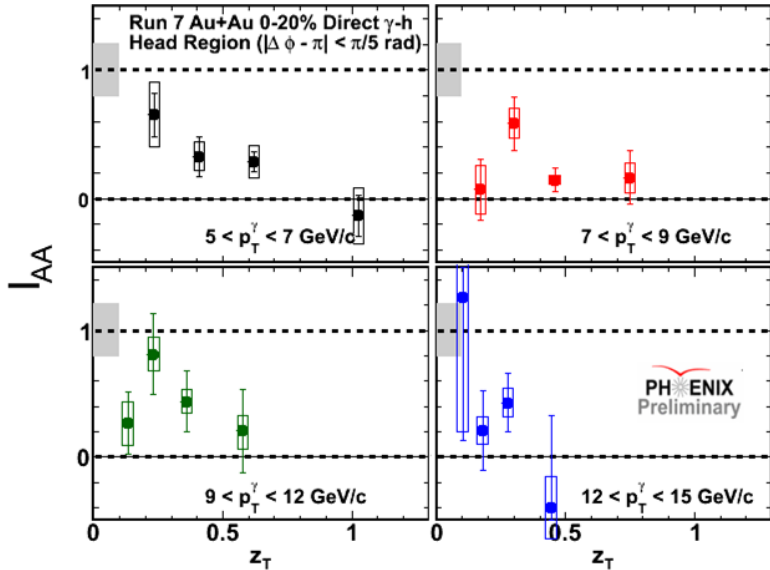
Figure 7.5: The ratio of the yield measured in $Au + Au$ over the yield in $p+p$. This is the ratio of the data plotted in Fig. 7.4 but in separated according to the trigger p_T.

This suppression is compared to the suppression measured in $\pi^0 - h$ in Fig. 7.6 for three different trigger p_T bins. With the possible exception of the lowest and highest z_T points, the I_{AA} of $\gamma_{\mathrm{dir}} - h$ and $\pi^0 - h$ are remarkably

consistent. This is surprising since $\pi^0 - h$ should include more gluon jets which are more suppressed. On the other hand, $\pi^0 - h$ suffers a surface bias, which reduces the suppression observed, while $\gamma_{\text{dir}} - h$ does not suffer such bias since the γ_{dir} trigger is not suppressed by the medium. Perhaps competing effects wash each other out. In a simpler picture, one could argue that the medium has an opaque core, which causes the γ_{dir}-h yield to be surface emission and the π^0-h I_{AA} is so surface biased that the energy loss difference between gluon and quark jets is irrelevant because of the small path length.
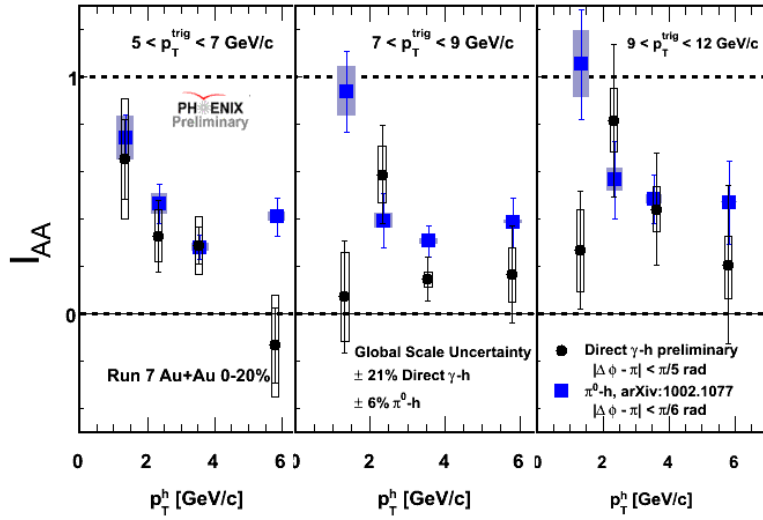
Figure 7.6: The I_{AA} measured in the head region for $\gamma_{\text{dir}} - h$ and $\pi^0 - h$ as a function of p_T^h for three different p_T^{trig}.

The I_{AA} for $\gamma_{\text{dir}} - h$ is also compared to several of the current theories as shown in Fig. 7.7. The ZOWW curve [13] shows suppression at high z_T and less suppression at low z_T due to the geometric dependence described previously. Renk's curve [39], however, does not have a strong z_T dependence because he allows for fluctuations in his energy loss model, washing out the geometric dependence effects. Finally, the data are compared to the BW-MLLA results from [40] in which the lost energy goes into production of low momentum particles. This enhances the low z_T region such that at very low z_T, the I_{AA} is above unity. The current measurements can not fully rule out any of these theories. However, these measurements will benefit from additional statistics from future runs and possibly improvements in the subtraction method. This comparison also highlights the need to explore lower z_T, since that is where the models start to diverge.

116
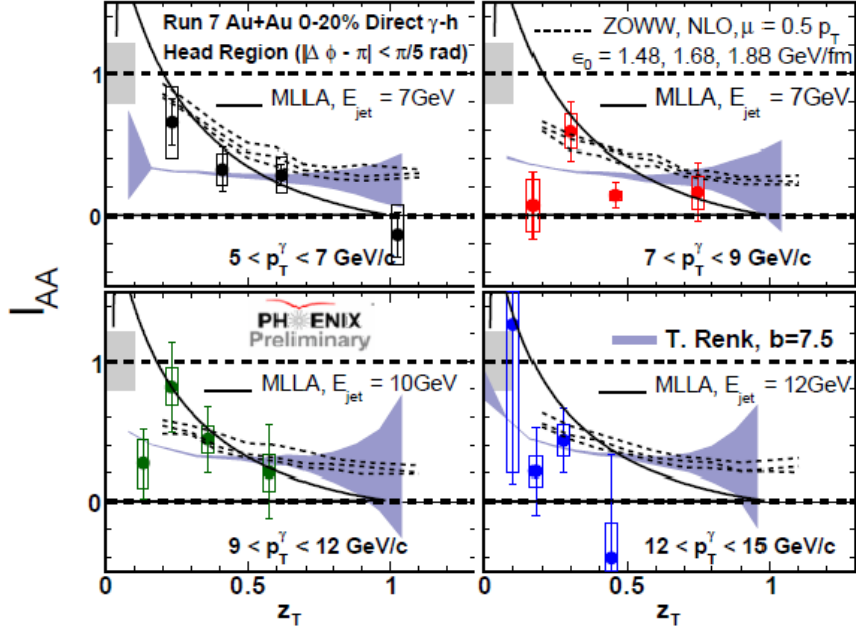
Figure 7.7: This is the same I_{AA} as plotted in Fig. 7.5 but now compared to various energy loss models.

Since the I_{AA} appears flat for $p_T^h > 2$ GeV/c and consistent for all triggers, the average I_{AA} was calculated using constant fits to the data. The average value for the 0-20% bin is $I_{AA} = 0.24 \pm 0.05^{stat} \pm 0.13^{sys}$. This averaging was done for two other centrality bins, 20-40% and 40-60% and plotted as a function of N_{part} as shown in Fig. 7.8. The 60-92% bin is still statistics starved and not included. The γ_{dir}-h result shown here is consistent with the Run 4 measurement and is compared here to the π^0 R_{AA} as well as the Run 7 $\pi^0 - h$ I_{AA}. Within the current uncertainties of the measurement, the $\gamma_{dir} - h$ I_{AA} is consistent with both these π^0measurements. However, the $\pi^0 - h$ I_{AA} is greater than the π^0 R_{AA} [30]. Initially one may expect the opposite effect, since triggering on a high p_T π^0 biases the measurement toward scatterings near the surface of the medium and thereby imposes a longer path length on the away-side parton. However, while this could still be the case, the p_T spectrum of the away-side hadrons is harder than the single hadron spectrum and would actually be less effected by the same spectral shift due to energy loss.

To summarize, the 2007 data greatly enhances the measurements by increasing the statistics by a factor of four and allowing measurements at higher hadron p_T. The $\gamma_{dir} - h$ and $\pi^0 - h$ I_{AA} agree extremely well, both as a

117
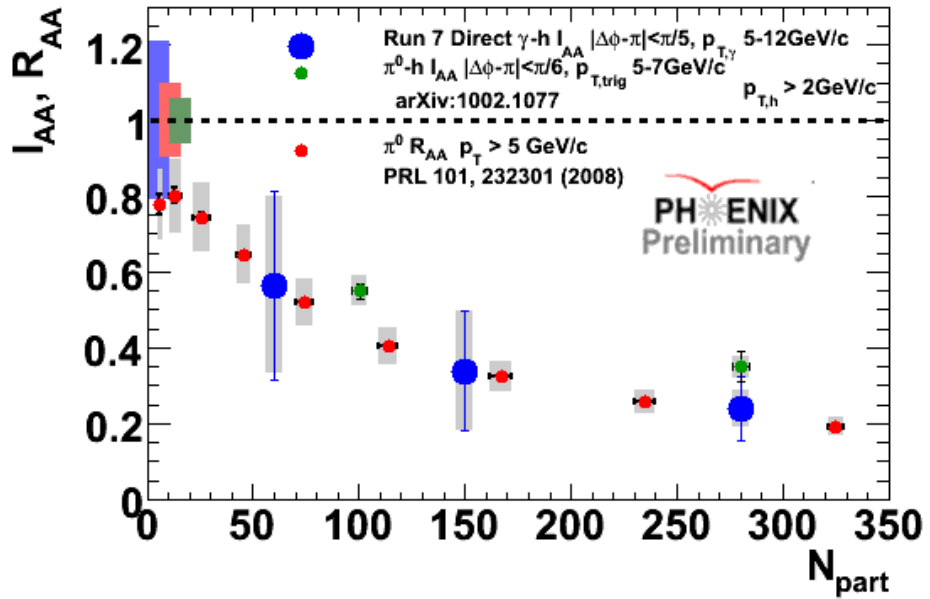
Figure 7.8: γ_{dir}-h I_{AA}(blue points) as a function of N_{part}compared to π^0-h $I_{AA}$and $\pi^0 R_{AA}$.

function of N_{part} averaged over p_T, as well as for separate trigger p_T bins. However, these results also illustrate the need to push lower in z_T and reduce the uncertainties in our measurements.

Chapter 8

Results and Discussion: Filltime Method with Improved $p + p$ Baseline

In this Chapter we use the $p + p$ analysis which includes event by event cuts to reduce the decay photon contribution as the baseline for the Au+Au comparisons. Both the $p + p$ analysis and Au+Au analysis in this chapter use the filltime method described in the Analysis Chapter to determine the fragmentation function variables instead of averaging over p_T bins. To make a fair comparison to models which follow the lost energy, such as BW-MLLA, the $\Delta\phi$ range was widened from the "head region" used previously to the full away-side, $|\Delta\phi - \pi| < \pi/2$. However, the results for the different angular ranges are statistically consistent.

8.1 $p + p$ Baseline

To improve the baseline $p + p$ measurement decay photons are removed on an event by event basis before applying a statistical subtraction. By improving the signal to background ratio before subtracting, the uncertainties in the measurement are reduced. Decay photons are removed via an isolation cut and a tagging method. These techniques are described in more detail in an earlier section but we review them briefly here. The isolation cut excludes photons that are surrounded by more than 10% of the photon's energy within a 0.3 rad cone. Trigger photons which can be paired with another photon in the event to produce an invariant mass which falls within the π^0 or η mass windows are also excluded from the inclusive sample. The correlations which result from applying these techniques are consistent with the pure statistical subtraction

method, as shown in Fig. 8.1. The underlying event was not subtracted from this data. The significance of the underlying event is illustrated by the dotted line in the plots. The underlying event starts to become significant for the lowest p_T^h bins. A systematic uncertainty was included to account for not subtracting the underlying event in the x_E distributions.
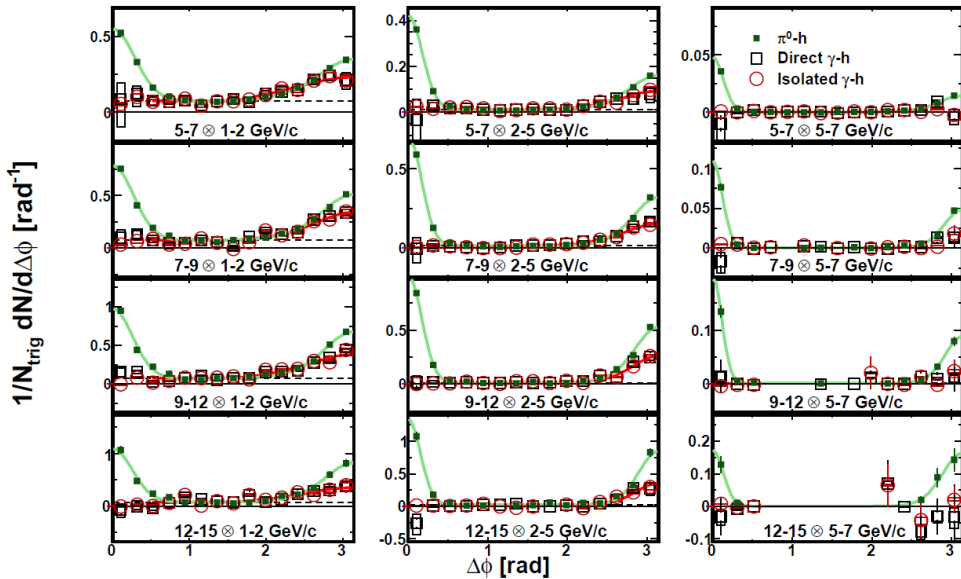
Figure 8.1: Per trigger yield as a function of $\Delta\phi$ for Run 5 and Run 6 p+p data combined. γ_{dir}-h via the statistical subtraction method and via the isolation and tagging cuts are plotted along with the π^0-h jet functions for comparison.

Several observations can be made directly from these plots. First, we note the absence of the near-side peak again in the $\gamma_{\mathrm{dir}} - h$ correlations, which is true by construction within the 0.3 cone for the isolated correlations. The peak is clearly evident for the π^0 triggered correlations since they come from a jet. The away-side yield for $\gamma_{\mathrm{dir}} - h$ is consistent for the different methods and is non-zero but is noticeably smaller than the π^0 case.

To measure the fragmentation function, the variable $x_E = \frac{-p_T^h \cos(\Delta\phi)}{p_{T\,trig}}$ was used to approximate z as was done in previous PHENIX measurements [18]. The yield on the away-side, $|\Delta\phi - \pi| < \pi/2$, is integrated and plotted as a function of x_E for the isolated γ_{dir}-h and π^0-h correlations in Fig. 8.2. The different trigger bins exhibit x_E scaling in both cases. The data are fit using a simple exponential function. The slope of the γ_{dir}-h distribution is $b = 8.2 \pm 0.3$ which is in excellent agreement with the slope of the quark fragmentation function, $b = 8.2$ and inconsistent with the slope for gluons, b=11.4 [18]. The

120
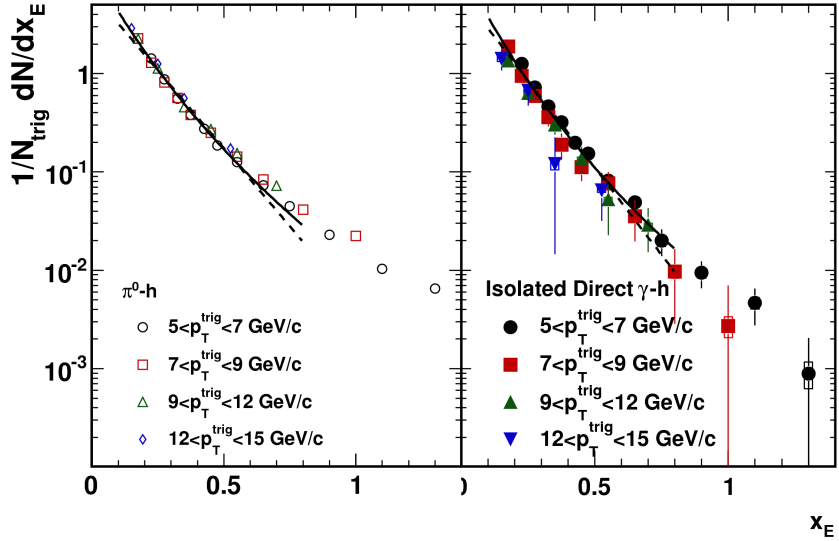
Figure 8.2: Direct photon-hadron yield as a function of x_E for the isolated direct photon-hadron $p + p$ measurement.

fit gives χ^2/DOF=48/26. The γ_{dir}-h distribution is slightly steeper than for π^0-h. The π^0s trigger on a mixture of quark and gluon jets, but they also trigger on higher momentum jets than the γ_{dir} triggers at the same p_T since the π^0 is a jet fragment and does not carry the full jet momentum.

An alternative way of plotting the fragmentation function is as a function of the variable ξ. This variable was introduced earlier in the text when discussing the BW-MLLA model and the e^+e^- data. The $\xi = -\ln(x_E)$ distribution for the $p + p$ γ_{dir}-h away-side yield is plotted in Fig. 8.3 and shows good agreement with the TASSO data. The TASSO distribution is the quark fragmentation function as measured from hadrons whose initial jet energy is known kinematically based on the collision energy. Since e^+e^- collisions with total energy, Q, result in di-jets of equal energy, the energy of each jet must be $Q/2$. Therefore, data from TASSO for 14 GeV collisions should be compared to our 7 GeV/c jets where we assume $p_T{}^\gamma \approx E_{jet}$. Because of the swing of the away-side jet along η and the limited η coverage in PHENIX, the TASSO points have been scaled down by an arbitrary factor of 10 [16]. The agreement between these measurements reaffirms the assertion that we are measuring the quark fragmentation function.

Since x_E scaling holds for triggers in the range, $5<p_T<15$ GeV/c, the distributions for the different trigger bins have been combined. Since we want

121
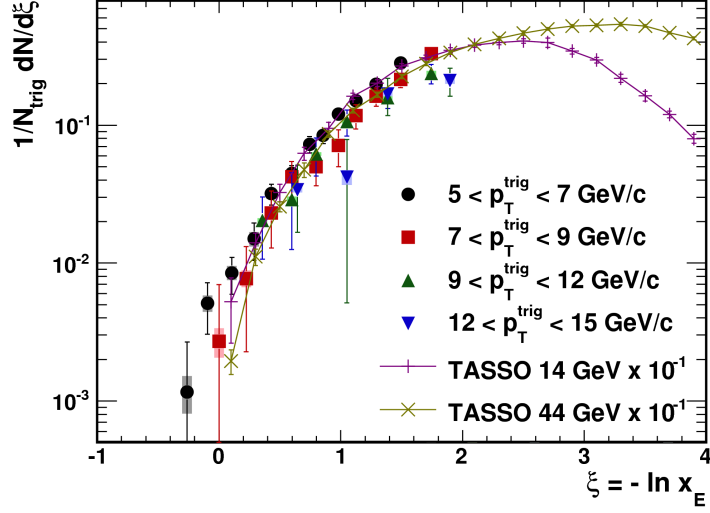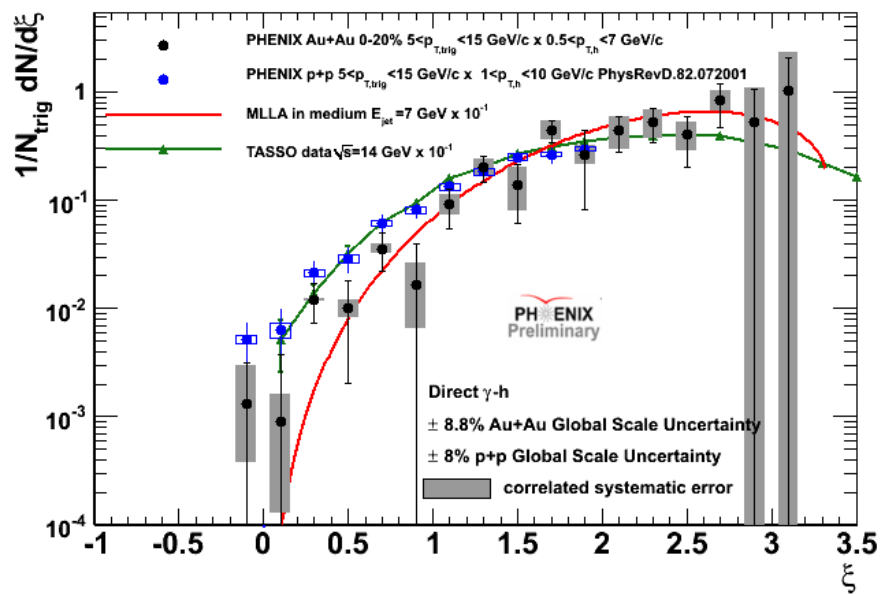
Figure 8.3: (Left) Direct photon-hadron yield as a function of x_E for the isolated direct photon-hadron $p + p$ measurement. (Right) $p + p$ yields vs. ξ compared to TASSO data scaled down by a factor of 10 [16].

this data as a baseline for the Au+Au studies, the data is also rebinned to match the ξ binning of the Au+Au analysis. The blue points in Fig. 8.4 are the rebinned and combined $p+p$ data from Fig. 8.3. The 14 GeV TASSO data is also included in Fig. 8.4 for comparison as connected green triangles.

8.2 Au+Au Results

The γ_{dir}-h ξ distribution was likewise measured using the fill time method for the Au+Au data from the 2007 RHIC Run. The combined ξ distribution for 5-15 GeV/c photon triggers and 0.5-7 GeV/c associated hadrons is shown in Fig. 8.4 as black points. The points at low ξ exhibit suppression compared to the blue $p+p$ data points. Moving toward higher ξ the suppression diminishes. This behavior is more clearly illustrated by the I_{AA} plotted in Fig. 8.5. The I_{AA} is the ratio of the yields from the black Au+Au points to the blue $p + p$ data from Fig. 8.4. The I_{AA} stops at $\xi = 1.8$ because the $p + p$ measurement was limited to hadrons with $p_T > 1$ GeV/c. However, to study the behavior at higher ξ the Au+Au data included hadrons with p_T as low as 0.5 GeV/c. Extending the $p + p$ is not trivial because as you recall no underlying event was subtracted in this analysis. However, if the hadron p_T is lowered to 0.5

Figure 8.4: ξ distribution for PHENIX Au+Au data (black circles) and $p + p$ data (blue circles) compared to the scaled TASSO data (green triangles) and MLLA in medium prediction (red line).

GeV/c the underlying event becomes significant and a subtraction is absolutely necessary. An extension of this $p + p$ analysis will be presented later after the change in the variable definitions, but first we propose an alternative approach to studying the implications of the Au+Au data.

Since the $p + p$ distribution agrees well with the TASSO data in the overlapping region, the TASSO distribution is used as a baseline for the higher ξ Au+Au points. The ratio of the PHENIX Au+Au and the TASSO e^+e^- data for similar jet energies is shown in Fig. 8.6. The suppression seen at low ξ in this ratio agrees with the linear fit to the I_{AA} from Fig. 8.5. The points at higher ξ appear to deviate from this flat line which indicates a shape change between the two measured fragmentation functions. This rise at the highest ξ also suggests an enhancement but, with the current uncertainties, is only a little more than a one sigma effect. It is important to note that one should interpret this ratio with caution, since k_T and other initial state effects, which are not present in e^+e^- collisions, could alter this distribution in hadronic collisions.

The red curve in Fig. 8.4 is based on a model [40] that uses the Modified Leading Logarithm Approximation and assumes that the energy that partons loose in the medium goes into soft particle production. Therefore, according to the model, one would expect to observe an enhancement at high ξ. Although the possible enhancement observed in the data is statistically limited, the model curve describes the data well with $\chi^2/NDF = 0.84$ which supports the idea that the energy lost at low ξ is redistributed to high ξ particles. However, we note that the model uses the collinear approximation which assumes $k_T = 0$.

8.3   A Change in Variables

To extend the $p + p$ baseline to include hadrons with p_T as low as 0.5 GeV/c, an underlying event must be subtracted. Because x_E depends on $\Delta\phi$, applying ZYAM to these distributions is not trivial since the underlying event shape would not be flat. The shape of the mixed event background is necessary. It is simpler to do a flat subtraction for the $z_T = p_T^{assoc}/p_T^{trig}$ distributions and define $\xi = -\ln(z_T)$. This ZYAM subtraction was explained with corresponding plots in Chapter 4. The relationship between the fragmentation function variables, $x_E \approx z_T \approx z$, was explored in Chapter 1 considering k_T effects. Although the distributions themselves differ for the different variables, the conclusions based on I_{AA} should be the same.
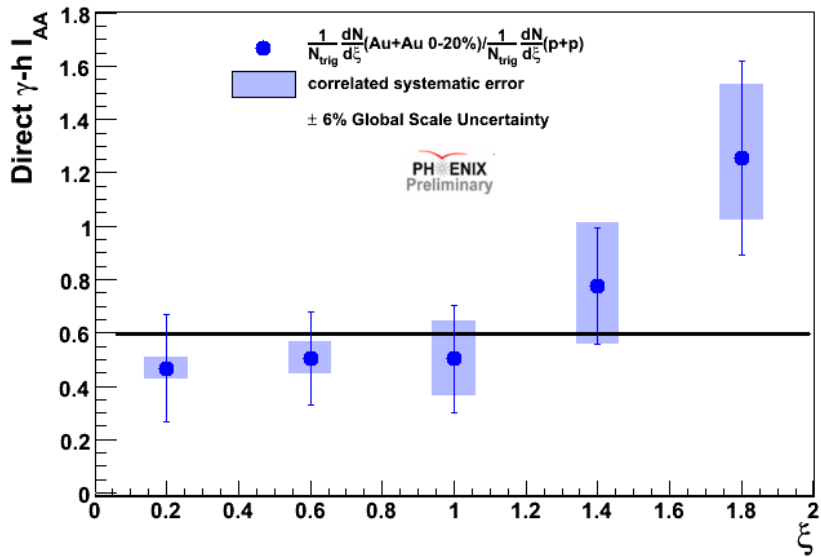
Figure 8.5: Direct photon-hadron I_{AA} using isolated $p+p$ measurement as the baseline for the Au+Au fit with a flat line.
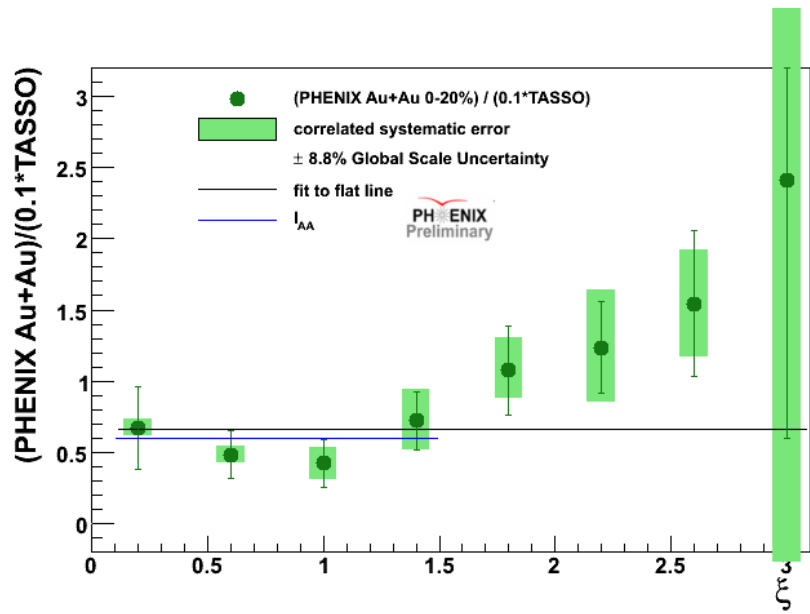
Figure 8.6: Ratio of Au+Au data to TASSO data scaled by a factor of 10. The black line is a fit to this ratio while the blue line is the fit to the I_{AA}.

8.3.1 z_T Space for the $p + p$ Baseline

The resulting $\gamma_{\text{dir}} - h$ yields integrated over the away-side, $|\pi - \Delta\phi| < \pi/2$, from the $p + p$ data are plotted for each trigger bin in Fig. 8.7 as a function of z_T and in Fig. 8.8 as a function of $\xi = -\ln(z_T)$ for $0.5\text{GeV}/c < p_T^h < 7$ GeV/c.
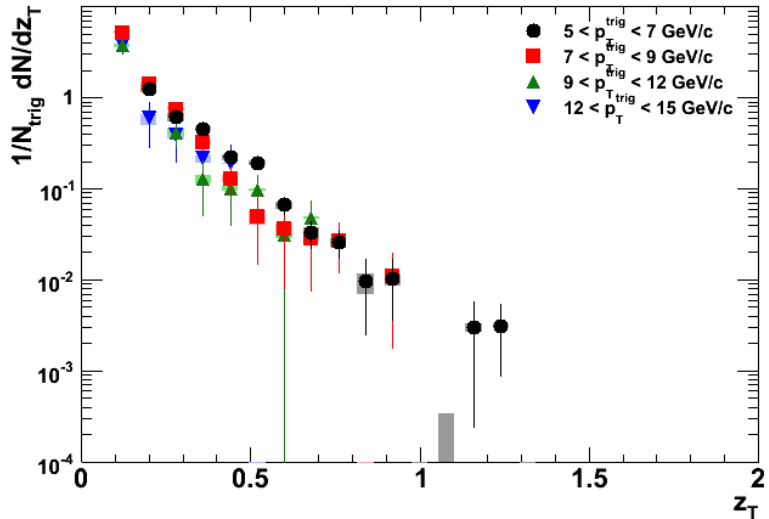
Figure 8.7: Yield vs z_T of the full away side in p+p for each trigger bin.

Since we have observed from this analysis that z_T scaling holds within the current uncertainties, over the present range of jet energies [16,17], the results for different $p_{T,trig}$ have been combined into one 5-12 GeV/c bin. The 12-15 GeV/c trigger bin is excluded from the combined result due to negative yields in the γ_{dec}-h measurements for the Au+Au data (which is not an issue when using x_E). Negative yields are possible in our measurement due to the flow subtraction and the direct photon extraction. However, negative yields are of course unphysical. The combined ξ distribution for $p + p$ is plotted in Fig. 8.9 along with the TASSO e^+e^- data for 7 GeV jets. Again we see good agreement between the two distributions for $\xi < 2$ but for $\xi > 2$ the $p + p$ data are above the e^+e^- distribution. This could be attributed to k_T effects which exist in $p + p$ but not in e^+e^- collisions.

The combined z_T distribution for 5-12 GeV/c triggers are plotted as solid points Fig. 8.10. Note that the yield above $z_T > 1$ is non zero. At LO, $z_T > 1$ is impossible since the momentum of the hadron cannot be greater than the jet momentum. However, because of the possible imbalance between the jet and direct photon momentum due to k_T and the possible influence of fragmentation
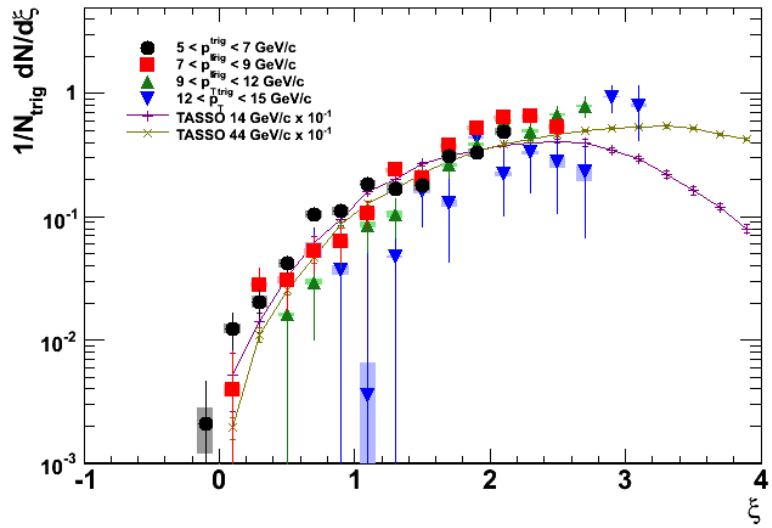
Figure 8.8: Yield vs $\xi = -\ln(z_T)$ of the full away side in p+p for each trigger bin.
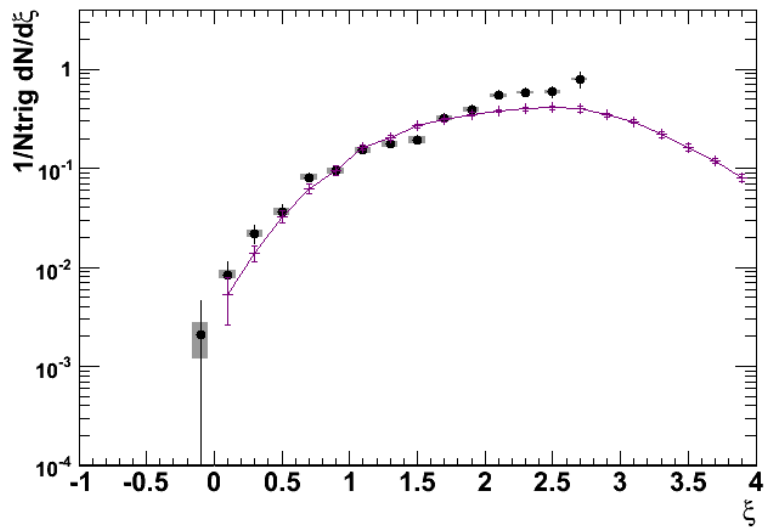
Figure 8.9: Yield vs $\xi = -\ln(z_T)$ of the full away side in p+p for the 5-12GeV/c trigger bins combined.

photons, the direct photon p_T may be less than the opposing jet p_T making $p_{Th} > p_{T\gamma}$, and therefore $z_T > 1$, kinematically possible. Although the z_T and ξ distributions shown here have been binned as a function of the variable being plotted, they are a simple mathematical transformation of the one another. As a consistency check, the data in Fig. 8.9 is transformed into a z_T distribution and plotted as open circles in Fig. 8.10. The two distributions agree well, while the binning in the ξ distribution allows us to look more closely at the low z particles.
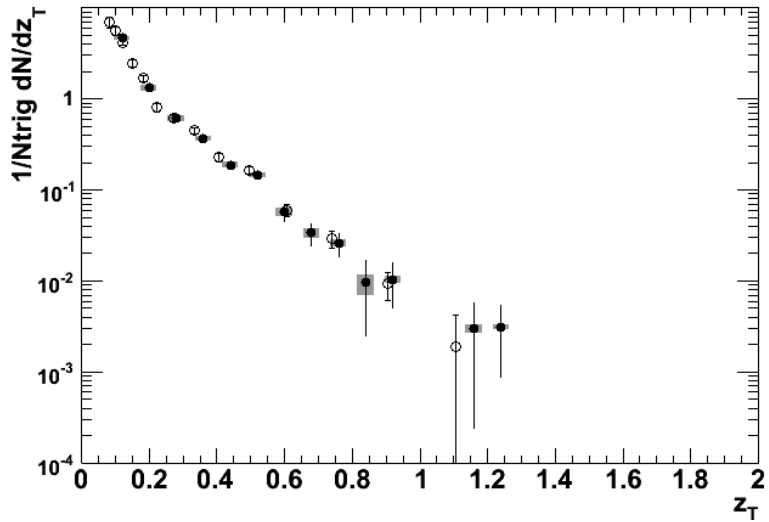
Figure 8.10: Yield vs z_T of the full away side in p+p for the 5-12GeV/c trigger bins combined. The data in figure8.9 is also transformed into a z_T distribution and plotted as open circles.

8.3.2 Comparison to Au+Au

First, the jet fragmentation function, $D(z_T)$, of the associated hadrons for Au+Au and $p+p$ are plotted as a function of z_T in Figure 8.11, as black circles and blue squares respectively. The statistical error bars include the uncorrelated systematic uncertainty from the background subtraction while the boxes around the points show the correlated uncertainties. There is an additional $\pm 8\%$ and $\pm 8.8\%$ global uncertainty on the $p+p$ and Au+Au yields respectively which is not depicted.

These distributions are fit with a simple exponential function, Ne^{-bz_T}. The slope of the $p+p$ distribution, $b = 8.26 \pm 0.33$, is consistent with that of quark
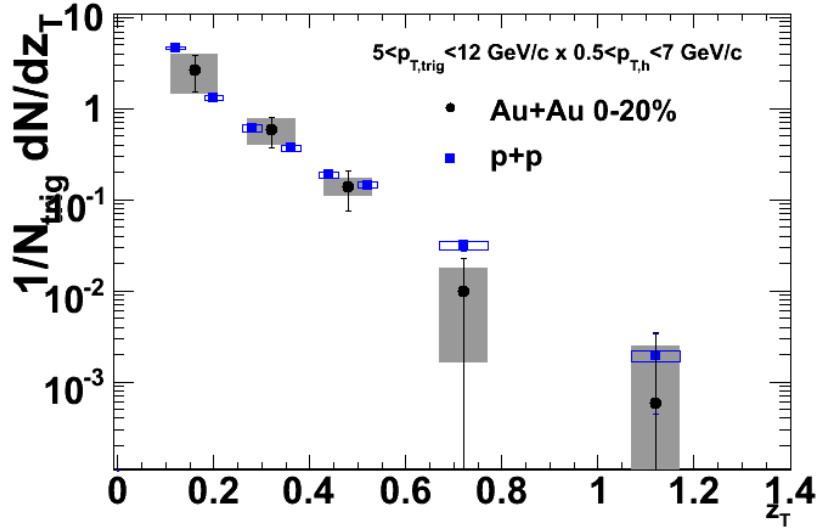
Figure 8.11: Per trigger yield as a function of z_T for $p+p$ collisions (blue) and Au+Au collisions (black).

fragmentation and previous measurements [16]. The Au+Au distribution gives $b = 9.62 \pm 1.49$ which is somewhat steeper than the $p+p$ baseline, suggesting modification to the shape of the fragmentation function, although still consistent within the current uncertainties. As quark energy loss is an established fact, an identical slope would indicate constant energy loss over all parton p_T. This would result in a shift of the spectrum such that the yield is suppressed yet the slope is preserved.

To search for the lost energy we would like to study the trend at lower z_T, which is also interesting because different descriptions of energy loss diverge at low z_T. Again, to focus on low z_T, we use an alternative variable, $\xi = -ln(z_T)$. The information at low z_T translates to high ξ. The per trigger yield as a function of ξ is plotted in the top panel of Figure 8.12. The 0-20% most central Au+Au data are the black circles, while the blue squares are from $p+p$. Also shown is the fragmentation function measured in e^+e^- collisions by the TASSO collaboration in green triangles [7]. While the jet fragmentation in e^+e^- and $p+p$ collisions should be the same, experimental measurement of correlations are affected by non-zero k_T in the proton. Consequently, the z_T distributions may differ even if the fragmentation function does not.

The red curve is the prediction from the BW-MLLA model for 7 GeV jets in medium [40], which can be compared to the Au+Au data. Both the TASSO measurements and the model prediction have been arbitrarily scaled by a factor
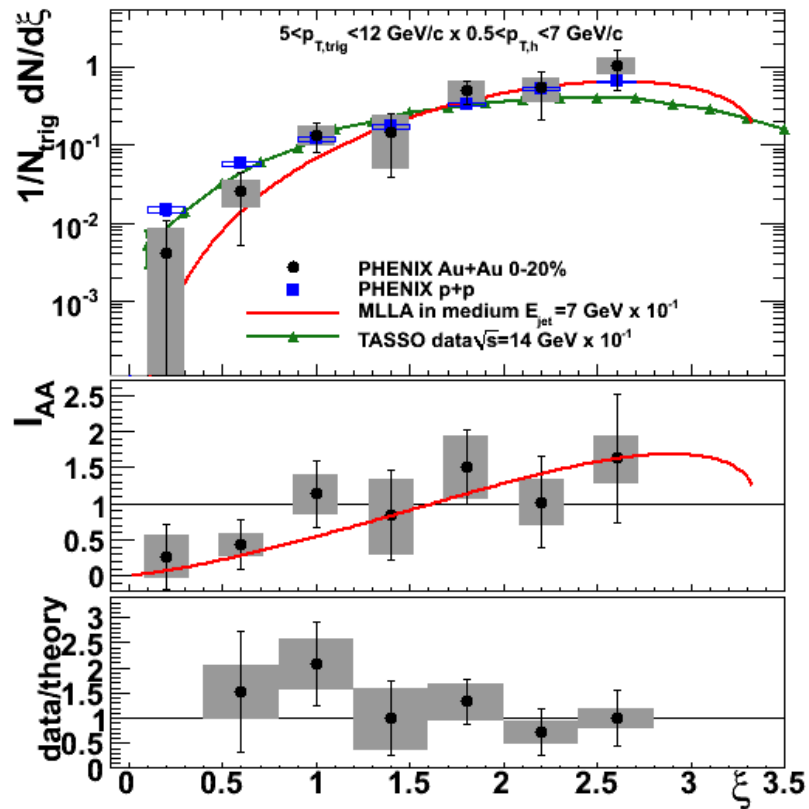
Figure 8.12: The top panel shows the $dN/d\xi$ distribution as a function of ξ for Au+Au and $p+p$ collisions as well as the TASSO measurement and BW-MLLA prediction. The middle panel is I_{AA} or the ratio of the yield in Au+Au to that in p+ and the red curve is the BW-MLLA prediction for I_{AA}. The bottom panel shows the ratio of the measured I_{AA} from the middle panel over the BW-MLLA curve.

of 10 to approximately account for the limited PHENIX η acceptance, as was done in [16]. We note, that BW-MLLA and many other theoretical calculations of energy loss use the collinear approximation, thus assuming that k_T=0.

To best quantify the modification between the measured fragmentation functions, we take a ratio of the distributions and measure I_{AA}. I_{AA} from these data is plotted as black points in the middle panel of Figure 8.12. This ratio is not flat, since a fit to a line gives a slope of $0.52 \pm 0.23 \pm 0.09$ and $\chi^2/NDF = 2.3/5$ while a flat line fit gives a poorer, although not terrible, $\chi^2/NDF = 7.4/6$. I_{AA} increases toward high ξ (low z_T). A flat line fit to the data below $\xi = 1.6$ gives an $I_{AA} = 0.60 \pm 0.22$ while above $\xi = 1.6$, $I_{AA} = 1.31 \pm 0.35$. This implies that the I_{AA} is not constant over the whole z_T range. These fits illustrate the suppression observed at low ξ and possible enhancement at high ξ, although the I_{AA} at high ξ is still consistent with 1. As discussed in Chapter 5, excluding the v_3 term from the flow subtraction can enhance the away-side yield. However, the study done for this centrality resulted in less than a 1% difference in the final yield, which would make no difference to any of these calculations.

In order to avoid confusion from effects of parton k_T in nucleons and nuclei and the arbitrary scale factor, we compare I_{AA} rather than dN/dz_T distributions between theory and experiment. As k_T in nuclei has been observed to be similar to that in nucleons [59] (although a system size dependence was observed at lower energies [60–62]), such effects cancel in the ratio of Au+Au to $p + p$. The red curve shows I_{AA} calculated from the model predictions for the in-medium and vacuum cases. The vacuum calculation agrees well with the measured ξ distribution in e^+e^- [40]. Both the I_{AA} from data and the theory curve show suppression at low ξ or high z_T. This is expected as the partons lose energy in Au+Au. I_{AA} increases with increasing ξ. In the model, this is due to energy loss at low ξ being redistributed by enhanced gluon splitting functions to lower momentum particles. The data indicate enhancement consistent with predictions of the theory, although the error bars are large. It should be noted that to further study systematics, the azimuthal angle range for integration of associated hadrons was also studied and that substantially reducing the range, can change the rising trend but still be within the quoted uncertainties.

The agreement between the data and theory is quantified by the ratio shown in the bottom panel of Figure 8.12. The model and data should not be compared near $\xi = 0$ ($z_T = 1$) since the model forces the yield there to be zero, though for $\gamma_{\mathrm{dir}} - h$ the p_{T_γ} can underestimate the opposing parton energy. Even in the $p + p$ case, the yield above $z_T = 1$ is not zero [16].

This is the first indications that the lost energy at high z_T is recovered at

low z_T for $\gamma_{\text{dir}} - h$ correlations. According to the above described studies, the deviation from a constant I_{AA} is a little more than a 1σ effect. This indicates a difference in the observed fragmentation functions between the two collision systems. However, the enhancement observed is not statistically significant. Improved statistical precision is required to confirm this enhancement and quantify the change in the shape of the distribution.

8.4 Incorporating the 20-40% Data

One way to improve the statistics of this measurement is to widen the centrality range and combine the statistics in the 0-20% and 20-40% bins. Because of the significant centrality dependence of v_2 and the background level, the centralities are not combined until the jet function stage. The γ_{inc}-h and γ_{dec}-h jet functions are each combined to form 0-40% jet functions and then propagated through the statistical subtraction equation. Recall that the third ingredient in the subtraction is R_γ. The R_γ value for 0-40% was calculated by weighting the 0-20% and 20-40% by the number of inclusive triggers, the same procedure used to combine the centrality bins from the original measurement into our analysis bins. By combining the centrality bins at this stage as opposed to the γ_{dir}-h yields, not only is the statistical uncertainty in the jet functions reduced, but also the statistical uncertainty in the R_γ is reduced. which in turn reduces the systematic uncertainties.

First, a plot of the 20-40% data is shown in Fig. 8.13. All the I_{AA} points are consistent with unity within errors. However, the central values exhibit a similiar trend to that observed in the 0-20% bin, i.e. $I_{AA} < 1$ for $\xi < 1.2$ and $I_{AA} > 1$ for $\xi > 1.2$ with the exception of the highest ξ point. The similar yields and I_{AA} indicate that the physics being probed in these two different centrality bins is similar. Also note that the π^0 supression is also similar for these centralities [55].

The combined 0-40% result is plotted in Fig. 8.14. Qualitatively, the data looks smoother, particulary when looking at the ratios. For $1.6 < \xi < 2.8$, $I_{AA} = 1.56 \pm 0.24 (stat) \pm 0.31 (sys)$ which is approximately 1.3σ above $I_{AA} = 1$. Fitting the data to a line, mx+b, gives a slope, $m = 0.62 \pm 0.20 (stat) \pm 0.06 (sys)$ which is about 3σ above zero. This indicates that the I_{AA} is not flat over this entire ξ range. Although the linear fit by eye does not describe the shape of data well, it gives an excellent $\chi^2/NDF = 1.1/5$ as opposed to the with $\chi^2/NDF = 10.9/6$ for a flat line. This deviation from flat indicates that the measured fragmenation function for Au+Au collisions is modified compared to the $p + p$ baseline. This is the first measurement of a modified fragmentation function via the $\gamma_{\text{dir}} - h$ channel. Previous measurements of
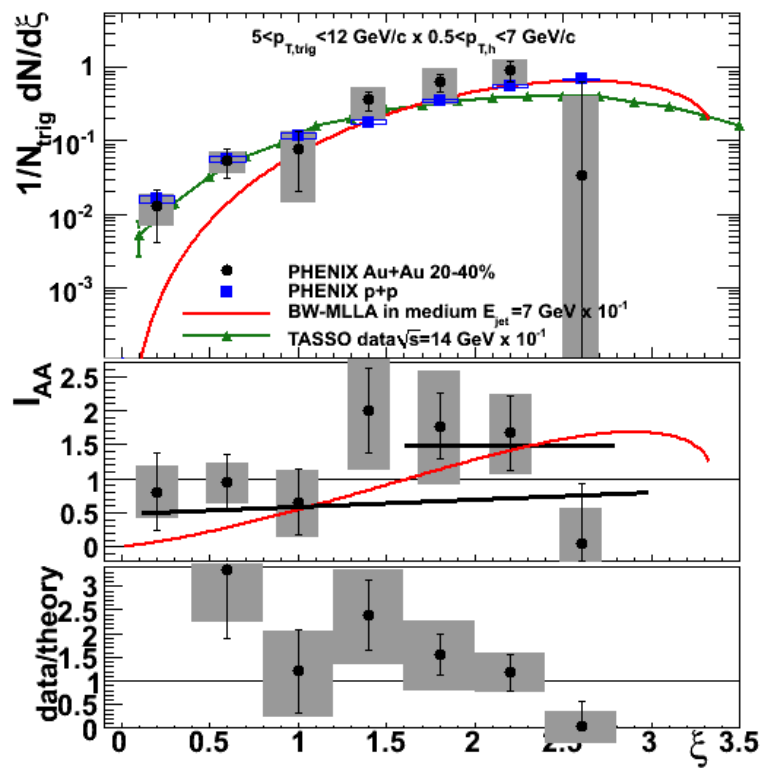
Figure 8.13: The 20-40% Au+Au data compared to the isolated p+p baseline, TASSO data and BW-MLLA prediction.

$\gamma_{\mathrm{dir}} - h$ I_{AA}, which are more limited in z_T, are all consistant with flat [17, 41].

The ratio of the I_{AA} from data to the I_{AA} from the BW-MLLA model is plotted in the bottom panel of the figure. Although the ratio is consistent with one, by eye one sees a trend in the ratio. The ratio sits at almost exactly one for $\xi = 2.6$ and then steadily increases moving toward lower ξ. There is a mismatch in centrality, since the model was tuned to match the suppression in the PHENIX π^0 R_{AA} for 0-10% central events but recall that the R_{AA} for 20-40% shows a similar level of suppression [55]. This discrepancy between the data and theory could also be due to the fact that the yield at $\xi = 0$ is forced to zero in the model which is not true in the data.
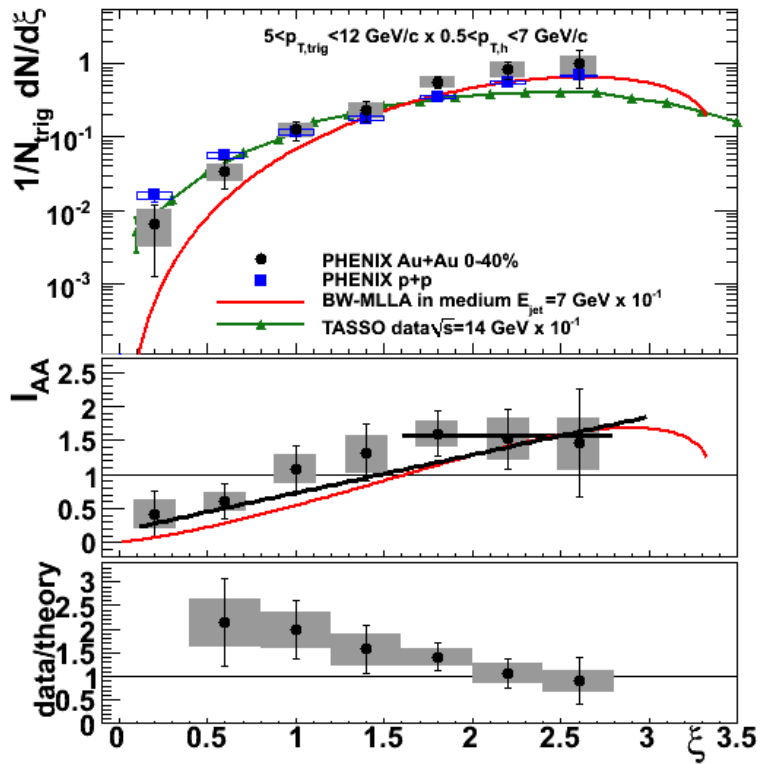
Figure 8.14: The 0-40% Au+Au data compared to the isolated p+p baseline, TASSO data and BW-MLLA prediction.

YAJEM, as discussed in Chapter 1, is another energy loss model which redistributes the lost energy to an increase of soft particle production. One appealing aspect of YAJEM over the BW-MLLA model is that the YAJEM calculation is done specifically for $\gamma_{\mathrm{dir}} - h$ correlation measurements which means $\xi < 0$ is kinematically possible in both the data and theory. A comparison of the YAJEM prediction for 5-7 GeV/c photon triggers to the 0-40% I_{AA}

is shown in Fig. 8.15. We note that the YAJEM curve is for a slightly different photon p_T range and different $\Delta\phi$ away-side integration range from the data. However, the trigger photon momentum makes little difference to the YAJEM prediction as evident in Fig. 1.23. Since the radiated gluons which results in the increase of soft particles is collinear in the model the angular cutoff is not expected to significantly alter the prediction [63]. The YAJEM curve is excellent agreement with the data giving $\chi^2/NDF = 2.9/7$. The ratio of the data to the curve is plotted in the bottom panel. Even though the YAJEM curve is calculated for collisions with an average impact parameter, $b = 2.4$, which also corresponds to the most central 0-5% Au+Au data, this ratio is more consistent with unity than the ratio between BW-MLLA and the data. To see how the two models compare, the I_{AA} from the BW-MLLA calculations is also plotted in the top panel of Fig. 8.15.
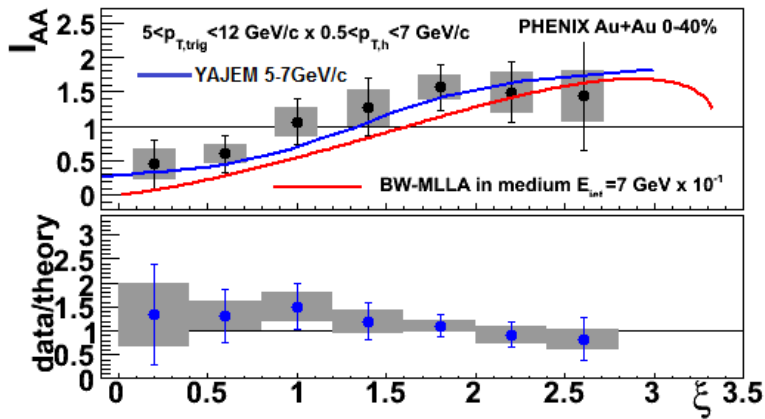
Figure 8.15: Comparison between the 0-40% Au+Au I_{AA} to the YAJEM curve for 5-7 GeV/c trigger photons. The I_{AA} values are plotted in the top panel and the ratio between the data and the YAJEM curve is plotted in the bottom panel. The BW-MLLA curve (red) is also plotted for comparison between models in the top panel.

By combining the jet functions into the 0-40% bin, we hoped to recover the 12-15GeV/c. However, including the limited statistics of this trigger bin does not make a significant difference in the results. The 12-15 GeV/c data dips down at $\xi = 2.6$ which slightly reduces the potential enhancement from $I_{AA} = 1.56$ to $I_{AA} = 1.51$. Although widening the centrality bin analyzed improved the significance of this measurement, more statistics are clearly needed to precisely describe the level of enhancement, if any, and the altered fragmentation function shape observed.

8.5 Measuring k_T

As discussed previously, the k_T effect smears the angular correlation between the direct photon trigger and the opposing jet axis, and can create an imbalance between the photon momentum and the opposing jet momentum. The measurements we make of the fragmentation function rely on $p_{T\gamma} \approx p_{Tjet}$. Although the agreement between the $p + p$ measurements and expected quark fragmentation function suggests that the smearing effects of k_T must be small compared to the jet energy, it is useful to quantify the value of k_T. In this section, the PHENIX $\gamma_{\mathrm{dir}} - h$ k_T measurements in $p + p$ from [11, 16] are summarized followed by introductory work on a similar measurement for Au+Au.

8.5.1 p_{out} in $p + p$

Recall that p_{out} is the component of the jet momentum transverse to the trigger axis and is defined as $p_{out} = p_{Th} \sin \Delta\phi$. If $k_T = 0$, then p_{out} would only depend on the fragmentation vector, j_T. By measuring p_{out} we have an approximate measure of the k_T broadening effect and can infer a value of k_T via a Monte Carlo simulation. The p_{out} distribution shown in Fig. 8.16 is filled while passing over the $p + p$ data directly, in the same way that the x_E and ξ distributions were constructed. The p_{out} distribution from the $\gamma_{\mathrm{dir}} - h$ and $\pi^0 - h$ correlations are plotted as solid and open symbols respectively. The lines are Gaussian fits to the data. The fits describe the $\pi^0 - h$ data well at small p_{out} values but the data deviate from the fit for larger p_{out} values. This has been observed previously in PHENIX data [18] and is believed to be related to the emission of a single gluon. For the $\gamma_{\mathrm{dir}} - h$ data, the Gaussian fits also work well at low p_{out} but not as well for large p_{out}. The statistically limited measurement in this range, makes it difficult to say if this appears to be the same effect as observed in the $\pi^0 - h$ case.

To determine the spread of the away-side jet due to k_T, we actually want to measure the R.M.S., $\sqrt{\langle p_{out}^2 \rangle}$, of the p_{out} distribution. This can, of course, be calculated directly from the measured p_{out} distributions. Alternatively, it can be calculated from a fit to the $\Delta\phi$ correlations according to Eqn. 8.1 as was done in [18].

$$\frac{dN_{\mathrm{real}}}{d\Delta\phi} = \frac{1}{N}\frac{dN_{\mathrm{mix}}}{d\Delta\phi} \cdot \left(C_0 + C_1 \cdot e^{-\Delta\phi^2/2\sigma_{\mathrm{near}}^2} + C_2 \cdot \frac{dN_{\mathrm{far}}}{d\Delta\phi}\bigg|_{\pi/2}^{3\pi/2} \right) \qquad (8.1)$$

was fit to the the away-side of the correlations where
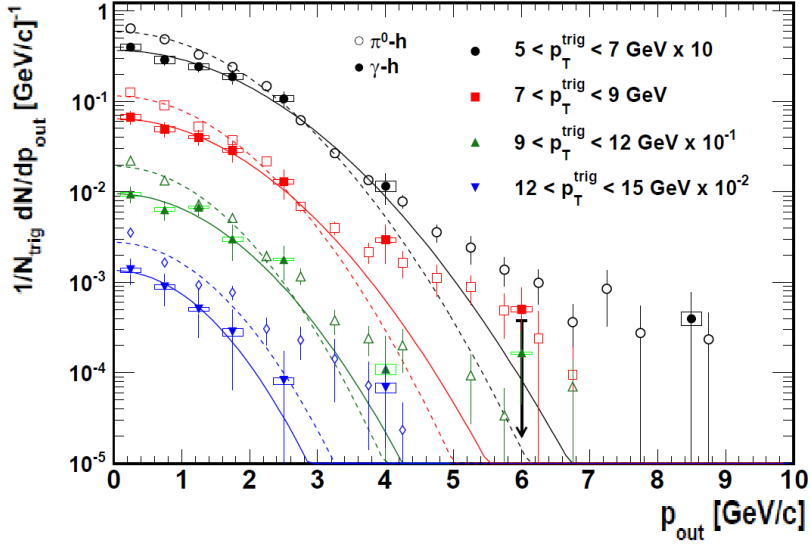
Figure 8.16: The p_{out} distributions for different trigger p_T bins in $p + p$ collisions for $\gamma_{\text{dir}} - h$ and $\pi^0 - h$ correlations [16].

$$\left.\frac{dN_{\text{far}}}{d\Delta\phi}\right|_{\pi/2}^{3\pi/2} = \frac{-p_T^{\text{assoc}}\cos\Delta\phi}{\sqrt{2\pi\langle p_{\text{out}}^2\rangle}\,Erf\left(\sqrt{2}p_T^{\text{assoc}}/\sqrt{\langle p_{\text{out}}^2\rangle}\right)}e^{\left(-\frac{|p_T^{\text{assoc}}|^2\sin^2\Delta\phi}{2\langle p_{\text{out}}^2\rangle}\right)}. \qquad (8.2)$$

The RMS resulting from these fits to the correlation functions are plotted in Fig. 8.17 as a function of trigger p_T for both $\pi^0 - h$ and $\gamma_{\text{dir}} - h$. The plot shows that the p_{out} width decreases with increasing jet momentum. The $\pi^0 - h$ widths are all smaller than the isolated $\gamma_{\text{dir}} - h$ widths, which is reasonable since the π^0 actually triggers on a higher momentum jet.

To extract a value of k_T from the $p + p$ correlation measurements in [16], a LO model with k_T smearing was used similar to [18]. The resulting k_T values from both $\pi^0 - h$ and $\gamma_{\text{dir}} - h$ are shown in Fig. 8.18 from [16]. Also included in the plot are data from previous PHENIX $\pi^0 - h$ measurements [18]. All data points are consistent and give $k_T \approx 3$ GeV/c. This is large compared to theoretical expectations of an intrinsic k_T value near 300 MeV. However, recall that the k_T in these measurements encompasses NLO effects as well as the theoretically defined intrinsic k_T.
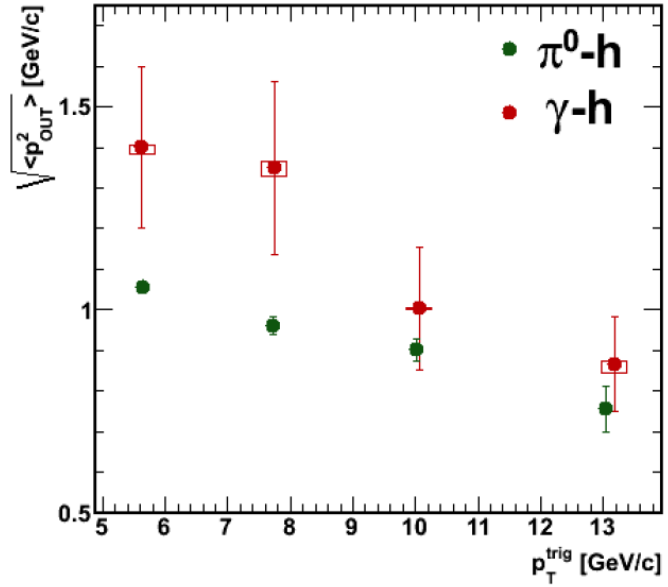
Figure 8.17: The p_{out} RMS for different trigger p_T bins in $p+p$ collisions for $\gamma_{\mathrm{dir}} - h$ and $\pi^0 - h$ correlations [16].
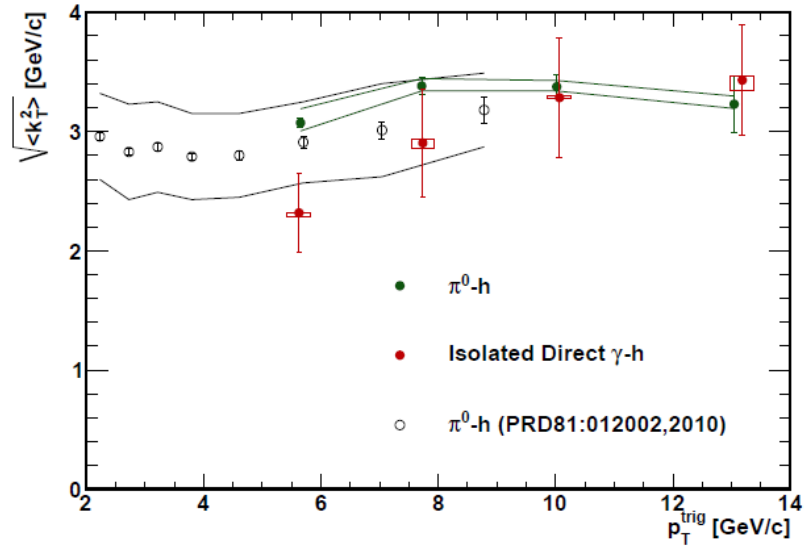
Figure 8.18: The k_T for different trigger p_T bins in $p+p$ collisions for $\gamma_{\mathrm{dir}} - h$ and $\pi^0 - h$ correlations [16]. These values of k_T agree well with previous PHENIX $\pi^0 - h$ measurements [18].

8.5.2 p_{out} in Au+Au

Based on the system size, one may expect the k_T, and therefore p_{out} distribution, to be different between $p+p$ and Au+Au collisions. Such a system size dependence was observed for collisions at low $\sqrt{s}$ [60–62]. However, PHENIX, for higher $\sqrt{s}$ collisions observed k_T in nuclei to be similar to that in nucleons based on comparisons of d+Au and $p+p$ data [59]. A similar measurement in Au+Au data would be useful for understanding if any system size dependence exists for higher energy collisions and the effect the medium has on the jet width. Consequently, the p_{out} distribution is measured with $\gamma_{\mathrm{dir}} - h$ correlations in 0-20% central Au+Au events for various trigger p_T bins. The p_{out} distributions for $\pi^0 - h$ and $\gamma_{\mathrm{dir}} - h$ correlations are plotted in Figures 8.19 and 8.20 respectively. The distributions measured in Au+Au are directly compared to the distributions from $p+p$. The hadron p_T ranges included in these distributions differ slightly and are 1-10Gev/c for $p+p$ and 1-7 GeV/c in Au+Au. Despite that difference, the distributions for the $\gamma_{\mathrm{dir}} - h$ seem to agree rather well between Au+Au and $p+p$ except in the $p_T^{trig} = 5-7$ GeV/c plots. Differences are clearly evident in the $\pi^0 - h$ measurements. Another strange feature in the Au+Au plots is a dip in the lowest p_{out} bin, which is present in nearly all the plots. This is not well understood yet and could be the result of medium response. For example a dip could form if the yield in the previously discussed shoulder regions of $\Delta\phi$ are enhancement compared to the suppressed yield of the head region. The overall enhancement in the Au+Au distributions at lower p_{out} may be result of the increased soft production that we discussed in the ξ distributions. These features warrant further investigation, but this study provides an interesting first look at the p_{out} distributions in Au+Au.

The p_{out} RMS determined in the previous section for $p+p$ used fits to the correlation functions. However, due to the complicated underlying event and modified away-side jet peak, this method cannot be used to extract the p_{out} RMS from the Au+Au data. Therefore, the $\sqrt{\langle p_{out}^2 \rangle}$ is determined directly from the p_{out} distributions according to Eqn 8.3.

$$\sqrt{\langle p_{out}^2 \rangle} = \sqrt{\langle p_{out} \rangle^2 + \delta(p_{out})^2} \tag{8.3}$$

To avoid any possible influence the alternate method may have, the $p+p$ RMS was also calculated the same way. The $\sqrt{\langle p_{out}^2 \rangle}$ for the $\gamma_{\mathrm{dir}} - h$ correlations from both collision species are plotted as a function of trigger p_T in Fig. 8.21. The data above 7 GeV/c are consistent for the two collision systems indicating a similar k_T value. The lowest trigger p_T point, however, results in a smaller width for Au+Au. This would imply a smaller k_T. However, this difference
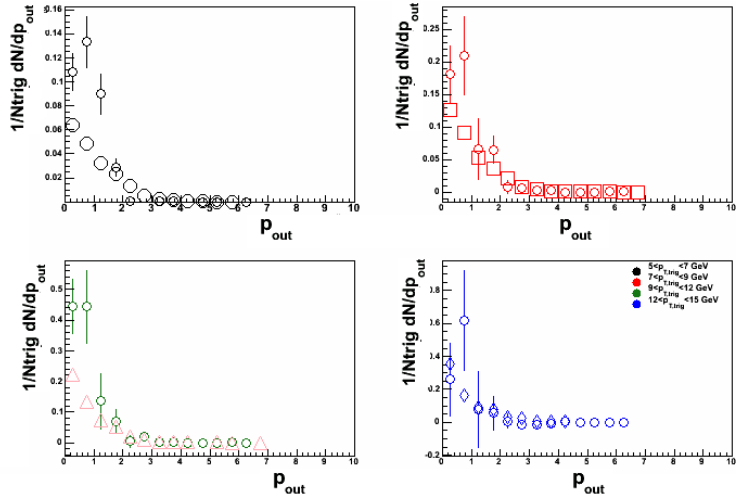
Figure 8.19: p_{out} for the different π^0 trigger p_T bins.
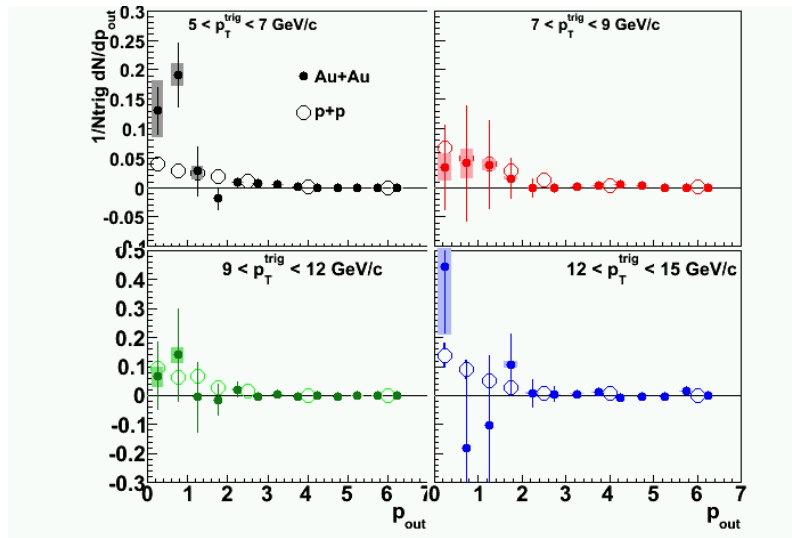
Figure 8.20: p_{out} for the various direct photon trigger p_T bins compared to the same measurement with the p+p data.

originates from the enhancement observed in the p_{out} distributions. If these low momentum particles are due to the response of the medium and not from the fragmentation process, our interpretation of these data on k_T may be misplaced. It is also important to understand how varying the lower limit of the hadron p_T influences the results. Studies beyond the scope of this thesis are warranted, particularly with the higher statistics data sets. However, the framework necessary for these studies has been established.
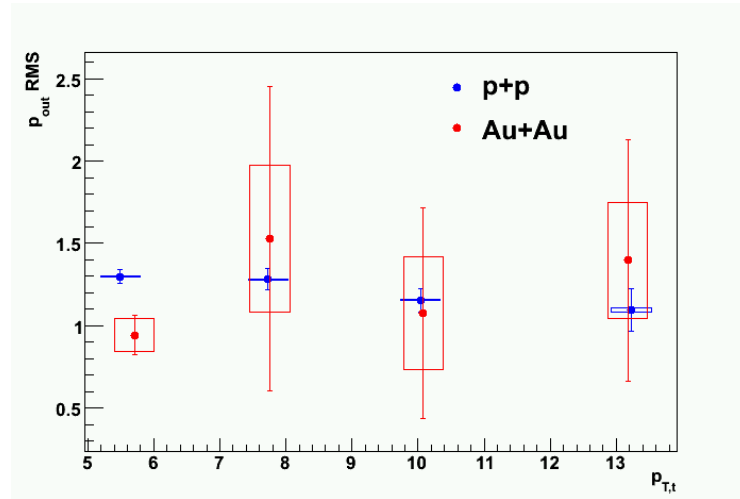
Figure 8.21: $\sqrt{\langle p_{out}^2 \rangle}$ for the various trigger bins.

Chapter 9

Conclusions

9.1 Summary of $p + p$ Results

Results from the $p + p$ analysis with and without event by event cuts to remove the decay background were presented and their consistency was demonstrated. The improvement to the uncertainties due to these additional techniques is clear. Although they really apply to both cases, the conclusions drawn here refer specifically to the latest results with the isolation and tagging cuts applied.

The γ_{dir}-h measurements from $p + p$ collisions confirm that the opposing jet is predominately from quark jets and that the away-side yield can be used to measure the quark fragmentation function. This is consistent with the expectation that the Compton scattering diagram is the dominant production process of direct photons at RHIC. This was demonstrated with several observables. First the slope of the x_E distribution, $b = 8.2 \pm 0.3$, agrees well with the expected quark fragmentation function slope, $b = 8.2$. The ξ distribution agrees well with the shape of the TASSO quark fragmentation function measurement with the exception of high ξ. The slight difference in the measured fragmentation function could be due to k_T effects in the $p + p$ data which do not exist in $e^+ e^-$ collisions.

The k_T was also determined from γ_{dir}-h measurements in $p + p$ collisions, by fitting the dependence of the width of the p_{out} distribution as a function of trigger p_T with a LO plus Gaussian k_T smearing model. The fits indicate a k_T of about 3 GeV/c which is consistent with previous PHENIX measurements of k_T. It is important to understand how k_T can smear the relationship between the trigger photon momentum and opposing jet momentum. It is reasonable not to be concerned for momenta much higher than k_T. However, caution should be applied for interpreting measurements for jet momenta near k_T. This

measurement is useful as a baseline for, and helps motivate, the investigation of the effect of k_T in heavy ion collisions. Without an independent measurement of k_T in Au+Au, we must assume a similar value of k_T and the effects of k_T on the measured distributions cancel in the ratios between Au+Au and $p + p$ measurements.

We also note that the p_{out} distributions from this analysis can be used by theorists to test TMD factorization [64].

9.2   Summary from the p_T Binned Results

Suppression has been observed on the away-side of the $\gamma_{\mathrm{dir}} - h$ channel in $Au + Au$ collisions at 200 GeV. This suppression is remarkably consistent with the suppression measured in the $\pi^0 - h$ correlations. The z_T distributions shown suggest a steeper slope in $Au + Au$, 9.49 ± 1.37, compared to the slope, 6.89 ± 0.64, measured in $p + p$ collisions. Preliminary measurements of the nearside show no evidence of enhancement in $Au + Au$ compared to $p + p$. With increased statistics and extended kinematic reach, experimental results of $\gamma_{\mathrm{dir}} - h$ are moving toward precision measurements of energy loss.

This suppression is compared to the suppression measured in $\pi^0 - h$ in Fig. 7.6 for three different trigger p_T bins. With the possible exception of the lowest and highest z_T points, the I_{AA} of $\gamma_{\mathrm{dir}} - h$ and $\pi^0 - h$ are remarkably consistent. This is surprising since $\pi^0 - h$ should include more gluon jets, which are more suppressed. On the other hand, $\pi^0 - h$ suffers a surface bias, which reduces the observed suppression for per trigger yields, while $\gamma_{\mathrm{dir}} - h$ does not suffer such bias, since the γ_{dir} trigger is not suppressed by the medium. Perhaps competing effects wash each other out. In a simpler picture, one could argue that the medium has an opaque core, which causes the γ_{dir}-h yield to be surface emission and the π^0-h I_{AA} is so surface biased that the energy loss difference between gluon and quark jets is irrelevant because of the small path length. However, a black core scenario is unlikely, taken in the context of other energy loss measurements such as di-hadron correlations with respect to the reaction plane [32].

9.3   Summary from the Filltime Method

The fragmentation function was measured in both $p+p$ and Au+Au collisions using direct photon-hadron correlations at PHENIX. Isolated $\gamma_{\mathrm{dir}} - h$ correlations reduce the uncertainty in the $p+p$ baseline for the Au+Au measurement. The $p + p$ fragmentation function is consistent with quark fragmentation ex-

pectations. Suppression has been observed in Au+Au compared to $p+p$ which results in an average $I_{AA} = 0.6 \pm 0.1$. Although the points at low ξ exhibit constant suppression, a rise in I_{AA} may be observed toward higher ξ. To investigate this beyond the current $p+p$ analysis, the ratio between the Au+Au and e^+e^- collisions from TASSO is also measured and indicates that the shape of the measured fragmentation functions is different for the two collision systems and suggests a possible enhancement at the highest ξ values. An important caveat in using the TASSO data as a baseline is the presence of k_T effects in Au+Au collisions which do not exist in e^+e^- collisions. These features warrant further studies and an extension of the $p+p$ analysis. Additional data collected in the 2010 and 2011 Au+Au runs will also improve the statistical precision of this measurement.

In the meantime, the $p+p$ analysis is extended to include hadrons with 0.5 GeV/c < p_T^h < 7 GeV/c and the Au+Au centrality bin is widened to 0-40%, which results in clear evidence for medium modification of jet fragmentation in direct photon-hadron correlations. The slope of the fragmentation function is steeper in Au+Au, but perhaps consistent within errors, to the $p+p$. The ratio of Au+Au to $p+p$ yields, I_{AA}, indicates that particles are depleted at low ξ or high momentum fraction, z, due to energy loss of quarks traversing the medium. The measured I_{AA} exhibits an increasing trend toward high ξ and suggests that the medium enhances production of soft particles in parton fragmentation. This is consistent with the BW-MLLA and YAJEM calculations, which redistribute the energy loss at high z to an enhancement at low z. The slope, $m = 0.62 \pm 0.20(stat) \pm 0.06(sys)$, of the I_{AA} for a linear fit is approximately 3σ away from flat indicating a clear change in shape between the fragmentation functions. The enhancement of $I_{AA} = 1.56 \pm 0.24(stat) \pm 0.31(sys)$ for $\xi > 1.6$ is about a 1σ effect.

Although the significance of this measurement is limited by the uncertainties, the data are highly suggestive, especially when considered in conjunction with other recent results. Correlations between fully reconstructed jets and away-side hadrons at STAR show an enhancement of I_{AA} at low p_T^h. This enhancement supports the concept that high p_T energy loss is redistributed as increased soft particle production. However, the enhancement seems to occur at the same p_T^h for all jet energies, implying that z scaling does not hold for these jet energies. CMS at the LHC has also recently presented results which show an increase of particles outside of their jet cone [65].

These measurements are now going beyond observations of energy loss to investigations of where the lost energy goes. These studies are important for gaining a more detailed understanding of how partons lose energy in the medium and the effects of the deposited energy.

9.4 Relation to Other Experimental Results on Jet Energy Loss

The other large RHIC experiment, STAR, likewise measures $\gamma_{\mathrm{dir}} - h$ correlations. Although the idea behind the method is the same, i.e. remove the correlation with meson decay photons from the $\gamma_{\mathrm{inc}} - h$ measurement, their direct photon extraction procedure is different from ours. The granularity of the PHENIX EMCal allows us to measure photons and reconstruct π^0s well, while STAR relies on what they call "π^0-rich" samples. However, because the STAR acceptance is greater than at PHENIX, the statical uncertainties in the STAR correlation results are smaller. Despite these differences, the STAR and PHENIX results are consistent. The STAR results from Run 7 measure the hadron yield opposite the 8-16 GeV/c photon triggers in the head region in $\Delta\phi$. The average STAR I_{AA} is consistent with our p_T binned results. They also observe the same similarity we do between the $\gamma_{\mathrm{dir}} - h$ and $\pi^0 - h$ I_{AA}. However, they do not measure $z_T < 0.3$, and therefore conclude that I_{AA} as a function of z_T is flat. Based on the STAR $\gamma_{\mathrm{dir}} - h$ combined with the near-side h-h I_{AA} studies at the LHC, Thorsten Renk believes that YaJEM needs a mixture of radiative and elastic drag which shifts the onset of the rise in I_{AA} towards lower z_T [63]. However, the data in this thesis for the wider centrality bins do not suggest the need to shift the YaJEM z_T distribution, although the uncertainties in the measurement to not exclude the possibility.

STAR has also studied jet-h correlations in the medium [19,66]. They fully reconstruct jets via the anti-k_T algorithm and then study the hadrons on the opposite side. The jets used in these studies are at slightly higher p_T than our photon triggered jets. The I_{AA} from STAR is plotted in Fig. 9.1, as a function of hadron p_T for three different jet energies. At high p_{Th} the I_{AA} seems flat. However, at about 2 GeV/c it shoots up and an enhancement is observed. For the 10 GeV jet this transition between flat and enhancement appears at about the same z_T value as observed in our analysis. However, instead of this transition occurring at the same z_T for the higher energy jets, it actually occurs at the same p_{Th}. Likewise, CMS has measured an excess of particles in the direction transverse to the di-jet axis for 2.7 TeV Pb+Pb collisions at the LHC [65]. These measurements along with the analysis presented in this thesis suggest that the energy loss by the parton in the medium is redistributed into soft hadron production.
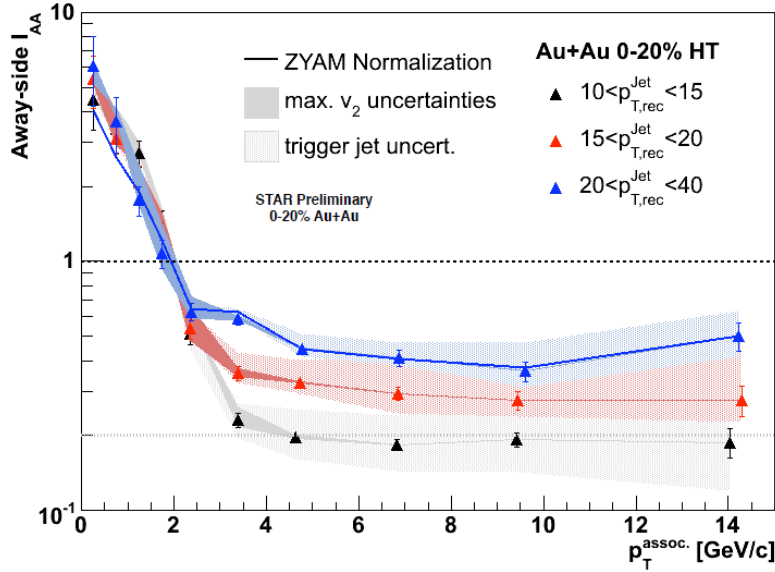
Figure 9.1: The I_{AA} of the away-side hadron yield triggering on fully recon-structed jets for 0-20% Au+Au collisions compared to $p + p$ [19].

9.5 Summary of Corner Stone Work

As part of this thesis, procedures were developed to extend these measurements and their implications. However, they were not all fully implemented or require more detailed studies. This includes applying event by event techniques in the Au+Au data and measuring k_T.

p_{out} distributions have been presented for Au+Au but all of their features are not understood and warrant further investigation. The comparison of the RMS of these distributions with the $p + p$ measurements indicate a similar k_T for both systems, but the goal is to extract an actual value of k_T. From the difference in k_T measured between in medium and $p + p$, the transport coefficient of the medium, $\widehat{q}$, can be determined according to [67]

$$\langle \Delta q^2 \rangle = \int \widehat{q} dy \tag{9.1}$$

It is also interesting to study the evolution of k_T using collisions at LHC energies.

The uncertainties in the γ_{dir}-h measurement, even with the Run 7 data, limit the interpretations. An increase in statistics is obviously beneficial but the uncertainties can be reduced with improving the procedure. Early work on

implementing event-by-event techniques in the heavy ion environment has been presented here and can be further developed and implemented to improve the physics impact of these measurements. Work is currently underway to apply an isolation cut in the Run 8 d+Au data. Combining the experience that this study will provide with the studies of the background in the heavy ion environment from jet reconstruction analyses, may show that an isolation cut is actually possible for heavy ion collisions. Jet reconstruction algorithms may also allow for a different type of isolation cut, where the algorithm determines if the the trigger photon is part of a jet or not.

The initial mathematics of how to implement the tagging method in Au+Au was presented. An R_γ with reduced uncertainties would make the current procedure more useful. Additional simulations are also required to understand how the tagging method really behaves in a high multiplicity environment. One technique used in other analyses is to embed a simulated photon into real data events and test the probability of falsely tagging it as a π^0 decay.

9.6 Future Prospects

As PHENIX embarks on its second decade of data collection, the future is bright. An additional large Au+Au data set has already been collected in 2010 and the γ_{dir}-h analysis is now underway to further improve the significance of the results presented here. A new R_γ analysis on the higher statistics data and further development and implementation of event by event techniques in a heavy-ion environment will reduce the systematic uncertainties in the γ_{dir} extraction in addition to the reduced statistical errors. However, there are many other $\gamma_{\mathrm{dir}} - h$ related measurements which need to be done.

Analysis of the Run 8 d+Au data also underway will aid in the development of these techniques. With increased statistics, studying γ_{dir}-h correlations as a function of reaction plane should also enhance our understanding of energy loss in the medium, since by varying the angle with respect to the reaction plane we control the path length of the parton through the medium. Also, the fragmentation function that we are studying can be specified by measuring identified hadrons on the away-side.

With the advent of the LHC experiments and upgrades to the RHIC experiments, as well as further developed algorithms and background subtraction methods, full jet reconstruction in heavy-ion collisions has been achieved and is becoming a major focus in the field of jet tomography. Reconstructed jet-hadron correlations are a great compliment to these γ_{dir}-h studies. γ_{dir}-h is cleaner than jet-h because it balances the away-side parton energy (modulo k_T of course), whereas the jet energy can be modified by both the medium

and jet finding algorithm's treatment of the background. By measuring γ_{dir}-reconstructed jet correlations at RHIC and the LHC, we can learn both about the jet finding algorithms used as well as the parton energy loss over a wide kinematic range. Jets at the LHC are dominated by gluon jets while at RHIC and in $\gamma_{\mathrm{dir}} - h$ correlations, we are dominated by quark jets. Gluon jets are expected to be more strongly suppressed by the medium than quark jets due to the difference color factors. However, this has yet to be experimentally measured at these experiments.

At the LHC, the collision energies reach a regime where Z bosons are produced and, like a photon, can be used to tag the energy of the opposing jet. While the smaller backgrounds to this channel should make it cleaner than γ_{dir}-h correlations, the lower production rate will limit the statistical precision that can be achieved.

Science is based on asking questions and then doing the research necessary to obtain the answers. However, a good scientist is never satisfied, because in the process of answering one question, several more questions arise. The results presented here are intriguing and teach us several aspects of energy loss which are summarized in the previous sections. However, the ever questioning scientist has to ask more. Some of these questions and potential research avenues have been described and hopefully will inspire more work along this vein.

In conclusion, RHIC has made several interesting measurements and discoveries but a great deal remains to be learned about energy loss and the QGP. More data, new detectors, more precision measurements and more detailed theoretical models continue to make correlations with direct photons a "golden channel" in this field.

Bibliography

[1] M. McCumber, *Measurements of Fast Parton Interactions with Hot Dense Nuclear Matter via Two Particle Correlations at PHENIX*, Stony Brook University Ph.D. Thesis (2010).

[2] A. Adare, *et al.* (PHENIX), *Phys. Rev. Lett.* **98**, 162301 (2007).

[3] J. Adams, *et al.* (STAR), *Nucl. Phys. A* **757**, 102 (2005).

[4] A. Adare, *et al.* (PHENIX), *Phys. Rev. C* **78**, 014901 (2008).

[5] E. Wenger, *et al.* (STAR), *J. Phys. G: Nucl. Part. Phys.* **35**, 104080 (2008).

[6] J. Pumplin, *et al. JHEP* **0207**, 012 (2002).

[7] W. Braunschweig *et al.* (TASSO Collaboration), *Z. Phys. C* **47**, 187 (1990).

[8] T. Sakaguchi (PHENIX) *Acta Phys. Hung. A* **25** 409 (2006).

[9] L.E. Gordon & W. Vogelsang, Phys. Rev. D **48**, 3136 (1993).

[10] G.Y. Qin, J. Ruppert, C. Gale, S. Jeon & G. D. Moore *Phys. Rev. C* **80** 054909 (2009).

[11] M. Nguyen, *Two Particle Correlations with Direct Photon and π^0 Triggers in 200 GeV p+p and Au+Au Collisions*, Stony Brook University Ph.D. Thesis (2009).

[12] X.N. Wang, Z. Huang *Phys. Rev. C* **55** 3047-3061 (1997).

[13] Zhang, J. Owens, E. Wang, and X. N. Wang, *Phys. Rev. Lett.* **103**, 032302 (2009).

[14] S. Milov, *PHENIX Internal Document* **AN**461 (2005).

[15] A. Adare, *Transverse momentum evolution of neutral pion triggered di-hadron correlations in Au+Au collisions at $\sqrt{s_{NN}}$ = 200 GeV*, University of Colorado Ph.D. Thesis (2009).

[16] A. Adare, *et al.* (PHENIX), *Phys. Rev. D* **82**, 072001 (2010).

[17] A. Adare, *et al.* (PHENIX), *arXiv:0903.3399* (2009).

[18] S. Adler, *et al.* (PHENIX), *Phys. Rev. D* **74**, 072002 (2006).

[19] J. Putschke, (STAR) *STAR: Jet Reconstruction, Direct Photon and Multi-hadron Correlations* **Hard Probes Conference Presentation**, Eilat, Israel (2010).

[20] K. Nakamura, *et al.* (Particle Data Group), *J. Phys. G* **37**, 075021 (2010).

[21] M.E. Peskin and D.V. Schroeder, *An Introduction To Quantum Field Theory*, Reading, USA: Addison-Wesley (1995), 842 p.

[22] A. Adare, *et al.* (PHENIX), *Phys. Rev. C* **77**, 064907 (2008).

[23] A. Dainese, C. Loizides, & G. Paic, *Eur. Phys. J. C* **38**, 461 (2005).

[24] M. Gyulassy, P. Levai, & I. Vitev, *Nucl. Phys. B* **571**, 197 (2000).

[25] M. Djordjevic, *et al. Phys. Lett. B* **632**, 81 (2006).

[26] S. Wicks, *et al. Nucl. Phys. A* **784**, 426 (2007).

[27] S. Bass, *et al.*, *Phys. Rev. C* **79**, 024901 (2009).

[28] R. Baier, *et al.*, *Nucl. Phys. B* **484**, 265 (1997).

[29] X.F. Chen *et al.*, *arXiv:1002.1165v1* (2010).

[30] A. Adare, *et al.* (PHENIX), *Phys. Rev. Lett.* **104**, 252301 (2010).

[31] A. Adare, *et al.* (PHENIX), *Phys. Rev. Lett.* **105**, 142301 (2010).

[32] A. Adare, *et al.* (PHENIX), *Phys. Rev. C* **84**, 024904 (2011).

[33] A. Sickles, M. McCumber, & A. Adare, *arXiV:0907.4113* (2009).

[34] B. Alver, *et al. Phys.Rev.C* **77** 014906 (2008).

[35] J. Huston, *et al.*, *Phys. Rev. D* **51** 6139 (1995).

[36] P. Stankus, *Annu. Rev. Nucl. Part. Sci.* **55**, 517 (2005).

[37] A. Adare, *et al.* (PHENIX), *Phys. Rev. Lett.* **104**, 132301 (2010).

[38] H. Zhang, *et al. Phys. Rev. Lett.* **98**, 212301 (2007).

[39] T. Renk, *Phys. Rev. C* **80** 014901 (2009).

[40] Borghini & Wiedemann, *arXiv:hep-ph/0506218* (2005).

[41] Abelev *et al.* (STAR) *Phys. Rev. C* **82** 034909 (2010).

[42] K. Adcox, *et al.*, *Nucl. Instrum. Meth.* **A499**, 469 (2003).

[43] K. H. Ackermann, *et al.* (STAR) *Nucl. Instrum. Meth. A* **499** 624 (2003).

[44] B. B. Back, *et al.* (BRAHMS) *Nucl. Instrum. Meth. A* **499** 437 (2003).

[45] M. Adamczyk, *et al.* (PHOBOS) *Nucl. Instrum. Meth. A* **499** 603 (2003).

[46] M. Aizawa, *et al.*, *Nucl. Instrum. Meth.* **A499**, 508 (2003).

[47] M. Allen, *et al.*, *Nucl. Instrum. Meth.* **A499**, 549 (2003).

[48] X. Wang & M. Gyulassy, *Phys. ReV. D* **44**, 3501 (1991).

[49] E. Richardson *et al.*, *Nucl. Inst. and Meth. A* **636** 99 (2011).

[50] W. Anderson, *et al.*, *arXiv:1103.4277v1*, (2011).

[51] K. Aamodt, *et al.* (ALICE), *Phys. Rev. Lett.* **105** 252302 (2010).

[52] A. Adare, *et al.* (PHENIX), *arXiv:1105.3928*, (2011).

[53] S. Adler, *et al.* (PHENIX), *Phys. Rev. C* **69**, 034910 (2004).

[54] T. Isobe, *Production of Direct Photons and Neutral Pions in Relativistic Au+Au Collisions*, Center for Nuclear Study, University of Tokyo, Ph.D. Thesis (2007).

[55] A. Adare, *et al.* (PHENIX), *Phys. Rev. Lett.* **101**, 232301 (2008).

[56] S. Adler, *et al.* (PHENIX), *Phys. Rev. Lett.* **94**, 232301 (2005).

[57] S. Adler, *et al.* (PHENIX), *Phys. Rev. Lett.* **98**, 012002 (2007).

[58] Ma ,& Wang *arXiv:1106.6126v1 Proceedings for Quark Matter 2011 Conference*, Annecy, France (2011).

[59] S. Adler, *et al.* (PHENIX), *Phys. Rev. C* **73**, 054903 (2006).

[60] C. Stewart, *et al.* (Fermilab E557 Collaboration), *Phys. Rev. D* **42** 1385 (1990).

[61] M. D. Corcoran *et al.* (Fermilab E609 Collaboration), *Phys. Lett. B* **259** 209 (1991).

[62] D. Naples *et al. Phys. Rev. Lett.* **72** 2341 (1994).

[63] T. Renk, *Private Communication* (2011).

[64] S. Mert Aybat & T.C. Rogers, *arXiv:1101.5057v1* (2011).

[65] F. Ma, (CMS) *Proceedings of XLVIth Rencontres de Moriond on QCD and High Energy Interaction* La Thuile, *arXiv:1107.3218v1*, 2011.

[66] E. Bruna, (STAR) *Nucl. Phys. A* **855**, 367 (2011).

[67] J. Casalderrey-Solana, & X.N. Wang, *Phys. Rev. C* **77**, 024902 (2008).

Appendix A

Additional Plots

A.1 Correlation Functions

The correlation functions which are measured for the p_T binned results for the Run 7 data are included here. Correlations are what one truly measures experimentally without any assumptions on the physics of the underlying event. Therefore, if new information is gained such as the neccessity of including higher order flow terms, the jet functions can be extracted with updated assumptions from these correlations.
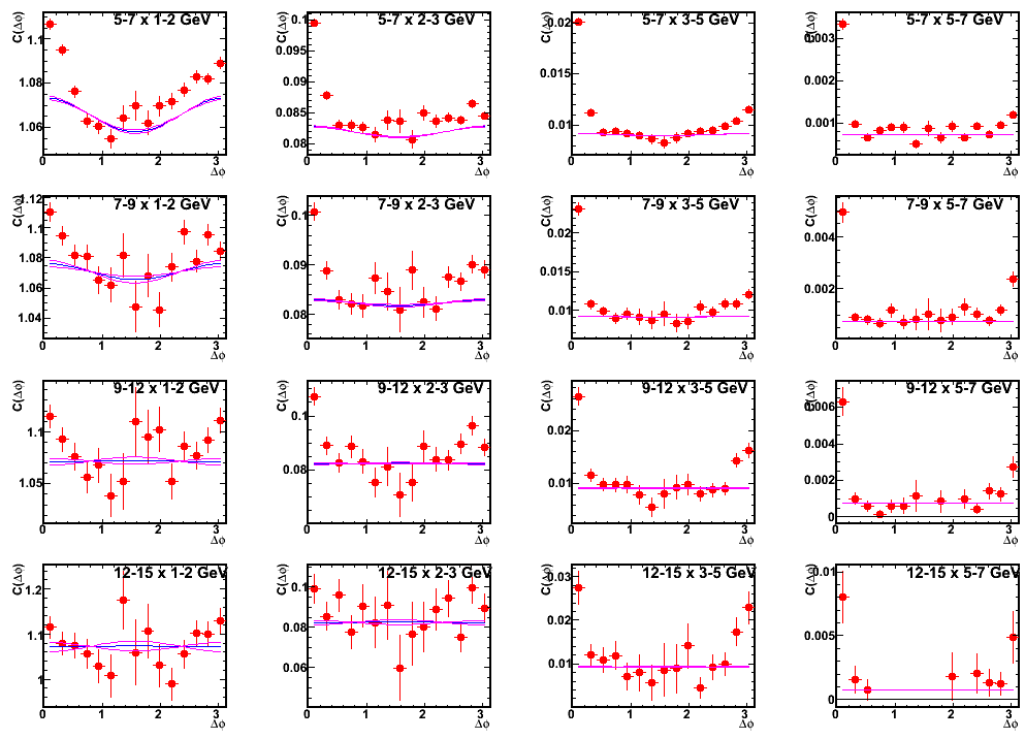
Figure A.1: Inclusive photon-hadron correlations for 0–20%.
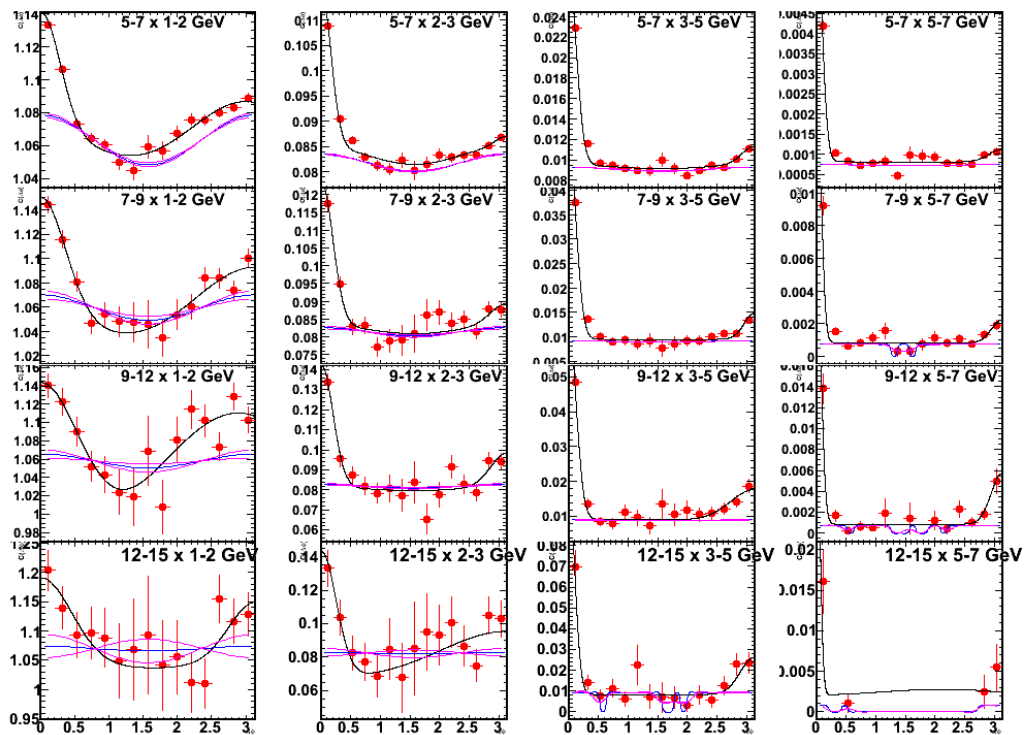
Figure A.2: π^0-hadron correlations for 0–20%.
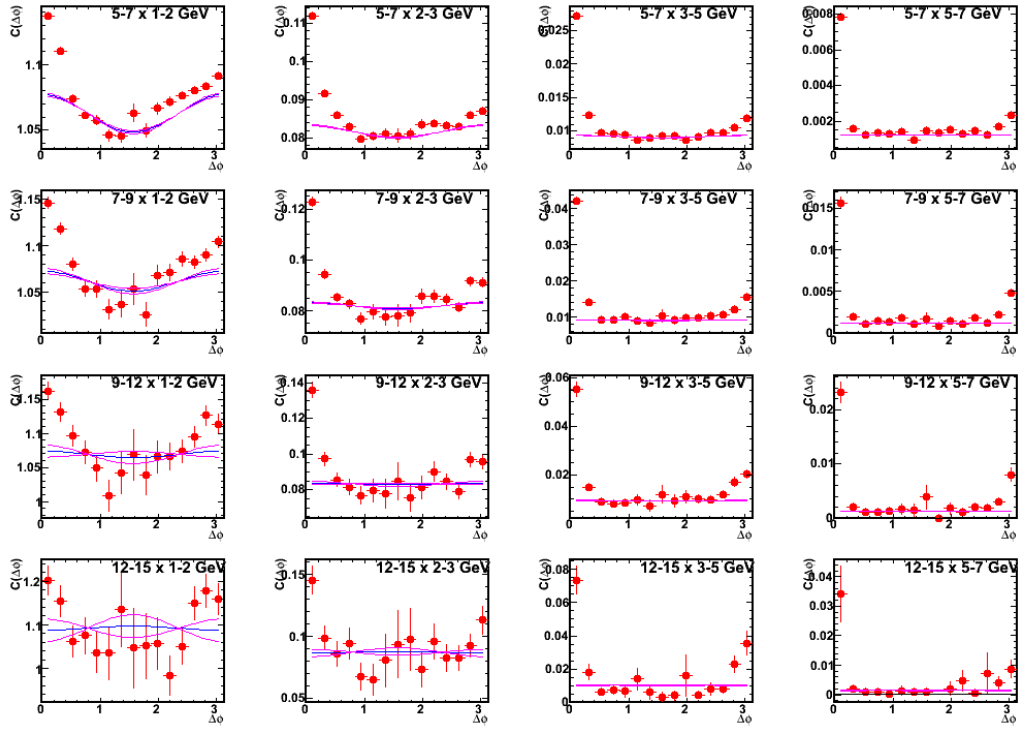
Figure A.3: Decay photon-hadron correlations for 0–20%.
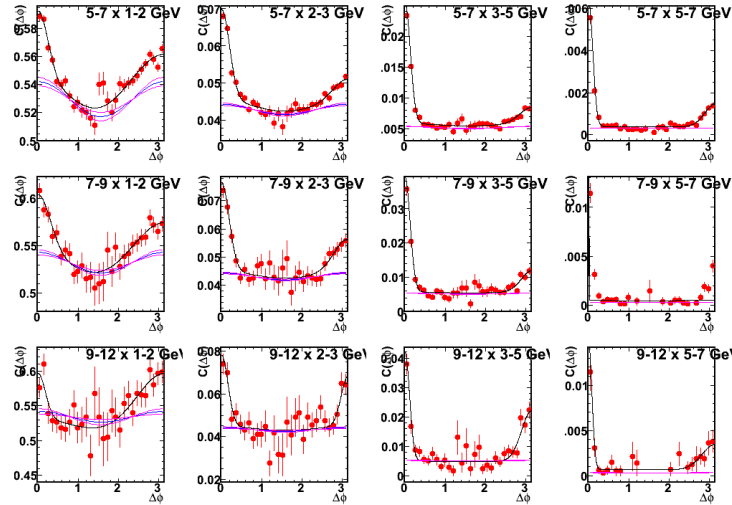
Figure A.4: $\gamma_{\text{inc}} - h$ correlation functions for $p_{T,h} = 1 - 7 Gev/c$ and $p_{T,\gamma} = 5 - 12 Gev/c$ for 20-40%

156
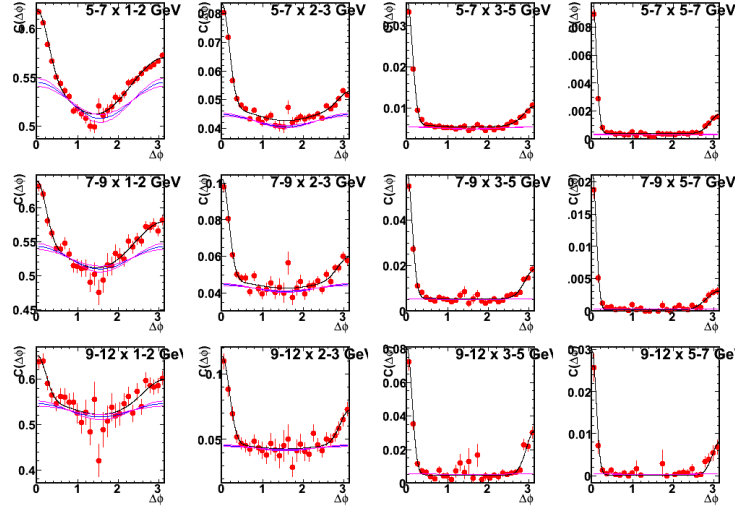
Figure A.5: $\gamma_{\mathrm{dec}} - h$ correlation functions for $p_{T,h} = 1 - 7 Gev/c$ and $p_{T,\gamma} = 5 - 12 Gev/c$ for 20-40%
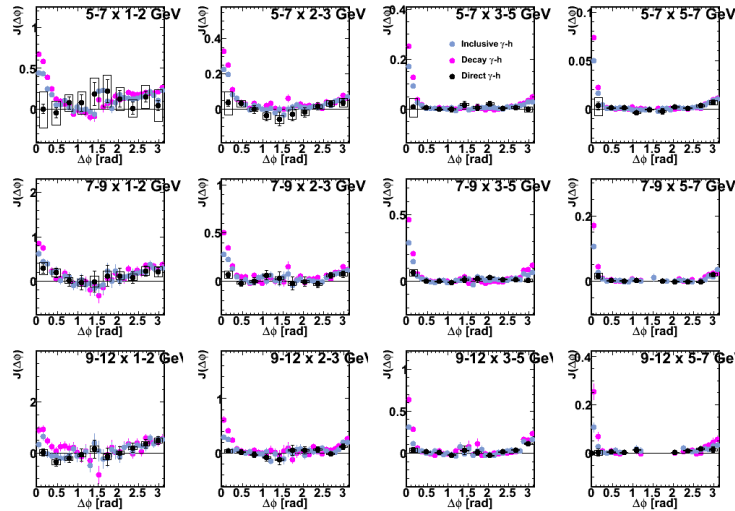
Figure A.6: $\gamma_{\mathrm{inc}} - h$ (blue), $\gamma_{\mathrm{dec}} - h$ (pink), and $\gamma_{\mathrm{dir}} - h$ (black) jet functions for $p_{T,h} = 1 - 7 Gev/c$ and $p_{T,\gamma} = 5 - 12 Gev/c$ for 20-40%

157
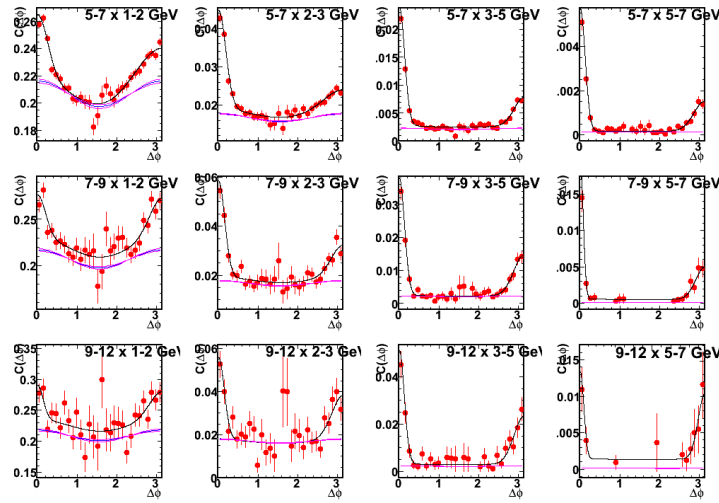
Figure A.7: $\gamma_{\mathrm{inc}} - h$ correlation functions for $p_{T,h} = 1 - 7 Gev/c$ and $p_{T,\gamma} = 5 - 12 Gev/c$ for 40-60%
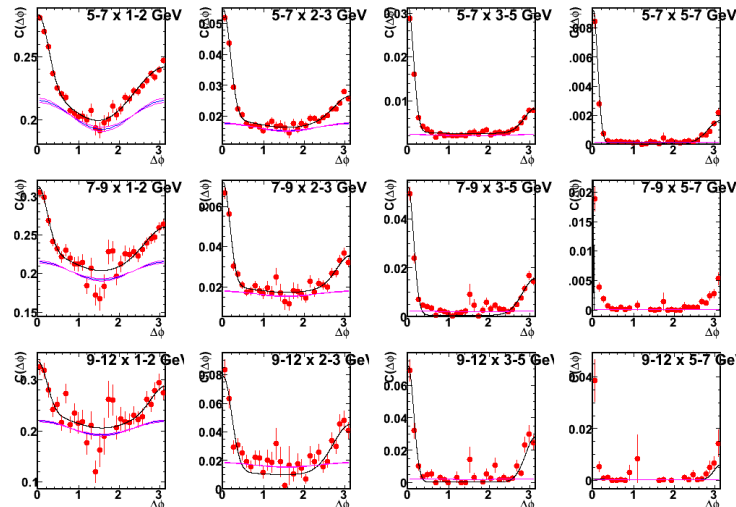
Figure A.8: $\gamma_{\mathrm{dec}} - h$ correlation functions for $p_{T,h} = 1 - 7 Gev/c$ and $p_{T,\gamma} = 5 - 12 Gev/c$ for 40-60%
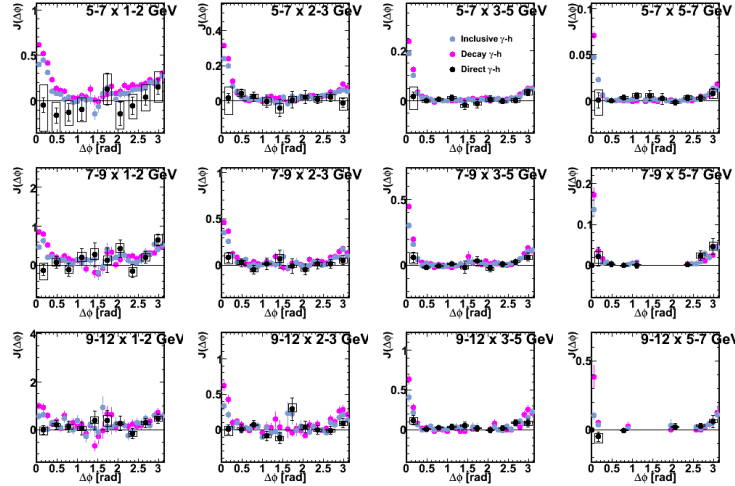
Figure A.9: $\gamma_{\mathrm{inc}} - h$ (blue), $\gamma_{\mathrm{dec}} - h$ (pink), and $\gamma_{\mathrm{dir}} - h$ (black) jet functions for $p_{T,h} = 1 - 7 Gev/c$ and $p_{T,\gamma} = 5 - 12 Gev/c$ for 40-60%
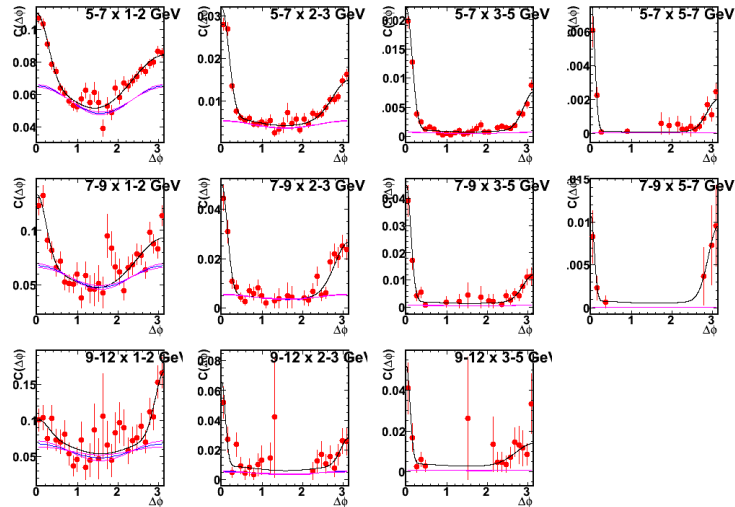
Figure A.10: $\gamma_{\mathrm{inc}} - h$ correlation functions for $p_{T,h} = 1 - 7 Gev/c$ and $p_{T,\gamma} = 5 - 12 Gev/c$ for 60-92%

159
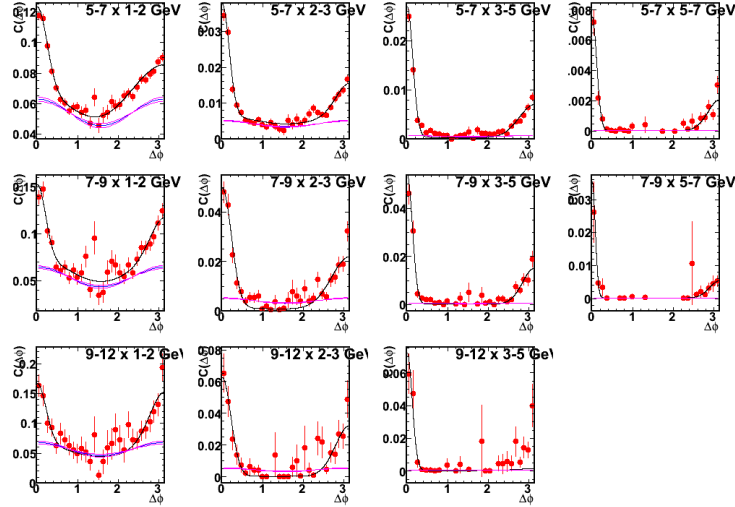
Figure A.11: $\gamma_{\mathrm{dec}} - h$ correlation functions for $p_{T,h} = 1 - 7 Gev/c$ and $p_{T,\gamma} = 5 - 12 Gev/c$ for 60-92%
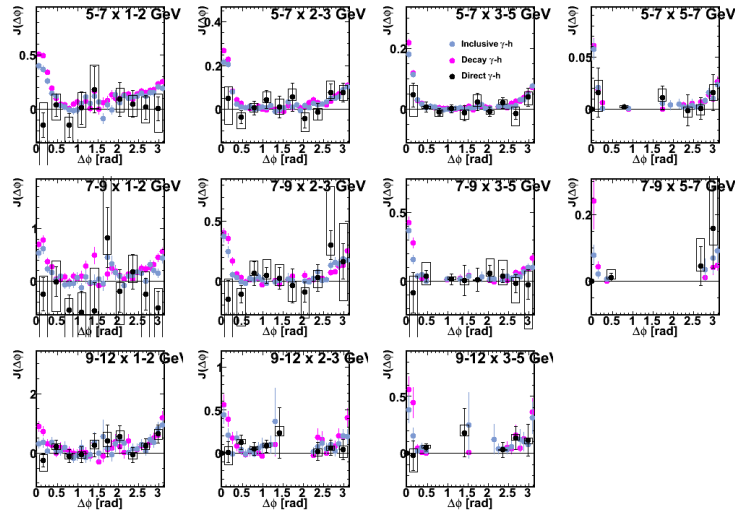
Figure A.12: $\gamma_{\mathrm{inc}} - h$ (blue), $\gamma_{\mathrm{dec}} - h$ (pink), and $\gamma_{\mathrm{dir}} - h$ (black) jet functions for $p_{T,h} = 1 - 7 Gev/c$ and $p_{T,\gamma} = 5 - 12 Gev/c$ for 60-92%
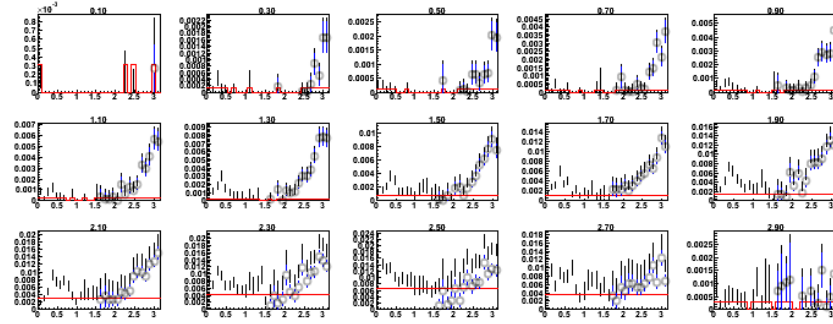
Figure A.13: Correlation functions are projected along $\Delta\phi$ for each ξ bin in black. The ZYAM level is shown in red and the resulting jet function for the awayside is shown as open circles. Inclusive isolated photon triggers 7-9GeV/c.
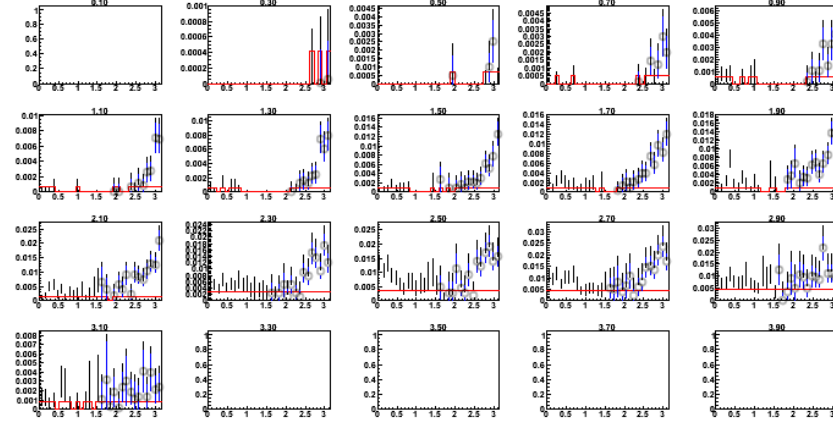
Figure A.14: Correlation functions are projected along $\Delta\phi$ for each ξ bin in black. The ZYAM level is shown in red and the resulting jet function for the awayside is shown as open circles. Inclusive isolated photon triggers 9-12GeV/c.
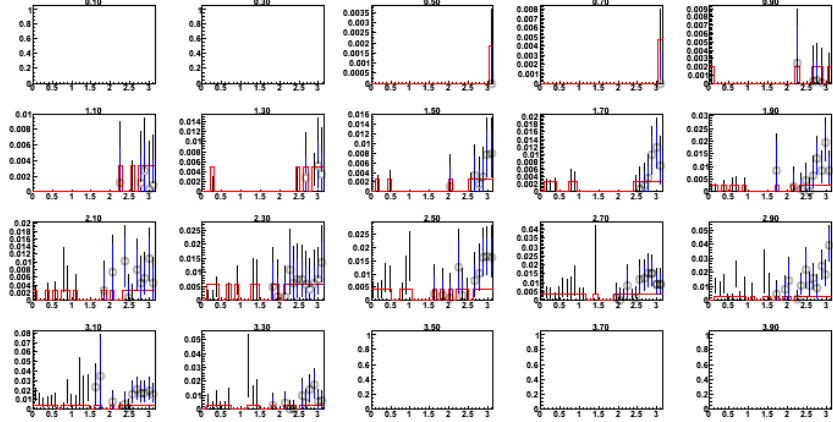
Figure A.15: Correlation functions are projected along $\Delta\phi$ for each ξ bin in black. The ZYAM level is shown in red and the resulting jet function for the awayside is shown as open circles. Inclusive isolated photon triggers 12-15GeV/c.
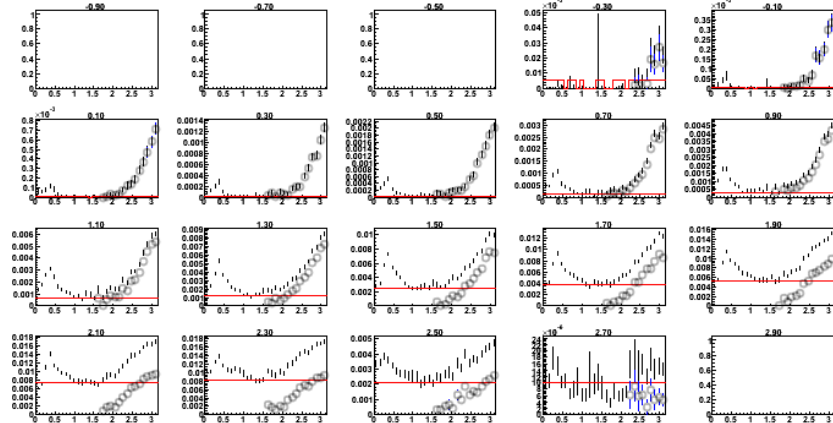
Figure A.16: Correlation functions are projected along $\Delta\phi$ for each ξ bin in black. The ZYAM level is shown in red and the resulting jet function for the awayside is shown as open circles. Tagged decay photon triggers 5-7GeV/c.
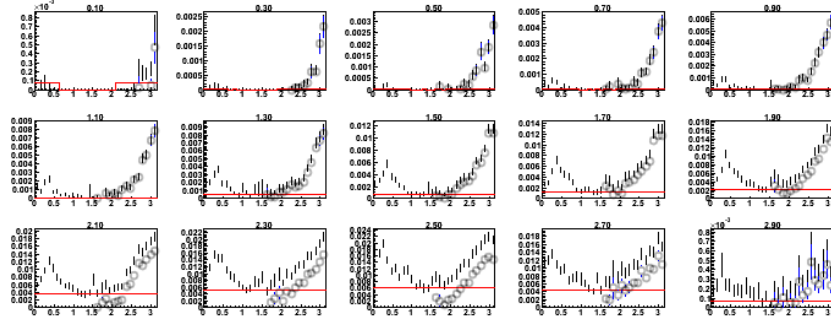
Figure A.17: Correlation functions are projected along $\Delta\phi$ for each ξ bin in black. The ZYAM level is shown in red and the resulting jet function for the awayside is shown as open circles. Tagged decay photon triggers 7-9GeV/c.
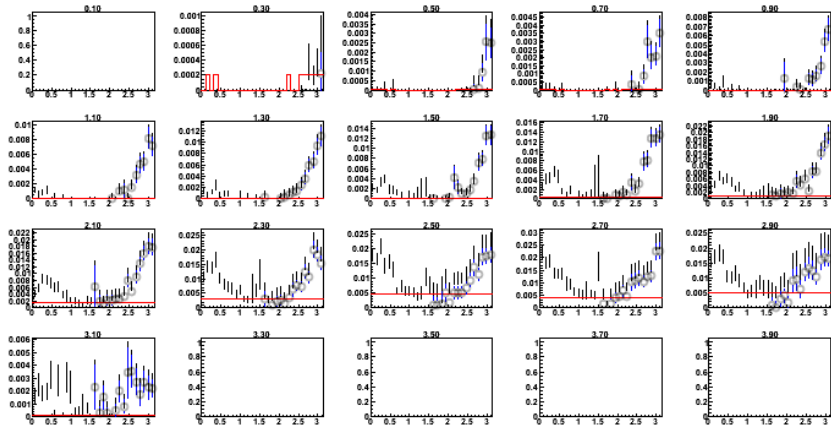
Figure A.18: Correlation functions are projected along $\Delta\phi$ for each ξ bin in black. The ZYAM level is shown in red and the resulting jet function for the awayside is shown as open circles. Tagged decay photon triggers 9-12GeV/c.
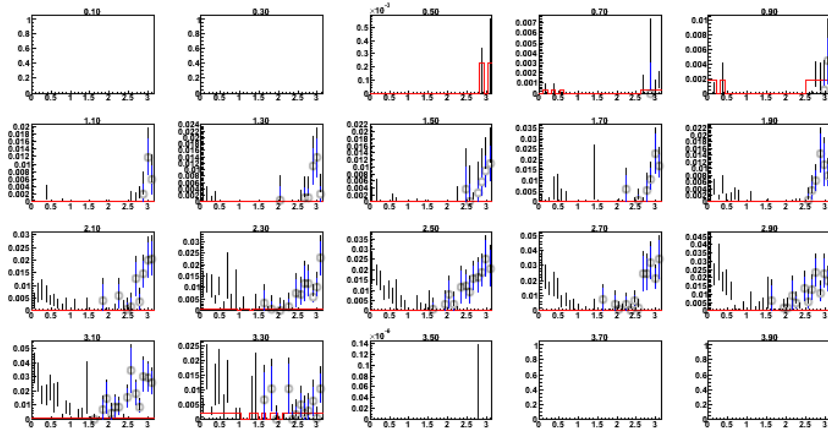
Figure A.19: Correlation functions are projected along $\Delta\phi$ for each ξ bin in black. The ZYAM level is shown in red and the resulting jet function for the awayside is shown as open circles. Tagged decay photon triggers 12-15GeV/c.

A.2 Cross Checks with other analyses

Several cross checks were performed on the results in this thesis. Figures for some of these cross checks are included here.
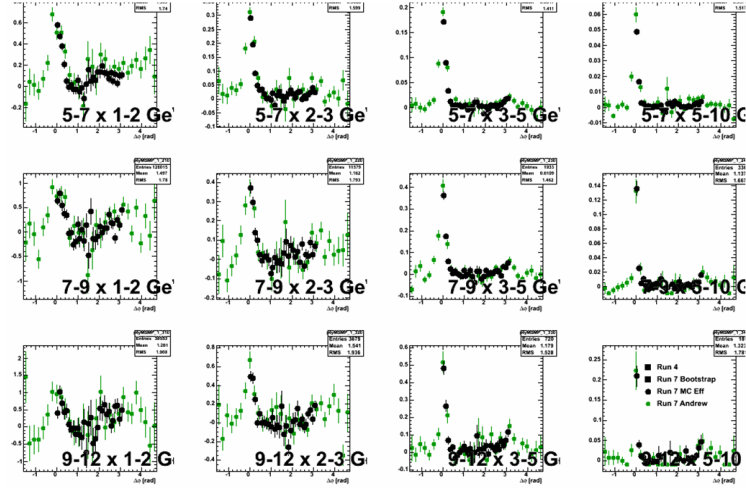
Figure A.20: Run 7 π^0–h jet functions as measured in this analysis compared to those measured by Andrew Adare's analysis.
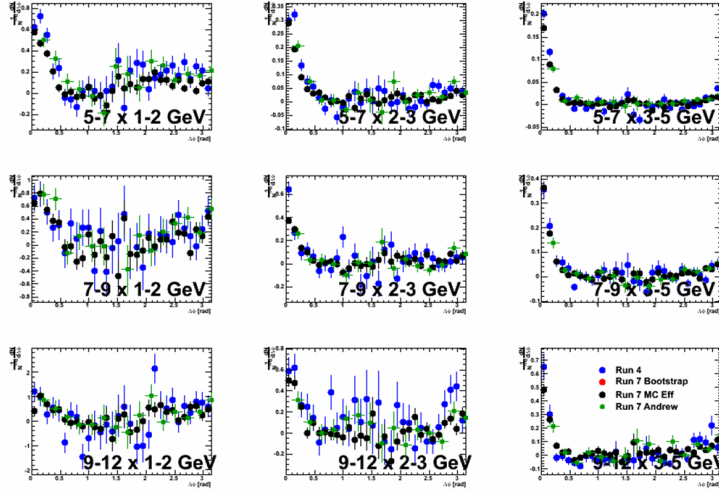
Figure A.21: Run 7 π^0–h jet functions as measured in this analysis compared to those measured in the Run 4 γ–jet analysis.
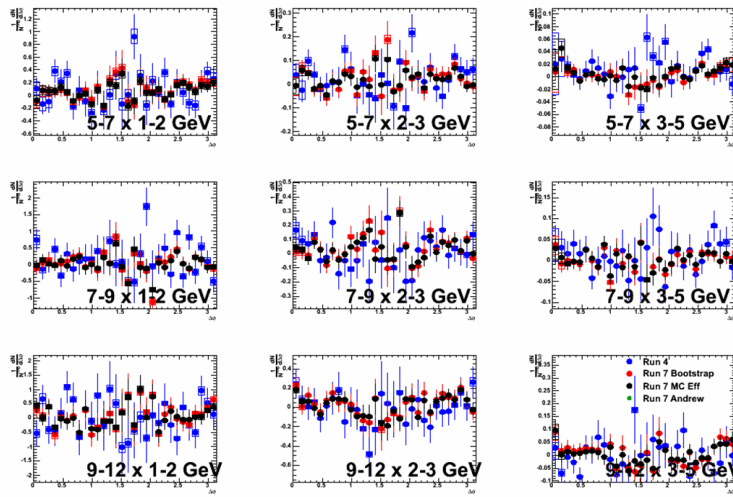
Figure A.22: Direct Photon-hadron jet functions as measured in this analysis for Run 7 with the MC calculate efficiencies compared to Run 7 results with bootstrapped efficiencies applied and final Run 4 results from ppg090.

Appendix B

Data Tables

B.1   Additional v_2 Values Used

Table B.1: v_2 values used in the jet function extraction for inclusive and decay photons in Run 4 Au+Au collisions.

Centrality	p_T^γ	Inclusive γ			Decay γ		
		v_2	Stat.	Sys.	v_2	Stat.	Sys.
0–20%	5–7	0.053	±0.009	±0.011	0.084	±0.009	±0.004
	7–9	0.047	±0.022	±0.015	0.069	±0.018	±0.003
	9–12	0.024	±0.042	±0.017	0.069	±0.020	±0.003
	12–15	0.064	±0.096	±0.094	0.069	±0.023	±0.003
20–40%	5–7	0.096	±0.010	±0.005	0.155	±0.011	±0.036
	7–9	0.079	±0.027	±0.011	0.105	±0.019	±0.025
	9–12	0.025	±0.050	±0.049	0.105	±0.020	±0.025
	12–15	0.287	±0.128	±0.104	0.105	±0.023	±0.024
40–60%	5–7	0.143	±0.023	±0.035	0.136	±0.022	±0.010
	7–9	0.146	±0.064	±0.026	0.126	±0.039	±0.008
	9–12	0.162	±0.126	±0.252	0.126	±0.042	±0.008
	12–15	-0.603	±0.308	±0.191	0.126	±0.046	±0.008

Table B.2:   Trigger particle v_2 values for 20-40%

Trigger	$p_{T,\gamma}$ [GeV]	v_2	Stat err	Sys. err
π^0	5-7	0.133537	0.00330527	0.0229443
	7-9	0.116202	0.00587208	0.0241762
	9-12	0.103055	0.011224	0.0385936
	12-15	0.0861201	0.029055	0.0246211
decay γ	5-7	0.127069	0.00292113	0.0236515
	7-9	0.114212	0.00505774	0.0261016
	9-12	0.100518	0.0104308	0.0335327
	12-15	0.0893677	0.0271222	0.0335694
inclusive γ	5-7	0.085271	0.00207489	0.0179611
	7-9	0.0738878	0.00558803	0.0150986
	9-12	0.0520371	0.0106242	0.0224717
	12-15	0.0644017	0.0252076	0.0259959

Table B.3:   Trigger particle v_2 values for 40-60%

Trigger	$p_{T,\gamma}$ [GeV]	v_2	Stat err	Sys. err
π^0	5-7	0.174446	0.00671865	0.0244753
	7-9	0.154815	0.0116477	0.0154511
	9-12	0.242351	0.0226531	0.0129369
	12-15	0.116911	0.0579355	0.0662867
decay γ	5-7	0.1708	0.00588472	0.0221
	7-9	0.172332	0.0104886	0.0193321
	9-12	0.201946	0.0222112	0.0121742
	12-15	0.130769	0.0609939	0.0715249
inclusive γ	5-7	0.137988	0.00432101	0.0183026
	7-9	0.143281	0.0120942	0.0126758
	9-12	0.124542	0.0234003	0.0123776
	12-15	0.0260897	0.0570124	0.0590142

Table B.4:   Trigger particle v_2 values for 60-90%

Trigger	$p_{T,\gamma}$ [GeV]	v_2	Stat err	Sys. err
π^0	5-7	0.421401	0.0295431	0.0485074
	7-9	0.546913	0.0502779	0.0388233
	9-12	0.563822	0.10233	0.0259706
	12-15	0.423104	0.31356	0.258514
decay γ	5-7	0.471666	0.0282416	0.0515539
	7-9	0.576252	0.0542437	0.0424481
	9-12	0.569893	0.111251	0.0395384
	12-15	0.337386	0.275169	0.373302
inclusive γ	5-7	0.441812	0.0193252	0.0197302
	7-9	0.510075	0.055292	0.0487202
	9-12	0.495211	0.112183	0.156611
	12-15	-0.299766	0.295892	0.797914

B.2 Results

The Au+Au results in these tables are for the Run 7 data set. Recall the head region and full away-side refer to the $\Delta\phi$ integration regions, $|\Delta\phi - \pi| < \pi/5$ and $|\Delta\phi - \pi| < \pi/2$ respectively.

Table B.5: Head region awayside yield in 0-20% Au+Au.

$p_{T,\gamma}$ [GeV]	p_T^h [GeV]	Yield	Stat	Sys.
5-7	1-2	9.38e-02	2.31e-02	+2.87e-02 -2.87e-02
	2-3	1.38e-02	6.14e-03	+2.54e-03 -2.54e-03
	3-5	4.47e-03	1.06e-03	+1.67e-03 -1.67e-03
	5-7	-3.04e-04	3.29e-04	+4.79e-04 -4.69e-04
7-9	1-2	1.27e-02	4.10e-02	+3.27e-02 -3.22e-02
	2-3	3.66e-02	1.11e-02	+3.26e-03 -3.27e-03
	3-5	3.28e-03	1.97e-03	+5.26e-04 -4.45e-04
	5-7	6.60e-04	7.15e-04	+4.39e-04 -4.14e-04
9-12	1-2	6.95e-02	6.39e-02	+4.50e-02 -4.40e-02
	2-3	5.71e-02	1.76e-02	+4.67e-03 -4.68e-03
	3-5	8.57e-03	3.35e-03	+9.15e-04 -7.03e-04
	5-7	9.61e-04	1.29e-03	+6.19e-04 -5.07e-04
12-15	1-2	1.52e-01	1.20e-01	+9.02e-02 -8.95e-02
	2-3	2.18e-02	3.22e-02	+1.02e-02 -1.01e-02
	3-5	1.84e-02	7.02e-03	+1.07e-03 -9.36e-04
	5-7	2.79e-03	3.58e-03	+8.10e-04 -7.26e-04

Table B.6: 0-20% Au+Au head region awayside yield as function of z_T.

$p_{T,\gamma}$ [GeV]	z_T	$\frac{1}{N_{trig}}\frac{dN}{dz_T}$	Stat	Sys.
5-7	0.23	5.31e-01	1.31e-01	+1.62e-01 -1.63e-01
	0.41	7.81e-02	3.47e-02	+1.44e-02 -1.44e-02
	0.62	2.53e-02	6.03e-03	+9.43e-03 -9.43e-03
	1.02	-1.72e-03	1.86e-03	+2.71e-03 -2.65e-03
7-9	0.17	9.82e-02	3.17e-01	+2.53e-01 -2.50e-01
	0.30	2.83e-01	8.64e-02	+2.53e-02 -2.53e-02
	0.46	2.54e-02	1.53e-02	+4.07e-03 -3.45e-03
	0.75	5.12e-03	5.54e-03	+3.40e-03 -3.21e-03
9-12	0.13	7.00e-01	6.43e-01	+4.53e-01 -4.43e-01
	0.23	5.75e-01	1.77e-01	+4.70e-02 -4.71e-02
	0.36	8.63e-02	3.38e-02	+9.22e-03 -7.08e-03
	0.58	9.68e-03	1.30e-02	+6.23e-03 -5.11e-03
12-15	0.10	1.98e+00	1.57e+00	+1.18e+00 -1.17e+00
	0.18	2.85e-01	4.21e-01	+1.34e-01 -1.32e-01
	0.28	2.40e-01	9.17e-02	+1.40e-02 -1.22e-02
	0.44	3.64e-02	4.68e-02	+1.06e-02 -9.49e-03

Table B.7: Head region awayside I_{AA} (0-20%).

$p_{T,\gamma}$ [GeV]	p_T^h [GeV]	I_{AA}	Stat	Sys.
5-7	1-2	6.52e-01	1.67e-01	+2.54e-01 -2.51e-01
	2-3	3.27e-01	1.52e-01	+1.14e-01 -1.08e-01
	3-5	2.88e-01	7.87e-02	+1.23e-01 -1.23e-01
	5-7	-1.34e-01	1.57e-01	+2.13e-01 -2.16e-01
7-9	1-2	7.31e-02	2.36e-01	+1.86e-01 -1.89e-01
	2-3	5.86e-01	2.07e-01	+1.22e-01 -1.18e-01
	3-5	1.45e-01	9.20e-02	+3.14e-02 -3.33e-02
	5-7	1.66e-01	2.05e-01	+1.13e-01 -1.18e-01
9-12	1-2	2.68e-01	2.48e-01	+1.71e-01 -1.75e-01
	2-3	8.15e-01	3.22e-01	+1.36e-01 -1.33e-01
	3-5	4.41e-01	2.38e-01	+9.47e-02 -9.57e-02
	5-7	2.07e-01	3.33e-01	+1.20e-01 -1.42e-01
12-15	1-2	1.27e+00	1.14e+00	+1.07e+00 -1.06e+00
	2-3	2.11e-01	3.17e-01	+1.06e-01 -1.07e-01
	3-5	4.32e-01	2.33e-01	+1.17e-01 -1.17e-01
	5-7	-4.04e-01	7.32e-01	+2.54e-01 -2.45e-01

Table B.8: Full awayside yield for 0-20% Au+Au.

$p_{T,\gamma}$ [GeV]	p_T^h [GeV]	Yield	Stat	Sys.
5-7	1-2	1.39e-01	4.91e-02	+5.66e-02 -5.66e-02
	2-3	2.82e-02	1.31e-02	+4.29e-03 -4.29e-03
	3-5	5.42e-03	2.17e-03	+1.83e-03 -1.83e-03
	5-7	-6.83e-04	6.53e-04	+7.41e-04 -7.22e-04
7-9	1-2	8.37e-03	8.70e-02	+4.47e-02 -4.40e-02
	2-3	6.22e-02	2.35e-02	+3.32e-03 -3.35e-03
	3-5	2.00e-03	3.88e-03	+7.83e-04 -6.42e-04
	5-7	2.30e-03	1.36e-03	+5.40e-04 -5.32e-04
9-12	1-2	1.98e-01	1.36e-01	+4.17e-02 -4.15e-02
	2-3	5.81e-02	3.64e-02	+3.29e-03 -3.29e-03
	3-5	6.10e-03	6.14e-03	+1.31e-03 -9.66e-04
	5-7	1.54e-03	1.84e-03	+6.26e-04 -5.30e-04
12-15	1-2	-6.01e-02	2.55e-01	+5.65e-02 -5.57e-02
	2-3	3.78e-02	6.87e-02	+5.79e-03 -5.39e-03
	3-5	1.90e-02	1.28e-02	+8.16e-04 -7.22e-04
	5-7	5.67e-03	4.76e-03	+1.16e-03 -1.09e-03

Table B.9: Full awayside I_{AA} for comparison to MLLA prediction.

$p_{T,\gamma}$ [GeV]	p_T^h [GeV]	I_{AA}	Stat	Sys.
5-7	1-2	8.43e-01	3.05e-01	+4.15e-01 -4.08e-01
	2-3	4.82e-01	2.30e-01	+1.30e-01 -1.29e-01
	3-5	3.16e-01	1.33e-01	+1.25e-01 -1.25e-01
	5-7	-2.35e-01	2.42e-01	+2.58e-01 -2.63e-01
7-9	1-2	4.12e-02	4.28e-01	+2.17e-01 -2.20e-01
	2-3	8.45e-01	3.50e-01	+1.49e-01 -1.46e-01
	3-5	7.03e-02	1.37e-01	+2.45e-02 -2.91e-02
	5-7	4.88e-01	3.90e-01	+1.50e-01 -1.49e-01
9-12	1-2	5.32e-01	3.69e-01	+1.19e-01 -1.19e-01
	2-3	6.48e-01	4.30e-01	+8.10e-02 -7.98e-02
	3-5	2.39e-01	2.55e-01	+5.20e-02 -6.17e-02
	5-7	3.24e-01	5.37e-01	+1.30e-01 -1.46e-01
12-15	1-2	-2.72e-01	1.16e+00	+2.68e-01 -2.71e-01
	2-3	3.51e-01	6.50e-01	+6.90e-02 -7.19e-02
	3-5	7.80e-01	7.88e-01	+3.63e-01 -3.57e-01
	5-7	-4.27e-01	4.96e-01	+1.20e-01 -1.16e-01

Table B.10: Near-side yield for p+p.

$p_{T,\gamma}$ [GeV]	p_T^h [GeV]	Yield	Stat	Sys.
5-7	1-2	4.14e-02	1.24e-02	+5.65e-02 -8.03e-02
	2-3	2.95e-02	6.28e-03	+1.82e-02 -2.37e-02
	3-5	1.07e-02	2.35e-03	+5.10e-03 -6.33e-03
	5-7	1.28e-03	1.09e-03	+1.18e-03 -1.62e-03
7-9	1-2	3.32e-02	2.08e-02	+4.09e-02 -4.66e-02
	2-3	9.22e-03	1.19e-02	+1.69e-02 -1.93e-02
	3-5	1.29e-02	4.55e-03	+4.77e-03 -5.20e-03
	5-7	-5.46e-04	2.44e-03	+1.21e-03 -1.42e-03
9-12	1-2	1.13e-01	2.99e-02	+3.08e-02 -3.27e-02
	2-3	1.42e-02	1.79e-02	+1.33e-02 -1.45e-02
	3-5	6.80e-03	6.99e-03	+4.31e-03 -4.67e-03
	5-7	2.20e-03	4.13e-03	+8.12e-04 -8.60e-04

Table B.11: Nearside yield for 0-20% Au+Au.

$p_{T,\gamma}$ [GeV]	p_T^h [GeV]	Yield	Stat	Sys.
5-7	1-2	1.51e-02	3.26e-02	+1.12e-01 -1.10e-01
	2-3	1.18e-02	8.78e-03	+2.06e-02 -1.95e-02
	3-5	3.70e-03	1.57e-03	+7.44e-03 -7.13e-03
	5-7	-1.51e-03	5.24e-04	+5.42e-03 -5.32e-03
7-9	1-2	5.16e-02	5.81e-02	+1.00e-01 -9.27e-02
	2-3	1.20e-02	1.56e-02	+1.72e-02 -1.30e-02
	3-5	2.34e-03	2.84e-03	+5.88e-03 -4.64e-03
	5-7	-1.60e-03	1.04e-03	+3.86e-03 -3.51e-03
9-12	1-2	-1.93e-02	8.99e-02	+1.16e-01 -1.28e-01
	2-3	5.46e-02	2.46e-02	+1.67e-02 -1.43e-02
	3-5	1.09e-02	4.57e-03	+6.61e-03 -4.59e-03
	5-7	-1.34e-03	1.58e-03	+5.28e-03 -4.49e-03

Table B.12:   The head yield measured in p+p.

$p_{T,\gamma}$ [GeV]	p_T^h [GeV]	Yield	Stat	Sys.
5-7	1-2	1.16e-01	1.07e-02	+3.02e-02 -3.20e-02
	2-3	3.16e-02	5.38e-03	+1.04e-02 -1.19e-02
	3-5	1.05e-02	2.04e-03	+3.08e-03 -3.41e-03
	5-7	2.30e-03	1.04e-03	+1.61e-03 -1.69e-03
7-9	1-2	1.49e-01	1.95e-02	+2.53e-02 -2.60e-02
	2-3	5.11e-02	1.08e-02	+1.03e-02 -1.08e-02
	3-5	1.79e-02	4.45e-03	+3.55e-03 -3.71e-03
	5-7	4.66e-03	2.35e-03	+2.02e-03 -2.06e-03
9-12	1-2	2.00e-01	2.99e-02	+2.10e-02 -2.14e-02
	2-3	6.83e-02	1.70e-02	+9.06e-03 -9.36e-03
	3-5	1.60e-02	7.29e-03	+3.76e-03 -4.00e-03
	5-7	7.59e-03	4.06e-03	+2.09e-03 -2.11e-03

Table B.13:   The head yield measured in Au+Au 20-40%.

$p_{T,\gamma}$ [GeV]	p_T^h [GeV]	Yield	Stat	Sys.
5-7	1-2	6.02e-02	2.85e-02	+1.05e-01 -1.05e-01
	2-3	2.18e-02	8.05e-03	+1.27e-02 -1.27e-02
	3-5	8.62e-04	1.55e-03	+2.39e-03 -2.10e-03
	5-7	1.60e-03	5.27e-04	+4.80e-04 -4.79e-04
7-9	1-2	1.38e-01	4.87e-02	+6.53e-02 -6.52e-02
	2-3	4.09e-02	1.41e-02	+8.01e-03 -7.91e-03
	3-5	2.47e-03	2.96e-03	+2.40e-03 -2.00e-03
	5-7	2.39e-03	1.16e-03	+5.64e-04 -5.37e-04
9-12	1-2	2.69e-01	6.98e-02	+5.61e-02 -5.61e-02
	2-3	3.28e-02	2.01e-02	+8.07e-03 -7.19e-03
	3-5	2.29e-02	5.13e-03	+1.36e-03 -1.24e-03
	5-7	4.93e-03	2.40e-03	+8.78e-04 -8.43e-04

Table B.14:   The I_{AA} measured in Au+Au 20-40%.

$p_{T,\gamma}$ [GeV]	p_T^h [GeV]	IAA	Stat	Sys.
5-7	1-2	5.18e-01	2.50e-01	+9.11e-01 -9.15e-01
	2-3	6.90e-01	2.81e-01	+4.78e-01 -4.63e-01
	3-5	8.22e-02	1.49e-01	+2.02e-01 -2.29e-01
	5-7	6.95e-01	3.90e-01	+5.52e-01 -5.29e-01
7-9	1-2	9.27e-01	3.50e-01	+4.68e-01 -4.67e-01
	2-3	8.02e-01	3.25e-01	+2.29e-01 -2.25e-01
	3-5	1.38e-01	1.69e-01	+1.15e-01 -1.37e-01
	5-7	5.14e-01	3.60e-01	+2.54e-01 -2.54e-01
9-12	1-2	1.35e+00	4.04e-01	+3.16e-01 -3.15e-01
	2-3	4.80e-01	3.18e-01	+1.24e-01 -1.34e-01
	3-5	1.44e+00	7.31e-01	+3.68e-01 -3.49e-01
	5-7	6.51e-01	4.70e-01	+2.12e-01 -2.13e-01

Table B.15:   The head yield measured in Au+Au 40-60%.

$p_{T,\gamma}$ [GeV]	p_T^h [GeV]	Yield	Stat	Sys.
5-7	1-2	6.05e-02	3.70e-02	+9.81e-02 -9.48e-02
	2-3	2.89e-03	1.10e-02	+1.75e-02 -1.33e-02
	3-5	5.63e-03	2.62e-03	+2.60e-03 -2.26e-03
	5-7	1.70e-03	1.07e-03	+6.41e-04 -5.98e-04
7-9	1-2	2.66e-01	6.62e-02	+6.32e-02 -6.42e-02
	2-3	2.26e-02	2.08e-02	+1.47e-02 -1.10e-02
	3-5	1.38e-02	5.87e-03	+2.93e-03 -2.44e-03
	5-7	1.10e-02	3.57e-03	+1.89e-03 -2.14e-03
9-12	1-2	2.40e-01	8.73e-02	+4.85e-02 -4.72e-02
	2-3	2.79e-02	2.85e-02	+1.87e-02 -1.13e-02
	3-5	2.78e-02	9.77e-03	+3.27e-03 -2.29e-03
	5-7	1.41e-02	7.63e-03	+2.23e-03 -2.23e-03

Table B.16:   The I_{AA} measured in Au+Au 40-60%.

$p_{T,\gamma}$ [GeV]	p_T^h [GeV]	IAA	Stat	Sys.
5-7	1-2	5.21e-01	3.22e-01	+8.28e-01 -8.55e-01
	2-3	9.15e-02	3.50e-01	+4.22e-01 -5.54e-01
	3-5	5.38e-01	2.71e-01	+2.78e-01 -2.95e-01
	5-7	7.39e-01	5.73e-01	+6.02e-01 -5.87e-01
7-9	1-2	1.79e+00	5.04e-01	+5.34e-01 -5.23e-01
	2-3	4.43e-01	4.17e-01	+2.35e-01 -3.01e-01
	3-5	7.69e-01	3.79e-01	+2.09e-01 -2.23e-01
	5-7	2.36e+00	1.41e+00	+1.14e+00 -1.10e+00
9-12	1-2	1.20e+00	4.73e-01	+2.69e-01 -2.74e-01
	2-3	4.09e-01	4.29e-01	+1.74e-01 -2.80e-01
	3-5	1.74e+00	1.00e+00	+4.59e-01 -4.59e-01
	5-7	1.86e+00	1.41e+00	+5.94e-01 -5.89e-01

Table B.17: The average I_{AA} for $p_{T,h} > 2 GeV/c, p_{T,\gamma} 5 - 12 GeV/c$ vs. N_{part}.

N_{part}	$Average I_{AA}$	Stat Error	Sys Error
279	0.2407	0.0478	0.1257
150	0.3397	0.0935	0.3040
60	0.5664	0.1578	0.4565

Table B.18: The average I_{AA} for $p_{T,h} > 1 GeV/c, p_{T,\gamma} 5 - 12 GeV/c$ vs. N_{part}.

N_{part}	$Average I_{AA}$	Stat Error	Sys Error
279	0.2525	0.0458	0.1246
150	0.3931	0.0896	0.2987
60	0.6758	0.1444	0.4356

Table B.19:   The average I_{AA} for $p_{T,h} > 2 GeV/c, p_{T,\gamma} 5 - 12 GeV/c$ vs. N_{part} with systematic errors listed separately.

N_{part}	Average I_{AA}	Stat Error	Type A Sys Error	Type B Sys Error
279	0.2407	0.0478	0.0703	0.0501
150	0.3397	0.0935	0.1262	0.1560
60	0.5664	0.1578	0.1923	0.2331

Table B.20: The average I_{AA} for $p_{T,h} > 1 GeV/c, p_{T,\gamma} 5 - 12 GeV/c$ vs. N_{part} with systematic errors listed separately.

N_{part}	Average I_{AA}	Stat Error	Type A Sys Error	Type B Sys Error
279	0.2525	0.0458	0.0671	0.0526
150	0.3931	0.0896	0.1230	0.1553
60	0.6758	0.1444	0.1830	0.2258

Table B.21: I_{AA} vs $\xi = -\ln(z_T)$ for Run 7 0-20% Au+Au using the filltime method.

ξ	I_{AA}	Stat	+ Sys	- Sys
0.2	2.54e-01	4.18e-01	2.73e-01	2.77e-01
0.6	4.44e-01	3.53e-01	1.53e-01	1.62e-01
1.0	1.16e+00	4.68e-01	2.72e-01	2.95e-01
1.4	8.14e-01	6.03e-01	4.79e-01	5.29e-01
1.8	1.43e+00	4.90e-01	3.98e-01	4.28e-01
2.2	9.80e-01	6.08e-01	3.02e-01	3.23e-01
2.6	1.56e+00	8.56e-01	3.04e-01	3.32e-01

Table B.22: $\xi = -\ln(z_T)$ distributions from Run 7 0-20% Au+Au collisions for 5-15 GeV/c triggers

ξ	Yield	Stat	Total Sys	$R\gamma$	Decay	v_2	ABS
0.2	3.6e-3	3.9e-3	+8.1e-3	+1.8e-3	+3.9e-3	+6.8e-3	+2.8e-4
			-8.4e-3	-2.9e-3	-3.9e-3	-6.9e-3	-2.8e-4
0.6	2.0e-2	1.0e-2	+2.5e-2	+2.8e-3	+8.6e-3	+2.3e-2	+2.4e-3
			-2.5e-2	-4.4e-3	-8.6e-3	-2.3e-2	-2.4e-3
1.0	7.4e-2	2.5e-2	+3.0e-2	+3.9e-3	+2.2e-2	+1.3e-02	+1.4e-2
			-3.0e-2	-6.1e-3	-2.2e-2	-1.3e-2	-1.4e-2
1.4	1.3e-1	4.9e-2	+1.8e-1	+9.7e-3	+4.2e-2	+1.6e-01	+4.8e-2
			-1.8e-1	-1.6e-2	-4.2e-2	-1.6e-1	-4.8e-2
1.8	2.5e-1	7.6e-2	+2.8e-1	+1.1e-2	+6.7e-2	+2.5e-01	+1.0e-1
			-2.8e-1	-1.6e-2	-6.7e-2	-2.5e-1	-1.0e-1
2.2	3.4e-1	1.4e-1	+4.3e-1	+1.2e-2	+3.5e-2	+4.2e-01	+1.2e-1
			-4.3e-1	-1.7e-2	-3.5e-2	-4.2e-1	-1.2e-1
2.6	2.3e-2	2.3e-1	+1.5e-1	+6.3e-2	+3.2e-2	+2.4e-02	+1.3e-1
			-1.7e-1	-1.0e-1	-3.2e-2	-1.8e-2	-1.3e-1

Table B.23: Isolated Direct Photon ξ distributions from $p + p$ collisions

$p_{T,t}$ [GeV/c]	ξ	Yield	Stat	Sys.(low)	Sys(high)
5.64	-0.1000	0.0052	0.0022	0.0005	0.0023
5.64	0.1000	0.0082	0.0030	0.0011	0.0032
5.64	0.3000	0.0227	0.0043	0.0016	0.0046
5.64	0.5000	0.0285	0.0054	0.0032	0.0063
5.64	0.7000	0.0684	0.0072	0.0046	0.0085
5.64	0.9000	0.0909	0.0089	0.0069	0.0112
5.64	1.1000	0.1487	0.0112	0.0104	0.0152
5.64	1.3000	0.2007	0.0138	0.0153	0.0206
5.64	1.5000	0.2756	0.0165	0.0205	0.0263
7.73	0.1000	0.0007	0.0048	0.0008	0.0049
7.73	0.3000	0.0177	0.0083	0.0012	0.0084
7.73	0.5000	0.0339	0.0106	0.0017	0.0107
7.73	0.7000	0.0494	0.0140	0.0034	0.0144
7.73	0.9000	0.0541	0.0162	0.0053	0.0170
7.73	1.1000	0.1044	0.0203	0.0068	0.0214
7.73	1.3000	0.1737	0.0240	0.0080	0.0253
7.73	1.5000	0.2056	0.0280	0.0109	0.0300
7.73	1.7000	0.3132	0.0340	0.0140	0.0367
10.04	0.3000	0.0190	0.0113	0.0005	0.0113
10.04	0.5000	0.0230	0.0140	0.0011	0.0140
10.04	0.7000	0.0430	0.0185	0.0017	0.0186
10.04	0.9000	0.0744	0.0234	0.0026	0.0235
10.04	1.1000	0.1179	0.0292	0.0037	0.0295
10.04	1.3000	0.1036	0.0338	0.0079	0.0348
10.04	1.5000	0.2241	0.0427	0.0080	0.0434
10.04	1.7000	0.2170	0.0438	0.0096	0.0449
10.04	1.9000	0.2808	0.0507	0.0121	0.0521
13.13	0.7000	0.0620	0.0386	0.0015	0.0387
13.13	0.9000	-0.0090	0.0229	0.0044	0.0233
13.13	1.1000	0.0703	0.0524	0.0062	0.0527
13.13	1.3000	0.1988	0.0728	0.0044	0.0730
13.13	1.5000	0.1479	0.0743	0.0088	0.0748
13.13	1.7000	0.1371	0.0829	0.0180	0.0848
13.13	1.9000	0.3483	0.0937	0.0077	0.0940
13.13	2.1000	0.2066	0.0946	0.0159	0.0959
13.13	2.3000	0.2954	0.1106	0.0167	0.1119

Table B.24: Direct Photon p_{out} distributions from Au+Au collisions

$p_{T,t}$ [GeV]	p_{out}	Yield	Stat	Sys.(low)	Sys(high)
5.64	0.2500	0.1303	0.0396	0.0486	0.0626
5.64	0.7500	0.1902	0.0543	0.0195	0.0577
5.64	1.2500	0.0278	0.0417	0.0115	0.0432
5.64	1.7500	-0.0187	0.0186	0.0000	0.0186
5.64	2.2500	0.0083	0.0086	0.0008	0.0087
5.64	2.7500	0.0072	0.0044	0.0006	0.0044
5.64	3.2500	0.0049	0.0026	0.0003	0.0026
5.64	3.7500	0.0006	0.0015	0.0000	0.0015
5.64	4.2500	-0.0001	0.0010	0.0000	0.0010
5.64	4.7500	-0.0002	0.0007	0.0000	0.0007
5.64	5.2500	-0.0003	0.0005	0.0000	0.0005
5.64	5.7500	0.0002	0.0005	0.0000	0.0005
7.73	0.2500	0.0344	0.0709	0.0223	0.0743
7.73	0.7500	0.0413	0.0972	0.0243	0.1001
7.73	1.2500	0.0389	0.0745	0.0096	0.0752
7.73	1.7500	0.0154	0.0334	0.0029	0.0335
7.73	2.2500	-0.0008	0.0152	0.0000	0.0152
7.73	2.7500	-0.0010	0.0081	0.0000	0.0081
7.73	3.2500	0.0012	0.0046	0.0001	0.0046
7.73	3.7500	0.0027	0.0032	0.0001	0.0032
7.73	4.2500	0.0048	0.0025	0.0002	0.0025
7.73	4.7500	0.0027	0.0018	0.0002	0.0018
10.04	0.2500	0.0682	0.1150	0.0355	0.1204
10.04	0.7500	0.1400	0.1578	0.0282	0.1603
10.04	1.2500	-0.0058	0.1203	0.0000	0.1203
10.04	1.7500	-0.0146	0.0533	0.0000	0.0533
10.04	2.2500	0.0210	0.0250	0.0018	0.0251
10.04	2.7500	-0.0027	0.0130	0.0000	0.0130
10.04	3.2500	0.0036	0.0072	0.0004	0.0072
10.04	3.7500	-0.0047	0.0037	0.0000	0.0037
13.13	0.2500	0.4450	0.2292	0.2359	0.3289
13.13	0.7500	-0.1821	0.3053	0.0000	0.3053
13.13	1.2500	-0.1019	0.2385	0.0000	0.2385
13.13	1.7500	0.1052	0.1063	0.0126	0.1070
13.13	2.2500	0.0068	0.0466	0.0032	0.0467
13.13	2.7500	0.0047	0.0261	0.0008	0.0261
13.13	3.2500	0.0052	0.0134	0.0014	0.0134
13.13	3.7500	0.0118	0.0123	0.0012	0.0123